Finite Element Analysis of a Functionally Graded Shaft with Transverse Cracks in a Rotor-Bearing System

A Thesis Submitted
in Partial Fulfillment of the Requirements
for the Degree of

DOCTOR OF PHILOSOPHY

by
Debabrata Gayen
(136103017)

Department of Mechanical Engineering
Indian Institute of Technology Guwahati
Guwahati – 781039, Assam, India
January – 2019

Department of Mechanical Engineering
Indian Institute of Technology Guwahati
Guwahati – 781039, Assam, India

CERTIFICATE

It is certified that the work contained in the thesis entitled **"Finite Element Analysis of a Functionally Graded Shaft with Transverse Cracks in a Rotor-Bearing System"** submitted by **Debabrata Gayen** to the Indian Institute of Technology Guwahati for the award of the degree of Doctor of Philosophy has been carried out under our supervision in the Department of Mechanical Engineering, Indian Institute of Technology Guwahati. This work has not been submitted elsewhere for the award of any other degree.

(Dr. Debabrata Chakraborty)
Professor
Department of Mechanical Engineering
Indian Institute of Technology Guwahati
Guwahati – 781039, Assam, India

(Dr. Rajiv Tiwari)
Professor
Department of Mechanical Engineering
Indian Institute of Technology Guwahati
Guwahati – 781039, Assam, India

Dedicated to my

Father – Nirmal Gayen

Mother – Rani Bala Gayen

Wife – Bithika Gayen

Daughter – Sreeja Gayen

Elder brother – Debprasad Gayen

ACKNOWLEDGEMENTS

This thesis is an outcome over the tenure of five and half years of research work at Indian Institute of Technology Guwahati and during this long period, I have been guided, supported and accompanied by many people. I now have the opportunity to acknowledge my indebtedness to all of them.

At very first, I would like to express my deepest appreciation and sincere gratitude to my supervisors Prof. Debabrata Chakraborty and Prof. Rajiv Tiwari, for their invaluable guidance and constant support, valuable advice and useful suggestions throughout the course of this thesis effort. I sincerely believe that without their inspiration and the guidelines, the research work would not have been possible. Their untiring guidance, demand for excellence, encouragement, experience and technical expertise brought the best from me, to complete this fruitfully.

I would like to offer my special thanks to my doctoral committee members, Prof. P. S. Robi, Prof. A. Dutta and Prof. K. S. R. K. Murthy for their remarkable advice, suggestions, comments and recommendations. I could not forget the contribution of Dr. Tarapada Roy, supervisor of Master Thesis at NIT Rourkela, India, who actually motivated me to undertake my PhD studies. I would like to thank to all the faculty members of Mechanical Engineering Department, IIT Guwahati in general and the Head Mechanical Engineering in particular for providing me a conducive environment to pursue my research work.

I would like to kindly acknowledge the financial assistance offered by Ministry of Human Resource Development, Govt. of India, during the doctoral program.

I would like to extend my thanks particularly to my colleague and friends Mr. Pranjol Paul, Mr. Sanjib Sarma, Sajith, Debleena, Mirzaul, Shahnawaz, Kamal, Sibananda, Vignesh, Dipendra, Pradeep, Abhishek, and other research scholars who helped me by allowing me to discuss and share my research related issues.

Last but not least, I wish express my immense gratitude to my *parents*, *family members* and especially my *wife* and daughter *Sreeja* for their endless love, patience, constant encouragement and infinite moral support, without which, I would not have been able to overcome many difficulties and challenges during this journey.

7th January 2019

IIT Guwahati Debabrata Gayen

Table of Contents

Abstract vii

Nomenclatures ix

Abbreviations xiii

List of Figures xv

List of Tables xix

Chapter 1 Introduction 1

1.1 Functionally graded materials (FGMs) – A brief insight 2

1.1.1 Background and importance 2

1.1.2 Gradient description of FGMs 3

1.1.3 Fabrication techniques of FGMs 5

1.1.4 Applications of FGMs 7

1.2 Rotor dynamics – A brief history and importance 11

1.2.1 Rotor-Bearing system – Importance 13

1.2.2 Internal damping – Importance 14

1.2.2.1 Internal viscous damping model 16

1.2.2.2 Internal hysteretic damping model 16

1.2.3 Cracked rotor/shaft – Overview and importance 18

1.2.3.1 Classification of crack in rotor/shaft 19

1.2.3.2 Fracture mechanics concept in rotor dynamics 21

1.3 Functionally graded cracked rotor/shaft – Importance 25

1.4 Research motivation 26

1.5 Thesis organization 27

`

Chapter 2 Literature Review **29**

2.1 Introduction 29

2.2 Functionally graded uncracked structures 30

2.2.1 Influences of temperature gradient 30

2.2.2 Buckling and post-buckling analysis 31

2.2.3 Vibration analysis 31

2.3 Homogeneous rotor-bearing system 32

2.4 Homogeneous cracked structures 35

2.4.1 Fracture and static analysis 36

2.4.2 Vibration analysis 37

2.4.3 Crack detection and identification 40

2.4.4 Stability analysis 41

2.5 Functionally graded cracked structures 42

2.5.1 Fracture analysis of FGM 43

2.5.2 Static analysis of FGM 44

2.5.3 Vibration analysis of FGM 46

2.5.4 Crack detection and identification 50

2.5.5 Dynamic analysis of FGM 51

2.6 Summary of literature review and gaps 52

2.7 Scope of the present work 54

2.8 Objectives of the present work 55

Chapter 3 Finite Element Formulation of a Rotor-Bearing System with a cracked FG Shaft **57**

3.1 Introduction 57

3.2 Modeling of functionally graded material properties 57

3.2.1 Estimation of effective material properties of FGMs 57

3.2.2 Steady-state temperature distributions 59

3.3 Rotor-Bearing system 61
3.3.1 Finite shaft element 62
3.3.2 Rigid disc 67
3.3.3 Consideration of bearings 68
3.3.4 Incorporation of internal damping 68
3.4 Modeling of transverse crack behavior on an FG shaft 71
3.4.1 Stationary transverse surface crack 71
3.4.2 Formulation of local flexibility coefficients for a rotating cracked shaft 78
3.5 System equations of motion 79
3.6 Solution procedure 79
3.7 Summary 81

Chapter 4 Transverse Vibration Analysis of a Rotor-Bearing System having an FG Shaft with Stationary Transverse Crack 83

4.1 Introduction 83
4.2 Rotor-Bearing system details 83
4.3 Convergence study and validations 85
4.3.1 A uniform non-rotating simply supported shaft 85
4.3.2 Whirling frequencies of a rotor-bearing system 87
4.3.3 Local flexibility coefficients of a shaft with stationary crack 88
4.3.4 Natural frequencies of a simply supported cracked shaft 88
4.3.5 Natural frequencies with boundary condition for a cracked FG beam 89
4.4 FE Analysis of an FG shaft with a transverse crack 90
4.4.1 Material properties variation for an FG shaft 90
4.4.2 Variation of dimensionless LFCs for an FG shaft 91
4.5 Analysis of a non-rotating FG cracked shaft 96
4.5.1 Variation of natural frequencies with α/R for metal and FG shaft 96
4.5.2 Effect of α/R and k on natural frequency 97

4.5.3 Effect of α/R and L_c/L on natural frequency 99

4.5.4 Effect of α/R and L/D on natural frequency 103

4.5.5 Effect of ΔT on natural frequency 103

4.5.6 Influences of k, α/R and ΔT on natural frequencies for an FGM II shaft 104

4.5.7 Influence of types of FGM on natural frequency 107

4.6 Analysis of a rotor-bearing system with a cracked FG shaft 108

4.6.1 Influences of k, α/R and ΔT on whirling frequencies 108

4.6.2 Influences of k and α/R on critical speeds 114

4.6.3 Influence of k on reduction in fundamental frequency, whirling frequency and critical speeds 115

4.7 Summary 115

Chapter 5 Transverse Vibration Analysis of a Rotor-Bearing System having an FG Shaft with Transverse Breathing Cracks 117

5.1 Introduction 117

5.2 Rotor-Bearing system details 118

5.3 Validations 119

5.3.1 Whirling frequencies of a rotor-bearing system with un-damped bearings 119

5.3.2 LFCs of a homogeneous shaft with breathing crack 120

5.3.3 Effect of double cracks on natural frequencies 120

5.4 Analysis of an FG shaft with transverse breathing crack 121

5.4.1 Variation of dimensionless LFCs for an FG shaft 121

5.5 Analysis of non-rotating FG shaft without/with cracks 124

5.5.1 Effect of k and ΔT on natural frequency for an FG uncracked shaft 126

5.5.2 Effect of k and ΔT on natural frequency for an FG shaft with a single transverse crack 127

5.5.3 Effect of L_{c2}/L on natural frequency for an FG shaft with two transverse cracks 128

5.5.4 Effect of θ_2 on natural frequency for an FG shaft with two transverse cracks 130

5.6 Analysis of a rotor-bearing system having an FG shaft with two transverse breathing cracks 134

5.6.1 Influences of L_{c2}/L, k and ΔT with θ_2 on whirling frequencies 134

5.6.2 Influences of k and θ_2 on critical speeds 137

5.7 Summary 138

Chapter 6 Stability Analysis of a Rotor-Bearing System having an FG Shaft with Transverse Breathing Cracks 141

6.1 Introduction 141

6.2 Rotor-Bearing system details 141

6.3 Validations 144

6.3.1 Natural frequencies and damping ratios of a rotor-bearing system with damped bearing 144

6.3.2 Influences of internal damping on whirling frequencies and logarithmic decrement 146

6.3.3 Effect of crack size, η_v and η_h on the stability threshold speed for a cracked rotor system 147

6.4 Influence of L/D, k, ΔT, disc, η_v and η_h on stability threshold speed of a rotating FG shaft in a rotor-bearing system 148

6.5 Influence of α/R, k, ΔT, η_v and η_h on stability threshold speed of a rotor-bearing system having an FG shaft with single crack 152

6.6 Influence of α_2/R, L_{c2}/L, θ_2, k and ΔT on stability threshold speed of a rotor-bearing system having an FG shaft with two transverse breathing cracks 158

6.6.1 Effect of relative location of second crack (L_{c2}/L) 159

6.6.2 Effect of relative orientation of second crack (θ_2) 162

6.7 Summary 168

Chapter 7 Conclusions and Scope of Future Work 171

7.1 General conclusions 171

7.2 Specific conclusions 172

7.2.1 Transverse vibration analysis of a FG shaft system with stationary transverse crack 172

7.2.2 Transverse vibration analysis of a FG shaft system with transverse breathing cracks 173

7.2.3 Stability analysis of a FG shaft system with transverse breathing cracks 174

7.3 Novelty and major contribution from the thesis 175

7.4 Scope for future work 175

Appendix A : Elementary matrices 177

A.1 Elementary translational mass matrix for a FG shaft 177

A.2 Elementary rotational mass matrix for a FG shaft 178

A.3 Elementary gyroscopic matrix for a FG shaft 179

A.4 Elementary stiffness matrix for a FG shaft 180

A.5 Elementary matrices for a rigid disc 180

A.6 Elementary circulatory stiffness matrix for a FG shaft 181

Appendix B : Pseudo-code 183

References 185

List of Publications 201

About the Author 205

Abstract

During last few decades, functionally graded materials (FGMs) have been recognized as future advanced composite material, featuring thermo-mechanical loading, multi functionality and gradation at micro and nano scales. In many rotating machineries, like gas turbine, steam turbine, shafts, blades etc. are exposed to very high temperature environment. Due to their superior performances in high temperature applications, these FGMs are also recognized as potential materials for rotating machinery components like shafts, blades etc. Similar to homogeneous structures, presence of cracks in functionally graded (FG) shafts also make a serious threat to their safe performances. It is therefore important to understand the dynamic behavior of such FG shafts under loading. Therefore, the present dissertation deals with finite element (FE) formulation and analysis of a FG shaft with transverse breathing crack/cracks in a rotor-bearing system. The FG rotor system is considered to comprise a set of interconnecting components consisting of shaft elements with internal viscous and hysteretic damping, rigid discs and bearings. Hamilton's principle and Lagrangian equation have been used to derive the equations of motion for FG shaft element and rigid disc element respectively. Two noded Timoshenko beam element with four degrees of freedom (DOF) per node is used considering the effects of translational and rotary inertia, transverse shear deformations, and gyroscopic moments. The FG material is considered to be composed of aluminum oxide (Al_2O_3) and zirconia (ZrO_2) as ceramics and stainless steel (SS) as metal. Temperature dependent thermo-elastic material properties of the FG shaft are considered graded in the radial direction following power law of material gradation. Fracture mechanics concepts have been combined with rotor dynamical system to obtained stress intensity factors (SIFs) as well as local flexibility coefficients (LFCs) of cracked FG shafts, which change the system dynamic behavior globally. Considering breathing crack, the LFCs are determined analytically as a function of size and orientation of crack, power law gradient index and temperature using the Castigliano's theorem and Paris's equations to compute the stiffness matrix of the cracked FG shaft in the FE analysis. Based on the formulation, an FE computer code has been developed using MATLAB for dynamic analysis of rotor bearing system having a cracked FG shaft and validated with the analytical and FE solutions reported in literatures.

Numerical simulation have been performed to study the behavior of cracked FG shafts under different conditions and considering different configuration and effect of some important parameters on the dynamic behavior of FG shafts are studied. Numerical results show that for a cracked FG shaft, the magnitude of LFCs is significantly affected by material gradient index thus influencing the performance. Results also show that the gradient index has significant influence on the natural whirling frequencies and critical speed for both un-cracked and cracked FG shaft and the gradient index could be judiciously chosen in designing of such FG shafts. Numerical results show that the choice of power law gradient index has significant importance on the dynamic behavior of an FG shaft in the event of multiple transverse cracks appearing and it is possible to decide gradation parameter in damage tolerant design of such shafts. Results from stability analysis show that while the depths, orientations and locations of cracks and temperature gradient along with damping properties of materials affect the stability threshold speed, the choice of power law gradient index has significant importance on the threshold speed in the event of multiple transverse cracks surfacing on the FG shaft. The present formulation could be useful in damage tolerant designing of FG shaft in high temperature applications where the desired range of stability threshold speed could be achieved.

Nomenclatures

Symbols

A	Cross section area of the shaft material
$C(T)$	Material properties as a function of temperature
$C(y,T)$	Material properties as a function of position and temperature
C_{11}^c, C_{22}^c, C_{33}^c, C_{34}^c, C_{44}^c	Local flexibility coefficients due to crack
$\overline{C}_{11}$, $\overline{C}_{22}$, $\overline{C}_{33}$, $\overline{C}_{34}$, $\overline{C}_{44}$	Dimensionless local flexibility coefficients
$\left[\mathbf{C}^e\right]$	Elementary damping matrix
D	Diameter of the shaft
E	Young's modulus of the shaft material
EI	Bending stiffness of the shaft material
$f(t)$	Opening-closing function
$\{\mathbf{F}\}$	Global external force vector including the shaft, disc and bearing
F_1, F_2, F_{II}, F_{III}	Form factors for different modes
$\left\{\mathbf{F}_{total}^e(t)\right\}$	Total elementary external force vector
G	Modulus of rigidity of the shaft material
$\left[\mathbf{G}^e\right]$	Total elementary gyroscopic matrix including shaft and rigid disc
$[\mathbf{G}]$	Global gyroscopic matrix including the shaft and rigid disc
I	Area moment of inertia of the shaft
I_d^s	Diametrical mass of inertia of the shaft
I_p^s	Polar mass of inertia of the shaft
$J(y,T)$	Strain energy density function
K	Thermal conductivity of the shaft material
$[\mathbf{K}]$	Global stiffness matrix including un-cracked and cracked shaft
$\left[\mathbf{K}^e\right]$	Elementary stiffness matrix of the shaft
$[\mathbf{K}_c]$	Global circulation stiffness matrix of the shaft

$\left[\mathbf{K}_c^e\right]$	Elementary circulation stiffness matrix of the shaft
K_{I}, K_{II} and K_{III}	SIFs of modes I, II, and III respectively
L	Total length of the shaft
L_e	Element length of the shaft
L_{c1}	Distance of first crack from the left end of the shaft
L_{c2}	Distance of second crack from the left end of the shaft
L/D	Slenderness ratio
L_c/L	Location of crack
L_{c1}/L	Location of first crack
L_{c2}/L	Location of second crack
m	Element mass per unit length
$[\mathbf{M}]$	Global mass matrix including the shaft and rigid disc
$\left[\mathbf{M}^e\right]$	Total elementary mass matrix including the rotary and translational masses of the shaft and rigid disc
P_1, P_2, P_5, and P_6	Shear forces
P_3, P_4, P_7, and P_8	Bending moments
P_{ext}	Externally applied load
$\left\{\mathbf{P}^e(t)\right\}$	Elementary nodal displacement vector
R	Radius of the shaft
T	Temperature
ΔT	Temperature gradient
u_i^c	Additional displacement due to crack of shaft
U^c	Additional strain energy due to crack of shaft
v	Nodal translation displacement along Y direction
w	Nodal translation displacement along Z direction
y	Radial direction

Greek letters

α	Depth of the crack
α/R	Size of crack
α_1	Depth of the first crack
α_1/R	Size of first crack
α_2	Depth of the second crack
α_2/R	Size of second crack
β	Nodal rotational displacement about Y axis
Γ	Nodal rotational displacement about Z axis
δ	Logarithmic decrement
ε_x	Axial strain
η_v	Shaft's internal viscous damping
η_h	Shaft's internal hysteresis damping
θ ($\theta = \Omega t$)	Crack orientation angle
θ_1 and θ_2	First and second crack orientation angle, respectively
κ_{sc}	Shear correction factor
$\lambda(\Omega)$	Speed dependent general complex eigenvalue
ν	Poisson's ratio
ξ	Damping ratio
$[\Pi]$	Transformation matrix
ρ	Mass density of the shaft material
σ_x	Axial stress
$\varphi(s)$	Rotational shape function
Φ	Shear deformation parameter
$\psi(s)$	Translation shape function
ω	Natural frequency
ϖ	Dimensionless natural frequency
Ω	Spin speed
$\overline{\Omega}_{\text{th}}$	Normalized threshold speed

Subscripts

b	Bending
d	Diametric
i	Inner
n	Mode number
o	Outer
p	Polar
r	Rotational
s	Shear
sc	Shear correction
t	Translation
tb	Bending translation
ts	Shear translation

Superscripts

b	Bearing
c	Crack
d	Disk
e	Element
k $(0 \leq k \leq \infty)$	Power law gradient index
n	Sigmoid law gradient index
s	Shaft
uc	Uncrack
$'$	Differentiation with respect to position
$\cdot$	Differentiation with respect to time

Abbreviations

Al_2O_3	Aluminium oxide
DOFs	Degrees of freedom
DQM	Differential quadrature method
E – FGM	Exponential law of material gradation
EBBT	Euler–Bernoulli beam theory
EOMs	Equations of motion
FE	Finite element
FEA	Finite element analysis
FEM	Finite element method
FG	Functionally graded
FGMs	Functionally graded materials
FOSDT	First order shear deformation theory
TOSDT	Third order shear deformation theory
HOSDT	Higher order shear deformation theory
LFCs	Local flexibility coefficients
P – FGM	Power law of material gradation
SERR	Strain energy release rate
S – FGM	Sigmoid law of material gradation
SIF	Stress intensity factor
SR	Slenderness ratio
SS	Stainless steel
TBT	Timoshenko beam theory
TMM	Transfer matrix method
ZrO_2	Zirconia

List of Figures

Fig. 1.1	Different types of FG microstructures [6]	5
Fig. 1.2	Processing methods of FGMs [7]	5
Fig. 1.3	Lathe bits type [9]: (a) conventional bi-material and (b) FGM	7
Fig. 1.4	Turbine blade and material properties [10]	8
Fig. 1.5	Schematic diagram of a FGM interface within a prosthesis [9]	8
Fig. 1.6	Schematic diagram: (a) FG disc model [11] and (b) shaft made of a three-phase FGM [12]	9
Fig. 1.7	Potentially applicable fields for FGMs	10
Fig. 1.8	A rotor-disc-bearing system: (a) rigid rotor with flexible bearings (b) flexible rotor with rigid bearings and (c) flexible rotor with flexible bearings	11
Fig. 1.9	A schematic diagram of a rotor-bearing system	13
Fig. 1.10	Stress-strain phasor	14
Fig. 1.11	Internal viscous damping model	16
Fig. 1.12	Stress-strain phasor diagram	16
Fig. 1.13	Crack developed in: (a) stiffening plate of a generator and (b) blade root of a steam turbine [23]	19
Fig. 1.14	A schematic diagram of a rotor with transverse crack, longitudinal crack and slant crack	20
Fig. 1.15	Three modes of fracture	21
Fig. 2.1	A flow chart highlighting the classification of literature review	29
Fig. 3.1	Material properties gradation in radial direction	59
Fig. 3.2	Typical finite shaft element and coordinate system	61
Fig. 3.3	Geometry of a disc mounted on a shaft	67
Fig. 3.4	A cracked FG shaft element: (a-b) FE discretization (c) shaft element with general loading and (d) geometry of the cracked cross-section	72
Fig. 3.5	Opening-closing function $f(t)$ of breathing crack during rotation of the shaft [97]	78
Fig. 3.6	A general flow chart highlighting the overall module and solving the eigenvalue problem	82
Fig. 4.1	A cracked FG shaft with FE discretization (a) simply supported ends and (b) flexible end bearings	84

Fig. 4.2	Schematic diagram of a rotor-disc-bearing system	87
Fig. 4.3	Young's modulus variation along the radial direction in an FG (SS/ZrO_2) shaft for $\Delta T = 0$ K	90
Fig. 4.4	Variation of material properties with functions of radial position, power law gradient index and temperature gradient: (a) Young's modulus (b) Poisson's ratio and (c) thermal conductivity	91
Fig. 4.5	Variation of LFCs with α/R and k for FGM I: **(a)** $\bar{C}_{11}$ **(b)** $\bar{C}_{22}$ **(c)** $\bar{C}_{33}$ **(d)** $\bar{C}_{34}$ and **(e)** $\bar{C}_{44}$	92
Fig. 4.6	Variation of LFCs with α/R and k for FGM II: **(a)** $\bar{C}_{11}$ **(b)** $\bar{C}_{22}$ **(c)** $\bar{C}_{33}$ **(d)** $\bar{C}_{34}$ and **(e)** $\bar{C}_{44}$	93
Fig. 4.7	Variation of LFCs with α/R and ΔT for FGM I: **(a)** $\bar{C}_{11}$ **(b)** $\bar{C}_{22}$ **(c)** $\bar{C}_{33}$ **(d)** $\bar{C}_{34}$ and **(e)** $\bar{C}_{44}$	94
Fig. 4.8	Variation of LFCs with α/R and ΔT for FGM II: **(a)** $\bar{C}_{11}$ **(b)** $\bar{C}_{22}$ **(c)** $\bar{C}_{33}$ **(d)** $\bar{C}_{34}$ and **(e)** $\bar{C}_{44}$	95
Fig. 4.9	Variation of natural frequencies with α/R and k: **(a)** first **(b)** second **(c)** third **(d)** fourth **(e)** fifth and **(f)** sixth	98
Fig. 4.10	Variation of natural frequencies with L_c/L and α/R: **(a)** first **(b)** second **(c)** third **(d)** fourth **(e)** fifth and **(f)** sixth	100
Fig. 4.11	Variation of natural frequencies with L_c/L and k: **(a)** first **(b)** second **(c)** third **(d)** fourth **(e)** fifth and **(f)** sixth	101
Fig. 4.12	Variation of natural frequencies with L/D and α/R: **(a)** first **(b)** second **(c)** third **(d)** fourth **(e)** fifth and **(f)** sixth	102
Fig. 4.13	Campbell diagram of a rotor-bearing system with an uncracked FG shaft for different k **(a)** first mode **(b)** second mode and **(c)** third mode	111
Fig. 4.14	Campbell diagram of a rotor-bearing system with an uncracked FG shaft for different ΔT **(a)** first mode **(b)** second mode and **(c)** third mode	112
Fig. 4.15	Campbell diagram of a rotor-bearing system with a FG shaft for different α/R **(a)** first mode **(b)** second mode and **(c)** third mode	113
Fig. 5.1	Rotor-Bearing system having a cracked FG shaft with FE discretization: (a) simply supported ends (b) flexible end bearings	117
Fig. 5.2	Schematic diagram of a rotor-disc-bearing system	119

Fig. 5.3	Variation of LFCs with θ for different α/R **(a)** $\overline{C}_{11}$ **(b)** $\overline{C}_{22}$ **(c)** $\overline{C}_{33}$ **(d)** $\overline{C}_{34}$ and **(e)** $\overline{C}_{44}$	122
Fig. 5.4	Variation of LFCs with θ for different k **(a)** $\overline{C}_{11}$ **(b)** $\overline{C}_{22}$ **(c)** $\overline{C}_{33}$ **(d)** $\overline{C}_{34}$ and **(e)** $\overline{C}_{44}$	123
Fig. 5.5	Variation of LFCs with θ for different ΔT **(a)** $\overline{C}_{11}$ **(b)** $\overline{C}_{22}$ **(c)** $\overline{C}_{33}$ **(d)** $\overline{C}_{34}$ and **(e)** $\overline{C}_{44}$	125
Fig. 5.6	Percentage reduction in fundamental frequency for an uncracked FG shaft with ΔT and k	126
Fig. 5.7	Percentage reduction of natural frequency for a centrally located cracked FG shaft with ΔT and k (a) vertical plane and (b) horizontal plane	128
Fig. 5.8	Percentage reduction of natural frequency for a FG shaft with double cracks with k and L_{c2}/L (a) vertical plane and (b) horizontal plane	129
Fig. 5.9	Percentage reduction of natural frequency for a FG shaft with double cracks with ΔT and L_{c2}/L (a) vertical plane and (b) horizontal plane	130
Fig. 5.10	Percentage reduction of natural frequency for a FG shaft with double cracks with L/D and θ_2 for $k=5.0,\ \Delta T=0$ K, $\theta_1=180°$ (a) vertical plane and (b) horizontal plane	131
Fig. 5.11	Percentage reduction of natural frequency for a FG shaft with double cracks with k and θ_2 for $L/D=12.5,\ \Delta T=0$ K, $\theta_1=180°$ (a) vertical plane and (b) horizontal plane	131
Fig. 5.12	Percentage reduction of natural frequency for a FG shaft with double cracks with ΔT and θ_2 for $L/D=12.5,\ k=5.0,\ \theta_1=180°$ (a) vertical plane and (b) horizontal plane	132
Fig. 5.13	Percentage reduction of natural frequency for a FG shaft with double cracks with α_2/R and θ_2 for $k=5.0,\ \Delta T=0$ K, $\theta_1=180°$ (a) vertical plane and (b) horizontal plane	133
Fig. 5.14	Percentage reduction of natural frequency for a FG shaft with double cracks with L_{c2}/L and θ_2 for $k=5.0,\ \Delta T=0$ K, $\theta_1=180°$ (a) vertical plane and (b) horizontal plane	134
Fig. 6.1	A rotor-disc-bearing system with a cracked FG shaft: (a) FE discretization with simply supported ends (b) FE discretization with flexible end bearings and (c) coordinate system and general loading	142

Fig. 6.2	Schematic diagram of a two-disc rotor-bearing system	145
Fig. 6.3	Campbell diagram of a FG shaft system for $k = 0.5$ with $\eta_v = 0.0015$ s and $\eta_h = 0.0015$	151
Fig. 6.4	Campbell diagram of a FG shaft system for $k = 5.0$ with $\eta_v = 0.0006$ s and $\eta_h = 0.0006$	151
Fig. 6.5	Campbell diagram of a rotor system having a shaft made of SS with $\eta_v = 0.0002$ s and $\eta_h = 0.0002$	152
Fig. 6.6	Variation in $\overline{\Omega}_{\text{th}}$ with k and α/R for $L/D = 12.5$, $\Delta T = 0$ K, $L_c/L = 0.5$ of a FG shaft system	154
Fig. 6.7	Variation in $\overline{\Omega}_{\text{th}}$ of a FG shaft supported on simply supported ends for $L/D = 12.5$, $L_c/L = 0.5$, $k = 5.0$, $\Delta T = 0$ K with α/R and different (a) η_h for $\eta_v = 0.0006$ s and (b) η_v for $\eta_h = 0.0006$	155
Fig. 6.8	Variation in $\overline{\Omega}_{\text{th}}$ of a FG shaft supported on flexible end bearings for $L/D = 12.5$, $L_c/L = 0.5$, $k = 5.0$, $\Delta T = 0$ K with α/R and different (a) η_h for $\eta_v = 0.0006$ s and (b) η_v for $\eta_h = 0.0006$	156
Fig. 6.9	Variation in $\overline{\Omega}_{\text{th}}$ with k and L_{c2}/L for $L/D = 12.5$, $L_{c1}/L = 0.50$, $\Delta T = 0$ K, $\alpha_1/R = \alpha_2/R = 0.8$ and $\theta_1 = \theta_2 = 180°$ of a FG shaft supported on (a) simply supported ends and (b) flexible end bearings	161
Fig. 6.10	Variation in $\overline{\Omega}_{\text{th}}$ with k and θ_2 for $L/D = 12.5$, $L_{c1}/L = 0.50$, $L_{c2}/L = 0.34$, $\alpha_1/R = \alpha_2/R = 0.8$, $\Delta T = 0$ K and $\theta_1 = 180°$ of a FG shaft supported on (a) simply supported ends and (b) flexible end bearings	164
Fig. 6.11	Variation in $\overline{\Omega}_{\text{th}}$ with α_2/R and θ_2 for $k = 5.0$, $\Delta T = 0$ K, $\eta_v = 0.0006$ s and $\eta_h = 0.0006$ of a FG shaft supported on (a) simply supported ends and (b) flexible end bearings	166
Fig. 6.12	Variation in $\overline{\Omega}_{\text{th}}$ with L_{c2}/L and θ_2 for $k = 5.0$, $\Delta T = 0$ K, $\eta_v = 0.0006$ s and $\eta_h = 0.0006$ of a FG shaft supported on (a) simply supported ends and (b) flexible end bearings	167

List of Tables

Table 1.1	General information of FGMs [7-9]	7
Table 1.2	FGMs with significance properties and applications [5, 7-10 and 13]	9
Table 2.1	Representation of published articles on FG rotor/shaft	53
Table 3.1	Temperature coefficients value for different mechanical properties [27] of FGMs	58
Table 4.1	Temperature coefficients value for different mechanical properties [27] of FGMs	84
Table 4.2	Dimensionless natural frequencies ϖ_n of uniform non-rotating simply supported beams	86
Table 4.3	Dimensionless first natural frequencies ϖ_n of a uniform non-rotating Timoshenko beam	86
Table 4.4	Dimensionless natural frequencies of a uniform non-rotating simply supported Timoshenko beam	87
Table 4.5	Comparison of natural frequencies (in Hz) for the rotor-bearing system	87
Table 4.6	Dimensionless compliance $\overline{C}_{33}$ and $\overline{C}_{44}$ as a function of α/R	88
Table 4.7	Variation of dimensionless natural frequencies with α/R for different L/D	89
Table 4.8	Variation of dimensionless natural frequencies with end conditions for a cracked FG beam	89
Table 4.9	Variation of natural frequencies (in Hz) with different α/R for metal and FG shaft	97
Table 4.10	Variation of natural frequencies (in Hz) of a cracked FG shaft with α/R and ΔT	103
Table 4.11	Variation of natural frequencies (in Hz) of a cracked FG shaft with L_c/L and ΔT	104
Table 4.12	Variation of ϖ_n with k for a non-rotating simply supported FGM II (SS/ZrO_2) shaft	105
Table 4.13	Variation of ϖ_n with α/R for a non-rotating simply supported FGM II (SS/ZrO_2) shaft for $L_c/L=0.5$ and $k=0.5$	106

Table 4.14	Natural frequency parameters ϖ_n of a non-rotating simply supported FGM II (SS/ZrO_2) shaft for $L_c/L=0.5$ and $\alpha/R=0.6$	106
Table 4.15	Variation of ω_n (in Hz) with k for non-rotating simply supported cracked ($\alpha/R=0.6$ and $L_c/L=0.5$) FG shafts	107
Table 4.16	Variation of ω_n (in Hz) with α/R for non-rotating simply supported cracked ($k=0.5$ and $L_c/L=0.5$) FG shafts	108
Table 4.17	Whirling frequencies ω (in Hz) of a FG (SS/ZrO_2) shaft with isotropic un-damped flexible bearings at $\Omega=66.667$ Hz	109
Table 4.18	Whirling frequencies ω (in Hz) of a FG (SS/ZrO_2) shaft with isotropic un-damped flexible bearings at $\Omega=66.667$ Hz for $L_c/L=0.5$ and $k=0.5$	110
Table 4.19	Whirling frequencies ω (in Hz) of a FG (SS/ZrO_2) shaft with isotropic un-damped flexible bearings at $\Omega=66.667$ Hz for $L_c/L=0.5$ and $\alpha/R=0.6$	110
Table 4.20	Critical speeds (in Hz) for a rotor-bearing system with a uniform FG shaft	114
Table 4.21	Percentage change in frequencies for a rotor-bearing system with a uniform FG shaft	115
Table 5.1	Temperature coefficients value for different mechanical properties of FGM [27]	118
Table 5.2	Natural frequencies (in Hz) at $\Omega=4000$ rpm for a rotor-bearing system	120
Table 5.3	Variation of local flexibility coefficients g_{22} and g_{33} with a function of θ	120
Table 5.4	Variation of first dimensionless natural frequencies with depth and location of second crack for $\alpha_1/R=0.2$, $L_{c1}/L=0.35$ and $L/D=8$	121
Table 5.5	Variation of natural frequency (in rad/s) for an uncracked FG shaft with ΔT and k	126
Table 5.6	Variation of natural frequency (in rad/s) for a centrally located cracked FG shaft with ΔT and k	127
Table 5.7	Whirling frequency (in rad/s) of an uncracked FG shaft system	135

Table 5.8	Percentage reduction in whirling frequency with L_{c2}/L and θ_2 for a FG shaft system	136
Table 5.9	Percentage reduction in whirling frequency with k and θ_2 for a FG shaft system	136
Table 5.10	Percentage reduction in whirling frequency with ΔT and θ_2 for a FG shaft system	137
Table 5.11	Percentage reduction in critical speed with k and θ_2 for a FG shaft system	138
Table 6.1	Temperature coefficients value for different mechanical properties of FGM [27]	144
Table 6.2	Variation of internal damping coefficients (η_v and η_h) with power law gradient index k	144
Table 6.3	Eigen frequencies (Hz) and damping ratios for a rotor-disc system with an isotropic damped bearing	145
Table 6.4	Influence of η_h on ϖ_n for a uniform non-rotating simply supported shaft	146
Table 6.5	Influence of η_v and η_h on ω_n for a shaft system at a spin speed $\Omega = 4000$ rpm	147
Table 6.6	Influence of η_v and η_h on δ for a shaft system at a spin speed $\Omega = 4000$ rpm	147
Table 6.7	Variation in normalized Ω_{th} with α/R for different η_v and η_h and $L/D = 8.0$	148
Table 6.8	Stability threshold speed Ω_{th} (in rpm) of a two-disc rotor system considering an isotropic un-damped bearing with L/D, k and ΔT for η_v and η_h corresponding to k and ΔT	149
Table 6.9	Stability threshold speed Ω_{th} (in rpm) of a rotor-bearing system considering an isotropic un-damped bearing with k and ΔT for $L/D = 12.5$ and for η_v and η_h corresponding to k and ΔT	150
Table 6.10	Variation in $\overline{\Omega}_{\text{th}}$ of a FG shaft supported on simply supported ends with L/D and α/R for $k = 5.0$, $\Delta T = 0$ K, $\eta_v = 0.0006$ s and $\eta_h = 0.0006$	153

Table 6.11 Variation in $\overline{\Omega}_{th}$ of a FG shaft supported on simply supported ends with k and ΔT for $L/D=12.5$, $\alpha/R=0.8$ and $L_c/L=0.5$ 157

Table 6.12 Variation in $\overline{\Omega}_{th}$ of a FG shaft supported on flexible end bearings with k and ΔT for $L/D=12.5$, $\alpha/R=0.8$ and $L_c/L=0.5$ 157

Table 6.13 Variation in $\overline{\Omega}_{th}$ of a FG shaft supported on simply supported ends with α_1/R, α_2/R and L_{c2}/L for $L/D=12.5$, $L_{c1}/L=0.50$, $k=5.0$, $\Delta T=0$ K, $\theta_1=\theta_2=180°$, $\eta_v=0.0006$ s and $\eta_h=0.0006$ 158

Table 6.14 Variation in $\overline{\Omega}_{th}$ of a FG shaft supported on flexible end bearings with α_1/R, α_2/R and L_{c2}/L for $L/D=12.5$, $L_{c1}/L=0.50$, $k=5.0$, $\Delta T=0$ K, $\theta_1=\theta_2=180°$, $\eta_v=0.0006$ s and $\eta_h=0.0006$ 159

Table 6.15 Variation in $\overline{\Omega}_{th}$ of a FG shaft supported on simply supported ends with ΔT and L_{c2}/L for $L/D=12.5$, $L_{c1}/L=0.50$, $k=5.0$, $\alpha_1/R=\alpha_2/R=0.8$, $\theta_1=\theta_2=180°$ 162

Table 6.16 Variation in $\overline{\Omega}_{th}$ of a FG shaft supported on flexible end bearings with ΔT and L_{c2}/L for $L/D=12.5$, $L_{c1}/L=0.50$, $k=5.0$, $\alpha_1/R=\alpha_2/R=0.8$, $\theta_1=\theta_2=180°$ 162

Table 6.17 Variation in $\overline{\Omega}_{th}$ of a FG shaft supported on simply supported ends with ΔT and θ_2 for $L/D=12.5$, $L_{c1}/L=0.50$, $L_{c2}/L=0.34$, $k=5.0$, $\alpha_1/R=\alpha_2/R=0.8$, $\theta_1=180°$ 165

Table 6.18 Variation in $\overline{\Omega}_{th}$ of a FG shaft supported on flexible end bearings with ΔT and θ_2 for $L/D=12.5$, $L_{c1}/L=0.50$, $L_{c2}/L=0.34$, $k=5.0$, $\alpha_1/R=\alpha_2/R=0.8$, $\theta_1=180°$ 165

CHAPTER 1

Introduction

Composite materials due to their inherent advantages like high specific strengths and stifnesses are extensively used in large scale engineering and industrial applications. However, traditional laminated composite materials have some major drawbacks in the form of thermo-elastic materials property mismatch leading interlaminar stresses at the interfaces especially in thermal environment. Therefore, emerging engineering fields demanded a new class of composite materials named Functionally Graded Materials (FGMs), which are able to overcome these shortcomings of traditional laminated composite materials and homogeneous materials especially at high temperature applications. Even though FGMs also have some limitations in the form of their fabrications and manufacturing in large scale compared to laminated composites, continuous efforts are on to improve upon those. A concise detailing of the historical background and importance, graded microstructure, fabrication techniques and applications of such materials is laid out in this chapter.

Rotating machineries are very common and widely used in modern industrial world for the applications in automobiles, aeroplanes, submarines, ships, power plants, household appliances, machine tools, medical equipment and so on. Power transmission shaft is a basic part of any rotating machinery. Rotating machineries, like gas turbine, steam turbine, shafts, blades etc. are exposed to a very high temperature environment. Thus, FGMs are recognized as potential materials for such components. Cracks in a shaft are a potential source for their catastrophic failure leading to increase in maintenance cost, loss of economic and human life. Therefore, it is important to study the vibrational characteristics of the rotating machineries so that machines can operate safely. The present chapter also discusses the importance of rotor-bearing system and internal damping, various causes and types of cracks in machine elements. Potential use of functionally graded (FG) materials in rotating shafts has been discussed. Fracture mechanics concepts are combined with rotor dynamical system to obtained local flexibility coefficients (LFCs) of an FG cracked shaft, which changes the system dynamic behaviour globally. Based on the discussion, motivation of the present study is presented in this chapter. Finally, the organization of the thesis is outlined.

1.1 Functionally graded materials (FGMs) – A brief insight

Composite materials are being widely used in aerospace, automobile industries and other structural applications due to their advantages of light weight, high strength-to-weight ratio, high stiffness-to-weight ratio, good fatigue resistant properties, good corrosion resistance properties etc. However, structures made of traditional composite materials and laminated composite materials have some major drawbacks, which adversely affect their performance and durability. First, because of the repeated cyclic load, impact load, high thermal and/or mechanical load at the interfaces of two adjacent laminae become weak and these leads to separation of the adjacent layers of the composite material, known as 'delamination'. Second, during fabrication and during service, because of mismatch in the material properties of fiber and matrix, high residual and thermal stresses develop. Third, the effect of inter-laminar stresses becomes even more dangerous when laminated structures are subjected to thermo-mechanical conditions. Finally, the interfacial strength in composite structures is generally poor. Therefore, emerging engineering fields demand materials which are more efficient in overcoming the above mentioned limitations of conventional laminated composites and homogeneous materials. In order to overcome these shortcomings of traditional composite materials and homogeneous materials, a new class of composite materials named FGMs was proposed. FGMs are the high performing, multi-functional, microscopically inhomogeneous advanced materials in the family of engineering composites made of two or more constituent phases with continuous and smooth variation of composition. FGMs are formed by varying composition of materials in any desired direction using different law of gradations (exponential, power and sigmoid laws) throughout the body of the structure, to achieve effective mechanical properties (Young's modulus, Poisson's ratio, shear modulus of elasticity and thermal conductivity).

1.1.1 Background and importance

Historically, the concept of gradation in material composition was first proposed for composites and polymeric materials by Bever and Duwez [1] and Shen and Bever [2] in 1972. However, their works had limited impact, probably due to lack of suitable production methods for FGMs at that time. The first practical application of FGMs was carried out by

Japanese material scientists at National Aerospace Laboratory of Japan in 1984 to prepare advanced ultra-high temperature resistance structural materials for using not only in space structures, fusion reactors and future space-plane system but also in various functional (optic and electronic) materials. In 1987-1991, the first national project entitled "Research on the Basis Technology for the Development of Functionally Gradient Materials for Relaxation of Thermal Stress (FGM Part I)" was carried out where they fabricated larger FGM test samples such as 300 mm square shells to be used for the base of the fuselage of space-planes and 50 mm diameter hemispherical bowls for nose-cones [3-5]. In 1993-1998, the second national project was initiated entitled "Research on Energy Conversion Materials with Functionally Gradient Structure (FGM Part II)" for improvement of energy conversion efficiency of FG structures, fabricated thermoelectric and thermionic materials [5]. Concurrently, the New Energy and Industrial Technology Development Organization (NEDO) promoted the FGM project entitled "Precompetitive Processing of Functionally Graded Materials" in 1996-1999 to develop large scale ceramic-metal FGMs and fabricated many FGMs such as polymide/Cu, PSZ/Ni etc. [5]. In 1996-1999, Ministry of Education, Science, Sports and Culture (MESSC) initiated "Physics and Chemistry of FGMs" to understand the basic problem on grading of physical and chemical properties and this project has made many achievements in promoting the investigation and applications of FGMs [5].

Ever since its development FGM has been an important area of research and in the recent years, large numbers of research works have been reported in the broad area of FGMs structures and in the dynamic responses of structures made of such materials in particular.

1.1.2 Gradient description of FGMs

Material gradient is referred as a structural unit of FGMs. It is a conceptual unit for constructing an FGM that includes various aspects of its chemical composition (inorganic, organic, ceramic, metal, polymer), physical state (electronic state, ionic state crystalline state, dipole moment, magnetic moment band gap, potential well, barrier), and geometrical configuration (granule, rod, needle, fiber, platelet, sheet pore, texture, orientation). There are mainly two type of approaches used to describe the material gradient for two phase

materials (i.e. ceramic and metal phase). The approaches are continuous and discontinuous (piecewise/stepwise/layerwise) of material compositions respectively. For continuous FGMs, variation of material compositions is changed smoothly along the graded direction. However, for another case, the compositions are varied in the form of layered distribution like the quasi-homogeneous material layer. FGMs usually consist of two distinct material phases, such as ceramic and metal phases, having microscopically inhomogeneous character. FGMs are the mixture of them such that the compositions of each constituent are varied continuously along a particular direction following different laws of material gradation (power law and exponential law).

The variation in microstructure induces material and micro-structural gradients which makes the FGMs different in behavior from homogeneous materials, traditional composite materials, and laminated composite materials. The most common FGMs are metal-ceramic composites, where the ceramic in an FGM offers good thermal and corrosion resistance capability and protects the metal from corrosion and oxidation, while the metallic part provides strong mechanical performance, superior fracture toughness and weldability and reduces the possibility of catastrophic fracture. The development of FGMs have demonstrated that they have the potential to reduce the magnitude of residual stresses, thermo-electro-mechanical stresses, density, stress concentration factors, inter-laminar stresses, and to improve the fracture toughness, strength, stiffness, temperature gradient, fatigue resistance, strength to weight ratio, etc.

In the successive development of FGMs, gradation in microstructure has an essential role and it can be achieved by changing volume fraction, orientation, shape and size of microstructure phases. FGMs can be classified into three types based on the distribution of constituent phases, namely continuous, discontinuous, and multiphase gradation of materials [6]. Different types of FG microstructures are presented in **Fig. 1.1** Based on material combinations, FGMs are divided as ceramic-metal, ceramic-ceramic, metal-metal, ceramic-plastic and many other combinations. In general, aerospace structures perform at service temperatures of 2100 K and temperature gradient of 1600 K across a cross section of less than 10 mm. Presently, no industrial materials are available to withstand such high-

temperature gradients without losing their structural integrity. Therefore, the unique idea of gradation of material composition was devised by gradually varying the composition from ceramic to metal and these FGMs have the potential advantage of the physical and chemical properties. Thus the recent applications emphasise more on graded structure of materials.

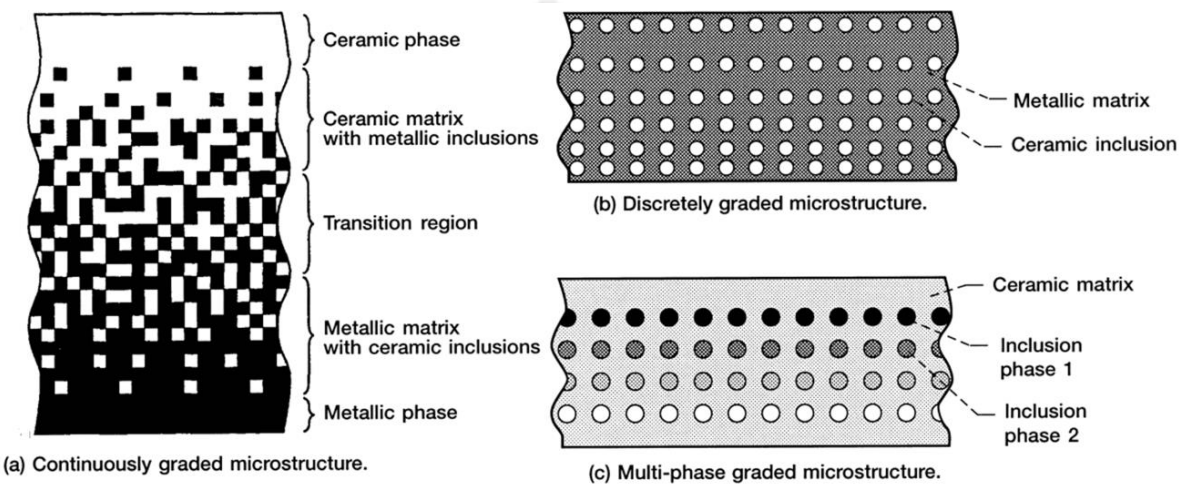

Fig. 1.1 Different types of FG microstructures [6]

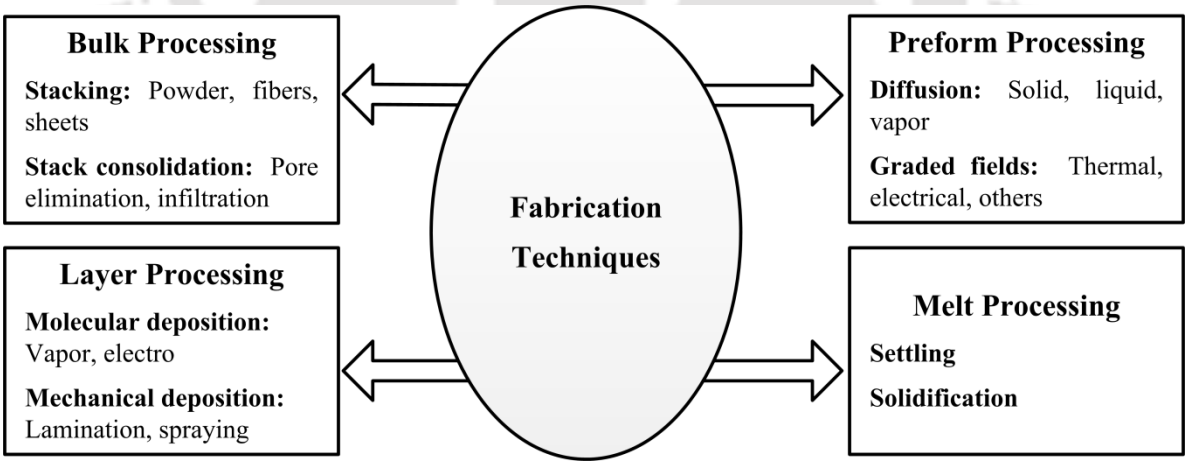

Fig. 1.2 Processing methods of FGMs [7]

1.1.3 Fabrication techniques of FGMs

An overview of existing techniques used for fabrication of FGMs based on different type of materials, application is reviewed in this subsection. In the published comprehensive reviews on the processing of FGMs various techniques tested and applied to prepare

different FGM samples and discussed with extensive explanations of manufacturing processes and design. The fabrication of FGMs have been categorized into bulk, layer, preform, and melt processing as shown in **Fig. 1.2**.

Bulk processing methods initially creates a bulk material with graded properties as porosity, composition, mechanical response, phase configuration. This is accomplished largely by forming stacks of powder, fibers, or sheets by means of normal gravity forces, centrifugal forces, pressure induced flow. The graded stacks are consolidated either by elimination process (solid state, liquid and transient phase sintering, and hot isostatic pressing) or by infiltration process without any shrinkage.

Layer processing can be achieved by mechanical deposition processes (micro lamination, cladding, spray forming, and thermal spraying). It also can be achieved by atomistic transport deposition processes based on vapor transport (physical and chemical vapor deposition), on diffusion in the solid or liquid states, and on electro migration processes. Most of the layer deposition methods can be used to produce bulk FGMs if adequate time is allocated, or if other specific processing parameters are applied. It also involves interlayers for transient liquid phase bonding of bulk and sheet components.

Preform processing is applied to initiate or to modify existing gradients in a preform. It can be used to enhance or reduce the gradients of graded performs. The conventional processing methods (solid state, liquid phase, or vapor phase diffusion) are used to create gradients in materials.

Melt processing can be achieved by constructive process and mass transfer process. The use of melt processing to form FGMs has been very limited because of difficulty in fine-tuning and controlling the formation gradients in melts and the incompatibility of many phases in the molten state. Also, advanced manufacturing techniques like solid freeform fabrication, sol-gel and fiber stacking, super plastic forming combined with diffusion bonding etc. can be used to manufacture FGMs.

There are some FGMs which are made of different manufacturing process such as Al/SiC FGM by powder metallurgy technique, Cu/Al_2O_3, Al-Mg/ZrO_2 FGMs by infiltration, ZrO_2/Ni, MgO/Ni (magnesium oxide/nickel), ZrO_2/TiAl (zirconia/titanium aluminide), and TiC/Ni_3Al (titanium carbide/nickel aluminide) FGMs by solid state sintering process, TiC/N_3Al FGM by hot pressing or hot isostatic pressing process, Ni/Al_2O_3 FGM by thermal spraying, SiC/C FGM by chemical vapor deposition (CVD) process, and so on. **Table 1.1** describes the general information of FGMs.

Table 1.1 General information of FGMs [7-9]

Type of FGMs	Processes	Properties	Applications
Ceramic-Metal	Powder metallurgy	Low thermal conductivity	Space vehicle
	Thermal spraying	Good thermal resistance	Combustion chamber
	Infiltration	High toughness and Strength	Fusion reactor
Ceramic-Polymer	Infiltration	High flexibility	Electrical devices
		Good toughness	Optics
		Good thermal and Electrical resistances	Biomedical engineering

1.1.4 Applications of FGMs

The development of application of FGMs has extended to different fields of industry in 1990. FGMs have been already recognized as an advanced inhomogeneous materials having tremendous potential in academic research and several industries. Although the practical applications of FGMs have not yet been fully realized and exploited, still from the 21st century the concept of FGM did potentially impact almost all materials research and development. Even though a wide variety of applications exist for structures made of FGMs, but here some of potential practical applications of FGMs are shown in **Figs. 1.3** to **1.7**.

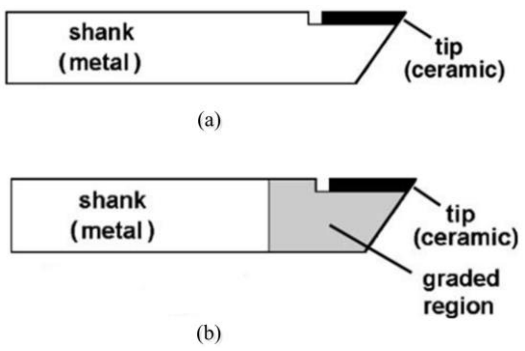

Fig. 1.3 Lathe bits type [9]:
(a) conventional bi-material and (b) FGM

Figs. 1.3(a) and **1.3(b)** show a comparison between conventional bi-material and FGM lathe bits in which FGM lathe bit used to reduce thermal stress concentration across the tip–shank interface and also to prevent the unexpected tool failure, as compared to conventional late bit. **Fig. 1.4** shows a heterogeneous turbine blade design in which the sharp interface between metal and ceramic was eliminated by controlling the composition, microstructure and porosity ratios of metal-ceramic FGM. **Fig. 1.5** shows the FG prosthesis joint which is composed of porous titanium (Ti) and hydroxyapatite (HAp) and used to increase adhesive strength and to reduce pain of human bone. **Fig. 1.6(a)** shows the Al/Al_2O_3 FG disc in which thermo-elastic field was controlled and optimized by controlling the proper combination of FGM composition and also this model recommended to design FG circular cutter or grinding disc to ensure the proper and reliable thermo-elastic characteristics in practical service. **Fig. 1.6(b)** shows three phases FGM comprising one active constituent piezoceramic (PZT), two passive constituent (carrying layer of Al and insulating layer of polyme), which reduce transverse vibration and operate at stabilize speed limits. **Fig. 1.7** shows the diverse areas of application of FGMs such as aerospace, chemical plants, engineering, energy conversion, nuclear energy, electronics, optics, commodities, biomaterials and defense.

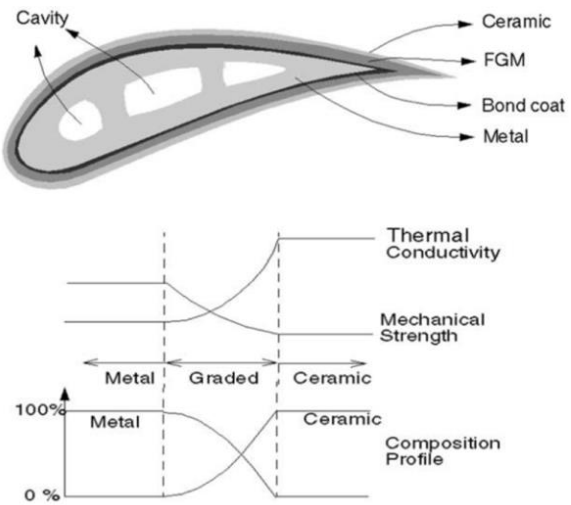

Fig. 1.4 Turbine blade and material properties [10]

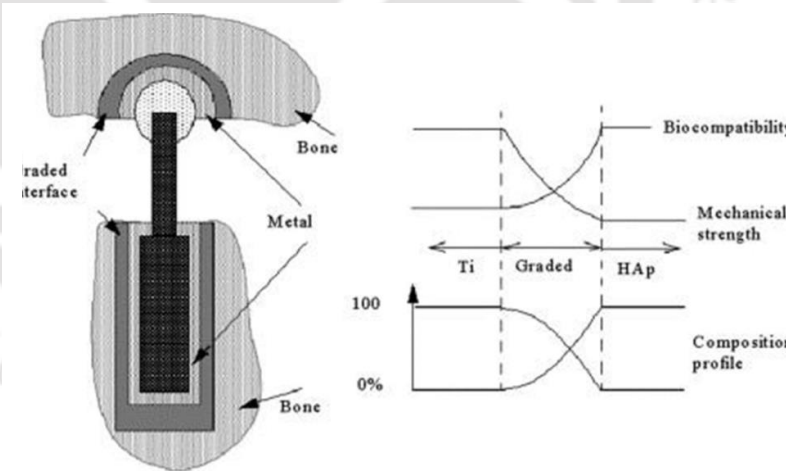

Fig. 1.5 Schematic diagram of a FGM interface within a prosthesis [9]

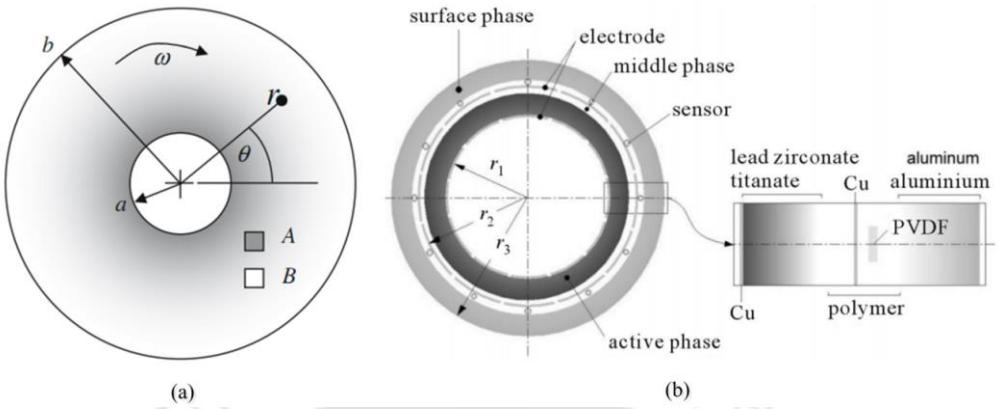

Fig. 1.6 Schematic diagram: (a) FG disc model [11] and (b) shaft made of a three-phase FGM [12]

Table 1.2 FGMs with significance properties and applications [5, 7-10 and 13]

FGMs	Property	Application
SiC-C, TiAl-SiC	High temperature fluctuations, thermal shocks and stress concentrations	Space plane project, heat exchange panels, rocket nozzle, solar panels, turbine blades
Al-SiC	Hardness and toughness	Combustion chambers, racing car breaks, Engine cylinder liners, flywheels
Al alloy-Al_2O_3	Good thermal and corrosive resistance	Rocket nozzle, wings and engine casting
E glass-Epoxy	Hardness and damping resistance	Leaf springs, brake rotors, solar domes, composite piping systems, pressure hull
Carbon-Epoxy	Lightweight and good damping properties	Helicopter components (landing gear doors), heat exchanger panels, engine parts
Graphite-Epoxy	High strength to stiffness ratio, good radiation resistant and reduces thermal distortions	Cylindrical pressure hulls, space telescopes, cryogenic tanks, satellite antennas
SiC-SiC	Corrosion resistance and hardness	Combustion chambers
SiCw-Al alloy	Thermal resistance, chemical inertness, hardness and toughness	Storage cylinders, diesel engine pistons, racing bicycle and vehicle frames
Al alloy-CNT	Lightweight and high stiffness	Artificial ligaments, MRI scanner spares, eye glass frames, dentistry parts, musical instruments, wheelchairs, camera tripods

Some potential practical FGMs with their significant property and application areas are listed in **Table 1.2**, and also some FGMs samples are available such as disc (SiC/C,

PSZ/SUS, PSZ/Ni, TiC/Ni, Cr_3C_2/Ni, AlN/SiC, TiB_2/Ni), rod (PSZ/Ni), shaft (Al_2O_3/SUS304, Al/SiC), cutting tools (TiCN/WC/Co) and many more.

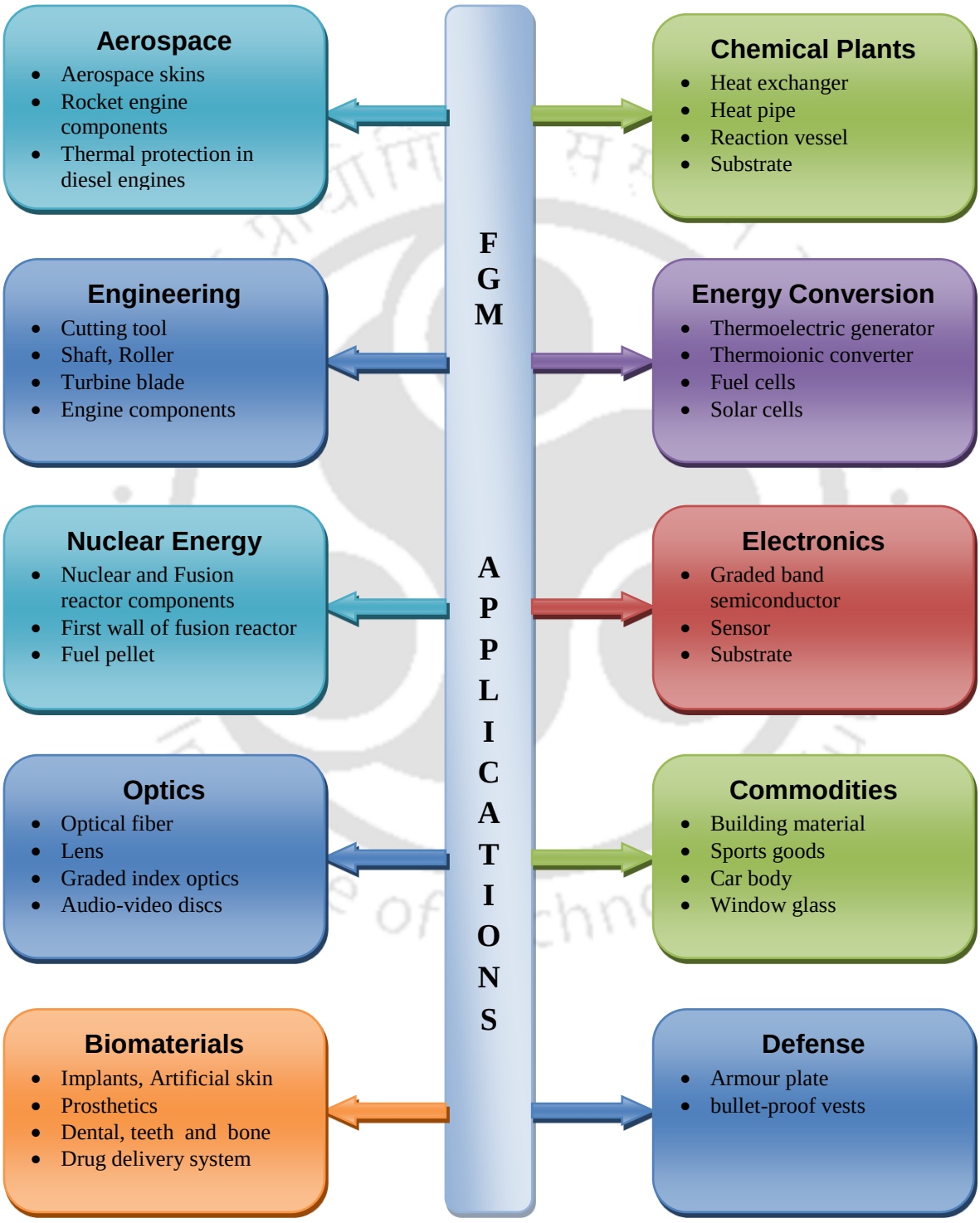

Fig. 1.7 Potentially applicable fields for FGMs

1.2 Rotor dynamics – A brief history and importance

Rotor dynamics is a specialized branch of applied mechanics concerned with the dynamic behavior and fault diagnosis of rotating machinery. It is commonly used to analyze the behavior of machinery ranging from jet engines and steam turbines to auto engines and computer disc storage. Basic level of rotor dynamic is concerned with rotor and stator. A rotor is a rotating part of a mechanical device or structure supported by bearings and influenced by internal phenomena that rotate freely about an axis fixed in space. Engineering components concerned with the subject of rotor dynamics are rotors in machines, especially of turbines, generators, motors, compressors, blowers, alternators, pumps, brakes, distributors and the like. The parts of the machine that do not rotate are referred as stator. In operation, rotors of machines have a great deal of rotational energy and a small amount of vibrational energy. The purpose of rotor dynamics as a subject is to keep the vibrational energy as small as possible. In operation rotors undergoes the transverse (bending), longitudinal (axial), and torsional (shear) vibrations, individually or in combination. Two types of rotor-bearing system are shown in **Figs. 1.8(a)** and **(b)** in which disc is mounted on shaft. In **Fig. 1.8(a)** the rigid disc is mounted on rigid rotor supported by

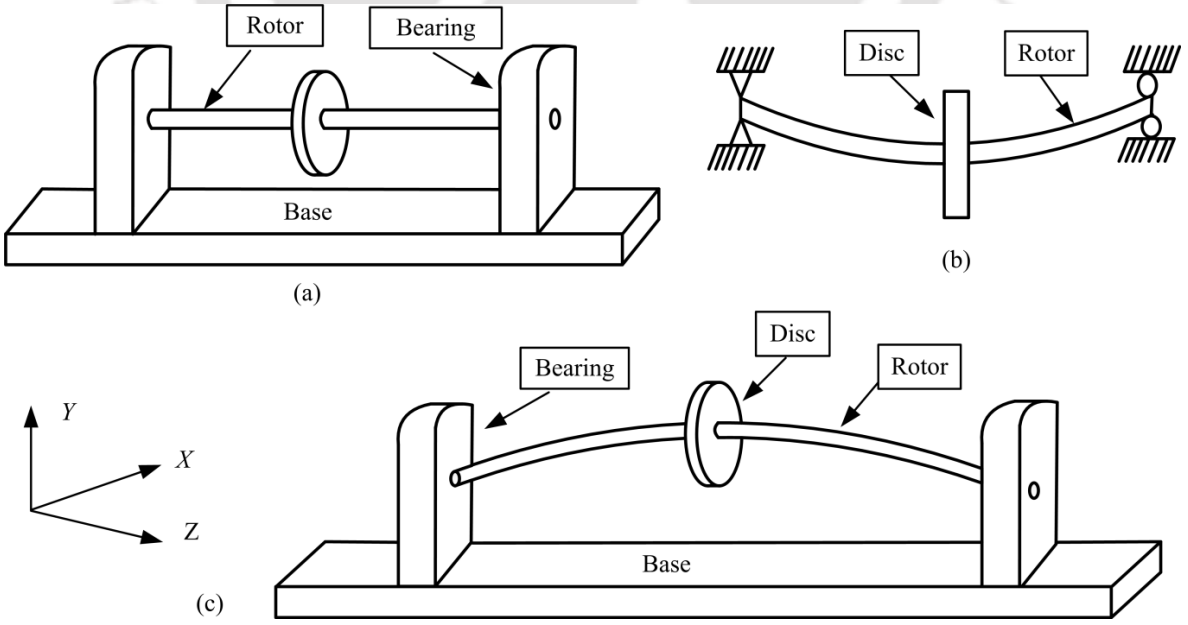

Fig. 1.8 A rotor-disc-bearing system: (a) rigid rotor with flexible bearings (b) flexible rotor with rigid bearings and (c) flexible rotor with flexible bearings

flexible end bearings, and in **Fig. 1.8(b)** the rigid disc is mounted on flexible rotor supported by rigid end bearings and in **Fig. 1.8(c)** the rigid disc is mounted on flexible rotor supported by flexible end bearings.

Historically, the theory of vibration was extensively developed in the 19th century and at the same time, the development of turbomachinery like locomotives and steam turbine progressed rapidly. In 1869, the first whirling of shafts was studied by William John Macquorn Rankine (1820-1872) showing that beyond whirling speed the radial deflection of the model increases without limit, which is not appropriate in actual case. He was the first to introduce whirling and critical speed but neglected the Coriolis accelerations in his model which confused the engineers for long time. In 1870's, a Swedish engineer Dr. Karl Gustaf Patrik de Laval (1845-1913) invented the milk separator with rotating speed at 6000-10000 rpm by using hand- or horse-driven with geared step-up of the speed. Also in 1883, Laval developed a single-stage steam impulse turbine for marine applications and succeeded in its operation at 42,000 rpm. He first used a rigid rotor, but latter using a flexible rotor and showed that it was possible to operate above critical speed by operating at a rotational speed about seven times the critical speed. In 1895, extensive investigations on complex shafts were reported by Stanley Dunkerley [14] based on the theory of Reynolds and calculated critical speeds with his formula, even for complicated compound rotor-shaft configuration with various geometries and boundary conditions. In 1895, German civil engineer August Föppl (1854-1924) exhibited a stable solution above Rankine's whirling speed using an alternate rotor model. In 1916 W. Kerr published experimental evidence that a second "critical speed" existed and it was obvious to all that a second critical speed could only be attained by the safe traversal of the first critical speed. In 1918, Ludwig Prandtl (1875-1953) was the first to study a Jeffcott rotor with a non-circular cross-section. In 1919, Henry Homan Jeffcott (1877-1937) first reported fundamental theory of rotor dynamics in his classical paper [15] and studied the flexural behavior of rotors and dynamic behavior and referred to as Jeffcott rotor. Jeffcott confirmed Föppl's prediction that a stable supercritical solution existed and he extended Föppl's analysis by including external damping and also Dunkerley's formula was proved theoretically by Jeffcott. The developments in rotor dynamics was written by Stodola [16] in his famous book "*Dampf- und Gasturbinen* (in

English: *Steam and Gas Turbines*)" and presented a remarkable discussion on the dynamics of elastic shaft with discs.

In past few decades, extensive complex rotor dynamics problems were reported by many authors and researchers for academic and industrial application. In the practical point of view, design of rotating machineries are necessary to determine accurately the natural whirling frequencies, mode shapes, critical speeds, stability threshold speeds and forced responses to unbalances in complex rotor systems by using numerically and experimentally. The most common methods used in rotor dynamics problems are lumped-parameters method, influence coefficient method, finite *element method* (FEM) and *Myklestad-Prohl method* or *Transfer Matrix Method* (TMM).

1.2.1 Rotor-Bearing system – Importance

The study of rotating machines and structures has an important role in modern industry as well as in academia. Rotor-Bearing systems affect a wide variety of machines like compressors, pumps, motors, large and small turbines and centrifuge machines etc. and these machines are widely used in engineering applications such as turbo machines, power stations, machine tools, automobile sectors, household accessories, aerospace, marine propulsion systems, medical equipment and many other applications. In most applications of rotating machines it is of great importance to know whether these machines are functioning within the correct operational speeds, and whether vibrations induced are within the limit to prevent failure. Failure of machinery equipment such as aero-engines, turbo-machines, military equipment, space satellites and others, creates huge amount of repair costs and more importantly human life. The manufacturers and operators and governments always look for rotating machines which ensure safe operations at higher rotating speeds. The objective of the designers and analyst

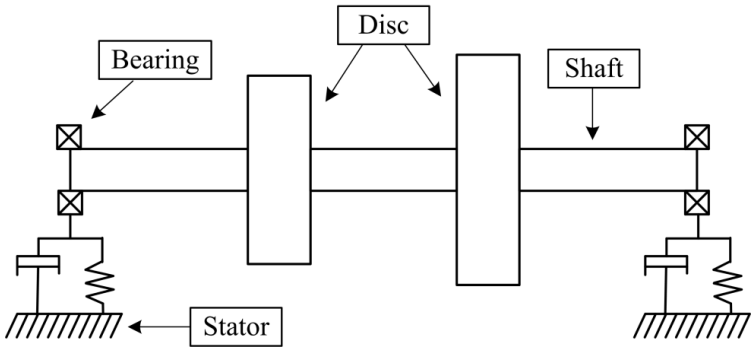

Fig. 1.9 A schematic diagram of a rotor-bearing system

is therefore to model, analyze and design in such a way that rotating machines could be operated at higher speeds with a low and safe level of amplitude of vibration. In addition, the accurate prediction of dynamics characteristics of such rotating systems is important for design of such rotating machines before it goes into manufacturing and service. A schematic diagram of rotor dynamic system is shown in **Fig. 1.9** with different components such as shaft, rigid discs, bearings with stiffness and damping coefficients and stator. Historically, before twentieth century, rotating shafts and bearings were not considered to interact with one another. But in the early years of twentieth century, due to the requirement of higher operating speeds of machines the importance of shaft flexibility and influence of bearing in the systems were better understood.

Many researchers have realized the importance of rotor dynamical systems in particular the dynamics of rotors, which is documented in many academic books during the last few decades. Determination of natural whirling frequencies, critical speeds and stability threshold speeds is important for rotor dynamic study and the parameters discussed in the next sub-section are important for such analysis.

1.2.2 Internal damping – Importance

During the shaft rotation, due to slight shaft imbalance or other external forces it experiences a motion through an orbit called the whirl or precession motion. Since the shaft material is not perfectly elastic, some additional work is performed on it at every rotation. This additional energy added to the rotor system is due to the internal damping of the shaft. As the whirling speed and work done on the shaft increase, the whirl orbit of the shaft begins to grow. At low speeds, the bearing can dissipate this energy to the ground/surrounding using an external damping. However, as the spin speed, energy increase, the bearing cannot dissipate all of the energy and shaft becomes unstable. This destabilizing effect of internal damping becomes important. Material damping and internal friction are examples of internal damping. Internal damping is modeled as viscous and hysteretic. Internal viscous damping is defined as a velocity dependent quantity. It can destabilize the system only after

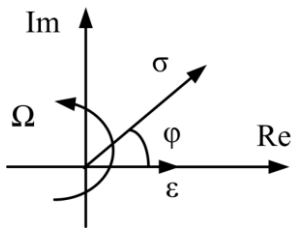

Fig. 1.10 Stress-strain phasor

the first critical speed. Internal hysteretic damping is defined as a displacement dependent quantity. The main difference between this two internal damping is that the viscous damping is frequency dependent whereas other one is not. Before modeling the internal viscous and hysteretic damping it is important to understand discussion of linear viscous model. In the linear viscous model, viscoelastic materials are used, in which the intermolecular bonds are viscous in nature [17].

For a viscoelastic material under a sinusoidal motion with spin speed Ω, the stress σ and strain ε in a complex plane (shown in **Fig. 1.10**) are assumed as

$$\sigma = \bar{\sigma} e^{i\Omega t} \text{ and } \varepsilon = \bar{\varepsilon} e^{i\Omega t} \tag{1.1}$$

where $\bar{\sigma}$ and $\bar{\varepsilon}$ are denotes amplitudes and real numbers of stress and strain respectively.

Now the Hooke's law of stress strain relationship is of the form

$$\bar{\sigma} = \bar{E}\bar{\varepsilon}, \text{ with } \bar{E} = E + iE' \tag{1.2}$$

where imaginary part E' represents the loss Young's modulus due to the material and expressed in the form as,

$$E' = E \tan\varphi \tag{1.3}$$

Now substituting **Eq. (1.3)** into the **Eq. (1.2)** leads to

$$\bar{\sigma} = E\left(1 + i\,E'/E\right)\bar{\varepsilon} \tag{1.4}$$

where E'/E represents the loss factor η i.e. $\eta = \tan\varphi = E'/E$ and finally the one dimensional stress-strain equation is expressed as

$$\bar{\sigma} = E\left(1 + i\eta\right)\bar{\varepsilon} \tag{1.5}$$

This linear model is the basis for both viscous and hysteretic types of internal damping.

1.2.2.1 Internal viscous damping model

Voigt model is one of the simplest mathematical models for describing internal viscous damping effect on rotor/shaft. Here, linear viscoelastic model is considered with an idealized dashpot of viscosity μ_i [18] as shown in **Fig. 1.11**.

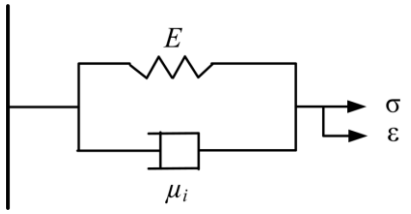

Fig. 1.11 Internal viscous damping model

The constitutive equation for the model is written as

$$\sigma = E\varepsilon + \mu_i \frac{d\varepsilon}{dt} \tag{1.6}$$

Using **Eq. (1.1)** into **Eq. (1.6)** leads to

$$\bar{\sigma} = \left(E + i\Omega\mu_i\right)\bar{\varepsilon} \tag{1.7}$$

Now comparing **Eq. (1.5)** and **Eq. (1.7)** the loss factor can be represents as

$$E\eta = \mu_i\Omega \;\Rightarrow\; \eta = \eta_v\Omega \tag{1.8}$$

where $\eta_v = \mu_i / E$ represents the internal viscous damping coefficient and it shows that the loss factor η for internal viscous damping increases linearly with spin speed of the rotor/shaft.

1.2.2.2 Internal hysteretic damping model

Internal hysteretic damping in a rotating system was first described by Newkirk and Kimball in 1924 [19]. **Fig. 1.12** shows the stress-strain phasor diagram. Referring **Fig. 1.12**, we have

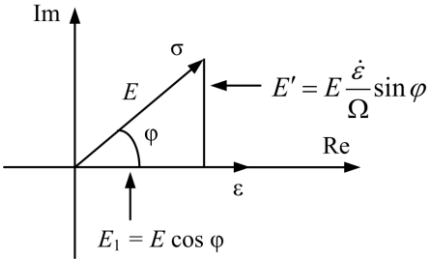

Fig. 1.12 Stress-strain phasor diagram

$$\sin\varphi = E'\Big/\sqrt{(E_1)^2 + (E')^2} \;\text{ and }\; \cos\varphi = E\Big/\sqrt{(E_1)^2 + (E')^2} \tag{1.9}$$

Now using $\eta = \tan\varphi = E'/E_1$ into the **Eq. (1.9)**, we get

$$\sin\varphi = \frac{E'}{\sqrt{(E_1)^2 + (E')^2}} = \frac{E'}{E\sqrt{1+\left(E'/E_1\right)^2}} = \frac{\eta_h}{\sqrt{1+\eta_h^2}} \text{ and } \cos\varphi = \frac{1}{\sqrt{1+\eta_h^2}} \tag{1.10}$$

where $\eta_h = E'/E_1$ is the material loss factor due to hysteretic damping and it depends on geometry and loading of the structure.

Axial stress/strain are calculated by constitutive equation for the hysteretic model using stress-strain phasor diagram (**Fig. 1.12**) as

$$\sigma = \mathrm{Re}[\sigma] + \mathrm{Im}[\sigma] = E\varepsilon\cos\varphi + E\frac{\dot{\varepsilon}}{\Omega}\sin\varphi \tag{1.11}$$

Using **Eq. (1.10)** into the **Eq. (1.11)**, we get

$$\sigma = E\left[\frac{\varepsilon}{\sqrt{1+\eta_h^2}} + \frac{\dot{\varepsilon}}{\Omega}\frac{\eta_h}{\sqrt{1+\eta_h^2}}\right] \tag{1.12}$$

Finally considering both the internal viscous and hysteretic damping (**Eq. (1.6)** and **Eq. (1.12)**), the stress-strain relation [20] is

$$\sigma = E\left[\frac{\varepsilon}{\sqrt{1+\eta_h^2}} + \left(\eta_v + \frac{\eta_h}{\Omega\sqrt{1+\eta_h^2}}\right)\dot{\varepsilon}\right] \tag{1.13}$$

If the Young's modulus is considered in complex plane then E in **Eq. (1.11)** and **Eq. (1.12)** will be replaced by $\bar{E}$ and then $\bar{E}$ can be express as $\bar{E} = \sqrt{E^2 + (E')^2} = E\sqrt{1+\eta_h^2}$. Using **Eq. (1.1)** and **Eq. (1.12)**, we have

$$\bar{\sigma} = \bar{E}\left[\frac{1}{\sqrt{1+\eta_h^2}} + i\frac{\eta_h}{\sqrt{1+\eta_h^2}}\right]\bar{\varepsilon} = E\sqrt{1+\eta_h^2}\left[\frac{1}{\sqrt{1+\eta_h^2}} + i\frac{\eta_h}{\sqrt{1+\eta_h^2}}\right]\bar{\varepsilon} = E\left(1+i\eta_h\right)\bar{\varepsilon} \tag{1.14}$$

where the loss factor η for the internal hysteretic damping and is independent of spin speed of the rotor/shaft.

1.2.3 Cracked rotor/shaft – Overview and importance

Rotating machines like small and large steam turbines and generators with cracked shafts are well documented in early 1970s and due to lack of clear statistics to the exact damage caused by cracked shafts, the Electric Power Research Institute estimated direct and indirect losses (repair, replacement and loss of revenue) at around US $1 billon in the conventional and nuclear power industry [21]. Historically, the first work was done by Dimarogonas [22] in the two internal reports of the General Electric Company where he presented vibration theory of cracked shafts. After 1972, many authors reported theory, laboratory and field experiments to develop methodology for crack detection, on-line electronic supervisory instrument for monitoring and early warning of cracked beams, rotors and turbines blades. The shafts affected by cracks were principally turbines, generators, centrifugal and axial compressors, nuclear pumps and boiler feed pumps.

Shafts are basic components subjected to perhaps the most arduous working conditions in high-performance rotating machinery equipment used in process and utility plant such as high-speed compressors, steam and gas turbines, generators, pumps etc. Due to different types of loading conditions (bending, torsional, shear, static, dynamic, cyclic loads and so on), and also due to manufacturing flaws serious defects (cracks, bent, mass unbalance, misalignment and so on) may appear in the shaft. Among these development and propagation of cracks is one of the most common causes of losses of structural integrity in mechanical structures. Cracks are defined as any unintentional discontinuities in the shaft material. Cracks in shafts have long been identified as limiting factors for the safe and reliable operation of turbomachines. In the presence of cracks, a structural component fails mainly in three stages. In first stage, cracks in rotating shafts most likely appear due to mechanical stress (sharp keyways, abrupt cross-sectional changes, heavy shrink fits, dents, grooves and so on), inherent flaw in the shaft material, long-term service, applied cyclic loads, high stress concentration regions (holes, slots for keys, threads), thermal stresses

generating high local stress intensity factors (SIFs). **Figs. 1.13(a)** and **1.13(b)** show a crack developed in the stiffening plate of a generator casing and in the blade root of a steam turbine [23]. In the second stage, cracks may grow due to certain conditions such as operating faults, residual stresses or welding heat affected zones, thermal stresses, metallurgical conditions or environmental conditions. In final stage, cracks grow to a certain depth in which the shafts cannot withstand the applied static and dynamic loads anymore and failure occurs very rapidly once the crack reaches into a critical size. Since, it may lead to structural failure associated with damage of equipment and loss of economic and human life, it is an important task to understand the selection of materials, manufacturing processes, and design parameters for designing shafts/rotors so that it can operate safely with high service speeds. Especially, it is more important to understand the safety of a rotating shaft once cracks appear in the shaft during the service.

(a) (b)

Fig. 1.13 Crack developed in: (a) stiffening plate of a generator and (b) blade root of a steam turbine [23]

1.2.3.1 Classification of crack in rotor/shaft

Based on their geometries, cracks in a shaft could be broadly classified [21] as follows

(a) Transverse crack – Cracks perpendicular to the shaft axis are known as transverse cracks. These are the most common and most serious as they reduce the cross-section which leads to damaging the rotating shaft component. They introduce a local flexibility in the

stiffness of the shaft due to strain energy concentration in the vicinity of the crack tip. A schematic diagram of rotor with transverse crack, longitudinal crack and slant crack is shown in **Fig. 1.14**.

(b) Longitudinal crack – Cracks parallel to the shaft axis are known as longitudinal cracks. These cracks are not that much common but they may be dangerous when the tensile load is applied at right angles to the crack direction or to the shaft axis.

(c) Slant crack – Cracks at an angle to the shaft axis are encountered as slant (oblique) cracks. Slant cracks influence the torsional behavior of the rotating shaft like the effect of transverse cracks on the lateral behavior. Their effect on lateral vibrations is less than that of transverse cracks.

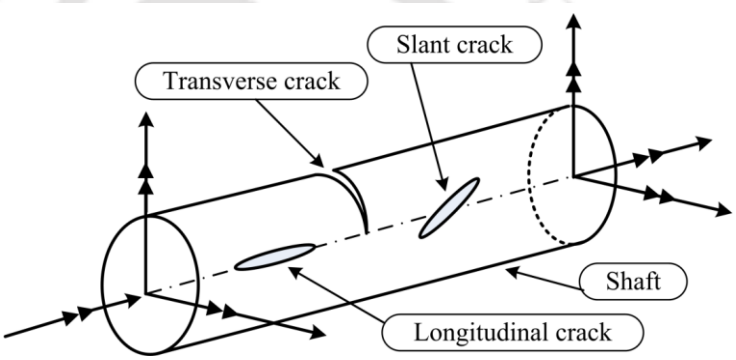

Fig. 1.14 A schematic diagram of a rotor with transverse crack, longitudinal crack and slant crack

In a rotating shaft, analysis of crack could be carried out by the following models

(i) Breathing crack – Cracks that are partially open/close with the continuous change of the shaft rotation known as breathing cracks. When cracks are in open state condition, the affected part of the material is subjected to tensile stresses and in the close state condition the stress is reversed. Shaft cracks breathe when crack sizes are small, running speeds are low and radial forces are large.

(ii) Switching crack – Cracks are completely open or completely closed with the sign of the shaft deflection in the crack direction known as the switching crack. Since the switching crack is not allowed to be partially open or closed, the cross-coupled stiffness vanishes and

the direct stiffness possesses bi-levels. It reduces the time and effort for calculation of various responses.

(iii) Gaping crack – Cracks that always remain open are known as gaping cracks. They are more correctly called notches. Gaping cracks are easy to mimic in a laboratory environment and hence most experimental work is focused on this crack.

1.2.3.2 Fracture mechanics concept in rotor dynamics

Man-made structural components may fail under different common conditions like yielding, buckling, fatigue, fracture, creep, environmental degradation, resonance, impact, wear and so on. Fracture is one of them important form of structural failure that often happens without any prior warning. Fracture of engineering components is usually caused by a flaw or a crack which may be defined as a very fine slit of nearly zero radius of curvature. Hence, if the development of crack under different loading conditions are continuous, local flexibility compliances increases in structural components and stiffness becomes so low that the components cannot sustained service load any longer leading to failure by the way of fracture. Fracture mechanics is an engineering discipline refers to the specialization of solid mechanics in which the study of causes and prevention of fracture in structures/materials are dealt. Fracture mechanics design philosophy is now extensively applied to the important fields like aircraft, aerospace, nuclear engineering, piping, offshore structures, locomotives, pressure vessels and so on. It is therefore important to analyse the rotors using fracture mechanics parameters when cracks appear in the rotor.

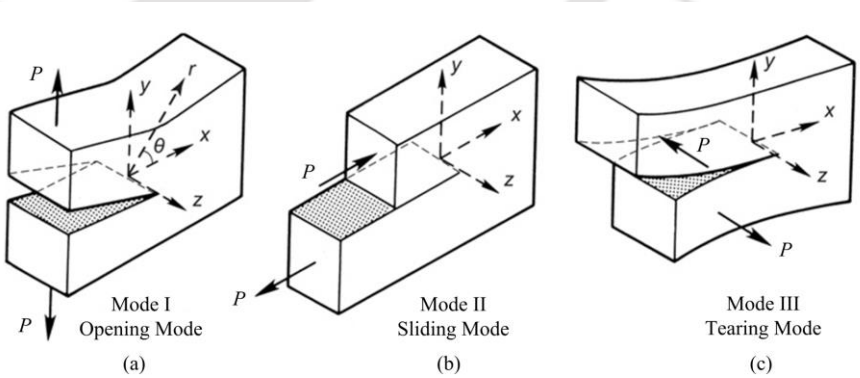

Fig. 1.15 Three modes of fracture

All cracked components are stressed in three different modes of fracture failure, each associated with a local mode of crack surface displacements as shown in **Fig. 1.15**. They are

- Opening mode or mode I – Tensile stress and corresponding displacements are perpendicular to the plane of the crack
- Sliding mode or mode II – In-plane shear stress and corresponding displacements acts parallel to the plane of the crack and perpendicular to the crack front
- Tearing mode or mode III – Out-of-plane shear stress and corresponding displacements acts parallel to both the crack plane and crack front

A combination of any two or all of the aforementioned modes leads to mixed mode of fracture. *Linear elastic fracture mechanics* (LEFM) is based on the concept of *small scale yielding conditions* (SSY), in which the plastic zone at the crack tip is very small compared to the crack length and other relevant geometric parameters. In LEFM, the load-displacement and stress-strain behavior are linear and here displacement and stress field are determined for elastic analysis of cracked bodies. Many of the engineering applications based on fracture mechanics approach are primarily on the brittle fracture which involve high strength materials and low fracture toughness. This theory is not valid when significant plastic deformation precedes the failure and also applications of LEFM to ductile fracture are restricted. In LEFM, two fracture mechanics parameters are widely used to assess the safety of an engineering component viz. SIFs and strain energy release rate (SERR).

Strain energy release rate (G)

In 1920, the founder of fracture mechanics Alan Arnold Griffith (1893-1963) first introduced the conceptual relation between fracture stresses to crack size for brittle materials, called strain energy release rate (SERR). Griffith invoked the first law of thermodynamics to formulate a fracture theory based on a simple energy balance. Griffith's model correctly predicted the relationship between strength and flaw size in glass specimens, but for metals the concept was unsuccessful. In 1957, the father of fracture mechanics George Rankin Irwin (1907-1998) modified the Griffith's theory [24] by adding an amount of energy from plastic deformation with the strain energy originally considered

by Griffith in order to work for both brittle and ductile materials. An unstable fracture occurs when G attains a critical value G_c, which is a size and geometry independent material properties of the cracked body and represents materials resistance to crack growth.

Stress intensity factor (K)

Due to practical problems in design and analysis, the basis of modern fracture mechanics was born in 1948 by Irwin and his co-authors through the introducing of stress intensity factor (SIF). The SIF K is a grouped parameter like Reynolds number and the SIF derived based on stress approach and also describes the local mechanical stress near the crack tip in linear elastic conditions. The magnitude of K depends on the geometry of the cracked structure, crack length and boundary conditions. SIF is most widely used in LEFM to characterize the crack under SSY (brittle or quasi brittle fracture conditions of metals). Unlike the concept of stress concentration factor that determines the magnitude of the stress at a single point, the parameter K provides a complete description of the state of stress, strain and displacement in the vicinity of a crack tip known as the singularity dominated zone. SIF approach could be used in many important applications to determine safe service loads, existing crack size, life prediction and so on. Due to its practical importance, many handbooks like Tada et al. [25] presented a collection of SIFs corresponding to various cracked configurations. Crack growth conditions can be predicted by comparing the K with the critical K_c (or fracture toughness) value. Therefore, it is clear that accurate determination of SIFs of a configuration is an essential task to the researcher/designers for application of real life components with cracks.

Referring to the crack-tip local coordinate system in **Fig. 1.15** (origin is placed at the center of the crack front), the stress field ahead of a crack tip for linear elastic materials under modes I, Π and ΠI loading conditions can be written as

$$\lim_{r\to 0}\sigma_{ij}^{(I)} = \frac{K_I}{\sqrt{2\pi r}}\, f_{ij}^{I}(\theta) \tag{1.15}$$

$$\lim_{r\to 0}\sigma_{ij}^{(II)} = \frac{K_{II}}{\sqrt{2\pi r}}\ f_{ij}^{II}(\theta) \tag{1.16}$$

$$\lim_{r\to 0}\sigma_{ij}^{(III)} = \frac{K_{III}}{\sqrt{2\pi r}}\ f_{ij}^{III}(\theta) \tag{1.17}$$

where r and θ are polar coordinates of a point as shown in **Fig. 1.15**, f_{ij} are universal functions depends on θ and loading mode, and K_I, K_{II} and K_{III} are the SIFs corresponding to mode I, mode II and mode III respectively. The values of K may be define as

$$K_{I,II,II} = \sqrt{2\pi r}\lim_{r\to 0}\sigma_{ij}^{(I,II,II)} \tag{1.18}$$

The SIFs can be determined through analytical methods, numerical methods and experimental methods.

The development and propagation of transverse cracks in rotating shafts are one of the most dangerous and important effect of damage of mechanical components. In the presence of crack, structural members develop local flexibility which affects dynamic behavior of such cracked system. Even for the presence of a small crack in a structural member, high SIFs will develop at the crack tip and allow the crack to propagate leading to structural failure associated with loss of economic and human life. Therefore, during last few decades several researchers combined the fracture mechanics concepts with rotor dynamic fields to calculate local compliances matrix. The stiffness change due to the presence of a crack is incorporated into the equations of motion to study the dynamic characteristics of the cracked shafts. Many researchers reported extensive analytical, numerical and experimental investigations on the dynamic responses of cracked rotors/shafts made of homogeneous materials. Potential use of FG shafts therefore also demands the dynamic analysis of such shafts in the presence of transverse cracks taking into account the change in compliances even though this is little more involved compared to that in homogeneous shafts.

1.3 Functionally graded cracked rotor/shaft – Importance

As already mentioned that functionally graded materials (FGMs) have received increasing attention in both research and engineering communities due to smooth and continuous gradient in both compositional profile and outstanding material properties and are regarded as one of the most promising candidates for future advanced composites in many engineering sectors such as the aerospace, aircraft, automobile, defence industries, and most recently the electronics and biomedical sectors. Due to increasing demands for energy and material conservation, structures can be designed with smaller safety margins. The existence of crack in any engineering structural member in the form of initial defects within the material or caused by fatigue or stress concentration certainly lower the structural integrity and affects its stiffness, mass, damping properties and then changes its vibration characteristics which may be measured and employed to detect and quantify the crack. The recognition of the influences of a flaw or crack is important due to its practical applications and may be employed in a damage detection procedure to predict an incipient structural failure, which may otherwise result in catastrophic, economic and human life loss. Cracks frequently occur in FGM structures, which form a serious threat to their safe performance. In order to maintain safety and integrity of structures, an extensive research has been conducted in the last four decades, eventhough all these were on homogeneous rotors. As a result, a wide range of techniques, algorithms and methods have been developed to detect damages in various structures, from basis structural elements (e.g. beams and plates) to sophisticated structural systems (e.g. buildings and bridges). The fracture mechanics and the dynamic characteristics of FGM structures have been the two subject areas attracting a lot of research efforts over the past few years and numerous research efforts have been devoted to the analysis of cracked FGM plates and beams structures.

Understanding the dynamic characteristics of cracked structural members, especially beams is of prime importance in structural health monitoring and non-destructive damage evaluation because the predicted vibration data can be used to detect, locate, and quantify the extent of the cracks or damages in a structure. In general, there exist three basic crack models, namely equivalent reduced section model, continuous crack flexibility model and

lumped flexibility models. The equivalent reduced section model is used to localize and quantify the damage from the vibration response data by using an equivalent reduction in the stiffness of a particular element or group of elements in structures. Continuous crack models attempt to explicitly incorporate the location and depth of crack as part of the equations of motion of the damaged structure by using FEM, Galerkin method, Rayleigh–Ritz method, approximate analytical approach, transfer matrix approach and dynamic stiffness matrix approach. In the lumped flexibility models, the intact parts of the structure are modeled using FEM, component mode synthesis or partial differential equations, and the crack is represented by means of a line spring and the equivalent lumped stiffness is determined through the expression of SERR or SIFs based on fracture mechanics approach.

In the past few decades, many research articles are published in which classical Euler–Bernoulli beam theory, equivalent rotational spring model, transfer matrix method, modal series expansion technique are used to obtain the natural frequencies, mode shapes and dynamic response of FGM beams with single or multiple cracks. In addition, parametric studies were conducted to demonstrate the effects of geometrical parameters, crack parameters and other parameters on the dynamic behavior of cracked FGM beams. However, the existing works reported on cracked intact FGM beams and very less attention was focused on vibration and diagnosis of cracked FGM members. It is possibly due to the novelty of such materials and the complexity of crack modelling in FGM. Therefore, analysis of buckling and postbuckling behaviour, dynamic behaviour and stability of FGM cracked structures (beams, shafts and plates) are most important research topic in structural safety assessment.

1.4 Research motivation

Rotating machineries has wide range of application from engineering to industrial area. The shaft is a basic part of any rotating machinery because it helps to transmit the power through a rotating shaft. Cracks in a shaft are a potential source for catastrophic failure of machine components. Therefore, accurate determination of dynamic responses of the rotating machinery is crucial to ensure that it operates safely. Cracks in FGMs are important keeping

in view the widespread usage and application of such materials as researchers and designers seek a way to address structures under combined thermal and mechanical loads. Analysis of performance of FGMs structures is important in order to understand the response under load of such structures which are potential candidate for replacement of traditional composite materials. With the advent of this new generation of materials, the reliability and integrity of rotor dynamical systems become central issues.

In view of the importance of FGMs rotors and the importance of understanding their dynamic response, it was motivating to undertake a research problem in the area of the rotors with a special attention on cracked FG rotors. In general determination of LFCs of such FG systems with the presence of transverse breathing cracks is essential for accurate dynamic analysis of such FG cracked rotor-bearing system in particular. Experimental investigations of the structural system made of FGMs may be possible but are prohibitively expensive and there is enough scope of numerical analysis for various dynamic analyses of such cracked FG systems. This has been the motivation to undertake these studies where dynamic responses are obtained for a FG rotator dynamical system with transverse breathing cracks and study the challenges involved. With this motivation, a thorough literature review has been done in the broad area of FG cracked shaft systems to understand the state of the art in this area and to decide the objectives of the present work. This literature review is presented in the next chapter.

1.5 Thesis organization

This thesis work is set out as follows. Chapter 1 presents a brief introduction on the manufacturing processes, design and the current applications of FGMs along with the importance of studying the behavior of functionally graded shaft in general and cracked functionally graded shaft in a rotor-bearing systems in particular. This chapter also states the research motivation of the present works.

Chapter 2 first presents a review of the literature on the analysis of FG uncracked structures, homogeneous rotor-bearing system, homogeneous cracked structures for better understanding the state of the art in the field of analysis of FG structures in general. This

chapter then presents a critical reiview of literartures on analysis of FG cracked structures and FG shafts. Subsequently, the research gaps are highlighted and the objectives of the present research are outlined.

Chapter 3 presents the details of finite element formulation of elementary governing equations of shaft, disc and bearing for analysis of cracked FG shaft incorporating the internal damping effects. This chapter also describes the derivation of LFCs for modelling transverse cracks in FG shafts using energy method along with LEFM. Finally, development of the FE code based on the formulations is presented in this chapter.

Chapter 4 presents the validation of the FE code and FE simulation of free vibration analysis of a rotor-bearing system having an FG shaft with stationary transverse surface crack. This chapter also presents the influences of geometrical, crack and other parameters on the vibration characteristics of the FG cracked shaft system obtained from the numerical simulations.

Chapter 5 presents the results of numerical simulations carried out using the FE code to analyze transverse vibration of rotor-bearing system having an FG shaft with multiple transverse breathing cracks. Based on the results, influences of geometrical, relative crack and other parameters on frequencies and critical speeds for the FG cracked system have been discussed in this chapter.

Chapter 6 presents the stability behavior of rotor-bearing system having an FG shaft with transverse breathing cracks. Using the FE code, numerical simulations have been performed to determine the stability threshold speed for a rotor-bearing system having a cracked FG shaft and the influences of geometrical, crack and other parameters on stability threshold speeds have been discussed.

Finally, the summary of the present work and important conclusions drawn from the present thesis work along with the scopes for future extension of this work has been described in Chapter 7.

CHAPTER 2

Literature Review

2.1 Introduction

This chapter presents the state of the art in the field of analysis of FG structures in general, cracked homogeneous structures and cracked FG structures in particular. Special emphasis is put on discussing the literatures reported on FG rotors even though very few in number. In order to have a better understanding, some of the important literatures on cracked homogeneous rotors are also discussed. Finally based on the literature review, research gaps have been highlighted and specific objectives of the thesis have been presented. For better readability literatures are classified and presented as shown in the **Fig. 2.1**.

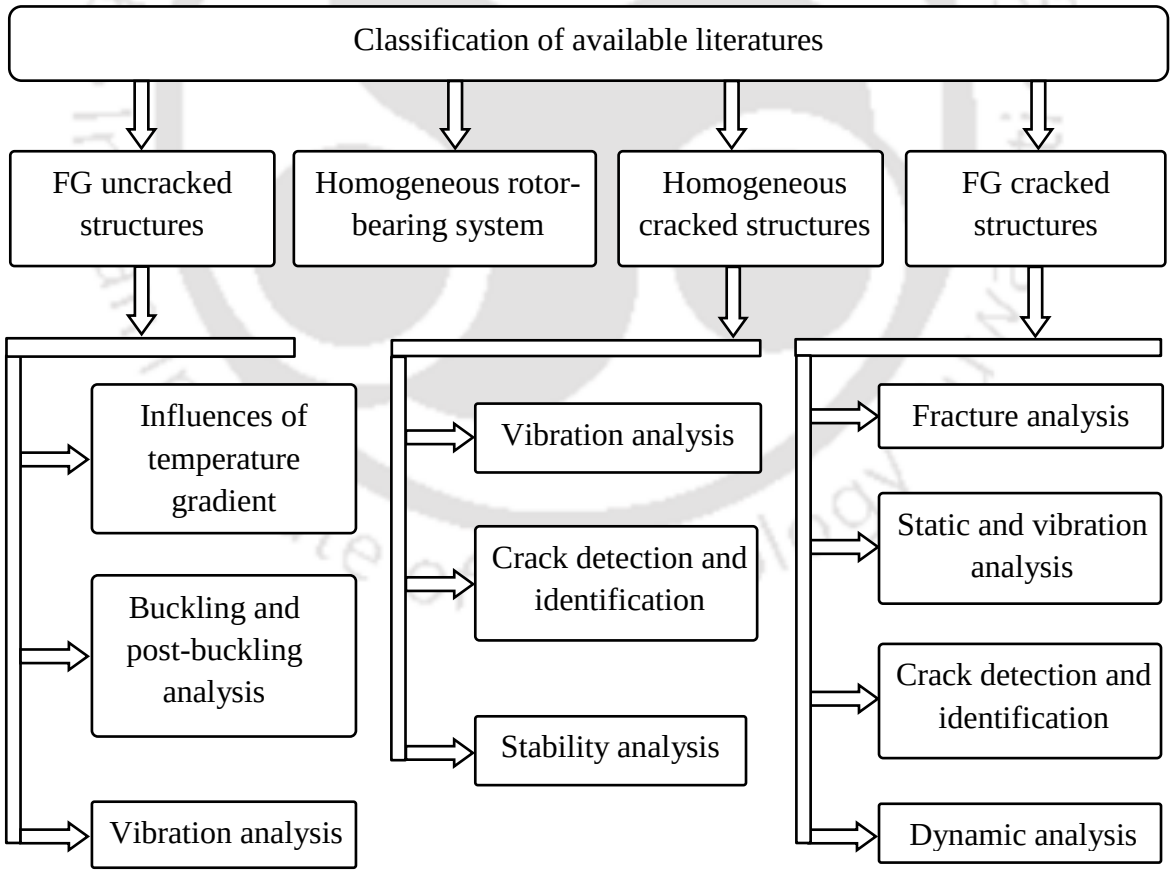

Fig.2.1 A flow chart highlighting the classification of literature review

2.2 Functionally graded uncracked structures

FGMs have already been recognized as an advanced inhomogeneous materials having tremendous potential in high temperature applications and in various fields of engineering. A survey of available literature revealed the existence of investigations in the analysis of FGM structures such as beams shafts, rotors, disc etc. There has been a large number of works already reported in literatures in the broad area of analysis of FGM structures like beams, plates subjected to mechanical, thermal and electrical loads mechanical load, thermal load, and electrical load.

2.2.1 Influences of temperature gradient

There has been large number of research articles already published in the broad area of effect of thermal load on the performances of FG structures. Reddy [26] developed theoretical formulations and FEA for thermomechanical, transient response of FG cylinders and plates. Thermomechanical responses of these materials under static, dynamic and thermal loading environments have been studied. They reported the influences of temperature and volume fraction on the deflection and stresses in the FG plates. Reddy and Chin [27] presented the dynamic analysis of thermomechanical response of FG plates and cylinders using FE formulation with power-law gradation. Chakraborty et al. [28] studied the thermo-elastic behavior of FG beam based on the first order shear deformation theory (FOSDT) considering both exponential and power-law gradation of material property distribution. Afsar and Go [11] reported the FE analysis of thermo-elastic field in a thin circular FGM disc subjected to a thermal load. Based on TBT, Rahimi and Davoodinik [29] studied the thermal behavior of FG beam considering the steady state of heat conduction with exponentially and hyperbolic variations through the thickness direction. Mahi et al. [30] studied free vibration of symmetric FGM beams based on higher order shear deformation theory (HOSDT), considering temperature-dependent material properties which varied continuously through the thickness according to different material law of gradation (power, exponential and sigmoid). Wattanasakulpong et al. [31] employed an improved third order shear deformation theory (TOSDT) to investigate thermal buckling and vibration of

FG beams considering temperature dependent material properties following power law distribution.

2.2.2 Buckling and post-buckling analysis

There has been a few number of research articles reported in the analysis of buckling and post-buckling for FG structures by Reddy [26], Wattanasakulpong et al [31]. Na and Kim [32] studied three-dimensional thermo-mechanical buckling analysis for FGMs, where materials properties were considered to vary along the thickness direction according to the power law gradation. Li et al. [33] reported FE analysis of thermal buckling and post-buckling of FG Timoshenko beam subjected to temperature loading. Using Tresca's yield criterion, Akis and Eraslan [34] reported analytical solutions of rotating FG shafts considering the material behavior as purely elastic, partially plastic and fully plastic. Material properties were assumed radially graded following exponential gradation function. It was reported that material gradient index significantly influenced the elastic and elastoplastic responses of the FG shaft. Kiani and Eslami [35] carried out buckling analysis of Euler–Bernoulli FG beam considering variation of material properties according to power law gradation under different types of thermal load (uniform temperature rise, linear and nonlinear temperature) and different end conditions. Kiani and Eslami [36] performed thermo-mechanical buckling analysis using Timoshenko FG beam considering thermo-mechanical material properties according to power law gradation.

2.2.3 Vibration analysis

There has been a large number of works reported in the vibration behavior of FG structures and only some of the important works are discussed here. Argeso and Eraslan [37] presented a computational model for elastic, partially plastic and residual stress analysis in a FGM rotating solid shafts by using the von Mises' yield criterion. Aydogdu and Taskin [38] studied free vibration analysis of FG beam considering material properties according to power law and exponential law gradation with simply supported edge by using different higher order shear deformation theories and classical beam theories. Kapuria et al. [39] presented a third order zigzag theory for layered FG beams in conjunction with the modified

rule of mixtures for determination of static and free vibration responses (theoretical and experimental) of such beams. Li [40] presented a unified approach for studying static and dynamic behaviors of FG beam considering rotary inertia and shear deformation and compared the natural frequencies of FG beam with those of layered beam. Piovan and Sampaio [41] studied the dynamic behavior of rotating FG beams accounting axial deformations and considering geometric nonlinearity. Alshorbagy et al. [42] reported the dynamic characteristics of FG beam with material gradation in axial or transverse direction through the thickness following power law gradation and using FEM. Shahba et al. [43] studied free vibration and stability analysis of axially FG tapered beams through FE approach using exact shape functions. Sheihlou et al. [44] studied the torsional vibration of radially graded FG micro-shafts using energy method and Hamilton's principle. The radially graded material properties were varied following power law function. The effects of end conditions and gradient index on frequency response of the FG shaft were discussed and reported the influence of gradient index on the responses. Gayen and Roy [45] presented the vibration and stability analyses of FG spinning shaft system under thermal environment using three nodded beam element based on TBT considering transverse shear deformation, rotary inertia and gyroscopic effect. Boukhalfa [46] studied the dynamic responses of spinning FG shaft using p-version FEM and considering TBT in the shaft model. Radially graded material properties were assumed following power function. The influences of gyroscopic effect, slenderness ratio and types of FGM on whirling frequencies were examined and reported that dynamic responses were influenced significantly by power law gradient index. Huang et al. [47] performed dynamic analysis of axially graded rotating Timoshenko FG beams, using spectral-Tchebychev method. Material properties gradations were assumed following power law. The influences of gradient index, end conditions, and slenderness on whirling frequencies, critical speeds, and mode shapes were examined. It was reported that material gradient showed a significant impact on dynamic responses.

2.3 Homogeneous rotor-bearing system

Rotor-Bearing systems find wide applications in different fields, like power stations, marine powers, machine tools, automobile sectors, and aircraft engines and dynamic characteristics

of such system is very important from the design point of view. There have been a number of studies relating to this field in the past few decades as reported by Dimentberg [48], Lund [49], Gunter [50], Ruhl and Booker [51], Lund [52], Rao [53], Goodwin [54], Genta [55], Sujatha [56], Friswell et al. [57], and Tiwari [58] for determination of accurate dynamic responses and stability of a rotor system using numerical methods namely TMM and FEM. In 1959, the first rotor dynamics monograph was written by Dimentberg [48] who presented an extensive discussion of most rotor dynamic problems. Lund [49] carried out stability analysis of an elastic rotor supported on journal bearings and reported the influence of rotor stiffness, dynamic properties of the bearing, flexibility and damping of the bearing supports on rotor instability speeds. In 1966, Gunter [50] studied the rotor dynamic stability problems, combined with Ruhl and Booker's [51], and Lund's [52] methods for calculating damped critical speeds. In 1970s, rotor dynamic instability was experienced in different high pressure compressors and high-pressure fuel turbo-pumps, liquid and gas seals in pumps and turbines. In 1972, the first application of the FEM to a rotor system was made by Ruhl and Booker [51]. Lund [52] reported analytical procedure in rotor dynamics problems based on TMM and the results showed good agreement with the experimental results.

Historically, Ruhl [59] were the first to utilize the FEM to understand the stability and unbalance response of a turbo-rotor system. In his FE formulations, only elastic bending energy and translational kinetic energy were included but the effect of rotatory inertia, gyroscopic moments, shear deformation, internal and external damping were neglected. Dimarogonas [60] combined the transfer matrix method and the constraint method for the stability analysis of rotating shafts including the rotary inertia, gyroscopic effect and internal damping. Bansal and Kirk [61] reported the transfer matrix approach to compute the stability map, damped critical speeds and instability threshold speed of multi-mass flexible rotor-bearing systems with the incorporation of the effects of disc gyroscopic moments, shear deformation, and bearing characteristics. Nelson and McVaugh [62] have generalized Ruhl's work by developing an FE modelling of Rayleigh beam including the effects of rotatory inertia, gyroscopic moments and axial load to compute natural whirl speeds and unbalance response. Zorzi and Nelson [20] extended the work [62] and included both internal viscous and hysteretic damping in the same FE model and studied the whirling

frequencies and stability. At the same time Nelson [63] utilized TBT and based on shape functions the system element matrices were derived. The accuracy of FE solution compared to that of classical closed form solutions was demonstrated and it was concluded that FE solution provided accurate dynamic responses, took less computational time and used less computer storage compared to those in the case of classical closed form solutions. Glasgow and Nelson [64] presented stability analysis of multi shaft rotor-bearings systems using component mode synthesis method which showed a significant reduction in the size of the overall problem while retaining the essential dynamic characteristics of the lower modes. Özgüven and Özkan [65] presented the combined effects of shear deformations and internal damping to analyze the natural whirl speeds, stability and unbalances responses of rotor-bearings system. Chen and Ku [66] used Ritz finite element technique to determine the regions of dynamic instability of a rotating shaft with the effects of rotatory inertia, transverse shear deformation, gyroscopic moment and static buckling load. Chen and Ku [67] developed a three nodded C^o Timoshenko beam FE model to analyze the natural whirl speeds of a rotating shaft with different end conditions and shaft's slenderness.

Wettergren and Olsson [68] reported dynamic instabilities of a horizontal rotor having a flexible asymmetric shaft considering internal viscous damping and supported on anisotropic bearings at the ends. Results showed that major instabilities appeared after the imbalance resonance and these instabilities could be avoided with the right combination of damping and asymmetric stiffness of the shaft and the damping and anisotropic stiffness of the bearings. Kumar et al. [69] proposed a semi-analytical method using three noded conical axisymmetric shell elements to model for a shaft-disc system and reported that the used element was observed to be computationally economical and could be used for solving a large rotor system consisting of a large number of discs. Kumar et al. [70] proposed a semi-analytical method for modelling of rotor using conical shell finite element which providing flexibility of the discs, shaft and the bearings. A parametric study was carried to study the influence of disc flexibility on the natural frequencies of the system and reported that the disc flexibility helped to predict the free-free modes of the system more accurately. Ku [71] has incorporated internal damping in the same model [67] to study the dynamic characteristics and the combined effect of transverse shear deformations and internal

damping on whirl speeds and damped stability. Results show that due to incorporation of internal viscous damping, instability threshold begins at spin speed higher than the critical speed for forward mode, whereas due to inclusion of internal hysteretic damping, forward modes become unstable at all spin speeds. However, for all kinds of internal damping in the rotor, all the backward modes are always stable for the entire spin-speed envelope. In addition, external damping of bearings improved the stability of the rotor system. Das et al. [72] proposed an active vibration control technique for reducing transverse vibration and enhancing stability limit speeds for safer operations at higher speeds of a rotor-shaft system using electromagnetic exciters.

Srinath et al. [73] studied instability of asymmetric continuous shaft system using perturbation and Whittaker's method. It was reported that the proposed superposition based method was useful for different boundary conditions such as simply supported, cantilever and fixed–fixed. Jain et al. [74] studied the influences of asymmetric stiffness on instabilities of multi-rotor-system using extended Lagrangian method and bond graph technique. A dynamic mathematical model of a multi-rotor-system was proposed for obtaining amplitude and natural frequencies of the system with asymmetric stiffness. Simulation results showed a considerable agreement with the theoretical results obtained using the proposed method and reported that amplitude of the rotor increases inversely with the stiffness of the rotor up to a certain limit.

2.4 Homogeneous cracked structures

Existences of cracks in structural members affect stiffness, mass, damping properties and its vibration characteristics. So, analysis of the influence of the presence of crack is very important. In order to maintain safety and integrity of structures, an extensive research has been conducted in the last four decades on cracked structures. As a result, a wide range of techniques, algorithms and methods have been developed to detect damages in various structures like beams, rotors, shafts and plates etc. Exhaustive literature reviews have been accomplished by Sabnavis et al. [21], Dimarogonas et al. [75], Wauer [76], Gasch [77],

Dimarogonas [78], Papadopoulos [79] and those covered many aspects of this area and provided valuable information and knowledge.

2.4.1 Fracture and static analysis

The crack tip is observed to follow the inverse-square-root-singularity in any structures and the singular stress feld at the crack tip area facilitates the driving force to initiate fracture. Therefore, determination of SIFs for a continuum singular feld near crack tip is required and various methods have been proposed to compute SIFs under different loading. There have been several works [80-85] reported to compute fracture and static analysis due to cracks in structural components during last few decades.

Cortínez and Dotti [80] evaluated mode I SIF analytically for cracked thin-walled beams considering a very common feature namely warping effect, using energy release rate approach. It was reported that the proposed technique might be useful in failure analysis and health monitoring of slender structures. Yuan et al. [81] determined mode I SIFs for cracked slender special-shaped shells subjected to bending loads, using a simple and practical technique based on elementary mechanics and conservation law. It was reported that the present method showed a good agreement with FE solution and suggested to apply for other similar cracked structural shells. Using TBT, Akbas [82] studied static behavior of edge cracked simply supported circular beams subjected to a non-follower transversal point load. The cracked beam was modeled using massless elastic rotational spring. Newton-Raphson iteration method and incremental displacement based FEM were used to solve the large deflection problems and the influences of depth and location of crack on linear and non-linear static responses of edge-cracked beams was studied. Akbas [83] performed analytically static bending of edge cracked cantilever and simply supported micro beams subjected to transverse load based on modified coupled stress theory. Crack was modeled based on classical cracked-beam theory and massless elastic rotational spring. The influences of crack location, crack depth, slenderness ratio and end supports on elastic deflection was studied. Using nonlocal elasticity theory and von Karman nonlinearity, Khorshidi et al. [84] studied buckling and post-buckling behavior of cracked nano-beams considering axial stretching effect. They also examined the influence of non-local parameter

on critical buckling loads and static nonlinear post-buckling responses and observed that the responses were strongly affected by the depth and location of crack, nonlocal parameter, and slenderness ratio. Alijani et al. [85] studied bending analysis of Euler–Bernoulli cracked beams on an elastic foundation using analytical, approximate and numerical approaches. The influences of depth and location of crack, end supports and elastic foundation on the deflection and reported that the FE method offered an uncomplicated and simpler way to obtain the responses in compared to the approximate and analytical methods.

2.4.2 Vibration analysis

Study of vibration behavior is important in order to design any structural member mainly when engineering structures are subjected to dynamic loads. Natural frequencies of structural systems are important system parameters that can be determined using different theories and methodologies. Due to the significances of vibration analysis for structural design, the interest in investigating vibration characteristics has increased considerably in the past few decades.

Mayes and Davies [86] carried out the flexural vibrational behavior of a rotor mounted on several bearings and having a transverse crack. Papadopoulos and Dimarogonas [87] studied coupled longitudinal and bending vibrations of a rotating shaft with an open transverse surface crack. The local flexibility due to the presence of the crack was represented by a 6x6 matrix for six degrees of freedom in a short shaft element which includes the crack without considering the shear effect. Papaeconomou and Dimarogonas [88] studied free vibration of a beam with surface crack for different end condition. Jun et al. [89] studied the vibration behavior of a rotor with a breathing crack and computed cross-coupled stiffness and direct stiffness based on fracture mechanics approach and compared the breathing crack model with the switching crack model. Ostachowicz and Krawczuk [90] reported the influence of transverse open cracks on the coupled torsional and bending vibrations of a rotor considering a beam finite element and a crack model. Cheng et al. [91] studied the dynamic behavior of a cracked beam using a simple non-linear fatigue crack model and the reduction in natural frequencies were compared with that in open crack model.

Chondros et al. [92] employed a continuous cracked beam theory to predict the changes in frequency of transverse vibration of a simply supported beam considering a breathing crack and reported that the changes in vibration frequencies for a fatigue-breathing crack were smaller than those for an open crack. Sinha and Friswell [93] simulated experimental time and phase responses of a free-free cracked beam with breathing bahavior and reported that the simulation results could closely resemble the experiment results. Darpe et al. [94] studied the coupled lateral and longitudinal vibrations with transverse surface crack in a Jeffcott rotor and steady state unbalance response of the rotor with a centrally located crack subjected to periodic axial impulses. Darpe et al. [95] presented the coupled longitudinal, lateral and torsional vibrations for a rotating cracked shaft using a response-dependent non-linear breathing crack based on a crack closure line method. Papadopoulos [96] calculated the local flexibility coefficient based on linear elastic fracture mechanics approach for a cracked shaft and reported that when the crack depth approached the diameter of the shaft, the compliance function approached infinity asymptotically. Sinou and Lees [97] studied the influence of transverse crack on dynamic response for a rotating shaft using an alternate frequency/time domain approach and parametric studies have been carried out in order to show their influences on the dynamic response.

Chasalevris and Papadopoulos [98] determined the natural frequency as a function of crack depth for cracked rotating shaft model using coupled bending vibration of a rotating Timoshenko shaft having a transverse breathing crack. Sinou and Lees [99] studied dynamic response of a rotor with a breathing crack mechanism by changing stiffness of the crack as a truncated Fourier series and also examined various parametric studies including the effects of the crack depth and location on the dynamic response of the cracked rotor. Kisa and Gurel [100] presented a numerical technique to analyze the free vibration response of uniform and stepped cracked beams with circular cross section based on fracture mechanics theory. Arem and Maitournama [101] developed a three-dimensional FE crack model with the unilateral contact between the crack lips based on an energy approach for dynamic and stability analysis. Giannopoulos et al. [102] reported coupled vibration response of a

breathing cracked shaft with time-dependent axial, bending and torsional loading using nonlinear FEM.

However, all the works reported above have focused on a rotor with a single transverse crack. But often more than one crack appears in a shaft and the dynamic characteristics become more complicated depending upon the relative positions and sizes of the cracks. There are few works where double crack on a homogeneous beam or rotor have been considered for determination of the natural frequencies with combination of different locations and sizes of the cracks. Ostachowicz and Krawczuk [103] presented the effect of two open cracks on the natural frequencies of vibrations in a cantilever beam subjected to cyclic and fluctuating loading. Tsai and Wang [104] studied free vibration of multi-cracked rotor using TMM and reported the influences of relative distances and orientations of cracks on free vibration response. Sekhar [105] reported the influences of relative crack size, locations, and slenderness ratio on the eigen-frequencies, mode shapes and threshold speed limits of a rotor-bearing system with two transverse open cracks. Darpe et al. [106] studied responses of a simple Jeffcott rotor with two transverse surface cracks based on the concepts of fracture mechanics and examined the effects of relative crack parameter on the dynamic responses for a simple Jeffcott rotor system. Chasalevris and Papadopoulos [107] reported the dynamic response of a cracked beam with two transverse surface cracks situated at any arbitrary angular position with respect to the longitudinal axis of the beam. Kisa and Gurel [108] proposed a model which combined the finite element method and component mode synthesis method for the modal analysis (natural frequencies and mode shapes) of beams with circular cross section with an arbitrary number of cracks and end conditions based on fracture mechanics theory. Aydin [109] presented a simple and efficient analytical approach to determine the vibrational frequencies and mode shape of axially-loaded Timoshenko beams with an arbitrary number of cracks and different support conditions by modeling the crack by massless rotational spring model.

Khorrami et al. [110] studied vibration responses of two cracked rotor bearing system using a modified harmonic balance method and studied the importance of relative depth, location and angular position of cracks on critical speeds, unbalance lateral response and

shaft center orbit. It was reported that the influence of second crack on critical speeds is higher, while shaft center orbit was affected more by relative angular position. Spagnol et al. [111] studied dynamic response of rotor with breathing phenomenon and examined the importance of crack parameters on critical speeds and unbalance responses. It was reported that a significant influence in computing the critical speed was observed while using the breathing crack method over the existing weight-dominant model. It was also suggested that rotor faults may be reduced with careful placement and size of unbalance mass by using the proposed breathing model. Yang et al. [112] studied dynamic behavior of cracked hollow shaft with parametric uncertainties in a rotor-bearing system using harmonic balance method and polynomial chaos expansion method. It was reported that the non-linear responses (first critical speed and sub-critical speeds) in harmonic components of the rotor system are key indicators for detecting the cracks.

2.4.3 Crack detection and identification

Crack detection and identification in a cracked structures using vibration data has been an active research topic during last few decades due to their increasing importance in industrial applications. Few important works have been reported on the crack detection and identification of beams made of homogeneous materials. Sinha et al. [113] developed a simple model for estimation of location and size of cracks in a cracked Euler-Bernoulli beam by minimizing the difference between the measured and predicted natural frequencies. Results showed that the estimation of location of cracks were more accurate than the estimation of size of cracks and also reported that this estimation of location of a crack is more important for predictive and preventive maintenance than its exact size for the real problems. Using a multi-objective genetic algorithm (GA) and transverse frequency response functions, Singh and Tiwari [114] studied the identification of cracks for a homogeneous shaft based on Timoshenko beam theory. Objective functions for the multi-objective GA were defined as the norm of the difference between the measured and the FEM predicted responses at different measurement locations and reported that the proposed method was tested for two open cracks for obtaining actual crack parameters. Sinha and Elbhbah [115] carried out a study on future possibility of vibration based condition monitoring of rotating machines such as turbo generator and also proposed a method to

reduce the number of vibration sensors for any fault in rotor and which is also useful to reduce the dependency on the experience and the engineering judgments in fault detection process.

2.4.4 Stability analysis

Shafts are basic components in most high-performance rotating machines and equipment, used in power transmission for the requirement of high power and high operational speed. Cracks may appear in a rotating element due to manufacturing defect, cyclic loading and high spin speeds leading to catastrophic failure. From design point of view, investigation of machine instability has been an important aspect of cracked rotor and prediction of appropriate machine design parameters is important to ensure that machine operates at normal operating speeds. Rotor instability may be responsible for economic loss, loss of production, and enhanced maintenance cost. Therefore, study of rotor instability has been an important area of research in last few decades.

There have been a few research works for the stability analysis of rotor/shaft system with single crack and double cracks. Some of them are presented here. Gasch [77] presented stability analysis of a rotating shaft with a transverse crack based on the hinged model. Papadopoulos and Dimarogonas [87] reported the first and second kind instability concepts of a rotating shaft with an open transverse surface crack. Papadopoulos and Dimarogonas [116] studied the stability analysis of cracked rotor in coupled vibration modes and also developed a method for the determination of the intervals of instability of the first and of second kind. Huang et al. [117] investigated dynamic response and stability analysis of a rotating shaft with a transverse breathing crack and showed that for an un-damped condition, instability occurred as rotation were close to an integer fraction or an integer multiple of the shaft bending frequency for a crack depth equal to half of the radius. Chen and Chen [118] studied the stability behavior of a rotating cracked shaft subjected to an end load, an axial compressive force, with the inclusion of effects of the rotatory inertia, shear deformations and gyroscopic moments. Results showed the existence of two major instability regions and a stable region between the major instability regions. It was also shown that the width of this region depends on the crack size and its location. Guo et al.

[119] studied the stability behavior of a Jeffcott rotor system with a transverse breathing crack and reported the influences of crack depth, rotating speed and damping on the instability of the system.

All these works reported in this section have considered only a single crack and did not consider multiple transverse cracks on the shaft. Sekhar [105] reported vibration and system stability study of a rotor-bearing system with two transverse open cracks on the shaft and studied the influences of crack size, location, and slenderness ratio of one crack over the other crack on the eigen-frequencies, mode shapes, and threshold speed limits. Using FEM, Sekhar and Dey [120] studied the stability threshold speed of a rotor-bearing system having single and two transverse breathing cracks and also studied the influences of various crack parameters, geometric parameters and internal damping on the instability speed. Han and Chu [121] reported the instability analysis of a rotor-bearing system with a single and two transverse breathing cracks and showed the influences of crack depths, orientation angles and positions on the stability of the system. Peng et al. [122] carried out stability analysis of an open cracked rotor with anisotropic rotational damping. Lagrange's principle was used to derive the system equations of motion for the cracked rotor system. Campbell diagram, decay rate plot and roots locus plot were obtained for proving destabilizing effect of anisotropy ratio of the rotating damping and reported that the anisotropy of stiffness as function of crack depth was observed to play a decisive role on the length of critical range both in damping and non-damping system.

2.5 Functionally graded cracked structures

Numbers of researches were performed to determine the influence of crack like defects on the static, dynamic and stability analysis of FGMs structures by many researchers. Analysis of cracked FGM structural members has been significant due to their increasing applications in various important engineering industries. Cracks also frequently occurred in FGM structures, which form a serious threat to their safe performance.

2.5.1 Fracture analysis of FGM

Many works have been reported studying the fracture mechanics of FGMs with several distinct problem areas. There has been several works [123-131] reported to compute stress intensity factors (SIFs), fracture toughness, R-curve, stress for cracks in structural member made of nonhomogeneous materials or FGMs for different geometry, loading conditions and thermal environments. Erdogan [123] briefly discussed the concepts of fracture mechanics in nonhomogeneous materials and solved some problems using energy balance-based theories based on conventional fracture mechanics related to the fracture of FGMs and results reported that bonding strength could be improved and residual stresses, thermal stresses, stress singularities, and crack driving force could be reduced by using FGMs as coatings and interfacial zones. Jin and Batra [124] summarized some general fracture mechanics problems for an edge-cracked strip made of FGM. The fracture toughness and R-curve of FGMs were studied based on the crack-bridging concept and rule of mixtures, residual strength behavior of the FGM were examined. Gu and Asaro [125] computed mixed mode SIFs of a semi-infinite crack in a strip made of isotropic and FG material under different loading conditions and the effects of material gradients and phase angles on the mode I and mode II SIFs were determined and also the nature of the crack tip fields and possible fracture criterion for functionally graded materials were discussed. Noda and Jin [126] computed SIFs of a cracked FGM strip subjected to prescribed surface temperature and reported that SIFs could be lowered substantially by selecting the material constants appropriately. The influence of the nonhomogeneity of the material on the temperature distribution and the SIFs were also studied.

Erdogan and Wu [127] reported surface crack problem for an FG plate under three different loading conditions namely fixed grip, membrane and bending. Assuming exponential material properties variation in the thickness direction, stress distribution, Mode I SIFs, and crack surface displacement were computed for embedded as well as edge cracks for various sizes and locations of crack and material non-homogeneity. These works may be useful to compute SIFs in three dimensional surface crack problems for FGM plates. Wang et al. [128] computed SIFs for mode I and mode II of metal-ceramic layered FGMs with penny-shaped cracks under dynamic loading using Laplace and Hankel transform method

with the stiffness matrix approach. Influences of gradient index on SIFs, strain energy density factor, fracture initiating angle were studied. Wang et al. [129] studied a multiple-crack problem for an FGM and a substrate/FGM coating structure with arbitrarily varying material properties. Utilizing a laminated composite plate model, they proposed an algorithm to solve stationary and dynamic fracture problems under thermal and mechanical loading condition, and computed transient and steady-state thermal SIFs due to a change in material gradient index and the location of the crack. Wang et al. [130] studied analytically a surface crack problem in a strip made of metal-ceramic FGM subjected to thermo-mechanical load for arbitrarily distributed material properties in the crack parallel to the gradient direction. Numerical examples indicated that under mechanical loading the effect of different material property distributions on the SIFs was relatively smaller, but under thermal loading, the influence of property distribution on the SIFs could be significant and the proposed model could be used to optimize the property distributions of such FGMs. Jin [131] reviewed the progress in fracture mechanics in FGMs including crack tip elastic fields, K-dominance, fracture toughness and R-curve and described several methods such as integral transform/integral equation method and cohesive zone approach to compute fracture parameters and also discussed some future directions.

2.5.2 Static analysis of FGM

As FGMs are exposed to high thermal environment, structural integrity of FG structure may be lost leading to instability due to excessive deflection, buckling and post-buckling. Deflection is one of the important parameter in design of FG structures because it decides how much bending moments and shear forces could be resisted safely. Buckling study in FGMs is important due to check the stable state. Therefore, during last few years, deflection, buckling and post-buckling analysis of FG structures subjected to different loads are analyzed and are reported which are discussed in the following sections.

There has been limited number of works investigated to study the buckling and post-buckling analysis of FG cracked beams/shafts. Yang and Chen [132] presented a theoretical investigation on free vibration and elastic buckling analysis for cracked FG beams using classical Euler–Bernoulli beam theory (EBBT). Cracked beams were modelled using an

elastic massless rotational spring and material properties followed an exponential variation along the thickness of the FG beam and Poisson's ratio was considered as a constant since its influence on the SIF is quite limited [127]. The mode I SIF was obtained from the study of Erdogan and Wu [127] and from Broek's investigation [133]. The SIF was determined through the boundary integrals using Gaussian quadrature approach and then solved using collocation method and reported that the SIF contained infinite terms which are quite inconvenient in practical calculation. The influences of number and locations of cracks, beam slenderness ratio, material gradient on the dynamic and elastic buckling analysis of cracked FG beams were discussed with different boundary conditions. In this work only bending SIF mode were considered. The influences of temperature, gyroscopic moment, hysteresis and viscous damping were not considered on free vibration and elastic buckling analysis. Shear deformation effect was also not considered.

Ke et al. [134] carried out analytical solutions for flexural vibration and elastic buckling behavior of cracked FG beams using TBT with different end conditions and crack model. The SIF was calculated using Lagrange interpolation technique and material properties of the FG beam were assumed exponentially graded along the thickness direction and Poisson's ratio was considered to be constant. The effects of material property distribution, crack depth, crack location, total number of cracks, slenderness ratio and boundary conditions were examined comprehensively for the vibration and buckling characteristics of the cracked FG Timoshenko beams. The effects of axial displacement and transverse displacement were considered to be negligible as compared with the bending slope. The influences of temperature, gyroscopic, hysteresis and viscous damping were not considered on flexural vibration and elastic buckling analysis.

Ke et al. [135] studied the post-buckling behavior of FG beam with an open edge crack based on TBT and von Karman nonlinear kinematics. Crack was modelled as massless rotational spring model and used material properties graded exponentially along the thickness direction. The influences of depth and location of crack, material property gradient and slenderness ratio on the post-buckling behavior of cracked FG beam were examined and reported that unlike isotropic homogeneous beams, bifurcation buckling does not occur for

both intact and cracked FG beams due to the presence of bending–extension coupling effect. Sherafatnia et al. [136] studied analytically the free vibration and buckling analysis of FG beams with an edge crack using four engineering beam theories (Euler-Bernoulli, Rayleigh, Shear and Timoshenko). The crack was modeled by two massless springs (extensional and rotational springs). The effects of crack position, crack depth, material properties and geometric properties on free vibration and buckling characteristics of the cracked FG beam have been investigated with clamped-free boundary condition.

2.5.3 Vibration analysis of FGM

It is well known that a structure becomes more flexible and its dynamic characteristics change due to the presence of cracks and it has been an active area of research in academic and industries over the last several decades. Researchers have conducted the investigation on free vibration, forced vibration, and dynamic responses either analytically or numerically or both by "direct problem'' and "inverse problem'' of FG cracked structures. The direct problem determined natural frequencies and dynamic response of a FG cracked structure with essential crack parameters and other parameters. The inverse problem deals with measured vibratory data to detect, locate, and quantify the extent of cracks or damages in a FG structure.

There has been limited number of works reported to study the linear vibration analysis of FG cracked beams/shafts. Some of them are already discussed [132, 134, 136] and remaining works are discussed here. Yang et al. [137] reported analytical solutions for free and forced vibration of cracked Euler-Bernoulli inhomogeneous beams under an axial force and a transverse moving load. Cracks were modelled as rotational spring and material properties of the beam were considered exponentially graded along the thickness direction and Poisson's ratio was considered constant. The influences of end conditions, number and location of cracks, material property gradient, slenderness ratio, axial compression and the speed of the moving load on force responses, natural frequencies and dynamic deflections of the cracked FG beam were examined. In this work the shear deformation effect was not considered and only bending SIF mode were considered. The influences of temperature,

gyroscopic moment, hysteresis and viscous damping were not considered on free vibration and elastic buckling analysis.

Matbuly et al. [138] employed line spring model to formulate the free vibration of an elastically supported cracked FG beam resting on a Winkler-Pasternak foundation and used Differential Quadrature Method (DQM) to explain the effects of Young's modulus gradation ratio, elastic and shear foundation modulus, depth and location of crack on the natural frequencies of the cracked FG beam. Based on wave method, Ferezqi et al. [139] reported an analytical solution for the free vibration of a Timoshenko FG beam containing a transverse open crack by using FOSDT and Hamilton's principle, and cracks were modelled based on rotational spring model and the material properties graded following power law gradation in the thickness direction. Parametric study have been performed to examine the influences of depth and location of crack, number of cracks, slenderness ratio, and power law index on the vibration characteristics of the cracked FG Timoshenko beam.

By using EBBT and rotational spring model, Zhang [140] studied the effect of mechanical and electrical characteristics on free vibration of cracked FG beams. The same crack model as in [132] is used and material properties graded exponentially along the thickness direction. The mode I SIF was derived from the investigation of Erdogan and Wu [127] and from Broek's investigation [133]. The influences of piezoelectric patches, multi cracks, material property distribution, end conditions, and the depth and location of crack were inspected on the vibration characteristics of FG beam. Yan and Yang [141] carried out forced vibration of Euler-Bernoulli FG beams with open edge cracks under a combined action of an axial force and a concentrated moving load with different end conditions, using the rotational spring model and the modal expansion technique and parametric studies were performed. Based on the transfer matrix method, Wei et al. [142] implemented a new analytical approach for free vibration analysis of the Euler Bernoulli and Timoshenko FG beam considering the axial load, rotary inertia and shear deformation with an arbitrary number of cracks and various end supports. The crack was modelled as a rotational spring and the SIF was obtained from the investigation of Erdogan and Wu [127] by using the Gaussian quadrature approach and collocation method. A parametric study was carried out

to examine the influences of location and number of crack, material gradation, axial load, rotary inertia, shear deformation, slenderness ratio and boundary conditions on the frequencies and vibration mode shapes of the cracked FG beams. Aydin [143] studied the free vibration analysis of FG beams containing an arbitrary number of open edge cracks considering EBBT and massless rotational spring model with different support conditions. The materials properties were assumed to vary exponentially through the thickness direction and Poisson's ratio has been taken as constant. The crack was modelled and the calculated the bending SIF same as Yang and Chen [132], Ke et al. [134] and Yang et al. [137]. A detailed parametric study has been carried out to examine the influences of depth and location of crack, material property distribution, and boundary conditions on the natural frequencies of the damaged FG beams.

Very few works have been reported on the nonlinear vibrational responses of FG cracked beams/shafts. Kitipornchai et al. [144] computed nonlinear natural frequencies and mode shapes of cracked FG beams using TBT, Ritz method, direct iterative method and von Karman geometric nonlinearity. The effects of crack size and location, slenderness ratio, material property and support conditions on the nonlinear vibration characteristics of the FG beam have been studied. By using TBT, von-Karman type geometric nonlinearity and rotational spring model, Yang and Yan [145] presented analytical solutions for the nonlinear free and forced vibrations of an open edge cracked FG beams subjected to a static compressive force and a harmonic excitation force. The nonlinear natural frequencies, steady state deflection response and excitation frequency-amplitude were obtained for the FG beam with different material property gradient, depth and location of crack, excitation frequency, and slenderness ratio. Ke et al. [146] studied the nonlinear vibration of FG beams containing an open edge crack based on von Karman geometric nonlinearity considering the effects of the transverse shear deformation and rotary inertia. The crack was modeled by massless elastic rotational spring and material properties were considered to be exponentially graded along the thickness direction. DQM and a direct iterative technique were employed to avoid the approximation and handle the nonlinear boundary conditions. The effects of the material property gradient, crack depth and boundary conditions were examined on the non-linear free vibration characteristics of the FG beams and reported that

the DQM was more efficient to solve the nonlinear free vibration problem of cracked FG beams than the Ritz method used in the work of Kitipornchai et al. [144]. Akbas [147] studied static analysis of edge cracked cantilever Timoshenko FG beams subjected to a non-follower transversal point load at the free end of the beam with large displacements and large rotations, considering geometrical nonlinearities. The nonlinear problem was solved by using incremental displacement-based FEM in conjunction with Newton-Raphson iteration method and also parametric studies have been performed.

Based on FEM, Chakraborty et al. [148] studied dynamic analysis of FG shell structures using Koiter shell theory and Mindline's hypothesis. A parametric study carried out to understand the importance of power law exponent on the dynamic response of FG shell structures and reported that the increase in power law exponent as well as radius of curvature, lead to the increase in central deflection of cylindrical FG shell structures. Ranjan and Chakraborty [149] studied the thermo-mechanical analysis of a FG shells based on Koiter's shell theory and Mindlin's hypothesis. The influences of important parameters such as power law gradient, temperature gradient on the natural frequencies and displacement, examined and reported that the power law gradient has a significant effect on the natural frequency as well as on the deflection under thermo-mechanical loading. Amirpour et al. [150] studied an analytical solution of a thick rectangular FG plates with power law of material distribution along the length using HOSDT with the stretching and shear deformation effects. They reported that the proposed exact formulation was not only accurate, but also simple to predict the analysis of FG plates and also showed the importance of material gradient index in obtaining the overall stiffness and maximum deflection of the FG plate. Amirpour et al. [151] derived an analytical formulation of a simply-supported thin rectangular FG plate with in-plane stiffness variation following power law of material gradation under transverse loading and the analytical solutions were compared with the FE solution using graded solid elements. They reported that direction of material stiffness gradient. Do et al. [152] studied the buckling and bending behaviors of 2D FG plates using FEM and a new TOSDT. The graded FG materialsproperties computed in two directions using the rule of mixture. A parametric study was carried out to understand the effects of volume fraction, end conditions, thickness to length ratio on static deflections

and critical buckling and reported the significant effects of aspect ratio on the mechanical behaviors of 2D FG plates.

2.5.4 Crack detection and identification

Crack detection and identification in FG cracked structural members have been a significant research area due to their increasing importance in industries applications. Very few works have been reported on the crack detection and identification of FG beams. Yu and Chu [153] reported p-version FEM to identify position and size of an open edge crack in FG beams assuming exponential gradation of material properties in thickness direction. The SIF in FG composnents was calculated by using a rational approximation function used by Yang and Chen [132], Ke et al. [134] and Yang et al. [137], and also it facilitated to determine local flexibility coefficient due to crack. They studied the influences of size and location of crack and material gradient on the natural frequencies of the cracked cantilever FG beam. Finally crack parameters predicted crack location and size by using the intersection of frequency contours from different modes. Eftekhari et al. [154] identified location and size of crack in a cantilever FG beam with an open edge crack. Cracked beam were modelled using massless rotational spring and EBBT. The crack model and the calculation of local flexibility due to crack were considered similar to those of Ke et al. [134], Zhang [140], and Kitipornchai et al. [144]. Using extended Hamilton's principle, equation of motions for the beam was presented as a function of size and location of crack, and Young modulus ratio and using conjugate gradient method the crack parameters were computed for given natural frequencies of the cracked FG beam. Using FEM, Abolbashari et al. [155] studied the vibration analysis of a cracked FG beam with different crack condition, and reported the influences of depth and location of cracks on natural frequencies of FG beam with single and multiple cracks. They also predicted the depth and location of the crack in the FG beam by using multi-layer feed-forward and artificial neural networks method based on particle swarm optimization and back-error propagation algorithms.

2.5.5 Dynamic analysis of FGM

Yan et al. [156] reported dynamic response of cracked FG Timoshenko beams with an open edge crack resting on an elastic foundation subjected to a transverse moving load at a constant speed considering a linear rotational spring for the crack model. The material properties were assumed to vary exponentially along the thickness direction and Poisson's ratio was taken as constant. Theoretical formulations were implemented based on TBT considering the effect of transverse shear deformation and rotary inertia, the governing equations of motion were derived by using Hamilton's principle and solutions were determined by Galerkin's procedure and Newmark-β method. A parametric study was conducted to highlight the effects of crack depth and location, material property gradient, slenderness ratio, foundation stiffness parameters, velocity of the moving load and end conditions on natural frequencies and dynamic response of the beam. Yan et al. [157] reported a parametric instability of shear deformable FG beam with an open edge crack subjected to a combination of a static compressive force and a harmonic excitation force, using TBT, linear rotational spring model and exponentially graded material properties in the thickness direction. They employed both Galerkin's technique and Bolotin's method to obtain the natural frequencies and principal unstable regions of a cracked FG beam for highlighting the influences of location and depth of crack, material property gradient, slenderness ratio, compressive load, and boundary conditions.

Yan et al. [158] reported an analytical solutions for the nonlinear dynamic behavior of a clamped FG beams with an open edge crack under axial parametric excitation using TBT, von-Karman type geometric nonlinearity and massless rotational spring model. Hamilton's principle, least-squares method and Galerkin technique were used to derive the nonlinear equation of motions, and Runge–Kutta method and multiple scale method were employed to compute natural frequencies, steady state deflection response, excitation frequenc, and amplitude responses. The influences of material property gradient, depth and location of crack, excitation frequency, and slenderness ratio on the nonlinear dynamic behavior of cracked FG beams were studied. Tung and Duc [159] carried out the stability of a simply supported rectangular FG plates under in-plane compressive, thermal and combined loads using a simple analytical approach. Formulation is based on the classical plate theory with

both von Karman type of kinematic nonlinearity and initial geometrical imperfections were accounted. Material properties were considered to be temperature-independent and graded in the thickness direction following power law of material distribution. The results showed that the significant influences of the volume fraction index, plate geometry, in-plane boundary conditions and imperfection on post bucklingand stability behavior ofthe FG plate.

2.6 Summary of literature review and gaps

The forgoing extensive literature survey could be summarized as follows

- Large number of works has been reported on the broad area of analysis of FGM structure in general and a limited number of research works on the FG rotor/shaft.
- Large number of works has been reported on the broad area of analysis of homogeneous cracked structures and there are mainly two approaches (lumped flexibility crack model and continuous crack model) available for crack modeling.
- There are also few works available in the analysis of FG cracked beam and most of those works used massless rotational spring model. But those works do not provide the variation of local flexibility coefficients for obtaining the coupled longitudinal, bending and torsional vibration in cracked FG beams.
- In the existing literature, most of papers have considered only Mode-I SIF and no other modes for the behavior of FG beam and shear deformation effect was also not considered.
- The influences of temperature and internal damping effects (hysteresis and viscous damping) have not been considered on vibration analysis of FG cracked shaft. Poisson's ratio was considered as constant since its influence on the SIF is quite limited [127].
- For a cracked FG shaft, the LFCs are not only a function of crack size but also depends on material gradient index and applied temperature gradients because of large requirements of high temperature applications of FGMs.

Table 2.1 Representation of published articles on FG rotor/shaft

Year	Reference	Method/ Theory	Material gradation law	Major outcome	Limitation
2007	[34]	Analytical method and Tresca's yield criterion	Exponential law of material gradation	Elastic and elastoplastic sate of stresses are evaluated for a rotating FG shaft	Power and sigmoidal laws, and thermal effect are not considered
2007	[37]	Analytical method and von Mises' yield criterion	Any prescribed functional forms	Elastic, plastic and residual stress are evaluated for rotating solid FG shafts	Temperature and crack effect are not considered
2009	[41]	FEM and TBT	Power law of material gradation	Dynamic behaviour are analyzed for rotating FG beams considering damping and geometric stiffening effect	Temperature effect is not considered
2013	[44]	Energy method and Hamilton's principle	Power law of material gradation	The influences gradient index and end conditions on frequency response of FG micro-shaft were examined and reported gradient index has significant impact	Only power function is used for material gradation and temperature effect is not considered
2014	[45]	FEM and TBT	Power law of material gradation	Dynamic analysis are performed for FG shaft under thermal environment	Crack effect is not considered
2014	[46]	FEM and TBT	Power law of material gradation	Whirling frequencies are determined for FG shafts and reported gradient index has huge role on dynamic responses	Crack and temperature effect are not considered
2018	[47]	Analytical method and TBT	Power law of material gradation	Parametric studies are conducted and reported the importance of gradient index on dynamic responses	Crack and temperature effect are not considered. Only power law is used for material gradation

- There is hardly any work reported in the vibration and stability analysis of cracked FG rotor/shaft even though analyses of cracked beam made of homogeneous materials has been an important area of research for a long time.
- Large number of works has been reported on the stability analysis of rotor-bearing system with single transverse fully open crack on the shaft made of homogeneous materials and limited works were also reported in the stability analysis with more than one crack.
- Very few works are reported in the broad area of uncracked FG shaft and even fewer works are reported on analysis of FG shaft with a single transverse breathing crack.
- To the best of author's knowledge, in spite of its gaining practical significance, stability analysis of a rotor-bearing system having an FG shaft with one or more transverse breathing crack has not been reported till date.

Table 2.1 shows the works related to the FG rotors reported in the open literatures till date which will provide a ready reference to the existing gap in this area making the objectives of the thesis more clear.

2.7 Scope of the present work

Summary of the literature review reveals that based on fracture mechanics approach determination of LFCs is very useful for dynamic responses of a FG cracked shaft system. While the cracked model based on rotational spring model [132, 134-137, 139, 140, 142, 143, 156 and 158] was successfully implemented for FG beams for numerical determination of SIFs, the reported crack model of FG beams could not describe all the modes of fracture as well as all the coupled vibration characteristics. In the literatures, the determination of LFCs as a function of crack size has been reported for calculating modified stiffness. However, for an FG cracked shaft the LFCs will also be functions of material gradient index, applied temperature gradients and crack orientations. This has not been reported till date. Temperature dependent material properties have important influence on the vibration and stability behavior of FG rotor shaft system with transverse breathing cracks. This forms the motivation for taking up the present study of analyzing the dynamic behavior of cracked

FG shaft. LFCs could be calculated as functions of crack size, material gradient index, applied temperature gradients and crack orientations and temperature dependent material properties could be used to study the influences of geometrical, crack and other parameters on dynamics responses of the cracked systems for different types of crack configurations.

2.8 Objectives of the present work

Based on the literature review and these observations, the objectives of the present work have been laid down as follows

1. To develop a finite element formulation for modelling FG shafts based on Timoshenko beam theory, considering temperature dependent material properties.
2. To derive local flexibility coefficients as functions of crack size, material gradient index, applied temperature gradient and crack orientation for an FG shaft using Castigliano's theorem and Paris's equations in conjunction with the expression for stress intensity factors K_I, K_{II} and K_{III}.
3. To incorporate the phenomenon of transverse breathing crack in an FG rotating shaft for calculation of modified stiffness degradation at each instant of shaft rotations in the FE formilation.
4. Coordinating the formulation for FG shafts, local flexibility coefficients and breathing cracks and to develop a complete code capable of obtaining the dynamic responses such as natural frequencies, whirling frequencies, critical speeds and stability threshold speeds for cracked FG shafts and validated the developed code.
5. To perform numerical simulation using the developed FE code to study the transverse vibration analysis of an FG shaft with a stationary transverse surface crack in order to understand the
    - ❒ Effects of power law gradient index and temperature gradient on local flexibility coefficients with different crack size.
    - ❒ Effects of slenderness ratio, size and location of crack, power law gradient index and temperature gradient on natural frequencies.

6. To perform numerical simulation using the developed FE code to study transverse vibration analysis of a rotor-bearing system having an FG shaft with single transverse fully open crack in order to understand the influences of crack size, power law gradient index and temperature gradient on the whirling frequencies and critical speeds.
7. To perform numerical simulation using the developed FE code to study the transverse vibration analysis of a rotor-bearing system having an FG shaft with multiple transverse breathing cracks in order to understand the
    - ❒ Influences of crack size, power law gradient index and temperature gradient on local flexibility coefficients with different crack orientation.
    - ❒ Influences of relative size, location and orientation of second crack, power law gradient index and temperature gradient on the dynamic responses such as natural frequencies, whirling frequencies and critical speeds.
8. To perform numerical simulation using the developed FE code for carrying out the stability analysis of a rotor-disc-bearing system having a cracked FG shaft considering both single and multiple breathing cracks to understand the
    - ❒ Influences of slenderness ratio, size and location of crack, relative size, location and orientation of second crack on the stability threshold speed.
    - ❒ Influences of shaft's internal viscous damping, internal hysteretic damping and temperature gradient on the stability threshold speed.
    - ❒ Influence of power law gradient index on the stability threshold speed for a cracked FG shaft with an objective to investigate whether the material gradient could be varied to acheive a desire range of stability threshold speed.

CHAPTER 3

Finite Element Formulation of a Rotor-Bearing System with a Cracked FG Shaft

3.1 Introduction

This chapter presents the finite element (FE) formulation of a rotor-bearing system having an FG shaft with transverse crack (stationary and breathing). Effective thermo-mechanical properties of FGMs are modeled theoretically and FE formulation of a typical rotor-bearing system having a cracked FG shaft has been presented considering different types of beam theories, namely Timoshenko beam theory, Rayleigh beam theory, Euler-Bernoulli beam theory and shear beam theory. Finally, transverse stationary and transverse breathing cracks are modeled based on fracture mechanics approach.

3.2 Modeling of functionally graded material properties

Since, FG structures are most commonly used in high temperature environment, where significant changes in mechanical properties of the constituent materials are expected, accurate and effective material property estimation is essential for analysis and design of any FG structures/system. In order to accurately model various FGM structures, temperature and position dependent material properties can be modelled by using rule of mixture (simple rule of mixture and modified rule of mixture), variational approach, and micromechanical approach.

3.2.1 Estimation of effective material properties of FGMs

FGMs are mainly proposed for structural members to suit high temperature applications. In evaluating the behaviour of FGMs, following the work of Touloukian [160], temperature dependency of material properties $C(T)$ are considered as

$$C(T) = C_0\left(C_{-1}T^{-1} + 1 + C_1T + C_2T^2 + C_3T^3\right) \tag{3.1}$$

where C_0, C_{-1}, C_1, C_2 and C_3 are temperature coefficients, unique to each constituent materials and T is the temperature in Kelvin. **Table 3.1** shows the values of these coefficients for some commonly used constituent materials in FGMs viz. stainless steel (SS) zirconia (ZrO_2) and alumina (Al_2O_3) for Young's modulus, Poisson's ratio, thermal conductivity.

Table 3.1 Temperature coefficients value for different mechanical properties [27] of FGMs.

Properties	Materials	C_0	C_{-1}	C_1	C_2	C_3
E (Pa)	SS	201.04×10^{9}	0	3.079×10^{-4}	-6.534×10^{-7}	0
	ZrO_2	244.27×10^{9}	0	-1.371×10^{-3}	1.214×10^{-6}	-3.681×10^{-10}
	Al_2O_3	349.55×10^{9}	0	-3.853×10^{-4}	4.027×10^{-7}	-1.673×10^{-10}
ν	SS	0.3262	0	-2.002×10^{-4}	3.797×10^{-7}	0
	ZrO_2	0.2882	0	1.133×10^{-4}	0	0
	Al_2O_3	0.2600	0	0	0	0
K (W/m K)	SS	15.379	0	-1.264×10^{-3}	2.092×10^{-6}	-7.223×10^{-10}
	ZrO_2	1.700	0	1.276×10^{-4}	6.648×10^{-8}	0
	Al_2O_3	-14.087	-1123.6	-6.227×10^{-3}	0	0
ρ (kg/m^3)	SS	8166	0	0	0	0
	ZrO_2	5700	0	0	0	0
	Al_2O_3	3750	0	0	0	0

Referring to **Fig. 3.1**, the material properties C in an FG shaft are graded along the radial direction (y) as a function of temperature (T), following the work of Reddy and Chin [27]

$$C(y,T) = C_i(T) + \{C_o(T) - C_i(T)\}\left[(y - R_i)/(R_o - R_i)\right]^k \tag{3.2}$$

where $C(y,T)$ represents the properties (Young's modulus E (in Pa), Poisson's ratio ν, thermal conductivity K (in W/m K), internal viscous damping coefficient η_v (in s) and internal hysteretic damping coefficient η_h). **Fig. 3.1** shows the continuous gradation of material properties along radial direction and the geometry of circular cross section of the

FG shaft, where R_i and R_o are the inner and outer radius of the shaft respectively and y represents any radius between R_i and R_o $(R_i \le y \le R_o)$. Subscripts o and i represent the outer and inner, respectively. k $(0 \le k \le \infty)$ is the power law gradient index with $k = 0$ and $k = \infty$ denotes the completely homogenous outer and inner material, respectively. For $k = 1$, **Eq. (3.2)** represent the linear law of material gradation and other values of the k **Eq. (3.2)** represent the power law of material gradation (P-FGM). In the present study outer side of the shaft presents the ceramic phase and inner side presents metalic phase of the FGMs.

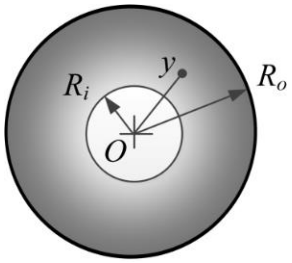

Fig. 3.1 Material properties gradation in radial direction

Material properties distribution following exponential law of material gradation (E-FGM) is given by

$$C(y,T) = C_i(T)\ e^{\lambda(y-R_i)},\ \lambda = \ln\left\{C_o(T)/C_i(T)\right\}/(R_o - R_i),\ R_o \le y \le R_i \tag{3.3}$$

Material properties distribution following sigmoid law of material gradation (S-FGM) is given by

$$\left.\begin{aligned} C(y,T) &= C_i(T) + \left\{C_o(T) - C_i(T)\right\}\left(\frac{y - R_i}{R_o - R_i}\right)^n,\ R_i \le y \le \frac{R_i + R_o}{2} \\ C(y,\mathrm{T}) &= C_o(T) + \left\{C_i(T) - C_o(T)\right\}\left(1 - \frac{y - R_i}{R_o - R_i}\right)^n,\ \frac{R_i + R_o}{2} \le y \le R_o \end{aligned}\right\} \tag{3.4}$$

where n is the sigmoid law gradient index.

3.2.2 Steady-state temperature distributions

The general form of heat conduction equation with variable thermal conductivity in cylindrical coordinates [161] is given

$$\left(\frac{1}{y}K(y)\frac{dT}{dy}+\frac{d^2T}{dy^2}+\frac{1}{y^2}K(\theta)\frac{d^2T}{d\theta^2}+K(z)\frac{d^2T}{dz^2}\right)+q_{hg}=\rho c_p\frac{dT}{dt} \tag{3.5}$$

where $K(y)$, $K(\theta)$ and $K(z)$ are the thermal conductivity along the coordinate axes y, θ and z, respectively. q_{hg} is the heat generation per unit volume and c_p is the specific heat capacity.

Using Eq. (3.5), for a hollow cylinder with axisymmetric case, steady state condition and in the absence of heat generation, temperature distributions along the radial direction in a thin circular cross section FG shaft the heat conduction equation becomes

$$\frac{d}{dy}\left[yK(y)\frac{dT}{dy}\right]=0 \tag{3.6}$$

This **Eq. (3.6)** could be solved subjected to thermal boundary conditions as

at $y=R_i,\ T=T_i$ (3.7)

at $y=R_o,\ T=T_o$ (3.8)

where T_o and T_i are the temperature in ceramic-rich (outer) and metal-rich (inner) surfaces, respectively.

Solution to this **Eq. (3.6)** could be obtained for different laws of material property gradation. For power law of material gradation, the solution takes the form [162]

$$T(y)=T_i\left(1-\frac{\int_{R_i}^{R}\{dy/yK(y)\}}{\int_{R_i}^{R_o}\{dy/yK(y)\}}\right)+T_o\left(\frac{\int_{R_i}^{R}\{dy/yK(y)\}}{\int_{R_i}^{R_o}\{dy/yK(y)\}}\right) \tag{3.9}$$

However for a solid shaft, this leads to singularity at the centre ($y=0$). Eventhough there are approximate methods of obtataining temperature distribution in a solid circular

shaft, there are issues of convergence and the accuracy of the solution depends upon the solution technique used. In view of this, in the present work a uniform temperature distribution along the radial direction has been assumed. Eventhough the actual temperature distribution will not be uniform, assumption of uniform temperature will actually underestimate the shaft performance from the view point of safety in the form of over predicting the compliances and underpredicting the stability threshold speeds. Thus in the present work temperature distribution has been considered as

$$T = T_o \text{ at any } y \ (0 \le y \le R) \tag{3.10}$$

These graded thermomechanical material properties are used in FE formulation of both the uncracked and cracked FG shaft which is described in this thesis work.

3.3 Rotor-Bearing system

The rotor-bearing system is considered to comprise a set of interconnecting components consisting of shaft elements with distributed mass, elasticity, rigid discs, and bearings. Four different types of beam theories, namely Timoshenko beam theory, Rayleigh beam theory, Euler-Bernoulli beam theory, and shear beam theory are considered in the present analysis. In the FE simulation, equations of motion (EOMs) of the shaft element are obtained using shape functions and extended Hamilton's principle [63]. Equations of motion of rigid disc are obtained using Lagrangian equation, and the bearing equation is employed based on classical linearized model with eight spring and damping coefficients [62 and 65]. Finally, the details of the solution procedure used in the present analysis of the FG rotor system have been discussed.

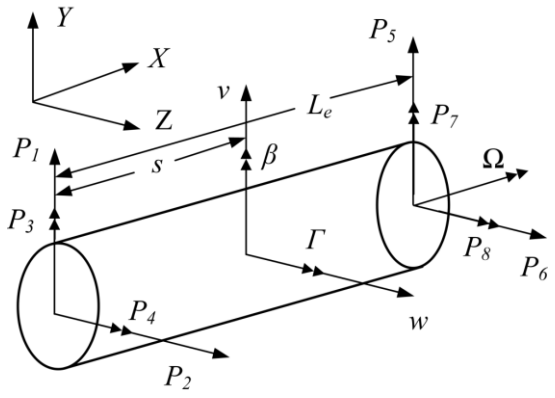

Fig. 3.2 Typical finite shaft element and coordinate system

3.3.1 Finite shaft element

A typical finite shaft element is considered with element length L_e and rotating at a constant speed Ω, shown in **Fig. 3.2** with general motion (translation and rotation) of the element. **Fig. 3.2** shows the finite shaft element, which is subjected to shear forces P_1, P_2, P_5 and P_6, and bending moments P_3, P_4, P_7 and P_8 during the general motion (translational and rotational) of the shaft element. It is assumed that, as compared to the translational motion, the axial motion is small enough to be reasonably neglected. Referring to **Fig. 3.2**, a typical cross-section of the shaft element located at a distance *s* from the left end is described by the translational displacements $v(s,t)$ and $w(s,t)$ in the Y and Z directions and rotational displacements $\beta(s,t)$ and $\Gamma(s,t)$ about Y and Z directions respectively. The translational displacements $v(s,t)$ and $w(s,t)$ consist of bending deformation $v_b(s,t)$ and $w_b(s,t)$ and shear deformation $v_s(s,t)$ and $w_s(s,t)$ and these are the function of axial position s and time t. The rotational displacements $\beta(s,t)$ and $\Gamma(s,t)$ are related to bending translational displacements $v_b(s,t)$ and $w_b(s,t)$. The relationship can be written as

$$v(s,t) = v_b(s,t) + v_s(s,t) \tag{3.11}$$

$$w(s,t) = w_b(s,t) + w_s(s,t) \tag{3.12}$$

$$\beta(s,t) = -\partial w_b(s,t)/\partial s \tag{3.13}$$

$$\Gamma(s,t) = \partial v_b(s,t)/\partial s \tag{3.14}$$

In the FE method the continuous displacement field can be approximated in terms of the discretized generalized displacements form of the element nodes. In the present FE model, each element has two nodes and each node has four generalized displacements viz. $v(s,t)$, $w(s,t)$, $\beta(s,t)$ and $\Gamma(s,t)$. Therefore the displacement field in an element could be written as

$$\{v(s,t),\ w(s,t),\ \beta(s,t),\ \Gamma(s,t)\}^T = \sum_{i=1}^{2} N_i(s)\{v_i,\ w_i,\ \beta_i,\ \Gamma_i\}^T \tag{3.15}$$

where i represents node number and shape function is written as summation of translation shape function $\psi(s)$ and rotational shape function $\varphi(s)$.

The translation displacement of a typical element at a typical point is

$$\begin{Bmatrix} v(s,t) \\ w(s,t) \end{Bmatrix} = \begin{Bmatrix} v_b(s,t) \\ w_b(s,t) \end{Bmatrix} + \begin{Bmatrix} v_s(s,t) \\ w_s(s,t) \end{Bmatrix} = [\psi(s)]\{\mathbf{P}^e(t)\} = \left([\psi_{tb}(s)] + [\psi_{ts}(s)]\right)\{\mathbf{P}^e(t)\} \tag{3.16}$$

where $\psi_{tb}(s)$ and $\psi_{ts}(s)$ are the bending translation and shear translation shape function respectively, and the translation shape function matrix $\psi(s)$ [63] and nodal displacement vector $\{\mathbf{P}^e(t)\}$ expressed as

$$[\psi(s)] = \begin{bmatrix} \psi_1 & \psi_3 & 0 & 0 & 0 & 0 & \psi_2 & \psi_4 \\ 0 & 0 & \psi_1 & \psi_3 & -\psi_2 & -\psi_4 & 0 & 0 \end{bmatrix} \tag{3.17}$$

$$\{\mathbf{P}^e(t)\} = [v_1 \quad v_2 \quad w_1 \quad w_2 \quad \beta_1 \quad \beta_2 \quad \Gamma_1 \quad \Gamma_2]^T \tag{3.18}$$

The elements of **Eq. (3.17)**, $\psi_i(s) = [\alpha_i(s) + \Phi\beta_i(s)]/(1+\Phi)$, (where $i = 1,\ 2,\ 3,\ 4$) represent the static displacement modes associated with a unit displacement of one of the nodal point with all others constrained to zero. The terms $\alpha_i(s)$ and $\beta_i(s)$ are related to the bending and shear deformation, respectively, for the Timoshenko beam [63] and are given as

$$\alpha_1 = 1-3\xi^2+2\xi^3,\ \alpha_2 = L_e\xi(1-2\xi+\xi^2),\ \alpha_3 = \xi^2(3-2\xi),\ \alpha_4 = L_e\xi(-1+\xi)/2 \tag{3.19}$$

$$\beta_1 = 1-\xi,\ \beta_2 = L_e\xi(1-\xi)/2,\ \beta_3 = \xi,\ \beta_4 = L_e\xi(-1+\xi)/2 \tag{3.20}$$

where $\xi = s/L_e$ and $\Phi = 12E(y,T)I/\kappa_{sc}(y,T)AG(y,T)L_e^2$

Similarly for a typical element rotations can be expressed as

$$\begin{Bmatrix} \beta(s,t) \\ \Gamma(s,t) \end{Bmatrix} = \left[\varphi(s)\right]\left\{\mathbf{P}^e(t)\right\} \tag{3.21}$$

where the rotational shape function matrix [63] is given as

$$\left[\varphi(s)\right] = \begin{bmatrix} \left[\varphi_x\right] \\ \left[\varphi_y\right] \end{bmatrix} \begin{bmatrix} 0 & 0 & -\varphi_1 & -\varphi_3 & \varphi_2 & \varphi_4 & 0 & 0 \\ \varphi_1 & \varphi_3 & 0 & 0 & 0 & 0 & \varphi_2 & \varphi_4 \end{bmatrix} \tag{3.22}$$

The elements of **Eq. (3.22)**, $\varphi_i(s) = \left[\varepsilon_i(s) + \Phi\delta_i(s)\right]/\left(1+\Phi\right)$, (where $i = 1,\ 2,\ 3,\ 4$) represent the static rotational modes associated with a unit displacement of one of the nodal point with all others constrained to zero. The terms $\varepsilon_i(s)$ and $\delta_i(s)$ are related to the bending and shear deformation, respectively, for the Timoshenko beam [63] and are given as

$$\varepsilon_1 = 6\xi\left(\xi-1\right)/L_e,\ \varepsilon_2 = 1-4\xi+3\xi^2,\ \varepsilon_3 = 6\xi\left(1-\xi\right)/L_e,\ \varepsilon_4 = \xi\left(3\xi-2\right) \tag{3.23}$$

$$\delta_1 = 0,\ \delta_2 = 1-\xi,\ \delta_3 = 0,\ \delta_4 = \xi \tag{3.24}$$

The kinetic energy of a shaft element rotating at constant spin speed $\dot{\varphi} = \Omega$, including the translational and rotational forms is given as

$$T_s^e = \left.\begin{aligned} &\underbrace{\frac{1}{2}\begin{Bmatrix} \dot{v} \\ \dot{w} \end{Bmatrix}^T \begin{bmatrix} m(y) & 0 \\ 0 & m(y) \end{bmatrix} \begin{Bmatrix} \dot{v} \\ \dot{w} \end{Bmatrix} ds}_{\text{Translational}} + \underbrace{\frac{1}{2}\begin{Bmatrix} \dot{\beta} \\ \dot{\Gamma} \end{Bmatrix}^T \begin{bmatrix} I_d^s(y) & 0 \\ 0 & I_d^s(y) \end{bmatrix} \begin{Bmatrix} \dot{\beta} \\ \dot{\Gamma} \end{Bmatrix} ds}_{\text{Rotatory inertia effect}} \\ &+ \underbrace{\frac{1}{2}\Omega^2 I_p^s(y)\, ds}_{\text{Spinning motion}} - \underbrace{\Omega I_p^s(y)\, \beta\dot{\Gamma} ds}_{\text{Gyroscopic effect}} \end{aligned}\right\} \tag{3.25}$$

The potential energy of the shaft element consists of elastic bending and shear energy, and is given as

$$V_s^e = \left.\begin{aligned} &\overbrace{\frac{1}{2}\begin{Bmatrix} v_b'' \\ w_b'' \end{Bmatrix}^T \begin{bmatrix} E(y,T)I & 0 \\ 0 & E(y,T)I \end{bmatrix} \begin{Bmatrix} v_b'' \\ w_b'' \end{Bmatrix} ds}^{\text{Bending load}} \\ &+ \overbrace{\frac{1}{2}\begin{Bmatrix} v_s' \\ w_s' \end{Bmatrix}^T \begin{bmatrix} \kappa_{sc}(y,T)G(y,T)A & 0 \\ 0 & \kappa_{sc}(y,T)G(y,T)A \end{bmatrix} \begin{Bmatrix} v_s' \\ w_s' \end{Bmatrix} ds}^{\text{Shear load}} \end{aligned}\right\} \tag{3.26}$$

Using **Eq. (3.16)** and **Eq. (3.21),** in **Eq. (3.25)** and **Eq. (3.26)**, we get

$$\left.\begin{aligned} T_s^e = &\frac{1}{2}m(y)\left\{\dot{\mathbf{P}}^e(t)\right\}^T[\psi]^T[\psi]\left\{\dot{\mathbf{P}}^e(t)\right\}ds + \frac{1}{2}I_d^s(y)\left\{\dot{\mathbf{P}}^e(t)\right\}^T[\varphi]^T[\varphi]\left\{\dot{\mathbf{P}}^e(t)\right\}ds \\ &+\frac{1}{2}\Omega^2 I_p^s(y)\,ds - \Omega I_p^s(y)\left\{\dot{\mathbf{P}}^e(t)\right\}^T\left[\varphi_y\right]^T[\varphi_x]\left\{\mathbf{P}^e(t)\right\}ds \end{aligned}\right\} \tag{3.27}$$

$$\left.\begin{aligned} V_s^e = &\frac{1}{2}E(y,T)I\left\{\mathbf{P}^e(t)\right\}^T\left[\psi_{tb}''\right]^T\left[\psi_{tb}''\right]\left\{\mathbf{P}^e(t)\right\}ds \\ &+\frac{1}{2}\kappa_{sc}(y,T)G(y,T)A\left\{\mathbf{P}^e(t)\right\}^T\left[\psi_{ts}''\right]^T\left[\psi_{ts}''\right]\left\{\mathbf{P}^e(t)\right\}ds \end{aligned}\right\} \tag{3.28}$$

The energy of the complete element is obtained by integrating equations over the length of the shaft element, as

$$T_s^e = \frac{1}{2}\left\{\dot{\mathbf{P}}^e(t)\right\}^T\left(\left[\mathbf{M}_t^e\right]+\left[\mathbf{M}_r^e\right]\right)\left\{\dot{\mathbf{P}}^e(t)\right\} + \frac{1}{2}\Omega^2 I_p^s(y) + \Omega\left\{\dot{\mathbf{P}}^e(t)\right\}^T\left[\mathbf{N}^e\right]^T\left\{\mathbf{P}^e(t)\right\} \tag{3.29}$$

$$V_s^e = \frac{1}{2}\left\{\mathbf{P}^e(t)\right\}^T\left(\left[\mathbf{K}_b^e\right]+\left[\mathbf{K}_s^e\right]\right)\left\{\mathbf{P}^e(t)\right\} = \frac{1}{2}\left\{\mathbf{P}^e(t)\right\}^T\left(\left[\mathbf{K}^e\right]\right)\left\{\mathbf{P}^e(t)\right\} \tag{3.30}$$

where

$$\left[\mathbf{M}_t^e\right] = \int_0^{L_e}\int_0^{R_o} m(y)[\psi]^T[\psi]\,dyds \tag{3.31}$$

$$\left[\mathbf{M}_r^e\right] = \int_0^{L_e}\int_0^{R_o} I_d^s(y)[\varphi]^T[\varphi]\,dyds \tag{3.32}$$

$$\left[\mathbf{K}_b^e\right] = \int_0^{L_e}\int_0^{R_o} E(y,T) I \left[\psi_{tb}''\right]^T \left[\psi_{tb}''\right] dyds \tag{3.33}$$

$$\left[\mathbf{K}_s^e\right] = \int_0^{L_e}\int_0^{R_o} \kappa_{sc}(y,T) G(y,T) A \left[\psi_{ts}''\right]^T \left[\psi_{ts}''\right] dyds \tag{3.34}$$

$$\left[\mathbf{N}^e\right] = \int_0^{L_e}\int_0^{R_o} I_p^s(y) \left[\varphi_y\right]^T \left[\varphi_x\right] dyds \tag{3.35}$$

where

$$m = 2\pi \int_0^{R_o} \rho(y)\, y\, dy,\quad I_d^s = \pi \int_0^{R_o} \rho(y)\, y^3\, dy \text{ and } I_p^s = 2\pi \int_0^{R_o} \rho(y)\, y^3\, dy \tag{3.36}$$

where $I_d^s(y)$ and $I_p^s(y)$ are the diametrical and polar mass moment of inertia per unit length for the shaft, $m(y)$ is the element mass per unit length, $E(y,T)I$ is the bending stiffness, $\kappa_{sc}(y,T)$ is the shear correction factor, $G(y,T)$ is the modulus of rigidity, and A is the cross section area of the shaft. The symbol $'$ and $\cdot$ are used as differentiation with respect to position and time, respectively.

If the rotatory inertia matrix $\left[\mathbf{M}_r^e\right]$ and the shear deformation parameter Φ are omitted in the shape functions, the present model represents the conventional **Euler-Bernoulli beam model (EB-BM)**. If only the parameter Φ is omitted then the present model represents the **Rayleigh beam model (R-BM)**. If only the parameter $\left[\mathbf{M}_r^e\right]$ is omitted then the present model represents the **shear beam model (S-BM)**.

The element equations can be determined using the extended Hamilton's principle, which states that the definite integral of any variation of a true path between two time instants t_1 and t_2 providing the path variations vanishes at the end points. So, the Hamilton's principle and EOMs are determined by the following relations

$$\delta \int_{t_1}^{t_2} I \, dt = 0, \text{ where } I = \left(T_s^e - V_s^e\right) \tag{3.37}$$

$$\delta \left(\int_{t_1}^{t_2} \left(T_s^e - V_s^e\right) dt \right) = 0 \tag{3.38}$$

The application of extended Hamilton's principle by **Eq. (3.38)** with the kinetic and potential energy form **Eq. (3.29)** and **Eq. (3.30)** produces the following EOMs for the finite shaft element for a fixed frame coordinates as

$$\left(\left[\mathbf{M}_t^e\right] + \left[\mathbf{M}_r^e\right]\right)\left\{\ddot{\mathbf{P}}^e(t)\right\} - \Omega\left[\mathbf{G}^e\right]\left\{\dot{\mathbf{P}}^e(t)\right\} + \left[\mathbf{K}^e\right]\left\{\mathbf{P}^e(t)\right\} = \left\{\mathbf{F}^e(t)\right\} \tag{3.39}$$

where the gyroscopic matrix and the external force vector for the shaft element is given by

$$\left[\mathbf{G}^e\right] = \left(\left[\mathbf{N}^e\right] - \left[\mathbf{N}^e\right]^T\right) \tag{3.40}$$

$$\left\{\mathbf{F}^e\right\} = \int_0^{L_e} P_{ext} \left[\psi\right]^T ds \tag{3.41}$$

The details element matrices of **Eq. (3.39)** are listed in **Appendix A** (**Eqs. (A.1)** to **(A.15)**) for a uniform cross-section shaft element. P_{ext} is the externally applied load.

3.3.2 Rigid disc

The kinetic energy of a typical rigid disc (refer **Fig. 3.3**) in translation and rotation with the mass center coinciding with the elastic rotor center line is given as

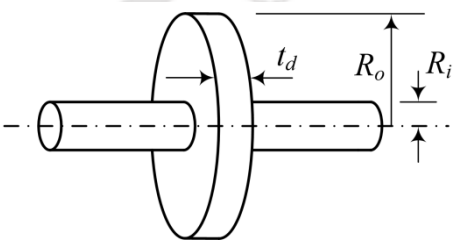

Fig. 3.3 Geometry of a disc mounted on a shaft

$$T^d = \frac{1}{2}\begin{Bmatrix} \dot{v} \\ \dot{w} \end{Bmatrix}^T \begin{bmatrix} m^d & 0 \\ 0 & m^d \end{bmatrix} \begin{Bmatrix} \dot{v} \\ \dot{w} \end{Bmatrix} + \frac{1}{2}\begin{Bmatrix} \dot{\beta} \\ \dot{\Gamma} \end{Bmatrix}^T \begin{bmatrix} I_d^d & 0 \\ 0 & I_d^d \end{bmatrix} \begin{Bmatrix} \dot{\beta} \\ \dot{\Gamma} \end{Bmatrix} - \dot{\varphi}\beta\dot{\Gamma} I_P^d \tag{3.42}$$

where

$$m^d = \pi\rho\left(R_o^2 - R_i^2\right)t_d,\quad I_d^d = \frac{\pi}{4}\rho\left(R_o^4 - R_i^4\right)t_d \text{ and } I_p^d = \frac{\pi}{2}\rho\left(R_o^4 - R_i^4\right)t_d \tag{3.43}$$

EOMs of the rigid disc can be determined using Lagrangian equation and considering the constant spin speed $\dot{\varphi} = \Omega$, as

$$\left(\left[\mathbf{M}_t^d\right] + \left[\mathbf{M}_r^d\right]\right)\left\{\ddot{\mathbf{P}}^d(t)\right\} - \Omega\left[\mathbf{G}^d\right]\left\{\dot{\mathbf{P}}^d(t)\right\} = \left\{\mathbf{F}^d(t)\right\} \tag{3.44}$$

where the individual matrices are provided in details in **Appendix A** (**Eqs. (A.16)** to **(A.17)**).

3.3.3 Consideration of bearings

Bearings are modeled based on the classical linearized model with eight springs and damping coefficients following the work of Nelson and McVaugh [62], and Özgüven and Özkan [65]. In this model the forces at each bearing are assumed to follow the governing equation as

$$\left[\mathbf{C}^b\right]\left\{\dot{\mathbf{P}}^b(t)\right\} + \left[\mathbf{K}^b\right]\left\{\mathbf{P}^b(t)\right\} = \left\{\mathbf{F}^b(t)\right\} \tag{3.45}$$

where $\left[\mathbf{C}^b\right]$ and $\left[\mathbf{K}^b\right]$ are the bearing damping and stiffness matrices, $\left\{\mathbf{F}^b(t)\right\}$ is the bearing external force vector and these matrices are

$$\left[\mathbf{C}^b\right] = \begin{bmatrix} C_{vv}^b & C_{vw}^b \\ C_{vw}^b & C_{ww}^b \end{bmatrix},\ \left[\mathbf{K}^b\right] = \begin{bmatrix} K_{vv}^b & K_{vw}^b \\ K_{vw}^b & K_{ww}^b \end{bmatrix},\ \left\{\mathbf{P}^b\right\} = \begin{Bmatrix} v \\ w \end{Bmatrix} \tag{3.46}$$

3.3.4 Incorporation of internal damping

Based on work of Zorzi and Nelson [20] the rotor dynamic equations of motion can be modified by including the contributions of both viscous and hysteretic internal damping. With the addition of internal damping effects into the FE formulation of rotor-bearing system and by assuming a constitutive relation relating the axial stress σ_x to the axial strain ε_x is given by [20]

$$\sigma_x = E\left[\frac{\varepsilon_x}{\sqrt{1+\eta_h^2}} + \left(\eta_v + \frac{\eta_h}{\sqrt{1+\eta_h^2}}\right)\dot{\varepsilon}_x\right] \tag{3.47}$$

Using viscous damping coefficient η_v and hysteretic loss factor η_h of the shaft materials, according to Zorzi and Nelson [20] the differential bending strain energy dP_{db}^e and the bending dissipated energy dD_{db}^e for an element are expressed as

$$dP_{db}^e = \frac{1}{2}E(y,T)I\begin{Bmatrix} v_b'' \\ w_b'' \end{Bmatrix}^T \left[\eta(y,T)\right]\begin{Bmatrix} v_b'' \\ w_b'' \end{Bmatrix} ds \tag{3.48}$$

$$dD_{db}^e = \frac{1}{2}\eta_v(y,T)\begin{Bmatrix} \dot{v}_b'' \\ \dot{w}_b'' \end{Bmatrix}^T \begin{bmatrix} E(y,T)I & 0 \\ 0 & E(y,T)I \end{bmatrix}\begin{Bmatrix} \dot{v}_b'' \\ \dot{w}_b'' \end{Bmatrix} ds \tag{3.49}$$

where

$$\left[\eta(y,T)\right] = \begin{bmatrix} \eta_a & \eta_b \\ -\eta_b & \eta_a \end{bmatrix}, \text{ and } \eta_a = \frac{1+\eta_h}{\sqrt{1+\eta_h^2}},\ \eta_b = \frac{\eta_h}{\sqrt{1+\eta_h^2}} + \Omega\eta_v \tag{3.50}$$

Using **Eq. (3.16)**, into the **Eq. (3.48)** and **Eq. (3.49)** the bending strain energy and the bending dissipated energy of the shaft element with internal viscous and hysteretic damping are

$$P_{db}^e = \frac{1}{2}E(y,T)I\left\{\mathbf{P}^e(t)\right\}^T\left[\psi_{tb}''\right]^T[\eta]\left[\psi_{tb}''\right]\left\{\mathbf{P}^e(t)\right\}ds \tag{3.51}$$

$$D_{db}^e = \frac{\eta_v}{2}E(y,T)I\left\{\dot{\mathbf{P}}^e(t)\right\}^T\left[\psi_{tb}''\right]^T\left[\psi_{tb}''\right]\left\{\dot{\mathbf{P}}^e(t)\right\}ds \tag{3.52}$$

So, for the whole length of the shaft element the bending strain energy and the bending dissipated energy with internal viscous and hysteretic damping are obtained by integrating **Eq. (3.51)** and **Eq. (3.52)** over the length of the shaft element in the form as

$$P_{db}^{e}=\frac{\eta_a(y,T)}{2}\left\{\mathbf{P}^{e}(t)\right\}^{T}\left[K_{b}^{e}\right]\left\{\mathbf{P}^{e}(t)\right\}ds+\frac{\eta_b}{2}\left\{\mathbf{P}^{e}(t)\right\}^{T}\left[K_{cb}^{e}\right]\left\{\mathbf{P}^{e}(t)\right\}ds \tag{3.53}$$

$$D_{db}^{e}=\frac{\eta_v(y,T)}{2}\left\{\dot{\mathbf{P}}^{e}(t)\right\}^{T}\left[K_{b}^{e}\right]\left\{\dot{\mathbf{P}}^{e}(t)\right\}ds \tag{3.54}$$

where

$$\left[\mathbf{K}_{cb}^{e}\right]=\int_0^{L_e}\int_0^{R_o}E(y,T)I\left[\psi_{tb}''\right]^{T}\left[\mathbf{N}\right]\left[\psi_{tb}''\right]dyds \tag{3.55}$$

and

$$\left[\mathbf{N}\right]=\begin{bmatrix}0 & 1\\ -1 & 0\end{bmatrix} \tag{3.56}$$

If we include the shear deformations into the above damping model, the strain energy and the dissipated energy with the internal viscous and hysteretic damping are obtained as

$$P_{d}^{e}=\frac{\eta_a(y,T)}{2}\left\{\mathbf{P}^{e}(t)\right\}^{T}\left[\mathbf{K}^{e}\right]\left\{\mathbf{P}^{e}(t)\right\}ds+\frac{\eta_b(y,T)}{2}\left\{\mathbf{P}^{e}(t)\right\}^{T}\left[\mathbf{K}_{c}^{e}\right]\left\{\mathbf{P}^{e}(t)\right\}ds \tag{3.57}$$

$$D_{d}^{e}=\frac{\eta_v(y,T)}{2}\left\{\dot{\mathbf{P}}^{e}(t)\right\}^{T}\left[\mathbf{K}^{e}\right]\left\{\dot{\mathbf{P}}^{e}(t)\right\}ds \tag{3.58}$$

where

$$\left.\begin{aligned}\left[\mathbf{K}_{c}^{e}\right]=&\int_0^{L_e}\int_0^{R_o}E(y,T)I\left[\psi_{tb}''\right]^{T}\left[\mathbf{N}\right]\left[\psi_{tb}''\right]dyds\\&+\int_0^{L_e}\int_0^{R_o}\kappa_{sc}(y,T)G(y,T)A\left[\psi_{ts}''\right]^{T}\left[\mathbf{N}\right]\left[\psi_{ts}''\right]dyds\end{aligned}\right\} \tag{3.59}$$

Finally, using extended Hamilton's principle, EOMs for a Timoshenko shaft element including the rigid disc, bearing, and internal damping effects, is obtained as

$$\left(\left[\mathbf{M}^e\right]\right)\left\{\ddot{\mathbf{P}}^e(t)\right\}+\left(\eta_v\left[\mathbf{K}^e\right]-\Omega\left[\mathbf{G}^e\right]+\left[\mathbf{C}^e\right]\right)\left\{\dot{\mathbf{P}}^e(t)\right\}$$
$$+\left[\frac{1+\eta_h}{\sqrt{1+\eta_h^2}}\left[\mathbf{K}^e\right]+\left(\Omega\eta_v+\frac{\eta_h}{\sqrt{1+\eta_h^2}}\right)\left[\mathbf{K}_c^e\right]\right]\left\{\mathbf{P}^e(t)\right\}=\left\{\mathbf{F}_{total}^e(t)\right\} \tag{3.60}$$

where $\left[\mathbf{M}^e\right]$ is the total elemental mass matrix (including the rotary and translational masses of the shaft, and rigid disc), $\left[\mathbf{K}^e\right]$ is the elemental stiffness matrix of the shaft elements, $\left[\mathbf{G}^e\right]$ is the total elemental gyroscopic matrix including shaft and rigid disc, $\left[\mathbf{C}^e\right]$ is the elemental damping matrix, $\left\{\mathbf{P}^e(t)\right\}$ is the elemental nodal displacement vector, and $\left\{\mathbf{F}_{total}^e(t)\right\}$ is the total elemental external force vector, and $\left[\mathbf{K}_c^e\right]$ is the circulation stiffness matrix given detail in **Appendix A** (**Eqs. (A.18)** to **(A.20)**).

3.4 Modeling of transverse crack behavior on an FG shaft

The theory of strain energy release rate (SERR) combined with linear elastic fracture mechanics and rotor dynamics in early 1970s, has been widely used over the last three decades in order to calculate the local flexibility coefficients (LFCs) that causes a transverse crack in a rotating FG shaft.

3.4.1 Stationary transverse surface crack

Transverse surface crack on the FG shaft is shown in **Figs. 3.4(a)** to **3.4(d)**. FG shaft has been modeled using two-nodded Timoshenko beam element with four DOFs (two translational and two rotational) at each node. Breathing crack is considered during rotation of the FG shaft for accurate prediction of the dynamic responses of the rotor system.

The FG cracked shaft has been discretized using beam elements with simply supported ends and shown in **Figs. 3.4(a)** and **3.4(b). Fig. 3.4(a)** shows the finite element discretization with a single crack and **Fig. 3.4(b)** shows the finite element discretization with a two cracks, where L is the total length of the shaft and L_e is the length of one element.

Depths of the first and second crack are α_1 and α_2, respectively, which are located at a distance L_{c1} and L_{c2}, respectively, from the left end of the shaft.

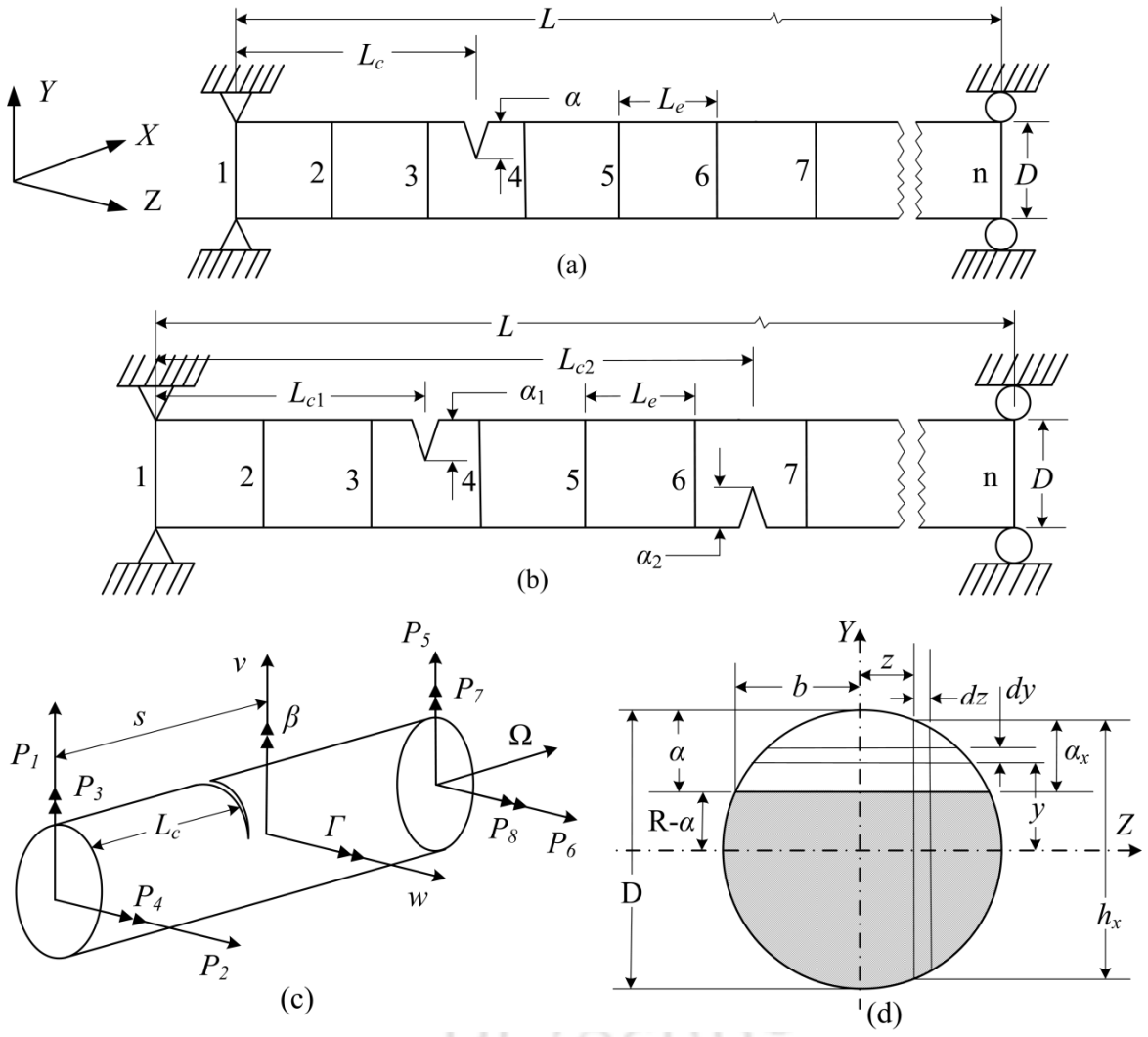

Fig. 3.4 A cracked FG shaft element (**a-b**) FE discretization (**c**) shaft element with general loading and (**d**) geometry of the cracked cross-section

Fig. 3.4(c) shows the shaft element, which is subjected to shear forces P_1, P_2, P_5 and P_6, and bending moments P_3, P_4, P_7 and P_8, rotating at a constant speed Ω. Here, v and w denote the translation displacements (bending and shear deformation) along Y and Z direction respectively, and β and Γ are the rotational displacements about

Y and Z axes, respectively, at a distance s from the left end of a cross-section of the shaft. In the present formulation, axial force and torsional moment are not considered. **Fig. 3.4(d)** shows the cross section of the shaft (solid) with a diameter $D(=2R)$ at one of the crack locations with crack depth α and crack half-width b.

Using Castigliano's theorem and Paris's equations [25] in conjunction with the expression for stress intensity factors (SIFs), the LFCs of an FG shaft with a stationary crack are derived in a similar way following the work of Papadopoulos and Dimarogonas [87] for homogenous shaft. The additional displacement u_i^c due to a crack is given by

$$u_i^c = \frac{\partial U^c}{\partial P_i} \tag{3.61}$$

where U^c is the additional strain energy and it is given by

$$U^c = \int_0^{\alpha_x} J(y,T)\, dy \tag{3.62}$$

where

$$\alpha_x = (\alpha - R) + \sqrt{R^2 - z^2} \tag{3.63}$$

and

$$J(y,T) = \frac{1}{E^*(y,T)}\left[\left(\sum_{i=1}^{4} K_{\mathrm{I}i}\right)^2 + \left(\sum_{i=1}^{4} K_{\mathrm{II}i}\right)^2 + \{1+\nu(y,T)\}\left(\sum_{i=1}^{4} K_{\mathrm{III}i}\right)^2\right] \tag{3.64}$$

where $J(y,T)$ is the strain energy density function that depends on the crack geometry, applied loads, and temperature dependent material properties, which are responsible for the three modes of fracture, i.e. opening (mode I), shearing (mode II) and tearing (mode III), respectively. Young's modulus, for the plane stress is $E^*(y,T) = E(y,T)$ and that for the plane strain is $E^*(y,T) = E(y,T)\big/\{1-\nu^2(y,T)\}$. Here $\nu(y,T)$ is the Poisson's ratio, and

$i = 1,\ 2,\ 3 \text{ and } 4$ are load indices. The expressions for SIFs (K_{I}, K_{II} and K_{III} corresponding to modes I, II, and III) in **Eq. (3.64)** are taken from Tada et al. [25] and are,

$$K_{\mathrm{I}3} = \frac{4P_3\, z}{\pi R^4}\sqrt{\pi y}\ F_1\left(\frac{y}{h_x}\right),\ K_{\mathrm{I}4} = \frac{4P_4}{\pi R^4}\sqrt{\pi y\left(R^2 - z^2\right)}\ F_2\left(\frac{y}{h_x}\right),\ K_{\mathrm{I}1} = K_{\mathrm{I}2} = 0 \tag{3.65}$$

$$K_{\mathrm{II}\,2} = \frac{\kappa_{sc} P_2}{\pi R^2}\sqrt{\pi y}\ F_{\mathrm{II}}\left(\frac{y}{h_x}\right),\ K_{\mathrm{II}\,1} = K_{\mathrm{II}\,3} = K_{\mathrm{II}\,4} = 0 \tag{3.66}$$

$$K_{\mathrm{III}\,1} = \frac{\kappa_{sc} P_1}{\pi R^2}\sqrt{\pi y}\ F_{\mathrm{III}}\left(\frac{y}{h_x}\right),\ K_{\mathrm{III}\,2} = K_{\mathrm{III}\,3} = K_{\mathrm{III}\,4} = 0 \tag{3.67}$$

where κ_{sc} is shear correction factor or shape coefficient for circular cross section and is given by

$$\kappa_{sc}\left(y,T\right) = 6\{1+\nu(y,\mathrm{T})\}/\{7+6\nu(y,T)\} \tag{3.68}$$

and

$$h_x = 2\sqrt{R^2 - z^2} \tag{3.69}$$

Finally, LFCs of an FG shaft with crack orientation $\theta = 0^{\mathrm{o}}$ are computed as follows (refer **Fig. 3.4(d)**)

$$C_{ij}^c = \frac{\partial u_i^c}{\partial P_j} = \frac{\partial^2}{\partial P_i\, \partial P_j}\int_{-b}^{b}\int_{0}^{\alpha_x} J\left(y,T\right) dy\, dz \tag{3.70}$$

where

$$b = \sqrt{R^2 - \left(R-\alpha\right)^2} \tag{3.71}$$

Here, unlike homogeneous shaft, integrations are performed (**Eq. (3.70)**) considering

$E(y,T)$ and $\nu(y,T)$ as functions of radial direction as well as temperature and LFCs of a cracked FG shaft are computed. Using **Eq. (3.70)**, LFCs are calculated corresponding to a fully open crack ($\theta = 180^{o}$). Local flexibility matrices $\mathbf{C}^{\mathrm{uc}}(\alpha,T)$ and $\mathbf{C}^{\mathrm{c}}(\alpha,T)$ corresponding to uncracked and fully open crack respectively are determined using energy methods, as

$$\mathbf{C}^{\mathrm{uc}}(\alpha,T) = \frac{L_e}{6E(y,T)I}\begin{bmatrix} 2L_e^2 & 0 & 0 & 3L_e \\ & 2L_e^2 & -3L_e & 0 \\ & & 6 & 0 \\ sym & & & 6 \end{bmatrix} \tag{3.72}$$

$$\mathbf{C}^{\mathrm{c}}(\alpha,T) = \begin{bmatrix} C_{11}^{\mathrm{c}}(\alpha,T) & 0 & 0 & 0 \\ & C_{22}^{\mathrm{c}}(\alpha,T) & 0 & 0 \\ & & C_{33}^{\mathrm{c}}(\alpha,T) & C_{34}^{\mathrm{c}}(\alpha,T) \\ sym & & & C_{44}^{\mathrm{c}}(\alpha,T) \end{bmatrix} \tag{3.73}$$

where I is the area moment of inertia of the cross section of the cracked shaft. Expressions of the elements of $\mathbf{C}^{\mathrm{c}}(\alpha,T)$ are

$$C_{11}^{\mathrm{c}}(\alpha,T) = \frac{4}{\pi R^4}\int_0^b\int_0^{\alpha_x} \frac{\{1+\nu(y,T)\}\{\kappa_{sc}(y,T)\}^2 y}{E(y,T)} F_{\mathrm{III}}^2\left(\frac{y}{h_x}\right) dy\, dz \tag{3.74}$$

$$C_{22}^{\mathrm{c}}(\alpha,T) = \frac{4}{\pi R^4}\int_0^b\int_0^{\alpha_x} \frac{\{1+\nu(y,T)\}\{\kappa_{sc}(y,T)\}^2 y}{E(y,T)} F_{\mathrm{II}}^2\left(\frac{y}{h_x}\right) dy\, dz \tag{3.75}$$

$$C_{33}^{\mathrm{c}}(\alpha,T) = \frac{64}{\pi R^8}\int_0^b\int_0^{\alpha_x} \frac{y\, z^2}{E(y,T)} F_1^2\left(\frac{y}{h_x}\right) dy\, dz \tag{3.76}$$

$$C_{34}^{\mathrm{c}}(\alpha,T) = \frac{64}{\pi R^8}\int_0^b\int_0^{\alpha_x} \frac{y}{E(y,T)} z\sqrt{R^2-z^2}\, F_1\left(\frac{y}{h_x}\right) F_2\left(\frac{y}{h_x}\right) dy\, dz \tag{3.77}$$

$$C_{44}^{\mathrm{c}}(\alpha,T) = \frac{64}{\pi R^8}\int_0^b\int_0^{\alpha_x} \frac{y}{E(y,T)}\left(R^2-z^2\right) F_2^2\left(\frac{y}{h_x}\right) dy\, dz \tag{3.78}$$

where the integrations are performed numerically using Simpson 1/3 rule and the MATLAB in-built quad command and here the form factors $F_1(y/h_x)$, $F_2(y/h_x)$, $F_{II}(y/h_x)$ and $F_{III}(y/h_x)$ are taken from Tada et al. [25] as

$$F_1\left(\frac{y}{h_x}\right)=\sqrt{\tan\left(\frac{\pi y}{2h_x}\right)\Big/\left(\frac{\pi y}{2h_x}\right)}\left[0.752+2.02\left(\frac{y}{h_x}\right)+0.37\left(1-\sin\left(\frac{\pi y}{2h_x}\right)\right)^3\right]\Big/\cos\left(\frac{\pi y}{2h_x}\right) \quad (3.79)$$

$$F_2\left(\frac{y}{h_x}\right)=\sqrt{\tan\left(\frac{\pi y}{2h_x}\right)\Big/\left(\frac{\pi y}{2h_x}\right)}\left[0.923+0.199\left(1-\sin\left(\frac{\pi y}{2h_x}\right)\right)^4\right]\Big/\cos\left(\frac{\pi y}{2h_x}\right) \quad (3.80)$$

$$F_{II}\left(\frac{y}{h_x}\right)=\left[1.122-0.561\left(\frac{y}{h_x}\right)+0.085\left(\frac{y}{h_x}\right)^2+0.18\left(\frac{y}{h_x}\right)^3\right]\Big/\sqrt{\left(1-\frac{y}{h_x}\right)} \quad (3.81)$$

$$F_{III}\left(\frac{y}{h_x}\right)=\sqrt{\tan\left(\frac{\pi y}{2h_x}\right)\Big/\left(\frac{\pi y}{2h_x}\right)} \quad (3.82)$$

Internal force and moment (torsional and bending) equilibrium conditions at both the nodes of the shaft element can be written as (ref. **Fig. 3.4(c)**)

$$\left.\begin{aligned} &P_1+P_5=0, \qquad P_2+P_6=0,\\ &P_3+P_7-P_6L_e=0, \qquad P_4+P_8+P_5L_e=0 \end{aligned}\right\} \quad (3.83)$$

Rewriting **Eq. (3.83)** in a matrix form, as

$$\{P_1,\ P_5,\ P_2,\ P_6,\ P_3,\ P_7,\ P_4,\ P_8\}^{\mathrm{T}}=[\mathbf{\Pi}]^{\mathrm{T}}\{P_5,\ P_6,\ P_7,\ P_8\}^{\mathrm{T}} \Rightarrow P=[\mathbf{\Pi}]^{\mathrm{T}}P_R \quad (3.84)$$

where P_R is the force vector at the right node and the transformation matrix $[\mathbf{\Pi}]$ is written as

$$[\mathbf{\Pi}] = \begin{bmatrix} -1 & 1 & 0 & 0 & 0 & 0 & -L_e & 0 \\ 0 & 0 & -1 & 1 & L_e & 0 & 0 & 0 \\ 0 & 0 & 0 & 0 & -1 & 1 & 0 & 0 \\ 0 & 0 & 0 & 0 & 0 & 0 & -1 & 1 \end{bmatrix} \tag{3.85}$$

Now relative displacements $(u_{ri},\ i = 1,\ 2,\ 3 \text{ and } 4)$ between two nodes is expressed as

$$\{u_{r1},\ u_{r2},\ u_{r3},\ u_{r4}\}^T = [\mathbf{\Pi}]\{u_1,\ u_5,\ u_2,\ u_6,\ u_3,\ u_7,\ u_4,\ u_8\}^T \Rightarrow u_r = [\mathbf{\Pi}]\ u \tag{3.86}$$

where

$$u_{r1} = u_5 - u_1 - u_4 L_e,\quad u_{r2} = u_6 - u_3 + u_3 L_e,\quad u_{r3} = u_7 - u_3,\quad u_{r4} = u_8 - u_4 \tag{3.87}$$

Forces at right node is obtained as

$$P_R = [\mathbf{C}]^{-1}\ u_r \tag{3.88}$$

From the definition of stiffness matrix $[\mathbf{K}]$, we have

$$P = [\mathbf{K}]\ u \tag{3.89}$$

Using **Eqs. (3.84)** to **(3.89)**, the expression of stiffness matrix is obtained as

$$P = [\mathbf{\Pi}]^{\mathbf{T}}\ P_R = [\mathbf{\Pi}]^{\mathbf{T}}\ [\mathbf{C}]^{-1}\ u_r \Rightarrow [\mathbf{\Pi}]^{\mathbf{T}}\ [\mathbf{C}]^{-1}\ [\mathbf{\Pi}]\ u = [\mathbf{K}]\ u \Rightarrow\ [\mathbf{K}] = [\mathbf{\Pi}]^{\mathbf{T}}\ [\mathbf{C}]^{-1}\ [\mathbf{\Pi}] \tag{3.90}$$

Using uncracked compliances from **Eq. (3.72)** and cracked compliances from **Eq. (3.73)** corresponding uncracked stiffness $[\mathbf{K}^{\text{uc}}]$ and cracked stiffness matrix $[\mathbf{K}^{\text{c}}]$ is computed using the virtual work principle as

$$[\mathbf{K}^{\text{uc, c}}] = [\mathbf{\Pi}]^{\mathbf{T}}[\mathbf{C}^{\text{uc, c}}]^{-1}[\mathbf{\Pi}] \tag{3.91}$$

Global stiffness matrix of the shaft is obtained by assembling the stiffness matrices of all the elements (uncracked and cracked) of the shaft and is used in the global equation.

3.4.2 Formulation of local flexibility coefficients for a rotating cracked shaft

Modelling of a transverse crack at any arbitrary orientation is an important task in the application area of turbines and generators, and to predict dynamic responses of the rotor system accurately. For a rotating cracked shaft, crack opening and closure depends on the angle of the rotation θ ($\theta = \Omega t$, where Ω and t are spin speed and time, respectively). Researchers [86, 95, 97, 99 and 116] developed different crack opening and closure model to study the breathing effect on rotor. Assuming that the gravity force is much greater than the imbalance force, stiffness variation is expressed mathematically by a cosine series function [97 and 99] as

$$\left[\mathbf{K}(t)\right] = \left[\mathbf{K}^{uc}\right] - f(t)\left[\mathbf{K}^{c}\right] \quad \text{with} \quad f(t) = \left(1 - \cos\ \Omega t\right)/2 \tag{3.92}$$

when $f(t) = 0$, the crack is totally closed and rotor stiffness is considered as the uncracked

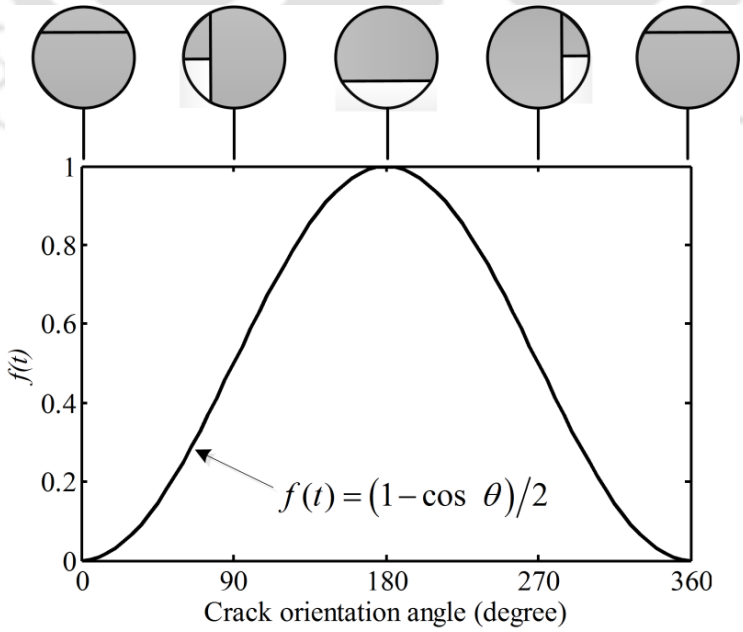

Fig. 3.5 Opening-closing function $f(t)$ of breathing crack during rotation of the shaft [97]

rotor stiffness $\left(\left[\mathbf{K}^{\mathrm{uc}}\right]=\left[\mathbf{K}^{e}\right]\right)$, $f(t)=1$, the crack is fully open, and $0<f(t)<1$, the crack is at any orientation between $0°$ to $360°$. The opening-closure cosine series function $f(t)$ [97] describe the breathing effect for a spinning cracked shaft and the breathing behavior is shown in **Fig. 3.5**.

3.5 System equations of motion

Following the works of Nelson [63] and Ku [71], and considering breathing crack behavior, the equation of motion for the complete rotor-bearing system can be expressed in a fixed coordinate configuration as

$$\left[\mathbf{M}\right]\left\{\ddot{\mathbf{P}}(t)\right\}+\left(\begin{array}{c}\eta_v\left[\mathbf{K}\right]-\Omega\left[\mathbf{G}\right]\\+\left[\mathbf{C}^{b}\right]\end{array}\right)\left\{\dot{\mathbf{P}}(t)\right\}+\left\{\begin{array}{l}\dfrac{1+\eta_h}{\sqrt{1+\eta_h^2}}\left[\mathbf{K}\right]+\left[\mathbf{K}^{b}\right]\\+\left(\Omega\eta_v+\dfrac{\eta_h}{\sqrt{1+\eta_h^2}}\right)\left[\mathbf{K}_c\right]\end{array}\right\}\left\{\mathbf{P}(t)\right\}=\left\{\mathbf{F}(t)\right\} \tag{3.93}$$

where $\left[\mathbf{M}\right]$ is the global mass matrix (including the rotary and translational masses of the shaft, and rigid disc), $\left[\mathbf{K}\right]$ is the global stiffness matrix, (including stiffness of the cracked and uncracked shaft elements), $\left[\mathbf{G}\right]$ is the global gyroscopic matrix including shaft and rigid disc, $\left[\mathbf{K}_c\right]$is the global circulation matrix, $\left\{\mathbf{P}(t)\right\}$ is the global nodal displacement vector and $\left\{\mathbf{F}(t)\right\}$ is the global external force vector.

3.6 Solution procedure

The equations of motin (EOMs) of the complete system can be obtained by assembling the contribution of each element's EOMs. For the analysis of natural whirl speeds of the rotor-bearing system with FG shaft, the force term can be omitted. Then the final system EOMs can be written as

$$\left[\mathbf{M}\right]\left\{\ddot{\mathbf{P}}\right\}+\left[\mathbf{C}\right]\left\{\dot{\mathbf{P}}\right\}+\left[\mathbf{K}\right]\left\{\mathbf{P}\right\}=\left\{0\right\} \tag{3.94}$$

where

$$[\mathbf{C}]=\left(\eta_v\ [\mathbf{K}]-\Omega[\mathbf{G}]+\left[\mathbf{C}^b\right]\right) \textbf{ and } [\mathbf{K}]=\frac{1+\eta_h}{\sqrt{1+\eta_h^2}}[\mathbf{K}]+\left[\mathbf{K}^b\right]+\left(\frac{\Omega\eta_v+\eta_h}{\sqrt{1+\eta_h^2}}\right)[\mathbf{K}_c] \tag{3.95}$$

The solution of the eigenvalue problem of the **Eq. (3.94)** is described in the first order state vector form as

$$[\mathbf{A}]\{\dot{h}\}+[\mathbf{B}]\{h\}=\{0\} \tag{3.96}$$

with

$$\{h\}=\begin{Bmatrix}\{\dot{\mathbf{P}}\}\\ \{\mathbf{P}\}\end{Bmatrix},\ [\mathbf{A}]=\begin{bmatrix}[0] & [\mathbf{M}]\\ [\mathbf{M}] & [\mathbf{C}]\end{bmatrix},\ [\mathbf{B}]=\begin{bmatrix}-[\mathbf{M}] & [0]\\ [0] & [\mathbf{K}]\end{bmatrix} \tag{3.97}$$

A solution of **Eq. (3.96)** is assumed to be of the form

$$\{h\}=\{h_0\}e^{\lambda t} \tag{3.98}$$

On substituting **Eq. (3.98)** into **Eq. (3.96)**, we get

$$\lambda[\mathbf{A}]\{h_0\}e^{\lambda t}+[\mathbf{B}]\{h_0\}e^{\lambda t}=\{0\} \tag{3.99}$$

Therefore, associated eigen value problem becomes

$$\left([\mathbf{B}]^{-1}[\mathbf{A}]+\lambda[I]\right)\{h_0\}=\{0\} \tag{3.100}$$

where $\lambda_n(\Omega)=\alpha(\Omega)\pm i\beta(\Omega)=-\xi_n\omega_n\pm i\omega_n\sqrt{1-\xi_n^{\,2}}$ is the speed dependent general complex eigenvalues, ξ, ω and n are the damping ratio, natural whirling frequency and mode number, respectively. The real part of the eigen value ξ_n indicates the damping in the system at a given speed. For the purpose of stability analysis the parameter logarithmic decrement is

defined as $\delta_n = -2\pi\alpha/\beta = 2\pi\xi_n/\sqrt{1-\xi_n^2}$ and the stability threshold speed is obtained at which operation speed of rotor $\delta_n = 0$. The response of a dynamic system is a decay function which involves the damping term and in order to get stable response the amplitude of vibration should decay as time increases. This will happen only when the damping index ($\xi_n < 0$) is negative. Therefore, if the parameter $\delta_n > 0$, the system is stable and when $\delta_n < 0$, the system is unstable. Natural whirling frequencies and stability threshold speeds are computed corresponding to the transverse cracks at any arbitrary orientation by solving the eigenvalue problem for the system in **Eq. (3.100)**.

Fig. 3.6 present a flow chart to describe the solution procedure for analysis of an FG shaft system with transverse cracks (stationary and rotating cracks) with the help of developed computer code for determination of natural whirling frequencies, critical speeds and stability threshold speeds. A pseudo-code is shown in appendix B which will provide the complete computation simulation works related to the FG shaft system.

3.7 Summary

In this chapter, detailed formulation of the development of effective thermo-mechanical material properties of FGMs are presented using different material gradation laws. These thermo-mechanical properties of FGMs are used in the FE formulation of both the uncracked and cracked FG shaft considering different beam models and with internal viscous and hysteretic damping. Transverse breathing cracks behavior on an FG shaft is presented based on linear elastic fracture mechanics approach. The expressions for LFCs as function of $\alpha, k, \Delta T$ and θ are derived for a cracked FG shaft, using Castigliano's theorem and Paris's equations [25] in conjunction with the expression for SIFs. This determination of LFCs for an FG shaft is a challenging task not reported till date. Finally, an FE based approach for determination of natural whirling frequencies, critical speeds and stability threshold speeds of the FG shaft in a rotor-disc-bearing is presented in detail and also a flow chart of the overall module is presented.

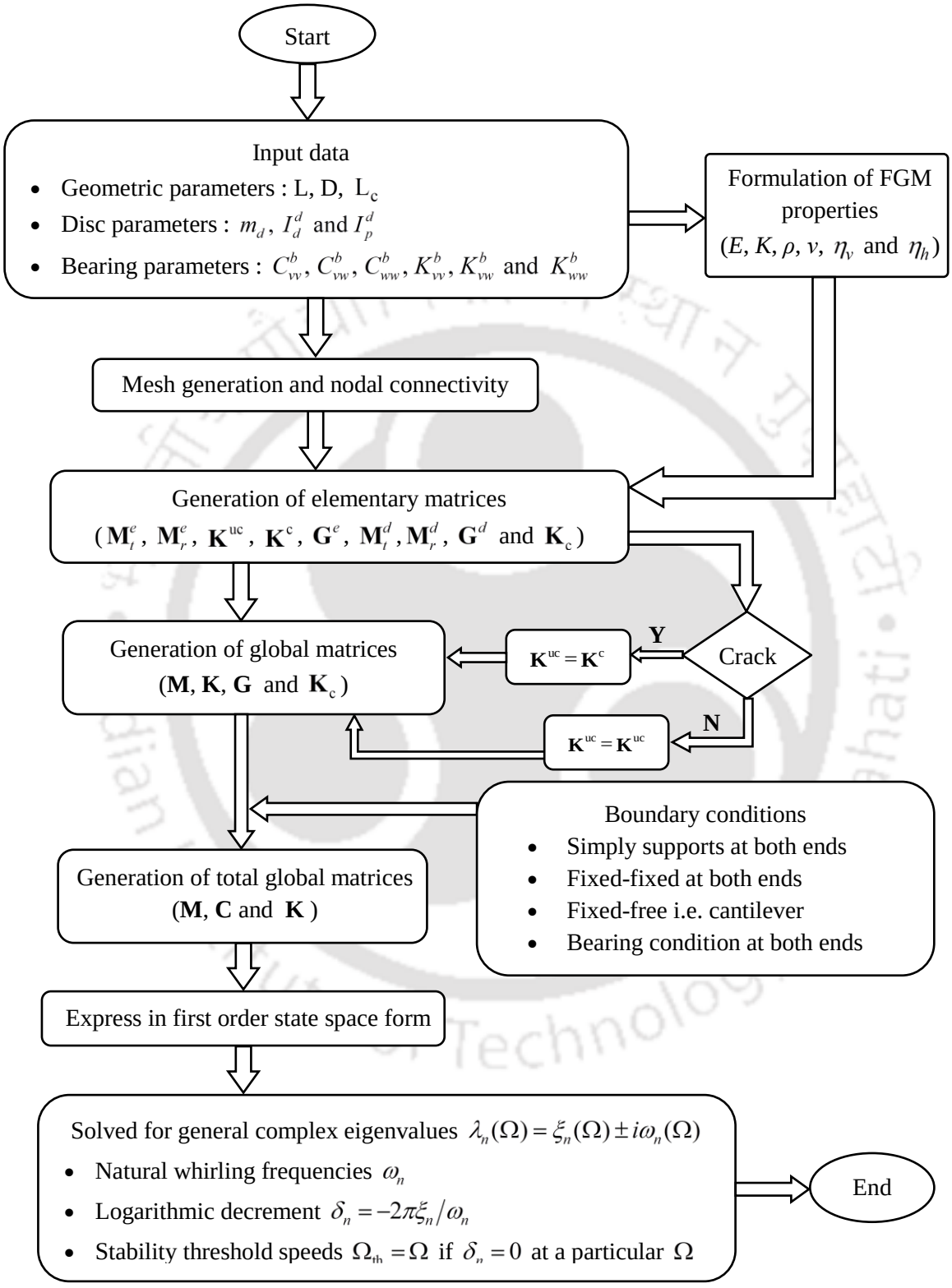

Fig. 3.6 A general flow chart highlighting the overall module and solving the eigenvalue problem

CHAPTER 4

Transverse Vibration Analysis of a Rotor-Bearing System having an FG Shaft with Stationary Transverse Crack

4.1 Introduction

This chapter presents free vibration analysis of rotor-bearing system having an FG shaft with single transverse surface crack. The stationary transverse surface crack is modeled based on the formulations discussed in the **chapter 3** (Sub-section **3.4.1**). An FE code has been developed using MATLAB, which is capable of performing vibration analysis of a rotor-bearing system considering the effect of a transverse surface crack on the rotating FG shaft. The code has been validated to ensure the correctness of formulations. Here, stainless steel (SS), alumina (Al_2O_3) and zirconia (ZrO_2) are used as constituent materials to form two different types of FGMs such as FGM I (SS/Al_2O_3) and FGM II (SS/ZrO_2), respectively, for the rotor where power law of material gradation is assumed and SS content is assumed to decrease towards the outer diameter, radially.

4.2 Rotor-Bearing system details

In the present problem, an FG shaft with single transverse surface crack is modeled using two-nodded Timoshenko beam element with four degrees of freedom (DOFs) at each node. **Fig. 4.1(a)** shows the FE discretization of the FG cracked shaft with simply supported ends and **Fig. 4.1(b)** show the FE discretization of FG cracked shaft with flexible end bearings condition. In **Figs. 4.1(a)** and **4.1(b)**, L and L_e are the total and element lengths of the shaft respectively, $D(=2R,\ R$ is the radius of the shaft) is the diameter of the shaft, α is the depth of the transverse surface crack and located at distance L_c from left end of the shaft. The fully open transverse crack is considered in the present problem. Here two types of FGMs are considered. FGM I is considered to be composed of stainless steel (SS) and alumina (Al_2O_3) and FGM II is considered to be composed of stainless steel (SS) and zirconia (ZrO_2).

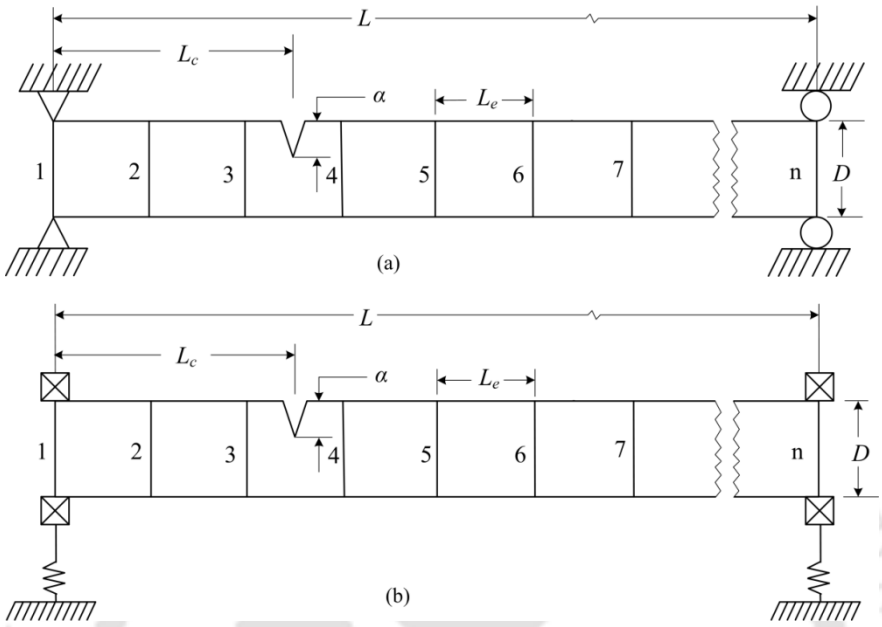

Fig. 4.1 A cracked FG shaft with FE discretization **(a)** simply supported ends and **(b)** flexible end bearings

Table 4.1 Temperature coefficients value for different mechanical properties [27] of FGMs.

Properties	Materials	C_0	C_{-1}	C_1	C_2	C_3
E (Pa)	SS	201.04×10^{9}	0	3.079×10^{-4}	-6.534×10^{-7}	0
	ZrO_2	244.27×10^{9}	0	-1.371×10^{-3}	1.214×10^{-6}	-3.681×10^{-10}
	Al_2O_3	349.55×10^{9}	0	-3.853×10^{-4}	4.027×10^{-7}	-1.673×10^{-10}
ν	SS	0.3262	0	-2.002×10^{-4}	3.797×10^{-7}	0
	ZrO_2	0.2882	0	1.133×10^{-4}	0	0
	Al_2O_3	0.2600	0	0	0	0
K (W/m K)	SS	15.379	0	-1.264×10^{-3}	2.092×10^{-6}	-7.223×10^{-10}
	ZrO_2	1.700	0	1.276×10^{-4}	6.648×10^{-8}	0
	Al_2O_3	-14.087	-1123.6	-6.227×10^{-3}	0	0
ρ (kg/m^3)	SS	8166	0	0	0	0
	ZrO_2	5700	0	0	0	0
	Al_2O_3	3750	0	0	0	0

In the present analysis, the FG shaft is supported by simply supported boundary conditions and flexible end bearings, as shown in **Figs. 4.1(a)** and **4.1(b)**, respectively and is modeled using nineteen (19) finite elements. Here, shaft diameter of $D = 0.1$ m and different length of the shaft are considered to vary the slenderness ratio (SR) such as length to diameter ratios $L/D = 12.5,\ 10.5$ and 8.5 for different analyses in the following sub-

sections. Mechanical properties of the constituents materials viz. stainless steel (SS), alumina (Al_2O_3) and zirconia (ZrO_2) comprising FGM I (SS/Al_2O_3) and FGM II (SS/ZrO_2) at different temperature (T) could be obtained using **Eq. (3.1)** and the temperature coefficient values listed in **Table 4.1** [27].

4.3 Convergence study and validations

Due to lack of relevant results for dynamic characteristics of FG rotor-bearing systems, the present FE formulation and developed code are validated in five steps. In the first step, natural frequencies of a non-rotating homogenous shaft obtained, using the present code, have been compared with the existing analytical and FE solutions to ensure the correctness of stiffness and mass matrix, and the accuracy of the present solution has been investigated through a convergence study. In the second step, natural frequencies of a spinning shaft (without crack), obtained from the present code, have been compared with those from published results to ensure the correct evaluation of the inertia and gyroscopic matrices. In the third step, LFCs calculated from the code have been compared with those from published results to ensure the correctness of crack compliances. In the fourth step, natural frequencies as a function of crack size α/R obtained, from the present FE code, have been compared with those available in published literatures to ensure the correct formulation of open transverse crack. In the last step, natural frequencies of a cracked FG beam are evaluated with different boundary conditions and compared with the exsiting analytical solutions to ensure the validation of formulation of cracked FG component.

4.3.1 A uniform non-rotating simply supported shaft

Dimensionless natural frequencies ϖ_n $\left(\varpi_n^4 = \rho_{SS} A L^4 \omega^2 / E_{SS} I\right)$ are obtained for a homogeneous non-rotating circular cross section shaft made of SS (properties are obtained in **Table 4.1** at ambient temperature $T = 300$ K) for different values of SR ($= R/2L$, R and L are the radius and length of the shaft) using different beam theories (Rayleigh beam, Shear beam and Timoshenko beam) and with different boundary conditions. These results are compared with already published results in literatures in **Tables 4.2** to **4.4**. It could be seen from **Table**

4.2 that the first two dimensionless natural frequencies agree well with the existing analytical solutions of Dym and Shames [163] for different beam theories. **Table 4.3** shows that for different boundary conditions, the present results agree well with those of existing FE solutions of Chen and Ku [67]. **Table 4.4** shows the first two natural frequencies obtained using the present FE code compared with the existing FE solutions of Nelson [63], Özgüven and Özkan [65], and Ku [71] and analytical solutions of Dym and Shames [163] and results show a good agreement. The natural frequencies are also determined with three different numbers of elements in order to provide an accurate solution for the FE model, thus validating the FE code for the stiffness and mass matrices.

Table 4.2 Dimensionless natural frequencies ϖ_n of uniform non-rotating simply supported beams

Modes	SR $(R/2L)$	Rayleigh beam		Shear beam		Timoshenko beam	
		Present	Dym and Shames [163]	Present	Dym and Shames [163]	Present	Dym and Shames [163]
1st	0.02	3.1387	3.1385	3.1330	3.1342	3.1300	3.1312
	0.04	3.1295	3.1293	3.1076	3.1125	3.0964	3.1012
	0.06	3.1145	3.1143	3.0673	3.0780	3.0452	3.0551
	0.08	3.0940	3.0939	3.0150	3.0327	2.9815	2.9971
	0.10	3.0687	3.0685	2.9539	2.9790	2.9104	2.9311
2nd	0.02	6.2638	6.2586	6.2261	6.2250	6.2037	6.2024
	0.04	6.1928	6.1877	6.0561	6.0653	5.9873	5.9943
	0.06	6.0829	6.0779	5.8168	5.8387	5.7098	5.7190
	0.08	5.9440	5.9391	5.5476	5.5811	5.4218	5.3995
	0.10	5.7864	5.7817	5.2763	5.3188	5.1478	4.9737

Table 4.3 Dimensionless first natural frequencies ϖ_n of a uniform non-rotating Timoshenko beam

SR $(R/2L)$	Clamped – Free			Hinged – Hinged			Clamped – Clamped		
	Present	Chen and Ku [67]	% Error	Present	Chen and Ku [67]	% Error	Present	Chen and Ku [67]	% Error
0.1	10.43	10.42	-0.096	70.94	70.38	-0.796	195.97	191.7	-2.227
0.04	12.00	12.00	0.000	91.70	91.58	-0.131	399.42	397.1	-0.584
0.02	12.27	12.27	0.000	95.92	95.92	0.000	470.92	470.8	-0.025
0.01	12.34	12.34	0.000	97.05	97.08	0.031	493.19	493.9	0.144
0.002	12.36	12.37	0.081	97.41	97.46	0.051	500.79	501.9	0.221

Table 4.4 Dimensionless natural frequencies of a uniform non-rotating simply supported Timoshenko beam

Modes	SR $(R/2L)$	Present			Nelson [63]	Özgüven and Özkan [65]	Ku [71]	Dym and Shames [163]
		(5)†	(7)	(10)				
1st	0.02	3.1300	3.1298	3.1296	3.1313	3.1316	3.1293	3.1312
	0.04	3.0964	3.0958	3.0955	3.1017	3.1007	3.0938	3.1012
	0.06	3.0452	3.0440	3.0434	3.0561	3.0476	3.0399	3.0551
	0.08	2.9815	2.9797	2.9788	2.9989	2.9717	2.9733	2.9971
	0.10	2.9104	2.9080	2.9067	2.9343	2.8733	2.8992	2.9311
2nd	0.02	6.2037	6.1960	6.1928	6.2074	6.2146	6.1913	6.2024
	0.04	5.9873	5.9711	5.9631	6.0079	6.0109	5.9497	5.9943
	0.06	5.7098	5.6846	5.6716	5.7482	5.7146	5.6462	5.7190
	0.08	5.4218	5.3894	5.3723	5.4752	5.3556	5.3374	5.3995
	0.10	5.1478	5.1101	5.0901	5.2126	4.9464	5.0481	4.9737

† Values in parentheses denote the number of finite elements

Table 4.5 Comparison of natural frequencies (in Hz) for the rotor-bearing system

Modes	$\Omega = 0$ rpm			$\Omega = 4000$ rpm		
	Present	Friswell et al. [57]	% Error	Present	Friswell et al. [57]	% Error
1BW	13.79	13.79	0.00	13.59	13.59	0.00
1FW	13.79	13.79	0.00	13.96	13.97	0.07
2BW	43.66	43.72	0.14	40.16	40.07	-0.22
2FW	43.66	43.72	0.14	46.94	46.90	-0.08
3BW	114.08	115.03	0.83	96.41	95.52	-0.93
3FW	114.08	115.03	0.83	132.29	131.63	-0.50

4.3.2 Whirling frequencies of a rotor-bearing system

A rotor-bearing system consisting of a rotor, two discs and bearings as shown in **Fig. 4.2** is considered for validating forward whirling (FW) and backward whirling (BW) frequencies obtained from the present code. The rotor and the discs are made of steel with

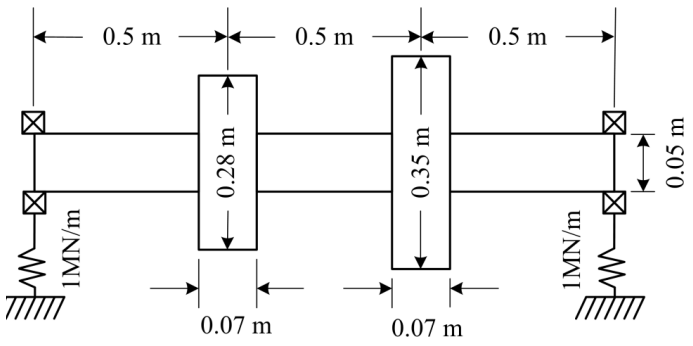

Fig. 4.2 Schematic diagram of a rotor-disc-bearing system

$E = 211\ \text{GN/m}^2$, $G = 81.2\ \text{GN/m}^2$ and $\rho = 7810\ \text{kg/m}^3$. The bearings are considered to be isotropic with stiffness of $1\ \text{MN/m}$ in both orthogonal directions. For this arrangement natural frequencies have been computed and are compared with the FE solution of Friswell et al. [57] as listed in **Table 4.5**. Results in **Table 4.5** show an excellent agreement, thus validating the FE code for stiffness, mass, inertia and gyroscopic matrices.

4.3.3 Local flexibility coefficients of a shaft with stationary crack

In order to validate the local flexibility coefficients (LFCs), a shaft of $D = 0.1\ \text{m}$, $L = 1.25\ \text{m}$ and made of SS is considered. The dimensionless compliances $\bar{C}_{33}$ and $\bar{C}_{44}$ as a function of crack size α/R have been determined using the present code and compared with already published results of Chasalevris and Papadopoulos [107], as shown in **Table 4.6**. It shows an excellent agreement, thereby validating the code for crack compliances.

Table 4.6 Dimensionless compliance $\bar{C}_{33}$ and $\bar{C}_{44}$ as a function of α/R

$\frac{\alpha}{R}$	$\bar{C}_{33}$			$\bar{C}_{44}$		
	Present	Ref. [107]	% Error	Present	Ref. [107]	% Error
0.04	0.0000349	0.000035	0.285714	0.0029731	0.002973	-0.00336
0.16	0.0043686	0.004368	0.013736	0.0854259	0.085426	0.00012
0.28	0.0307849	0.030785	0.00032	0.3171666	0.317167	0.00013
0.40	0.1090427	0.109043	0.00028	0.7248795	0.724880	6.9E-05
0.52	0.2854224	0.285422	-0.00014	1.3405230	1.340520	-0.000224
0.64	0.6382421	0.638242	-1.57E-05	2.2190961	2.219100	0.00018
0.76	1.3137215	1.313720	-0.000114	3.4560272	3.456030	8.1E-05
0.88	2.6143349	2.614330	-0.000187	5.2157804	5.215780	-7.67E-06
1.00	5.2663511	5.266350	-2.09E-05	7.7903871	7.790390	3.7E-05

4.3.4 Natural frequencies of a simply supported cracked shaft

The ratio of the cracked and uncracked natural frequencies, as a function of α/R and L/D, has been obtained for a centrally located crack and the values are compared with the already published results of Sekhar and Prabhu [164] as shown in **Table 4.7**. It could be observed from **Table 4.7** that an excellent agreement is achieved, thus validating the FE code for formulation

of a single crack.

Table 4.7 Variation of dimensionless natural frequencies with α/R for different L/D

Modes	L/D	$\alpha/R=0.2$		$\alpha/R=0.6$		$\alpha/R=1.0$	
		Present	Sekhar and Prabhu [164]	Present	Sekhar and Prabhu [164]	Present	Sekhar and Prabhu [164]
1st	12.5	0.9953	0.9958	0.9433	0.9452	0.7798	0.7882
2nd		0.9999	0.9998	0.9981	0.9978	0.9839	0.9818
3rd		0.9974	0.9962	0.9591	0.9540	0.8748	0.8683
1st	8.0	0.9931	0.9955	0.9152	0.9165	0.7050	0.7187
2nd		0.9999	0.9997	0.9966	0.9964	0.9742	0.9771
3rd		0.9921	0.9934	0.9407	0.9347	0.8475	0.8369

4.3.5 Natural frequencies with boundary condition for a cracked FG beam

After validating the FE formulation for homogenous cracked shaft, the code has also been validated for a cracked FG component. In the absence of appropriate results for a cracked FG shaft, validation has been done by comparing the results obtained from the present code for a cracked FG beam with the already published analytical results of Yang and Chen [132] and Wei et al. [142]. For this a cracked FG beam with different end conditions (cantilever, simply supported, fixed-fixed), dimensions ($L/D=10.0$, $\alpha/R=0.4$ and $k=2.0$) and material properties ($E_1=70$ GPa, $\rho_1=2780$ kg/m^3 and $\nu=0.33$) similar to those used by Yang and Chen [132] and Wei et al. [142] are used. Computed dimensionless natural frequencies using the present code are compared with published analytical results (Yang and Chen [132] and Wei et al. [142]) and are tabulated in **Table 4.8**, which show a very good agreement, thus validating the FE code for formulation of cracked FG components.

Table 4.8 Variation of dimensionless natural frequencies with end conditions for a cracked FG beam

$\frac{E_2}{E_1}$	Cantilever			Simply supported			Fixed-Fixed		
	Present	Yang and Chen [132]	Wei et al. [142]	Present	Yang and Chen [132]	Wei et al. [142]	Present	Yang and Chen [132]	Wei et al. [142]
0.2	0.9748	0.9811	0.9755	0.9376	0.9535	0.9501	0.9867	0.9871	0.9855
1.0	0.9956	0.9951	0.9921	0.9890	0.9912	0.9874	0.9971	0.9966	0.9954
5.0	0.9983	0.9986	0.9949	0.9956	0.9992	0.9985	0.9988	0.9990	0.9987

4.4 FE Analysis of an FG shaft with a transverse crack

After validating the formulation and the developed FE code, this code has been used to analyze FGM I (SS/Al_2O_3) and FGM II (SS/ZrO_2) shafts having a fully open transverse crack to evaluate the material property variations and to determine the direct and cross couple LFCs for such FG shafts.

4.4.1 Material properties variation for an FG shaft

The variation of Young's modulus along the radial distance of the FGM II (SS/ZrO_2) shaft following power law distribution (**Eq. (3.2)**) and for different values of power law gradient index k is shown in **Fig. 4.3** at $T = 300$ K. **Fig. 4.3** shows that following **Eq. (3.2)**, for $k = 1.0$ the variation is linear and for any other values of power law gradient index k, it is non-linear. Similar trend is also obtained for other material properties.

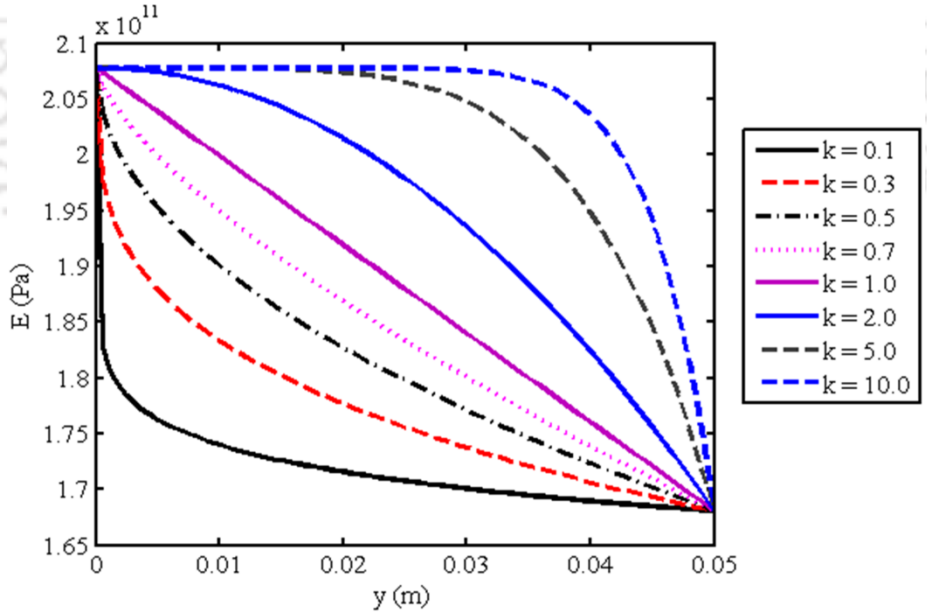

Fig. 4.3 Young's modulus variation along the radial direction in an FG (SS/ZrO_2) shaft for $\Delta T = 0$ K

Since temperature dependent material properties are considered, **Figs. 4.4(a)** to **4.4(c)** show the variation of E, ν and K along the radial direction of the shaft for the different values of k. It may be noted that these variations are due to the combined effect of power law gradient k and temperature gradient ΔT.

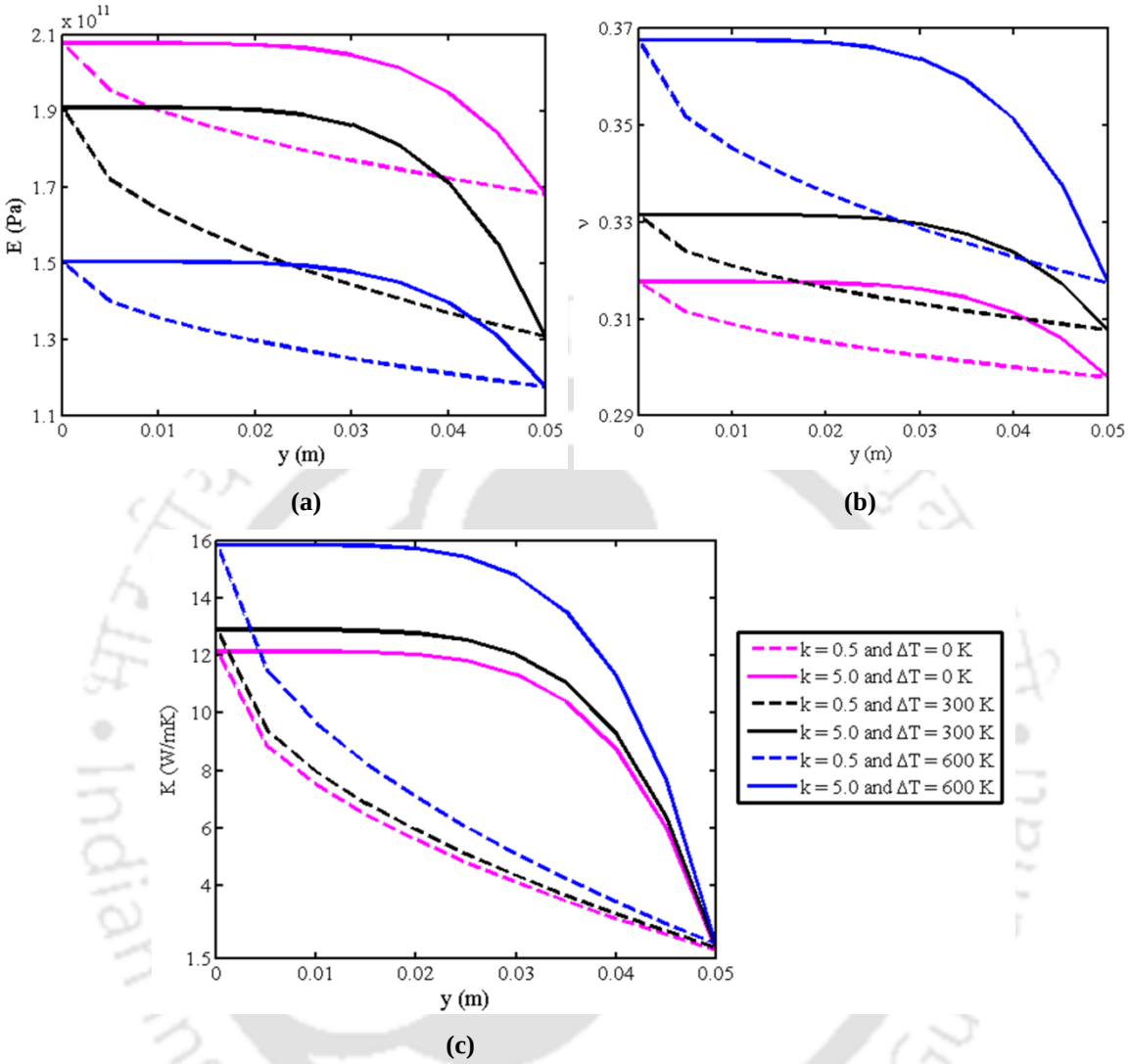

Fig. 4.4 Variation of material properties with functions of radial position, power law gradient index and temperature gradient: **(a)** Young's modulus **(b)** Poisson's ratio and **(c)** thermal conductivity

4.4.2 Variation of dimensionless LFCs for an FG shaft

Determination of LFCs is important to study the effect of stiffness as well as vibration characteristics for a cracked FG shaft with the temperature dependent material properties. Since stiffness terms are also temperature dependent, it is important to study the effect of temperature on LFCs for FG shafts. Using **Eq. (3.74)** to **Eq. (3.78)** along with **Eq. (3.2)** and **Eq. (3.10)**, direct and cross couple LFCs have been computed in dimensionless quantities such as, $\overline{C}_{11} = C_{11} / \pi E_{ss} R$, $\overline{C}_{22} = C_{22} / \pi E_{ss} R$, $\overline{C}_{33} = C_{33} / \pi E_{ss} R^3$, $\overline{C}_{34} = C_{34} / \pi E_{ss} R^3$ and $\overline{C}_{44} = C_{44} / \pi E_{ss} R^3$.

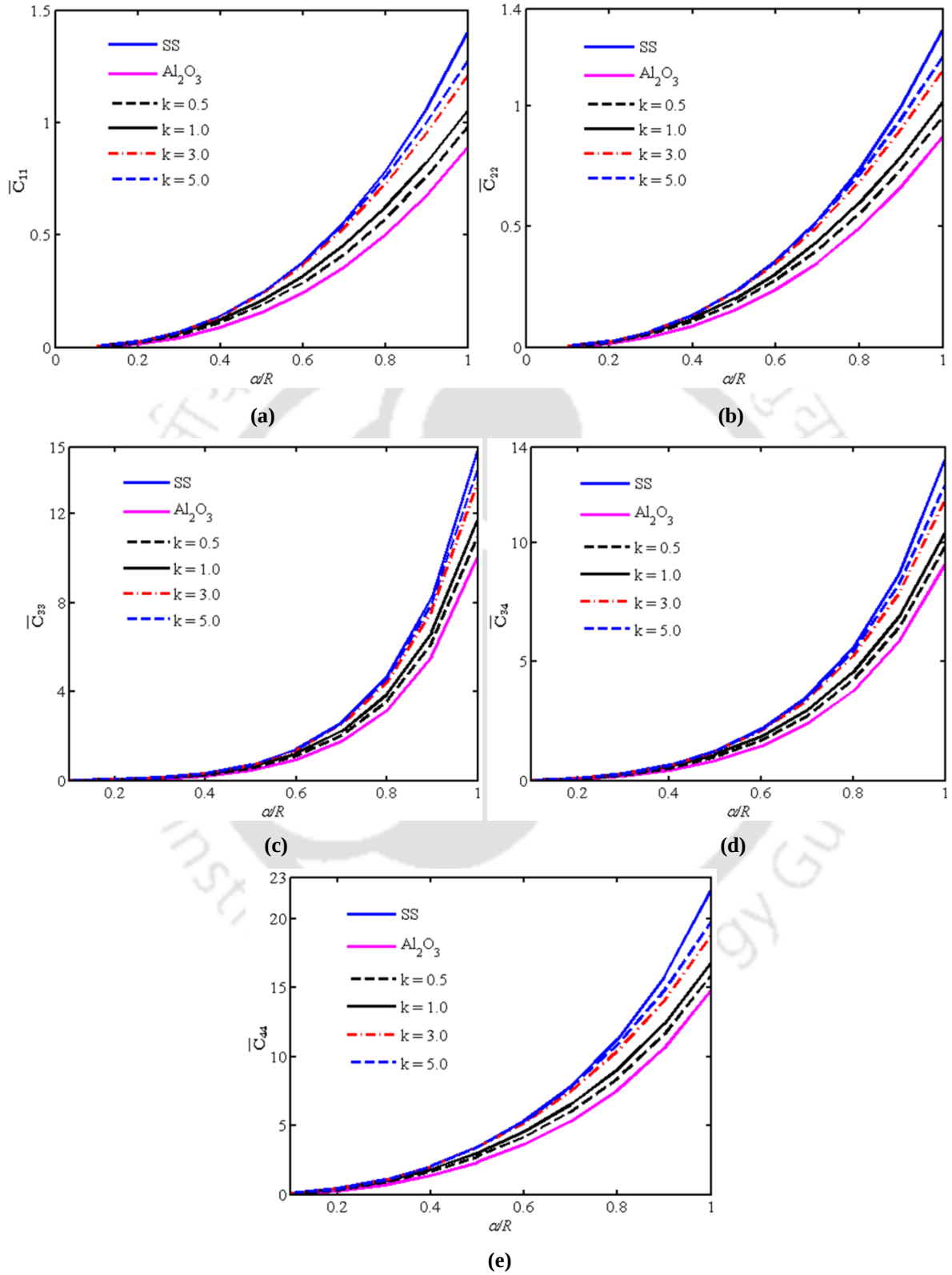

Fig. 4.5 Variation of LFCs with α/R and k for FGM I: **(a)** $\overline{C}_{11}$ **(b)** $\overline{C}_{22}$ **(c)** $\overline{C}_{33}$ **(d)** $\overline{C}_{34}$ and **(e)** $\overline{C}_{44}$

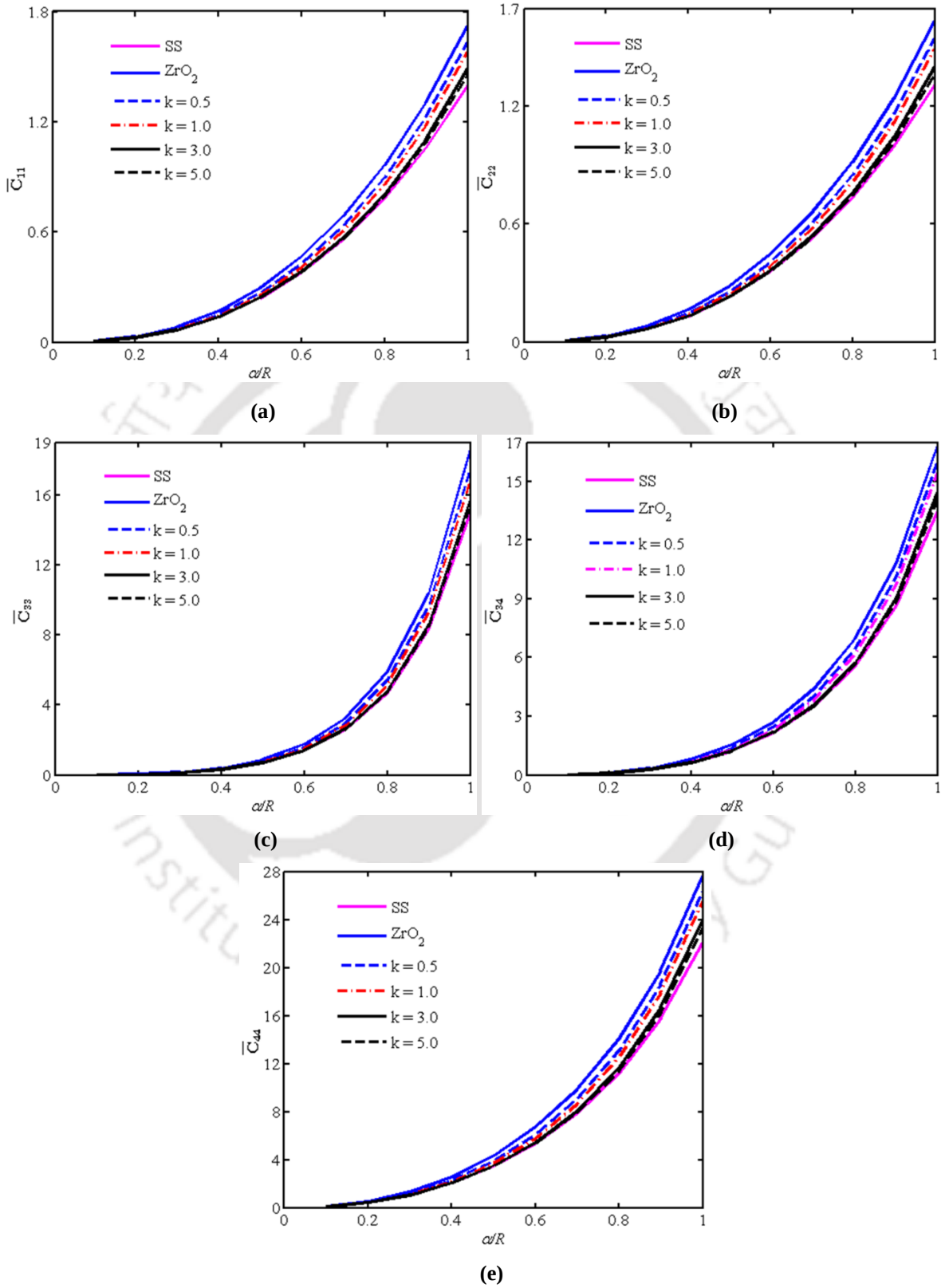

Fig. 4.6 Variation of LFCs with α/R and k for FGM II: **(a)** $\overline{C}_{11}$ **(b)** $\overline{C}_{22}$ **(c)** $\overline{C}_{33}$ **(d)** $\overline{C}_{34}$ and **(e)** $\overline{C}_{44}$

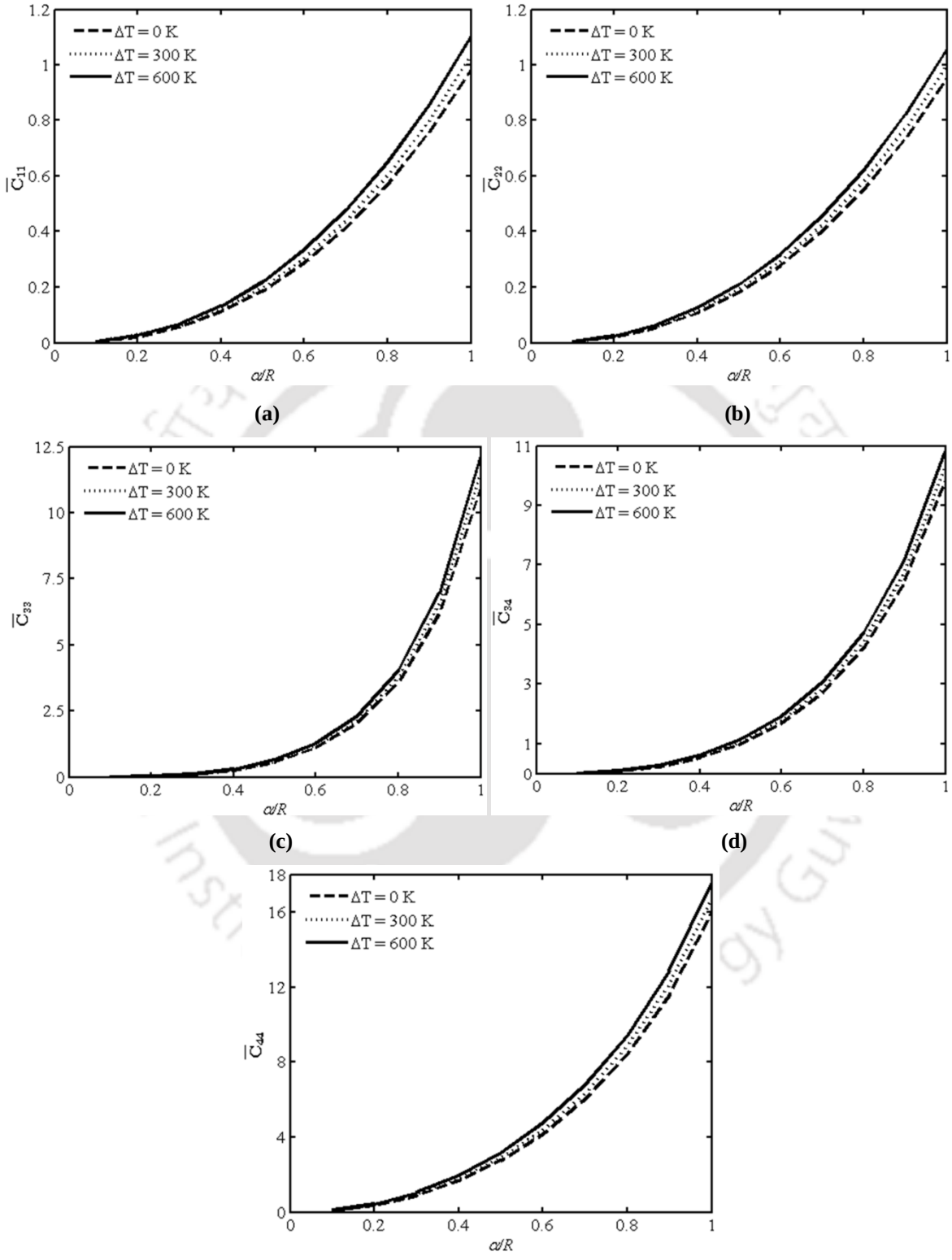

Fig. 4.7 Variation of LFCs with α/R and ΔT for FGM I: **(a)** $\overline{C}_{11}$ **(b)** $\overline{C}_{22}$ **(c)** $\overline{C}_{33}$ **(d)** $\overline{C}_{34}$ and **(e)** $\overline{C}_{44}$

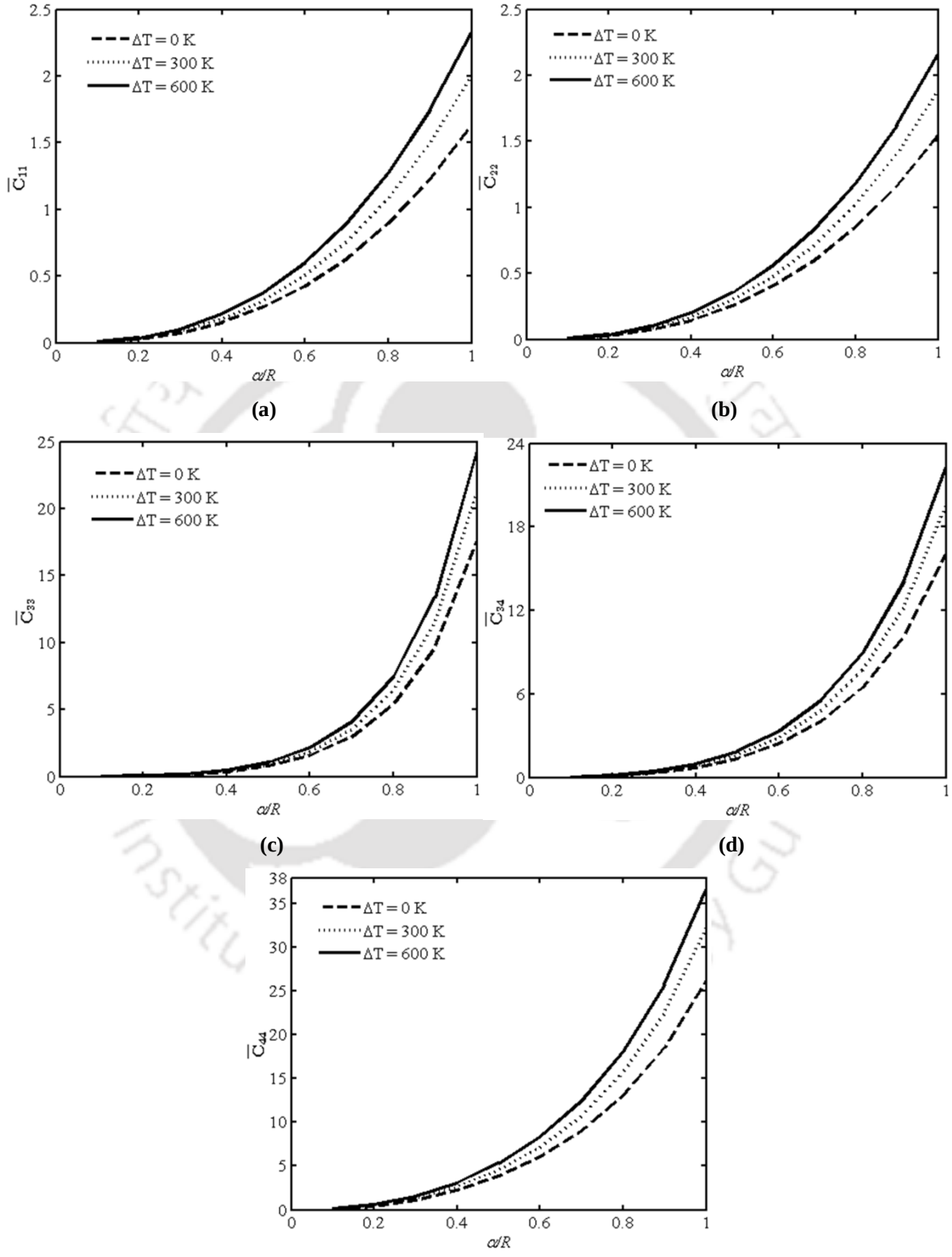

Fig. 4.8 Variation of LFCs with α/R and ΔT for FGM II: **(a)** $\bar{C}_{11}$ **(b)** $\bar{C}_{22}$ **(c)** $\bar{C}_{33}$ **(d)** $\bar{C}_{34}$ and **(e)** $\bar{C}_{44}$

Variation of LFCs with α/R and different k have been estimated for FGM I (SS/Al_2O_3) and FGM II (SS/ZrO_2), for $\Delta T = 0$ K. These results are plotted in **Figs. 4.5(a)** to **4.5(e)** and **Figs. 4.6(a)** to **4.6(e)**. It could be observed from **Figs. 4.5(a)** to **4.5(e)** and **Figs. 4.6(a)** to **4.6(e)** that the LFCs increase with the increase in α/R and for a given α/R, LFCs increase as k increases for FGM I and also LFCs decrease as k increases for FGM II. This is due to the increase in the metal content with the increase in k.

For FGM I (SS/Al_2O_3) and FGM II (SS/ZrO_2), variations of the direct and cross couple LFCs with α/R and different ΔT have been determined for $k = 0.5$ and are plotted in **Figs. 4.7(a)** to **4.7(e)** and **Figs. 4.8(a)** to **4.8(e)**, and these show that the LFCs increase with the increase in α/R and for a specific α/R, LFCs also increase with the increase in ΔT. This is due to fact that the material becomes softer at higher temperature.

4.5 Analysis of a non-rotating FG cracked shaft

In the present analysis, vibration characteristics of a non-rotating simply supported cracked shaft made of FGM I (SS/Al_2O_3) and FGM II (SS/ZrO_2) have been determined without considering the bearing stiffness and damping to understand the influences of different important parameters (slenderness ratio L/D, crack size α/R, temperature gradient ΔT and power law gradient index k) on the free vibration response of the shafts.

4.5.1 Variation of natural frequencies with α/R for metal and FG shaft

First six natural frequencies have been computed for both cracked FGM I (SS/Al_2O_3) and metal (SS) shafts with power law gradient index $k = 0.5$, slenderness ratio $L/D = 12.5$ and temperature gradient $\Delta T = 0$ K for different crack size α/R. **Table 4.9** shows the first six computed natural frequencies corresponding to different values of crack size α/R. Results in **Table 4.9** show that for each mode, natural frequency of the FG shaft is more than that of the metal shaft and natural frequencies are higher for the uncracked shaft than those for the cracked shaft.

Table 4.9 Variation of natural frequencies (in Hz) with different α/R for metal and FG shaft

Modes	Un-cracked	Crack size, α/R						
		0.2	0.3	0.4	0.5	0.6	0.7	0.8
		Cracked FG (SS/Al_2O_3) shaft, $k = 0.5$						
1st	189.72	180.75	168.95	154.35	138.73	123.23	108.41	94.46
2nd	189.72	189.53	188.94	187.61	185.14	181.01	174.66	165.48
3rd	754.47	753.37	751.89	750.03	747.98	745.88	743.79	741.69
4th	754.47	754.32	754.03	753.54	752.79	751.70	750.21	748.25
5th	1681.36	1608.55	1527.43	1446.36	1378.15	1325.00	1284.69	1254.24
6th	1681.36	1679.67	1674.59	1663.29	1642.82	1610.47	1564.68	1506.33
Modes	Un-cracked	Cracked metal (SS) shaft						
1st	126.53	121.46	114.29	104.98	94.60	84.02	73.73	63.95
2nd	126.53	126.42	126.08	125.30	123.78	121.20	117.11	111.05
3rd	503.16	502.53	501.64	500.45	499.09	497.66	496.21	494.74
4th	503.16	503.07	502.91	502.61	502.14	501.44	500.47	499.15
5th	1121.31	1079.69	1028.93	974.87	927.34	889.36	860.29	838.35
6th	1121.31	1120.37	1117.45	1110.73	1098.17	1077.68	1047.82	1008.72

Results also show that for a given L/D, crack location L_c/L and k, as α/R increases, natural frequencies decrease for all the modes. However, the percentage reduction in frequency is higher for the first, third and fifth modes than those in the second, fourth and sixth modes as mode shapes corresponding to the first, third and fifth modes have anti-nodes at crack location. It is also seen that the percentage reduction in frequency is higher in the FG shaft than those of the metal (SS) shaft. The percentage reduction in natural frequency is calculated as

$$\% \ \omega_i = \left[\left(\omega_i^{uc} - \omega_i^{c}\right)/\omega_i^{uc}\right] \times 100 \tag{4.1}$$

4.5.2 Effect of α/R and k on natural frequency

Figures 4.9(a) to **4.9(f)** show the variations of first, second, third, fourth, fifth and sixth frequencies, respectively, with α/R and k for a centrally located crack in an FG (SS/Al_2O_3) shaft system having $L/D = 12.5$ and $\Delta T = 0$ K. It could be observed that all the six natural

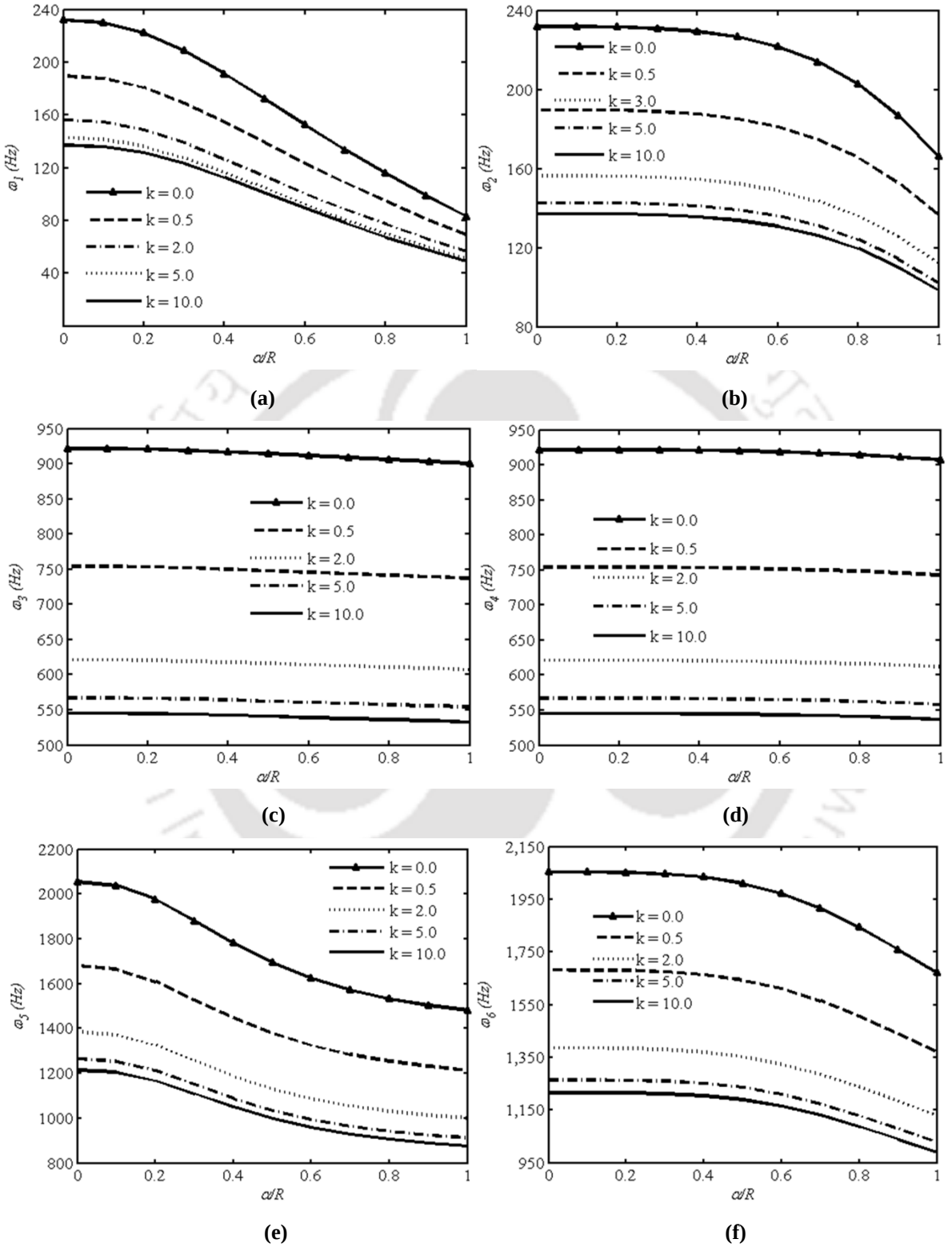

Fig. 4.9 Variation of natural frequencies with α/R and k : **(a)** first **(b)** second **(c)** third **(d)** fourth **(e)** fifth and **(f)** sixth

frequencies decrease as α/R increases and for a given α/R, natural frequencies increase as k decreases. Decrease in natural frequency with α/R is more pronounced for higher values of α/R. It is also observed that the variations of natural frequencies are more for $k<1$, for all the six modes due to increase in the ceramic content in the FG shaft.

4.5.3 Effect of α/R and L_c/L on natural frequency

Figures 4.10(a) to **4.10(f)** show the first six dimensionless natural frequencies for cracked FG (SS/Al_2O_3) shaft for different values of size of crack α/R and location of crack L_c/L, with slenderness ratio $L/D=12.5$, power law gradient index $k=3.0$ and temperature gradient $\Delta T=0$ K. Results show that for a given slenderness ratio L/D, size of crack α/R and power law gradient index k, the first six dimensionless natural frequencies monotonically decrease with the increase in crack size and the reduction in natural frequency is maximum for the first mode and is minimum for the third mode. However, for an offset crack located at $L_c/L=0.1645$, reduction in the natural frequency is the maximum for third mode and is minimum for the first mode for any values of size of crack α/R.

Figures 4.11(a) to **4.11(f)** show the reduction in first six dimensionless natural frequencies of an FG (SS/Al_2O_3) shaft with different locations of crack for different values of power law gradient index k with slenderness ratio $L/D=12.5$, crack size $\alpha/R=0.6$ and temperature gradient $\Delta T=0$ K. Results show that the increase in power law gradient index k leads to more reduction in natural frequencies in all the six modes, for a given slenderness ratio L/D, crack size α/R and power law gradient index k. However, the extent of reduction in natural frequency is dependent on the crack location.

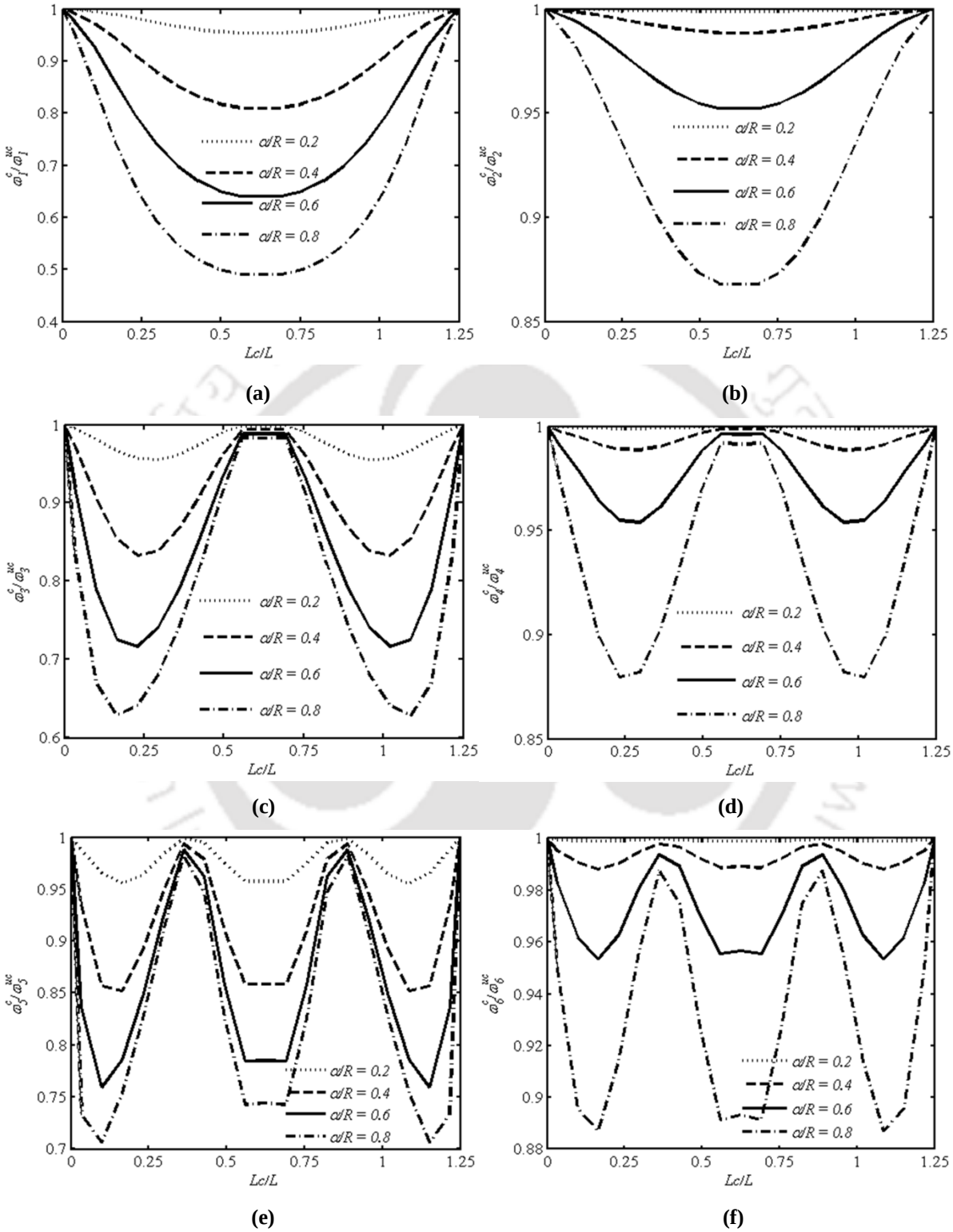

Fig. 4.10 Variation of natural frequencies with L_c/L and α/R: **(a)** first **(b)** second **(c)** third **(d)** fourth **(e)** fifth and **(f)** sixth

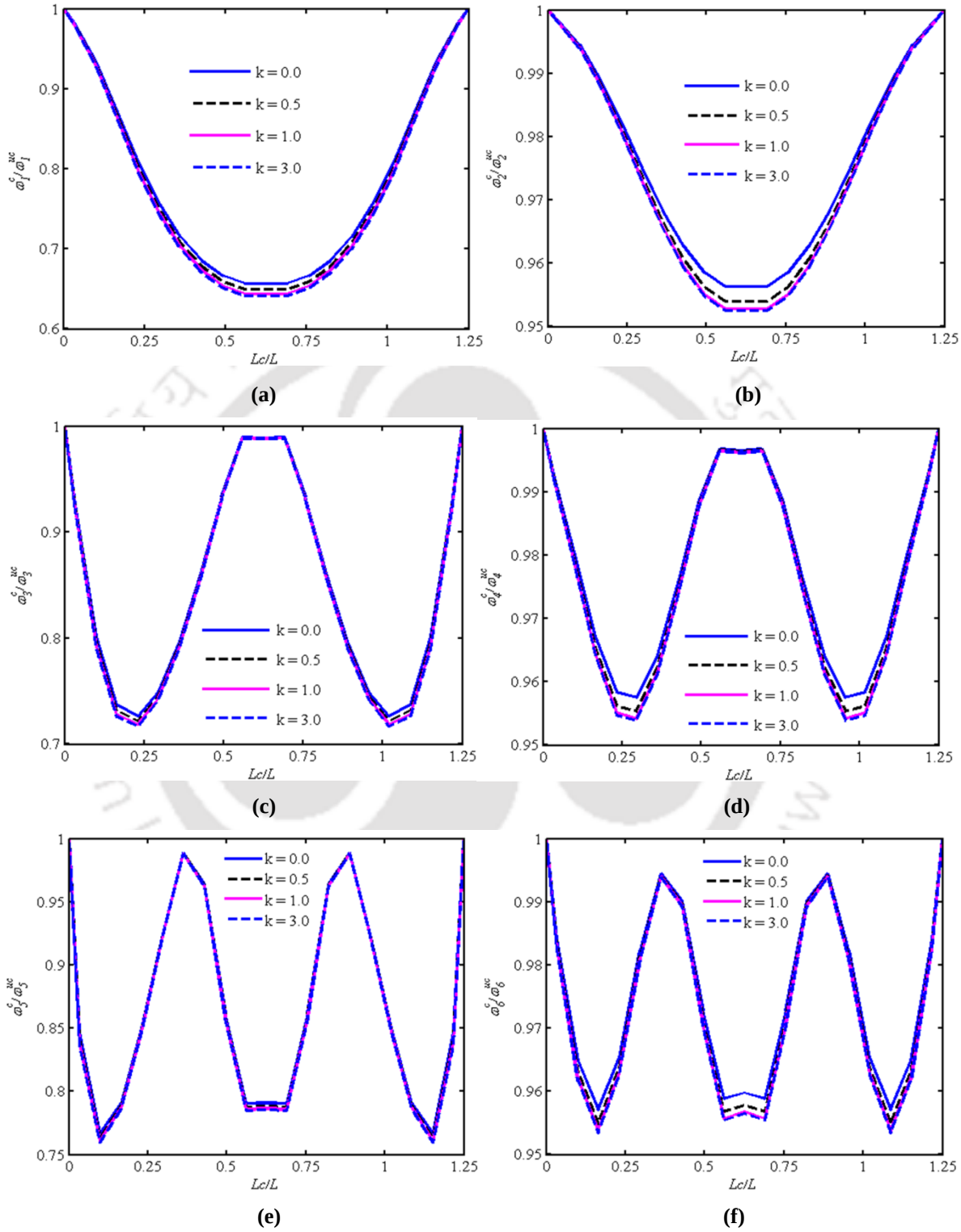

Fig. 4.11 Variation of natural frequencies with L_c/L and k : **(a)** first **(b)** second **(c)** third **(d)** fourth **(e)** fifth and **(f)** sixth

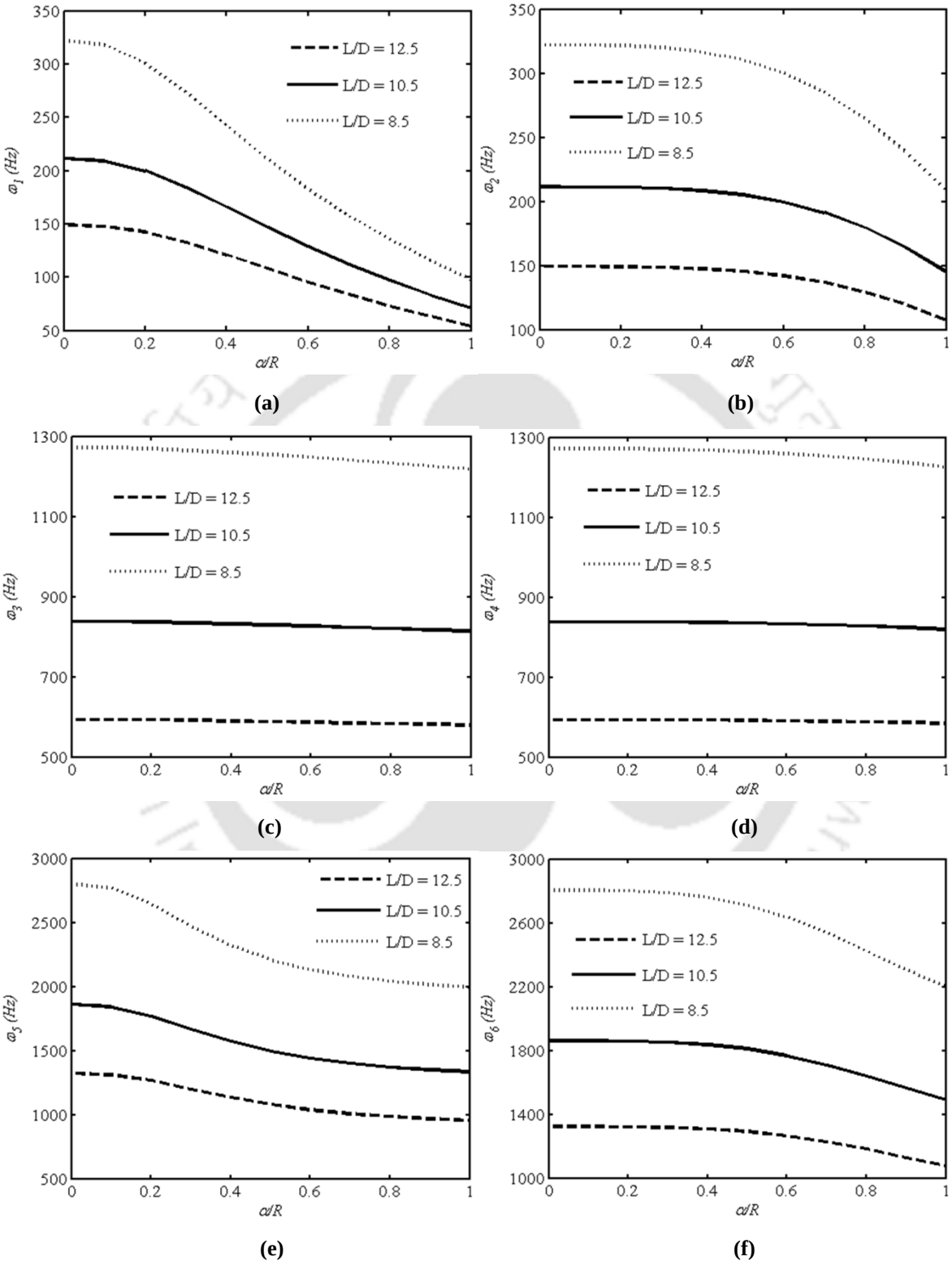

Fig. 4.12 Variation of natural frequencies with L/D and α/R : **(a)** first **(b)** second **(c)** third **(d)** fourth **(e)** fifth and **(f)** sixth

4.5.4 Effect of α/R and L/D on natural frequency

Figures 4.12(a) to **4.12(f)** show the first, second, third, fourth, fifth and sixth natural frequencies, respectively, for a cracked FG (SS/Al_2O_3) shaft with $L_c/L = 0.5$, $k = 3.0$ and $\Delta T = 0$ K for different values of L/D and α/R. These results show that for a given L/D, L_c/L and k, the natural frequencies decrease with the increase in the crack size for all the six modes. However, the reductions are more for the first, third and fifth modes than those in the second, fourth and sixth modes. It also shows that in the presence of a crack in an FG shaft, natural frequencies increase as L/D decreases for a constant length.

Table 4.10 Variation of natural frequencies (in Hz) of a cracked FG shaft with α/R and ΔT

Modes	$\alpha/R = 0.1$			$\alpha/R = 0.4$		
	$\Delta T = 0$ K	$\Delta T = 300$ K	$\Delta T = 600$ K	$\Delta T = 0$ K	$\Delta T = 300$ K	$\Delta T = 600$ K
1st	187.87	183.07	177.22	154.35	150.31	144.79
2nd	189.71	184.88	179.12	187.61	182.83	177.06
3rd	754.25	735.06	712.15	750.03	730.93	708.05
4th	754.45	735.26	712.36	753.54	734.37	711.47
5th	1665.44	1622.89	1571.12	1446.36	1408.99	1361.03
6th	1681.20	1638.44	1587.40	1663.29	1620.89	1569.73
Modes	$\alpha/R = 0.7$			$\alpha/R = 1.0$		
	$\Delta T = 0$ K	$\Delta T = 300$ K	$\Delta T = 600$ K	$\Delta T = 0$ K	$\Delta T = 300$ K	$\Delta T = 600$ K
1st	108.41	105.65	102.09	68.84	67.19	65.44
2nd	174.66	170.20	164.73	136.63	133.24	129.32
3rd	743.79	724.86	702.21	737.39	718.64	696.29
4th	750.21	731.12	708.30	742.71	723.84	701.35
5th	1284.69	1252.01	1212.37	1213.29	1182.56	1146.17
6th	1564.68	1524.80	1476.12	1370.17	1335.62	1294.89

4.5.5 Effect of ΔT on natural frequency

In order to understand the effect of temperature gradient (ΔT) on the natural frequencies of the cracked FG (SS/Al_2O_3) shaft, the first six natural frequencies have been computed for different values of ΔT (= 0 K, 300 K and 600 K) and for different values of α/R and L_c/L, with

$L/D = 12.5$ and $k = 0.5$. These results are tabulated in **Table 4.10** for $L_c/L = 0.5$ and **Table 4.11** for $\alpha/R = 0.6$. Results from both the **Tables 4.10** and **4.11** show that natural frequencies decrease with the increase in temperature gradient. This is due to the fact that the material becomes softer at higher temperature gradients.

Table 4.11 Variation of natural frequencies (in Hz) of a cracked FG shaft with L_c/L and ΔT

Modes	$L_c/L = 0.05$			$L_c/L = 0.20$		
	$\Delta T = 0$ K	$\Delta T = 300$ K	$\Delta T = 600$ K	$\Delta T = 0$ K	$\Delta T = 300$ K	$\Delta T = 600$ K
1st	186.13	181.39	175.69	152.23	148.32	143.28
2nd	189.36	184.54	178.79	186.17	181.43	175.71
3rd	697.05	679.23	657.22	544.41	530.44	512.69
4th	748.70	729.64	706.80	721.49	703.06	680.54
5th	1415.21	1378.89	1332.74	1426.34	1389.97	1345.80
6th	1653.01	1610.89	1560.13	1620.36	1579.02	1528.80
Modes	$L_c/L = 0.35$			$L_c/L = 0.50$		
	$\Delta T = 0$ K	$\Delta T = 300$ K	$\Delta T = 600$ K	$\Delta T = 0$ K	$\Delta T = 300$ K	$\Delta T = 600$ K
1st	128.57	125.25	120.83	123.23	120.04	115.78
2nd	182.25	177.60	171.92	181.01	176.39	170.73
3rd	647.92	631.39	611.15	745.88	726.90	704.16
4th	735.56	716.80	694.13	751.70	732.57	709.70
5th	1619.33	1578.05	1528.31	1325.00	1291.15	1249.36
6th	1663.93	1621.56	1570.72	1610.47	1569.36	1519.21

4.5.6 Influences of k, α/R and ΔT on natural frequencies for an FGM II shaft

Having determined the direct and cross couple LFCs as a function of crack depth for a given temperature gradient ΔT, it is important to understand the dynamics of such a cracked FG (SS/ZrO_2) shaft and the influence of different important parameters (k, α/R and ΔT) on the free vibration characteristics. A non-rotating simply supported FGM II (SS/ZrO_2) shaft with slenderness ratio $SR = 0.02$, having a centrally located, fully open transverse crack is considered, and the first, second, third, fourth, fifth and sixth dimensionless natural frequencies ϖ_n have been computed. Analysis has also been performed for uncracked shafts to study the reduction in natural frequencies due to presence of crack. Results have

been obtained for different values of k, α/R and ΔT to understand the importance of those parameters.

Table 4.12 shows the first six dimensionless natural frequencies ϖ_n ($\varpi_n^4 = \rho_{SS} A L^4 \omega^2 / E_{SS} I$) for both the uncracked and cracked ($\alpha/R = 0.6$ and $L_c/L = 0.5$) FGM II (SS/ZrO_2) shaft with $\Delta T = 0$ K for different values of power law gradient index k. It could be observed that the natural frequencies ϖ_n monotonically decrease with the increase in k for both uncracked and cracked FG shaft. However, the percentage reduction in dimensionless natural frequencies ϖ_n ($\% \varpi_{n,i} = \left\{\left(\varpi_{n,i}^{uc} - \varpi_{n,i}^{c}\right)/\varpi_{n,i}^{uc}\right\} \times 100$, where superscripts uc and c denote the uncracked and cracked respectively, and subscript i denote mode numbers) due to the presence of a crack is comparatively less pronounced for higher values of k. In addition, percentage reduction in ϖ_n are more for the first, third and fifth modes than those in the second, fourth and sixth modes as mode shapes corresponding to the first, third and fifth modes have anti-nodes at the crack location. Therefore, in FG shafts, power law gradient index k influences the reduction in natural frequency and k may be chosen to keep the overall stiffness of the shaft and the temperature resistance within desired limit.

Table 4.12 Variation of ϖ_n with k for a non-rotating simply supported FGM II (SS/ZrO_2) shaft

Modes	Uncracked				Cracked, $\alpha/R = 0.6$, $L_c/L = 0.5$			
	k				k			
	0.5	1.0	5.0	10.0	0.5	1.0	5.0	10.0
1st	3.2059	3.1859	3.1505	3.1436	2.6237	2.6130	2.5856	2.5759
2nd	3.2059	3.1859	3.1505	3.1436	3.1401	3.1215	3.0866	3.0791
3rd	6.3455	6.3059	6.2356	6.2220	6.3202	6.2810	6.2111	6.1973
4th	6.3455	6.3059	6.2356	6.2220	6.3423	6.3028	6.2326	6.2189
5th	9.3684	9.3096	9.2054	9.1852	8.4184	8.3710	8.2791	8.2571
6th	9.3684	9.3096	9.2054	9.1852	9.2033	9.1479	9.0451	9.0235

Table 4.13 shows the first six dimensionless natural frequencies ϖ_n ($\varpi_n^4 = \rho_{SS} A L^4 \omega^2 / E_{SS} I$) for both the uncracked and cracked ($L_c/L = 0.5$) FGM II (SS/ZrO_2)

shaft with power law gradient index $k = 0.5$ and $\Delta T = 0$ K for different values of size of crack, α/R. It could be observed that for the FG shaft considered, the natural frequencies ϖ_n decrease with the increase in α/R and the reduction is more pronounced for higher values of α/R. It also shows that percentage reductions in ϖ_n are more for the first, third, and fifth modes than those in the second, fourth, and sixth modes, for the reason stated earlier.

Table 4.13 Variation of ϖ_n with α/R for a non-rotating simply supported FGM II (SS/ZrO_2) shaft for $L_c/L = 0.5$ and $k = 0.5$

Modes	Un-cracked	α/R				
		0.2	0.4	0.6	0.8	1.0
1st	3.2059	3.1461	2.9327	2.6237	2.2822	1.9270
2nd	3.2059	3.2046	3.1912	3.1401	3.0061	2.7239
3rd	6.3455	6.3488	6.3368	6.3202	6.3025	6.2840
4th	6.3455	6.3517	6.3491	6.3423	6.3286	6.3054
5th	9.3684	9.2176	8.7981	8.4184	8.1780	8.0386
6th	9.3684	9.3651	9.3298	9.2033	8.9238	8.5197

Table 4.14 Natural frequency parameters ϖ_n of a non-rotating simply supported FGM II (SS/ZrO_2) shaft for $L_c/L = 0.5$ and $\alpha/R = 0.6$

Modes	Different ΔT and $k = 0.5$			Different ΔT and $k = 3.0$		
	0 K	300 K	600 K	0 K	300 K	600 K
1st	2.6237	2.5105	2.4153	2.5945	2.5287	2.4018
2nd	3.1401	2.9945	2.8813	3.0951	3.0019	2.8506
3rd	6.3202	6.0231	5.7956	6.2273	6.0352	5.7300
4th	6.3423	6.0440	5.8157	6.2489	6.0557	5.7496
5th	8.4184	8.0313	7.7270	8.3027	8.0590	7.6515
6th	9.2033	8.7743	8.4412	9.0699	8.7942	8.3481

Table 4.14 shows the first six dimensionless natural frequencies ϖ_n ($\varpi_n^4 = \rho_{SS} A L^4 \omega^2 / E_{SS} I$) for cracked ($L_c/L = 0.5$ and $\alpha/R = 0.6$) FGM II (SS/ZrO_2) shaft having power law gradient index $k = 0.5$ and $k = 3.0$ for different values of temperature

gradient ΔT. It could be observed that ϖ_n decreases for a given α/R with the increase in temperature gradient ΔT as the material become softer at higher values of ΔT. In addition, **Table 4.14** shows changes in ϖ_n with ΔT is more for lower value of k. Thus in a high temperature application, it is important to choose k in such a way so that the reduction in ϖ_n with temperature is minimized while keeping enough material at the outer layer for providing temperature resistance.

Table 4.15 Variation of $\bar{\omega}_n$ (in Hz) with k for non-rotating simply supported cracked ($\alpha/R = 0.6$ and $L_c/L = 0.5$) FG shafts

Modes	FGM I (SS/Al_2O_3)				FGM II (SS/ZrO_2)			
	k				k			
	0.5	2.0	5.0	10.0	0.5	2.0	5.0	10.0
1st	0.6495	0.6410	0.6441	0.6496	0.6678	0.6726	0.6716	0.6694
2nd	0.9540	0.9522	0.9534	0.9547	0.9589	0.9598	0.9594	0.9589
3rd	0.9886	0.9883	0.9883	0.9886	0.9892	0.9894	0.9893	0.9892
4th	0.9963	0.9961	0.9962	0.9963	0.9967	0.9968	0.9967	0.9967
5th	0.7881	0.7852	0.7862	0.7881	0.7945	0.7963	0.7959	0.7951
6th	0.9578	0.9563	0.9573	0.9584	0.9621	0.9628	0.9625	0.9621

4.5.7 Influence of types of FGM on natural frequency

In order to understand the selection of FG materials, the influence of the power law gradient index k and crack size α/R are studied by obtaining the natural frequencies of two types of FGM shafts with different values of k and α/R for simply supported end conditions for $\Delta T = 0$ K. Natural frequency of cracked FG shaft is normalized with respect of an un-cracked shaft and the normalized natural frequency is defined as $\bar{\omega}_n = \omega_n^c / \omega_n^{uc}$. **Table 4.15** shows the first six normalized natural frequencies for two types of FGM shafts for a given crack configuration ($\alpha/R = 0.6$ and $L_c/L = 0.5$) and for different values of power law gradient index k. It could be observed that for both the types of FGM I (SS/Al_2O_3) and FGM II (SS/ZrO_2) shafts, the normalized natural frequencies decrease with the increase in k as the metallic content increases. **Table 4.16** shows the first six natural frequencies for two

types of FGM shafts for a given crack configuration ($k=0.5$ and $L_c/L=0.5$) and for different values of size of crack α/R. It could be observed that for a given k the normalized natural frequencies decrease with increase in α/R for both the FGM I and FGM II shafts. However, the reduction in natural frequencies is comparatively more pronounced for FGM I shaft for higher values of k and higher values of α/R than those of FGM II shaft. Thus the power law gradient index and crack size have significant influences in choosing the material selection for an FG shaft.

Table 4.16 Variation of $\bar{\omega}_n$ (in Hz) with α/R for non-rotating simply supported cracked ($k=0.5$ and $L_c/L=0.5$) FG shafts

Modes	FGM I (SS/Al_2O_3)				FGM II (SS/ZrO_2)			
	α/R				α/R			
	0.2	0.4	0.6	0.8	0.2	0.4	0.6	0.8
1st	0.9527	0.8135	0.6495	0.4979	0.9627	0.8355	0.6678	0.5047
2nd	0.9989	0.9888	0.9540	0.8722	0.9992	0.9907	0.9589	0.8782
3rd	0.9985	0.9941	0.9886	0.9831	0.9988	0.9948	0.9892	0.9833
4th	0.9998	0.9988	0.9963	0.9918	0.9998	0.9990	0.9967	0.9921
5th	0.9567	0.8602	0.7881	0.7460	0.9653	0.8729	0.7945	0.7475
6th	0.9990	0.9893	0.9578	0.8959	0.9992	0.9910	0.9621	0.8999

4.6 Analysis of a rotor-bearing system with a cracked FG shaft

In the present analysis, dynamic parameters (whirling frequencies and critical speeds) of rotor-bearing system with a cracked FG shaft made of FGM II (SS/ZrO_2) have been computed by considering the undamped bearing stiffness to understand the influences of important parameters (k, α/R and ΔT) on the whirling frequencies of the system.

4.6.1 Influences of k, α/R and ΔT on whirling frequencies

To understand the effects of k, α/R and ΔT on the vibration characteristics of rotor-bearing system with a cracked FG shaft including the effects of the rotary inertia, shear effect and gyroscopic effect, first three modes of forward whirling (FW) and backward

whirling (BW) frequencies have been computed. In the present analysis, the FG shaft is considered with diameter $D = 0.1\,\text{m}$, slenderness ratio $\text{SR} = 0.02$, temperature dependent material properties shown in **Table 4.1**, and the FG rotor is supported by identical un-damped isotropic bearings of stiffness coefficients $K_{vv}^{b} = K_{ww}^{b} = 1.7513\times10^{7}\ \text{N/m}$ and $K_{vw}^{b} = K_{wv}^{b} = 0$. The present analysis has been done for both uncracked and cracked (centrally located fully open transverse crack) shaft for different values of k, α/R and ΔT.

Table 4.17 Whirling frequencies ω (in Hz) of a FG (SS/ZrO_2) shaft with isotropic un-damped flexible bearings at $\Omega = 66.667$ Hz

Modes	Uncracked				Cracked ($\alpha/R = 0.6$ and $L_c/L = 0.5$)			
	k				k			
	0.5	1.0	5.0	10.0	0.5	1.0	5.0	10.0
1BW	36.349	35.315	33.449	33.081	35.078	34.138	32.407	32.052
1FW	36.353	35.319	33.453	33.085	36.257	35.230	33.374	33.005
2BW	64.237	62.343	58.930	58.259	64.234	62.341	58.928	58.257
2FW	64.862	62.968	59.557	58.885	64.859	62.966	59.554	58.883
3BW	304.615	300.501	293.266	291.870	197.819	195.776	190.922	189.343
3FW	307.127	303.014	295.779	294.383	291.232	287.506	280.528	279.032

Table 4.17 shows the first three modes of FW and BW frequencies for both the uncracked and cracked ($\alpha/R = 0.6$ and $L_c/L = 0.5$) FG (SS/ZrO_2) shaft system with $\Delta T = 0$ K and spin speed $\Omega = 66.667$ Hz $(4000\ \text{rpm})$ for different values of power law gradient index k. It could be observed that the changes in both the whirling frequencies (FW and BW) decrease with increase in k due to transition of the shaft from ZrO_2, for both the uncracked and cracked shaft system and the percentage change in whirling frequencies $\omega\{\%\ \omega_i = (1-\omega_i^c/\omega_i^{uc})\times100\}$ due to presence of a crack decreases with the increase in k, even though the decrease is not very significant in the present FG shaft system and as expected, the change is appreciable in 1st and 3rd mode and marginal in the 2nd mode.

Table 4.18 shows the first three modes of FW and BW frequencies for both the uncracked and cracked ($L_c/L = 0.5$ and $k = 0.5$) FG (SS/ZrO_2) shaft system with

$\Delta T = 0$ K and spin speed $\Omega = 66.667$ Hz $(4000$ rpm$)$ for different values of size of crack α/R. It could be seen that for a given power law gradient index k, the both the whirling frequencies (FW and BW) decrease with the increase in α/R due to degradation of stiffness in the FG shaft. It also shows that the percentage reduction in whirling frequencies are more for the first, third and fifth modes than those in the second, fourth and sixth modes as expected and for the reason stated earlier.

Table 4.18 Whirling frequencies ω (in Hz) of a FG (SS/ZrO_2) shaft with isotropic un-damped flexible bearings at $\Omega = 66.667$ Hz for $L_c/L = 0.5$ and $k = 0.5$

Modes	Uncracked	α/R				
		0.2	0.4	0.6	0.8	1.0
1BW	36.349	36.266	35.895	35.078	33.498	30.451
1FW	36.353	36.348	36.330	36.257	36.036	35.390
2BW	64.237	64.238	64.237	64.234	64.229	64.219
2FW	64.862	64.863	64.862	64.859	64.854	64.842
3BW	304.615	292.420	249.400	197.819	153.046	118.226
3FW	307.127	305.708	302.568	291.232	263.496	213.321

Table 4.19 Whirling frequencies ω (in Hz) of a FG (SS/ZrO_2) shaft with isotropic un-damped flexible bearings at $\Omega = 66.667$ Hz for $L_c/L = 0.5$ and $\alpha/R = 0.6$

Modes	Different ΔT and $k = 0.5$			Different ΔT and $k = 3.0$		
	0 K	300 K	600 K	0 K	300 K	600 K
1BW	35.078	34.640	34.202	32.818	32.607	32.126
1FW	36.257	36.001	35.759	33.806	33.669	33.399
2BW	64.234	63.861	63.800	59.723	59.378	59.311
2FW	64.859	65.105	65.040	60.348	60.627	60.554
3BW	197.819	183.456	171.899	192.420	184.135	168.520
3FW	291.232	266.804	248.612	282.228	266.693	242.347

Table 4.19 shows the first three modes of FW and BW frequencies for cracked ($L_c/L = 0.5$ and $\alpha/R = 0.6$) FG (SS/ZrO_2) shaft system with power law gradient index $k = 0.5$ and $k = 3.0$, spin speed $\Omega = 66.667$ Hz $(4000$ rpm$)$ for different values of

temperature gradient ΔT. It could be seen that for a given α/R, the reduction in whirling frequencies due to the presence of a crack decreases with the increase in ΔT as the material become softer at higher values of ΔT. In addition, **Table 4.19** shows that the changes in whirling frequencies with ΔT is more for lower values of k.

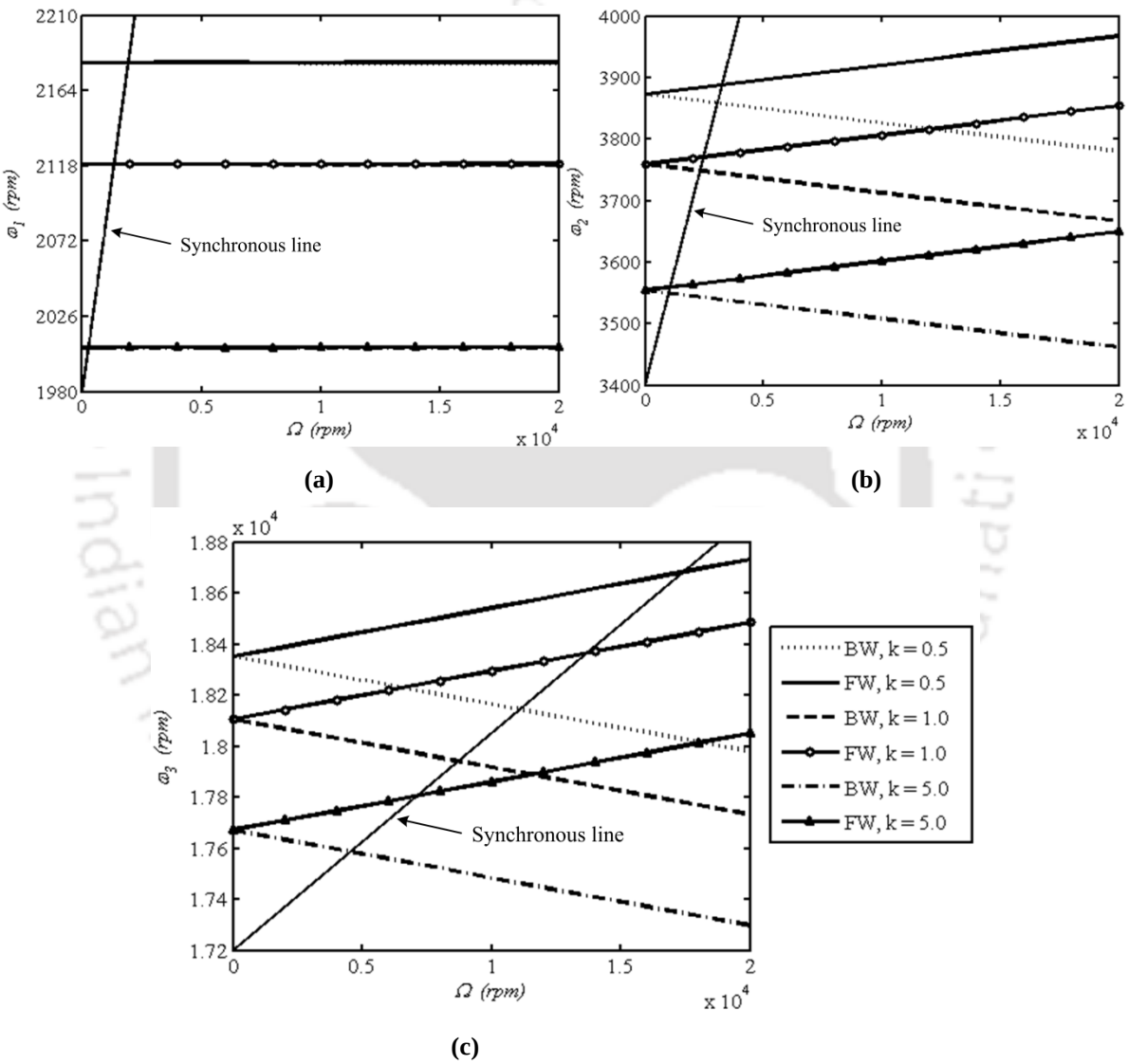

Fig. 4.13 Campbell diagram of a rotor-bearing system with an uncracked FG shaft for different k **(a)** first mode **(b)** second mode and **(c)** third mode

Figures 4.13(a) to **4.13(c)** show the variation of first three modes (including FW and BW) of natural whirling frequencies ω (in rpm), respectively, with spin speed Ω (range 0 to 20000 rpm) of the rotor-bearing system with an uncracked FG (SS/ZrO_2) shaft with

slenderness ratio $SR = 0.02$ and $\Delta T = 0$ K for different values of k. It could be observed from **Figs. 4.13(a)** to **4.13(c)** that in all the three modes, with increase in the spin speed, while the FW frequencies increase, the BW frequencies decrease. Both the FW and BW frequencies decrease with the increase in k due to transition of the shaft from ZrO_2, in all the three modes. Therefore, in order to keep the whirling frequencies of an FG shaft system within a desired limit power law gradient index k can be chosen appropriately.

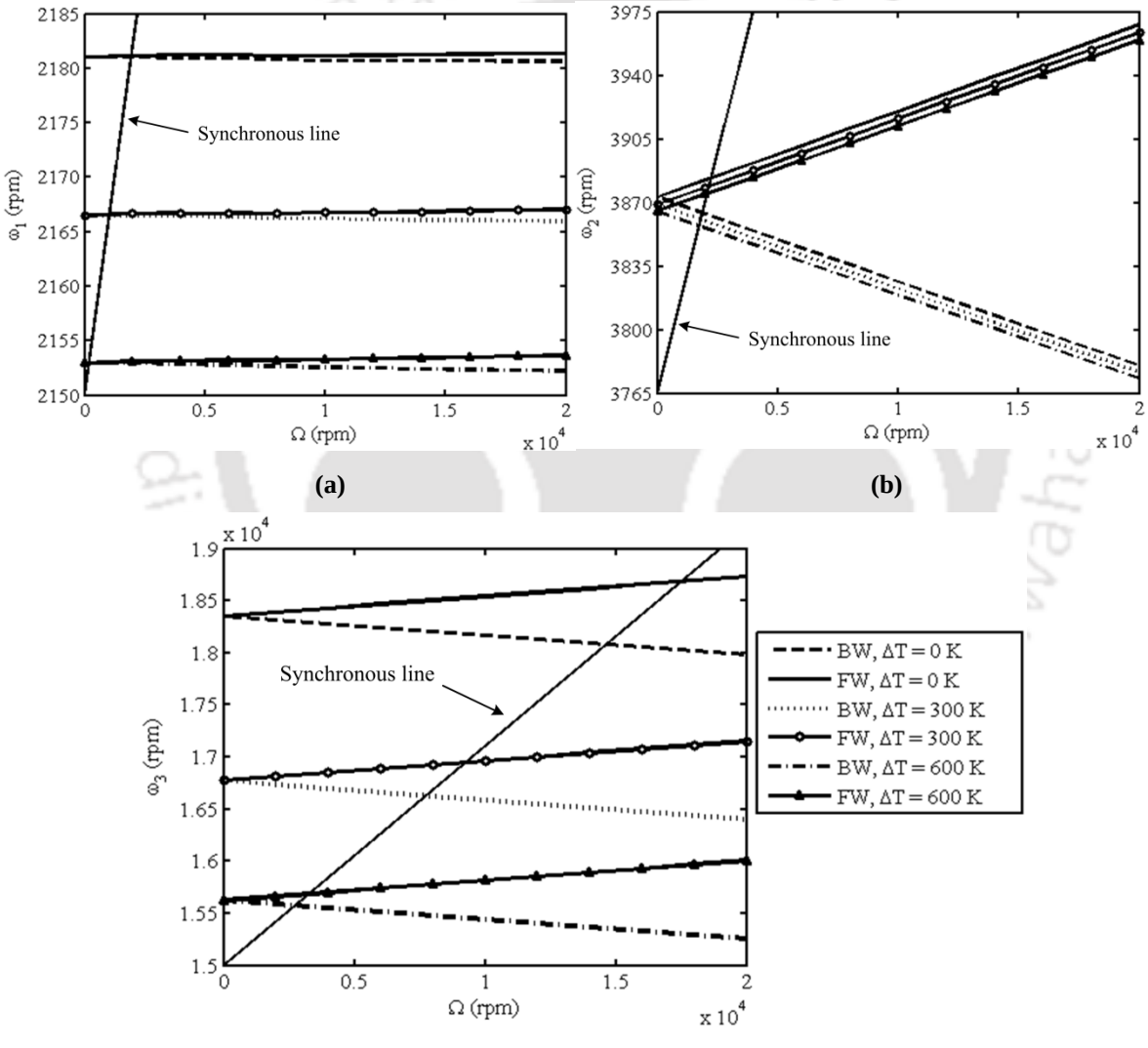

Fig. 4.14 Campbell diagram of a rotor-bearing system with an uncracked FG shaft for different ΔT **(a)** first mode **(b)** second mode and **(c)** third mode

Figures 4.14(a) to **4.14(c)** show the variation of first three modes (including FW and BW) of natural whirling frequencies ω (in rpm), respectively, with spin speed Ω (range 0 to 20000 rpm) of the rotor-bearing system with an uncracked FG (SS/ZrO_2) shaft with $SR = 0.02$ and $k = 0.5$ for different values of temperature gradient ΔT. It could be observed from **Figs. 4.14(a)** to **4.14(c)** that in all the three modes, with increase in the spin speed, while the FW frequencies increase, the BW frequencies decrease. At a given speed, both the FW and BW frequencies decrease with the increase in ΔT as the material become softer at higher values of ΔT, but decrease is more pronounced in higher modes and higher spinning speeds.

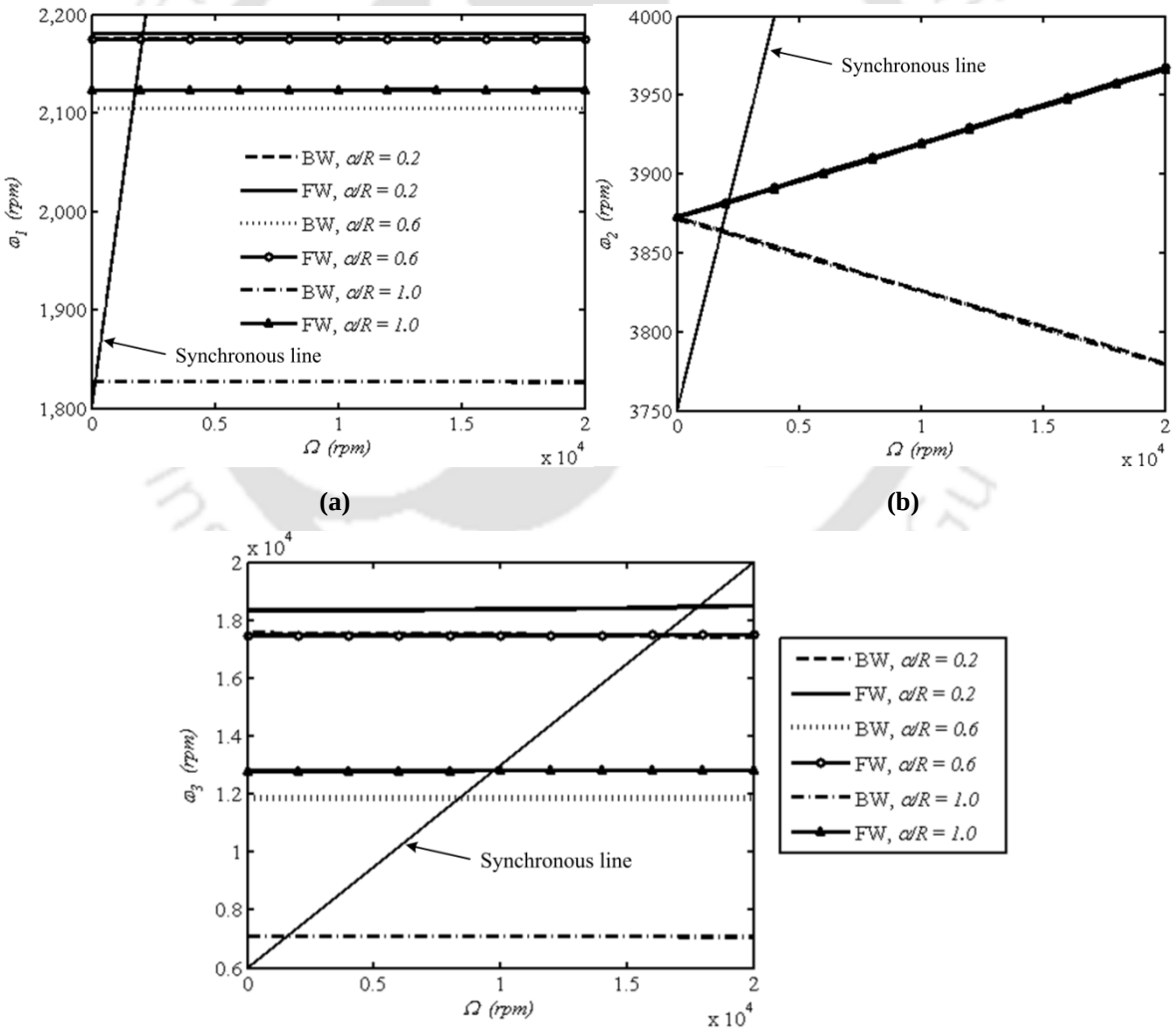

Fig. 4.15 Campbell diagram of a rotor-bearing system with a FG shaft for different α/R

(a) first mode **(b)** second mode and **(c)** third mode

Figures 4.15(a) to **4.15(c)** show the first three modes (including FW and BW) of natural whirling frequencies ω (in rpm), respectively, as a function of spin speed Ω (range 0 to 20000 rpm) of the rotor-bearing system with a cracked FG (SS/ZrO_2) shaft with $SR = 0.02$, $\Delta T = 0$ K and $k = 0.5$ for different values of α/R. It could be observed from **Figs. 4.15(a)** to **4.15(c)** that in all the three modes FW frequencies increase with increasing spin speed however BW frequencies decrease. It is also observed that at a particular spin speed, both FW and BW frequencies decrease as α/R increases, due to degradation of stiffness in the FG shaft, but the decrease is more pronounced in higher modes.

4.6.2 Influences of k and α/R on critical speeds

In order to understand the influence of power law gradient index k on the critical speeds in a rotor-bearing system having an FG (SS/ZrO_2) rotor, critical speeds have been computed using the present developed FE code for different values of k for both uncracked and cracked FG shaft and the results are tabulated in **Table 4.20**. In the present analysis, the FG shaft is considered with diameter $D = 0.1$ m, slenderness ratio $SR = 0.02$, temperature dependent material properties (shown in **Table 4.1**) and crack configuration ($\alpha/R = 0.6$ and $L_c/L = 0.5$) along with the same bearing parameters (given in the section 4.6.1). Results from this **Table 4.20** show that in general critical speeds decrease as the value of k increases, due to transition of the shaft from ZrO_2. It addition, percentage reduction in critical speeds due to the presence of a crack is more pronounced for higher value of k.

Table 4.20 Critical speeds (in Hz) for a rotor-bearing system with a uniform FG shaft

Modes	Uncracked				Cracked ($\alpha/R = 0.6$ and $L_c/L = 0.5$)			
	k				k			
	0.5	1.0	5.0	10.0	0.5	1.0	5.0	10.0
1BW	36.350	35.315	33.448	33.080	35.083	34.138	32.407	32.054
1FW	36.353	35.321	33.455	33.091	36.250	35.228	33.373	33.006
2BW	64.250	62.383	58.966	58.300	64.241	62.360	58.964	58.292
2FW	64.875	62.966	59.525	58.850	64.850	62.948	59.520	58.842
3BW	300.250	296.225	289.120	287.750	197.728	195.681	190.821	189.255
3FW	311.800	307.583	300.230	298.803	291.550	287.825	280.833	279.333

4.6.3 Influence of k on reduction in fundamental frequency, whirling frequency and critical speeds

In order to understand the effect of power law gradient index k on the reduction in fundamental frequency, whirling frequency and critical speed, percentage change in these quantities with different values of k for a cracked FG shaft with $\mathrm{SR}=0.02$, $\alpha/R=0.6$, $L_c/L=0.5$ are computed and tabulated in **Table 4.21**. It could be seen from **Table 4.21** that the percentage reduction in all the cases are reduced with the increase in k due to transition of the shaft from ZrO_2, even though the reduction is less at higher values of k. Further increase in k does not have any effect on the percentage change in fundamental frequency, whirling frequency and critical speed.

Table 4.21 Percentage change in frequencies for a rotor-bearing system with a uniform FG shaft

k	Frequencies, $\Omega=0$ Hz		Whirling frequencies, $\Omega=66.667$ Hz		Critical speeds	
	1st	2nd	1BW	1FW	1BW	1FW
0.5	18.2	2.05	3.5	0.26	3.49	0.28
1.0	18.0	2.02	3.3	0.25	3.33	0.26
5.0	17.9	2.03	3.1	0.24	3.11	0.24
10.0	18.0	2.05	3.1	0.24	3.10	0.26

4.7 Summary

LFCs for cracked FG shafts are derived considering temperature gradient, temperature dependent material properties and following power law gradation of material properties. Based on these LFCs, modified stiffness of the cracked FG shaft as a function of power law gradient index and temperature gradient are determined. These are then used to develop an FE code for analysis of dynamic behavior of a rotor-bearing system with an FG (SS/ZrO_2 and SS/Al_2O_3) shaft having a fully open transverse surface crack. Using the developed FE code, effects of power law gradient index on the dynamic behavior of the cracked FG shaft have been studied along with the influence of other important parameters such as slenderness ratios, crack sizes, and temperature gradients. Change in natural whirling

frequencies, critical speeds, reduction in whirling frequencies with crack size for an FG shaft has been studied and the following important conclusions have been drawn.

- For a cracked FG shaft, the values of LFCs are not only a function of crack size but also depend on power law gradient index as well as the applied temperature gradient. Therefore, while designing an FG shaft, the power law gradient index may be chosen to limit the increase in flexibility coefficients due to the presence of transverse surface crack.
- In the case of a cracked FG shaft, natural whirling frequencies (FW and BW) and critical speeds of the rotor-bearing system decrease with the increase in crack size for a certain slenderness ratio and crack location. However, the amount of reduction is decided by the value of the power law gradient index. It is observed that as the power law gradient increases, the reduction decreases.
- For all the six modes studied maximum changes in natural frequency is observed for a power law gradient index less than one.
- Even though the presence of a transverse crack in the FG shaft of a rotor-bearing system leads to reduction in natural whirling frequencies (FW and BW) and critical speeds with increasing slenderness ratio, the power law gradient index could be suitably chosen to limit these reductions thereby allowing more slenderness ratio in design.
- The reduction in natural whirling frequencies and critical speeds of the rotor-bearing system with the crack depth increase with the increase in applied temperature gradient. However, the reduction is dependent on the power law gradient index. Therefore, in a high temperature application, power law gradient index could be suitably chosen to design the FG shaft.

CHAPTER 5

Transverse Vibration Analysis of a Rotor-Bearing System having an FG Shaft with Transverse Breathing Cracks

5.1 Introduction

This chapter presents the analysis of transverse vibration of a rotor-bearing system having an FG shaft with multiple transverse breathing cracks. The transverse breathing cracks are modeled based on the formulation discussed in **Chapter 3** (Sub-section **3.4.2**). In this study, stainless steel (SS) and zirconia (ZrO_2) are used as constituent materials of the FGM (SS/ZrO_2) for the rotor and power law gradation is assumed. An FE code has been developed in MATLAB, which is capable of performing analysis of a FG shaft with multiple transverse breathing cracks in a rotor-bearing system and to study the effect of relative size, location and orientation of crack, power law gradient index, slenderness ratio, and temperature gradient on the dynamics of such system.

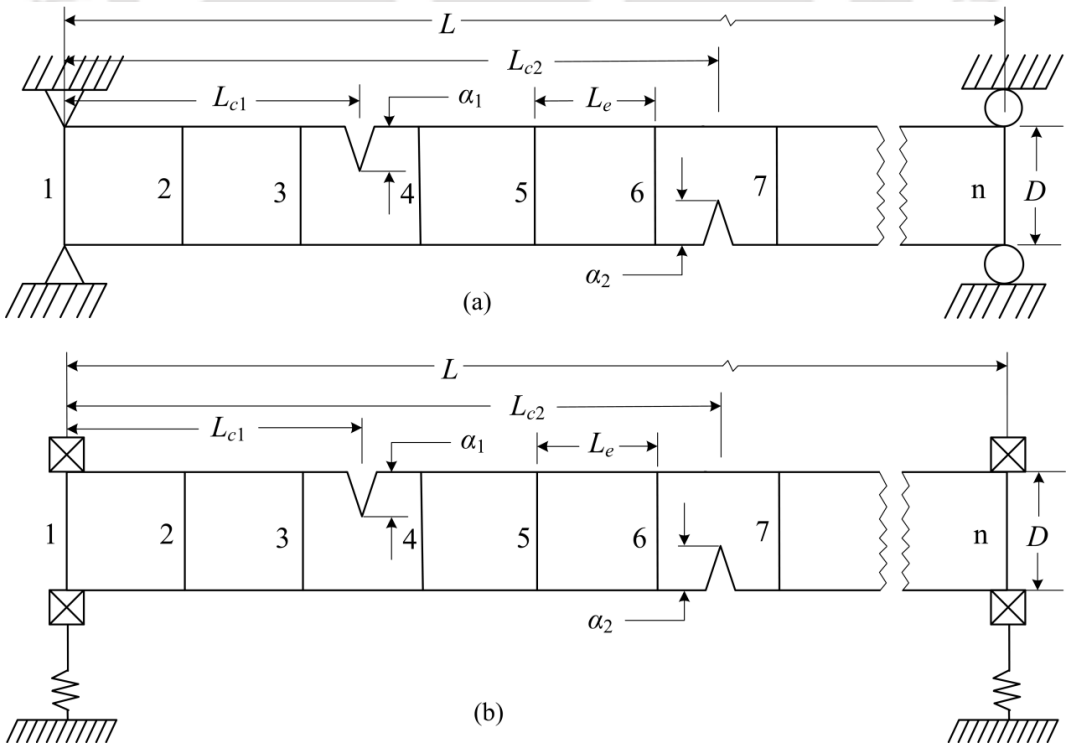

Fig. 5.1 Rotor-Bearing system having a cracked FG shaft with FE discretization:
(a) simply supported ends (b) flexible end bearings

5.2 Rotor-Bearing system details

In the present problem, an FG shaft having two transverse cracks and considering breathing behavior is modeled using two-nodded Timoshenko beam element with four DOFs (two translational and two rotational) at each node. Breathing crack behavior is considered during rotation of the FG shaft for accurate prediction of the dynamic responses of the rotor-bearing system. The FG cracked shaft is discretized with equal finite beam elements. Two types of supports viz. simply supported ends and flexible end bearings, and shown in **Figs. 5.1(a)** and **5.1(b)** are considered. In **Figs. 5.1(a)** and **5.1(b)**, L is the total length, L_e is the length of one element, α_1 and α_2 are the depth of the first and second crack located at a distance L_{c1} and L_{c2}, respectively, from the left end of the shaft, $D\,(=2R,\ R$ is the radius of the shaft) is the diameter of the shaft.

Table 5.1 Temperature coefficients value for different mechanical properties of FGM [27]

Properties	Materials	C_0	C_{-1}	C_1	C_2	C_3
E (Pa)	SS	201.04×10^{9}	0	3.079×10^{-4}	-6.534×10^{-7}	0
	ZrO_2	244.27×10^{9}	0	-1.371×10^{-3}	1.214×10^{-6}	-3.681×10^{-10}
ν	SS	0.3262	0	-2.002×10^{-4}	3.797×10^{-7}	0
	ZrO_2	0.2882	0	1.133×10^{-4}	0	0
K (W/m K)	SS	15.379	0	-1.264×10^{-3}	2.092×10^{-6}	-7.223×10^{-10}
	ZrO_2	1.700	0	1.276×10^{-4}	6.648×10^{-8}	0

In the present analysis, the FG (SS/ZrO_2) rotor is modeled using twenty-five (25) equal finite elements as shown in **Figs. 5.1(a)** and **5.1(b)**. Here, the shaft diameter $D = 0.1$ m and different lengths are considered to vary the slenderness ratios (SR) of the shaft. Density for stainless steel (SS) is 8166 kg/m^3 and for zirconia (ZrO_2) is 5700 kg/m^3. **Table 5.1** shows the different temperature coefficients [27] for obtaining temperature dependent material properties at different values of temperature (T) for the FG (SS/ZrO_2) shaft. An FE code is developed based on the FE formulation of an FG shaft with two transverse cracks and is validated for its accuracy. After validating the FE formulations of the cracked FG shaft, responses of the rotor-bearing system are computed and also the effect of relative crack

sizes, locations and orientations, material gradient indices and temperature gradients on dynamic responses of the rotor system is studied.

5.3 Validations

The present formulation and the developed code are validated in three steps. In the first step, the stiffness, mass, inertia and gyroscopic matrices are validated through the determination of whirling frequencies of an un-damped rotor-disc-bearing system. In the second step, comparisons of the LFCs of the cracked rotor as a function of crack orientation angle θ with those available in published literature have been made to ensure the correct formulation of breathing transverse crack. In the last step, natural frequencies of the simply supported steel shaft with two cracks are compared with those from published works to show the correctness of the formulation for multiple cracks.

5.3.1 Whirling frequencies of a rotor-bearing system with un-damped bearings

Following the work of Friswell et al. [57], a rotor-disc-bearing system, shown in **Fig. 5.2**, is considered for validating whirling frequencies obtained from the present developed FE code. The rotor and discs are considered to be made of steel with $E = 211\ \text{GN/m}^2$, $G = 81.2\ \text{GN/m}^2$ and $\rho = 7810\ \text{kg/m}^3$. Isotropic bearings with stiffness of $1\ \text{MN/m}$ in both the directions are considered. For this system, natural frequencies have been computed and compared with those from published results of Friswell et al. [57] as listed in **Table 5.2**. It could be observed from **Table 5.2** that the forward whirling (FW) frequency and backward whirling (BW) frequency at spin speed $\Omega = 4000\ \text{rpm}$ obtained from the present analysis show excellent agreement with the published results of Friswell et al. [57], thus validating the stiffness, mass, inertia and gyroscopic matrices.

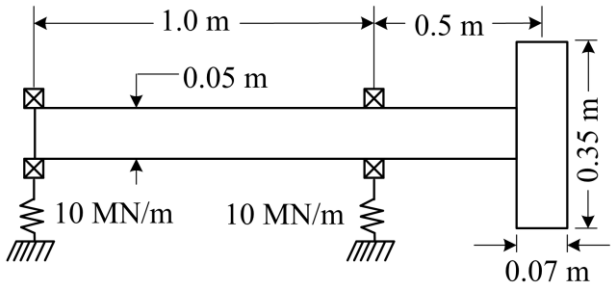

Fig. 5.2 Schematic diagram of a rotor-disc-bearing system

Table 5.2 Natural frequencies (in Hz) at $\Omega = 4000$ rpm for a rotor-bearing system

	Modes					
	1BW	1FW	2BW	2FW	3BW	3FW
Present	12.13	16.53	91.00	100.85	103.42	190.90
Friswell et al. [57]	12.13	16.54	90.08	100.94	103.09	186.88
% Error	0.00	0.06	-1.02	0.08	-0.32	-2.15

5.3.2 LFCs of a homogeneous shaft with breathing crack

Based on the formulation of rotating cracked shaft, the LFCs have been computed considering a cracked shaft element with length $L_e = 0.05$ m, diameter $D = 0.015$ m, $\alpha/R = 0.8$ and the variation of LFCs $g_{22}\{=(\kappa L_e/GA)+(L_e^3/3EI)+C_{22}^c+L_c^2C_{44}^c\}$ and $g_{33}\{=(\kappa L_e/GA)+(L_e^3/3EI)+C_{11}^c+L_c^2C_{33}^c\}$ as a function of crack orientation angle θ are shown in **Table 5.3**. Results in **Table 5.3** show an excellent agreement with the already published result of Darpe et al. [95], thus validating the computation of LFCs with the breathing crack.

Table 5.3 Variation of local flexibility coefficients g_{22} and g_{33} with a function of θ

θ (degree)	g_{22} (m/N)			g_{33} (m/N)		
	Present	Darpe et al. [95]	% Error	Present	Darpe et al. [95]	% Error
0	8.349×10^{-8}	8.290×10^{-8}	-0.711	8.382×10^{-8}	8.317×10^{-8}	-0.781
45	9.753×10^{-8}	9.635×10^{-8}	-1.224	8.469×10^{-8}	8.324×10^{-8}	-1.741
90	1.043×10^{-7}	1.029×10^{-7}	-1.360	8.725×10^{-8}	8.864×10^{-8}	-1.568
135	1.082×10^{-7}	1.069×10^{-7}	-1.227	9.116×10^{-8}	8.998×10^{-8}	-1.311
180	1.094×10^{-7}	1.089×10^{-7}	-0.459	9.464×10^{-8}	9.389×10^{-8}	-0.798

5.3.3 Effect of double cracks on natural frequencies

Here, two cracks at different locations on a simply supported steel shaft with $D = 12.5$ cm and $L = 1$ m are considered. In the present analysis, the shaft with $E = 210$ GPa, $\nu = 0.3$ and $\rho = 7800$ kg/m^3 are considered. The dimensionless frequencies of the system have been determined for $L/D = 8$, considering first crack with $\alpha_1/R = 0.2$ at $L_{c1}/L = 0.35$ and

varying the crack location and crack size of the second crack and the results are tabulated in **Table 5.4**. These results are compared with the published FE solutions of Sekhar [105] and an excellent agreement has been obtained, thus validating the multiple cracks formulation.

Table 5.4 Variation of first dimensionless natural frequencies with depth and location of second crack for $\alpha_1/R = 0.2$, $L_{c1}/L = 0.35$ and $L/D = 8$

$\frac{L_{c2}}{L}$	$\alpha_2/R = 0.2$		$\alpha_2/R = 0.4$		$\alpha_2/R = 0.6$		$\alpha_2/R = 0.8$	
	Present	Sekhar [105]	Present	Sekhar [105]	Present	Sekhar [105]	Present	Sekhar [105]
0.15	0.990	0.987	0.979	0.978	0.957	0.960	0.915	0.926
0.25	0.988	0.985	0.968	0.966	0.928	0.936	0.859	0.865
0.45	0.985	0.980	0.956	0.952	0.899	0.900	0.810	0.817
0.85	0.992	0.988	0.989	0.984	0.982	0.975	0.969	0.958

5.4 Analysis of an FG shaft with transverse breathing crack

After validating the finite element formulation, the developed FE code has been used to determine the direct and cross couple terms of LFCs for an FG (SS/ZrO_2) shaft having a transverse breathing crack behavior and also to understand the influences of the parameters such as size of crack α/R, power law gradient index k, temperature gradient ΔT and crack orientation angle θ on computing those LFCs for such an FG shaft.

5.4.1 Variation of dimensionless LFCs for an FG shaft

Determination of the direct and cross couple terms of LFCs is important to study the effect of stiffness as well as vibration characteristics for an FG (SS/ZrO_2) shaft with the temperature independent material properties and with breathing crack behavior. Since temperature dependent material properties are considered and stiffness is temperature dependent, it is important to study the effect of temperature on those LFCs and using **Eq. (3.74)** to **Eq. (3.78)** along with **Eq. (3.2)** and **Eq. (3.10)**. LFCs have been computed as dimensionless quantities such as, $\bar{C}_{11} = C_{11}/\pi E_{ss} R$, $\bar{C}_{22} = C_{22}/\pi E_{ss} R$, $\bar{C}_{33} = C_{33}/\pi E_{ss} R^3$, $\bar{C}_{34} = C_{34}/\pi E_{ss} R^3$ and $\bar{C}_{44} = C_{44}/\pi E_{ss} R^3$. Variations of those LFCs with α/R, k and ΔT have been determined for different θ and are plotted in **Figs. 5.3(a-e)** to **5.5(a-e)**.

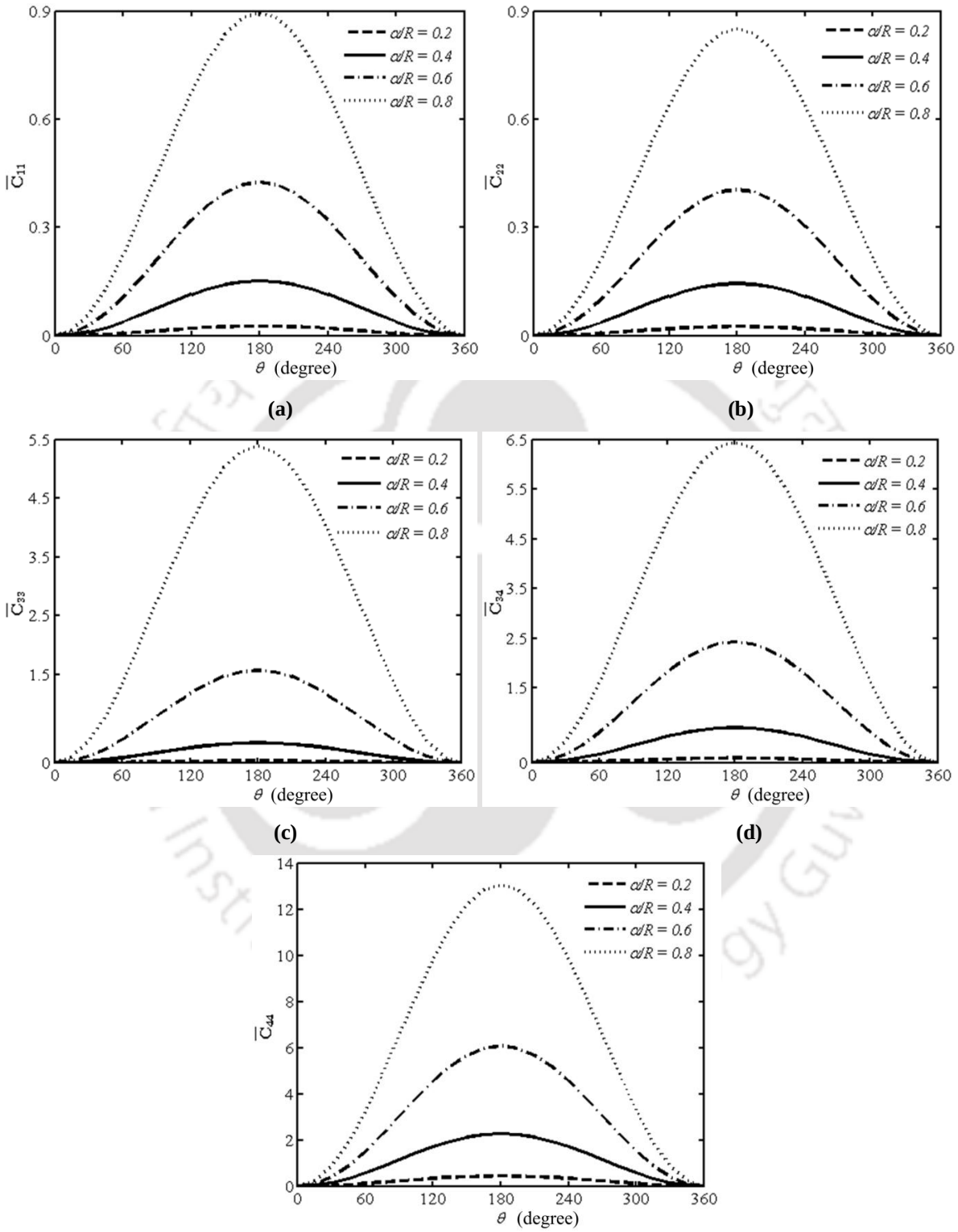

Fig. 5.3 Variation of LFCs with θ for different α/R **(a)** $\overline{C}_{11}$ **(b)** $\overline{C}_{22}$ **(c)** $\overline{C}_{33}$ **(d)** $\overline{C}_{34}$ and **(e)** $\overline{C}_{44}$

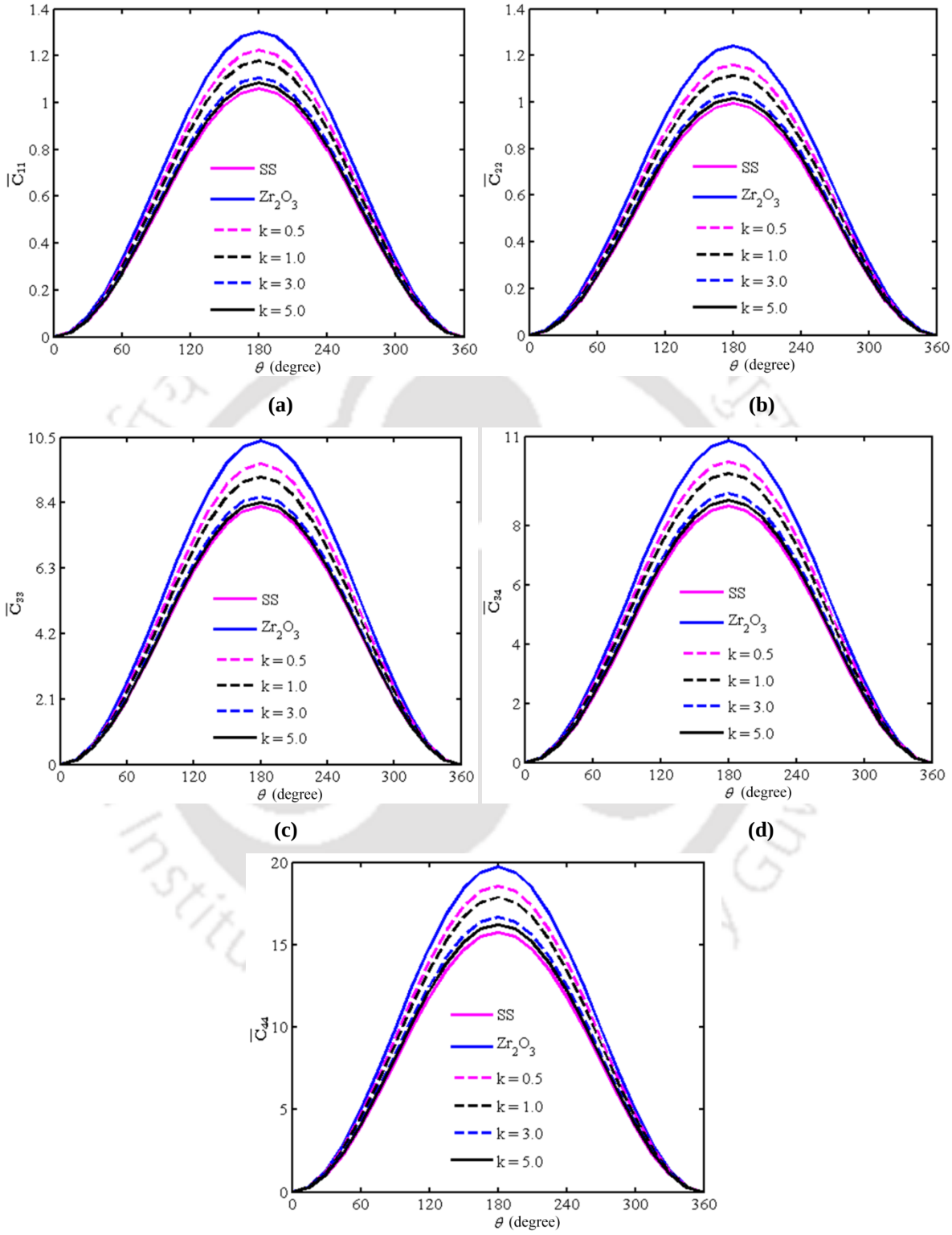

Fig. 5.4 Variation of LFCs with θ for different k **(a)** $\overline{C}_{11}$ **(b)** $\overline{C}_{22}$ **(c)** $\overline{C}_{33}$ **(d)** $\overline{C}_{34}$ and **(e)** $\overline{C}_{44}$

Figures 5.3(a) to **5.3(e)** show the variation of $\overline{C}_{11}$, $\overline{C}_{22}$, $\overline{C}_{33}$, $\overline{C}_{34}$ and $\overline{C}_{44}$ respectively as a function of θ with α/R for $k=0.5$ and $\Delta T=0$ K. As shown in these figures the dimensionless LFCs increase with the increase in α/R and they increase in magnitude as the crack gradually opens. It could also be observed that the increase in LFCs with α/R is relatively more pronounced for $\overline{C}_{34}$ and $\overline{C}_{44}$. Similarly, increase in LFCs with θ is more pronounced for larger α/R.

Figures 5.4(a) to **5.4(e)** show the variation of $\overline{C}_{11}$, $\overline{C}_{22}$, $\overline{C}_{33}$, $\overline{C}_{34}$ and $\overline{C}_{44}$ as a function of θ with different k for $\alpha/R=0.9$ and $\Delta T=0$ K. As shown in these figures the dimensionless LFCs increase with the decrease in k as metallic content decreases in the FGM and they increase in magnitude as the crack gradually opens. It could also be observed that the increase in LFCs with k is relatively more pronounced for $\overline{C}_{34}$ and $\overline{C}_{44}$. Similarly increase in LFCs with θ is more pronounced for lower values of k.

Figures 5.5(a) to **5.5(e)** show the variation of $\overline{C}_{11}$, $\overline{C}_{22}$, $\overline{C}_{33}$, $\overline{C}_{34}$ and $\overline{C}_{44}$ as a function of θ with different ΔT for $k=5.0$ and $\alpha/R=0.8$. As shown in these figures, the dimensionless LFCs increase with the increase in ΔT as material becomes softer at higher temperature and they increase in magnitude as the crack gradually opens. It could also be observed that the increase in LFCs with ΔT is relatively more pronounced for $\overline{C}_{34}$ and $\overline{C}_{44}$. Similarly, increase in LFCs with θ is more pronounced for higher values of ΔT.

5.5 Analysis of non-rotating FG shaft without/with cracks

In the present analysis, free vibration characteristics of a non-rotating simply supported without/with cracked shaft made of FGM (SS/ZrO_2) has been presented without considering the bearing stiffness and damping to understand the influences of the different important parameters such as slenderness ratio L/D, power law gradient index k, temperature gradient ΔT, relative location of second crack L_{c2}/L, relative size of second crack α_2/R, and orientation of second crack θ_2 on free vibration response of the FG shaft.

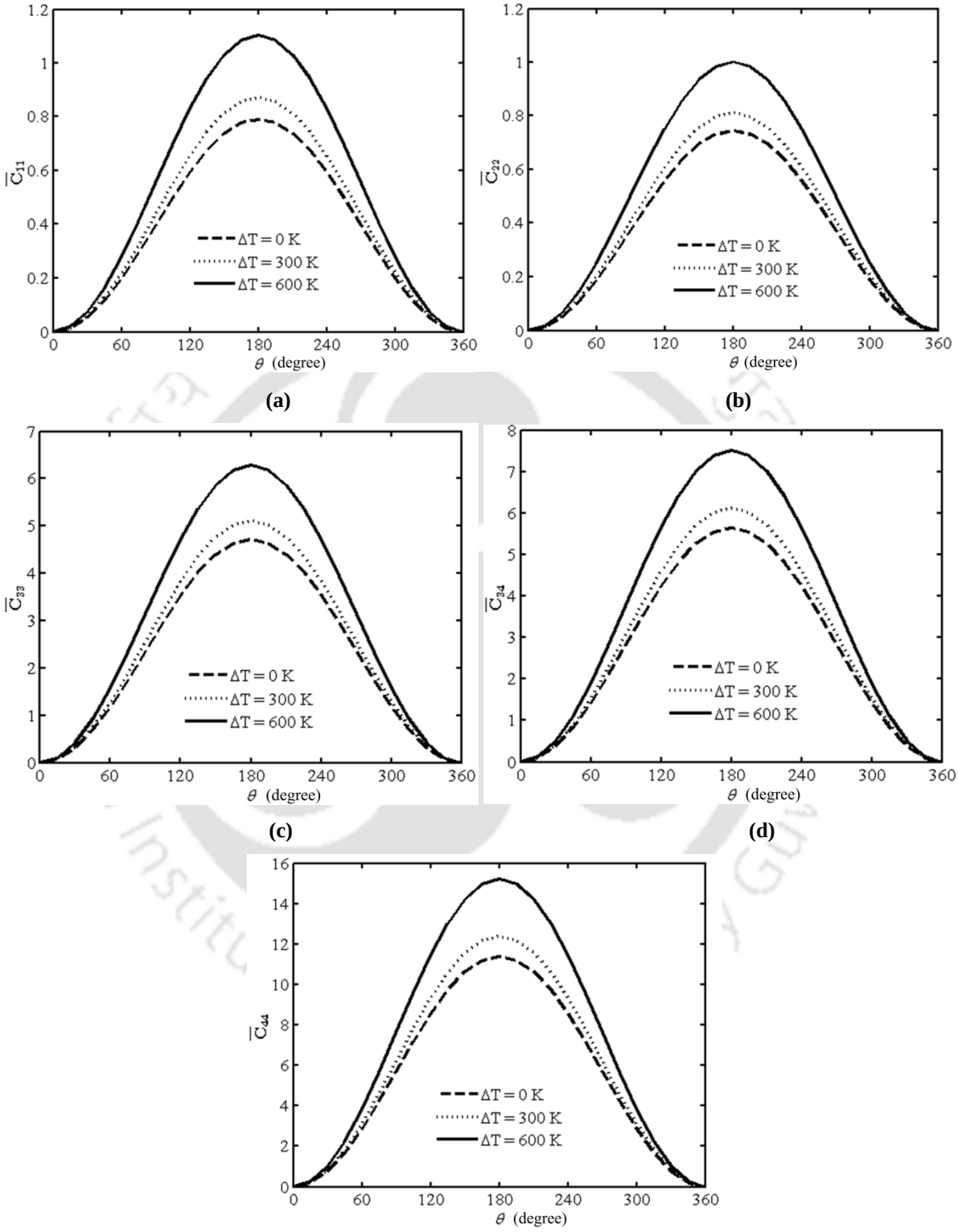

Fig. 5.5 Variation of LFCs with θ for different ΔT **(a)** $\overline{C}_{11}$ **(b)** $\overline{C}_{22}$ **(c)** $\overline{C}_{33}$ **(d)** $\overline{C}_{34}$ and **(e)** $\overline{C}_{44}$

Table 5.5 Variation of natural frequency (in rad/s) for an uncracked FG shaft with ΔT and k

ΔT(K)	$\omega_{1V,1H}$	$\omega_{1V,1H}$	$\omega_{1V,1H}$	$\omega_{1V,1H}$	$\omega_{1V,1H}$	$\omega_{1V,1H}$	$\omega_{1V,1H}$	$\omega_{1V,1H}$
	$k=0.0$	$k=0.5$	$k=1.0$	$k=3.0$	$k=5.0$	$k=10.0$	$k=50.0$	$k=200.0$
0	855.79	833.90	823.55	809.54	805.36	801.86	799.56	799.54
300	754.59	757.33	758.60	760.28	760.78	761.19	761.46	761.47
600	715.62	701.37	694.65	685.60	682.91	680.66	679.18	679.17

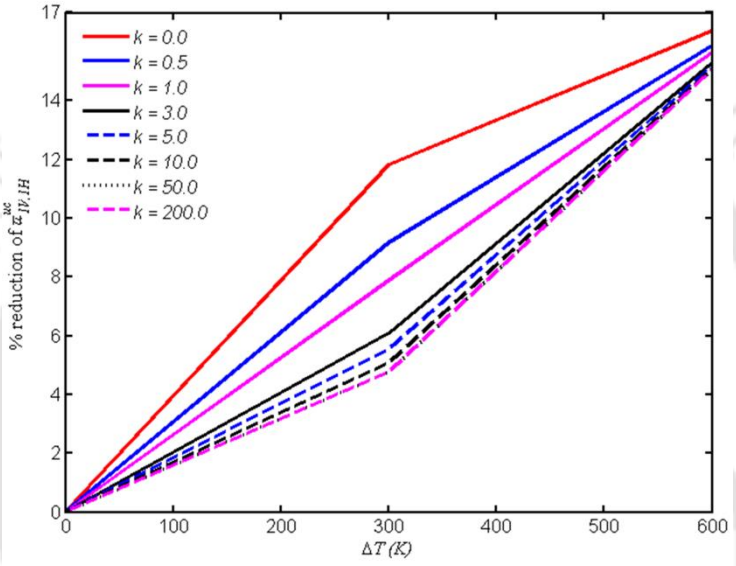

Fig. 5.6 Percentage reduction in fundamental frequency for an uncracked FG shaft with ΔT and k

5.5.1 Effect of k and ΔT on natural frequency for an FG uncracked shaft

Fundamental frequencies associated with vertical plane ω_{1V} and horizontal plane ω_{1H} are obtained for a non-rotating simply supported uncracked FG (SS/ZrO_2) shaft for $L/D=12.5$ and influences of ΔT and k are studied. The reduction in fundamental frequencies have been defined as ϖ_i ($\%\ \varpi_i=(1-\omega_i^{\Delta T=0\,\mathrm{K},\ 300\,\mathrm{K},\ 600\,\mathrm{K}}/\omega_i^{\Delta T=0\,\mathrm{K}})\times 100$). The results are tabulated in **Table 5.5** and shown in **Fig. 5.6**. **Table 5.5** show that ϖ_i decreases with the increase in k due to the increase in metal content in the FG shaft. In addition, ϖ_i also decreases with the increase in ΔT as the material becomes softer at higher values of ΔT. It is observed from **Fig. 5.6** that the percentage reduction in natural frequencies increases with the increase in ΔT. It could also be observed that even though at lower value of ΔT, there has been significant reduction in natural frequencies with the increase in k, but for higher values of

ΔT, the reduction is not much with the increase in k. Therefore, in a high temperature application, it is possible to choose k such that the reduction in ϖ_i with temperature will be minimum while keeping sufficient material at the outer layer for providing the required temperature resistance.

5.5.2 Effect of k and ΔT on natural frequency for an FG shaft with a single transverse crack

Fundamental frequencies associated vertical plane ω_{1V} and horizontal plane ω_{1H} are computed for a non-rotating simply supported FG (SS/ZrO_2) shaft with a centrally located fully open transverse crack for $L/D = 12.5$, $\alpha/R = 0.8$ and the influences of ΔT and k have been studied. The reduction in natural frequencies has been defined as ϖ_i $\{\% \varpi_i = (1-\omega_i^c/\omega_i^{uc})\times 100\}$. The results are tabulated in **Table 5.6** and also shown in **Figs. 5.7(a)** and **5.7(b)**. Results in **Table 5.6** show that the fundamental frequencies (ω_{1V} and ω_{1H}) decrease with the increase in k due to increase in metal content in the FG shaft. it is also observed that with the increase in ΔT fundamental frequencies decreases as the material become softer at higher values of ΔT. **Figs. 5.7(a)** and **5.7(b)** show that for the present case the reduction in fundamental frequencies decreases as k decreases, reaches a minimum at $k = 5.0$ and with further increase in k, reduction in fundamental frequencies increases. Therefore, in designing FG shaft, depending upon the applications, k could be chosen in such a way that the overall stiffness of the shaft and the temperature resistance could be kept within the desired limit.

Table 5.6 Variation of natural frequency (in rad/s) for a centrally located cracked FG shaft with ΔT and k

k	$\Delta T = 0$ K		$\Delta T = 300$ K		$\Delta T = 600$ K	
	ω_{1V}	ω_{1H}	ω_{1V}	ω_{1H}	ω_{1V}	ω_{1H}
0.5	420.87	732.24	383.73	666.31	356.81	617.52
1.0	417.10	724.07	386.46	668.73	355.40	612.81
3.0	413.08	713.03	392.00	672.05	354.83	606.55
5.0	411.56	709.40	393.16	672.52	354.36	604.35
10.0	409.37	705.92	392.66	672.24	352.98	602.06
50.0	407.06	703.28	390.97	671.50	351.14	600.19

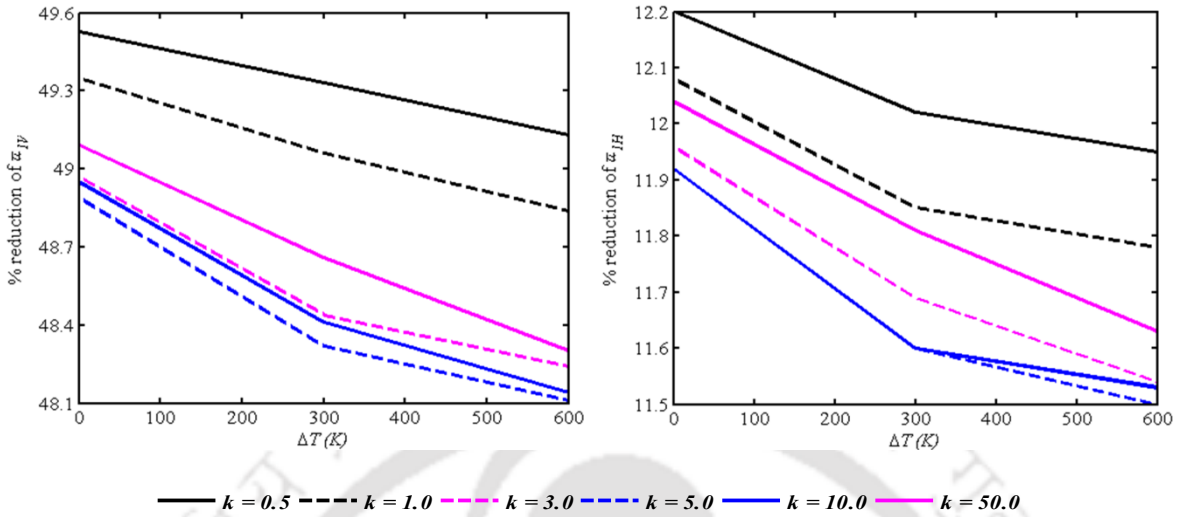

(a) (b)

Fig. 5.7 Percentage reduction of natural frequency for a centrally located cracked FG shaft with ΔT and k (a) vertical plane and (b) horizontal plane

5.5.3 Effect of L_{c2}/L on natural frequency for an FG shaft with two transverse cracks

Fundamental frequencies associated with vertical plane ω_{1V} and horizontal plane ω_{1H} are obtained for a simply supported FG (SS/ZrO_2) shaft having two fully open transverse cracks ($\theta_1 = \theta_2 = 180°$) for $L/D = 12.5$, $\alpha_1/R = \alpha_2/R = 0.8$, $L_{c1}/L = 0.34$, while location of the second crack (L_{c2}/L) is varied. The influences of k and ΔT on free vibration responses have been studied and the results are plotted in **Figs. 5.8(a-b)** to **Figs. 5.9(a-b)**. The reductions in the natural frequencies have been defined as ϖ_i $\{\% \varpi_i = (1-\omega_i^c/\omega_i^{uc}) \times 100\}$.

The variations of percentage reduction in the frequencies ϖ_i of the cracked FG shaft, as a function of k and L_{c2}/L for $\Delta T = 0$ K are computed and are shown in **Figs. 5.8(a)** and **5.8(b)**. For an un-cracked FG shaft, natural frequency (in rad/s) associated with vertical and horizontal planes are same, and they are 855.79 for $k = 0.0$, 833.90 for $k = 0.5$, 823.55 for $k = 1.0$, 805.36 for $k = 5.0$, and 801.86 for $k = 10.0$. **Figures 5.8(a)** and **5.8(b)** show that the percentage reduction in ϖ_i decreases with the increase in k due to increase in the metal content in the FG shaft, reaches minimum at $k = 5.0$ and then again

increases. The maximum percentage reduction in ϖ_i occurs while two cracks are located close to middle section of the shaft, and the highest changes in ϖ_i occurs in the vertical plane due to crack orientations. Therefore in FG shaft, power law gradient index k influences the reduction in natural frequency and k may be chosen to keep the overall stiffness of the shaft within the desired limit.

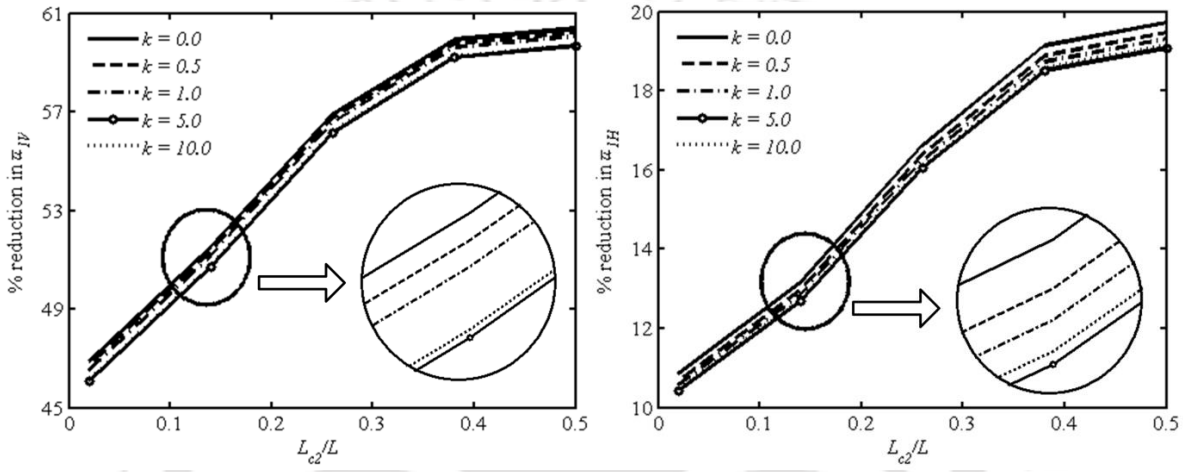

(a) (b)

Fig. 5.8 Percentage reduction of natural frequency for a FG shaft with double cracks with k and L_{c2}/L (a) vertical plane and (b) horizontal plane

Figures 5.9(a) and **5.9(b)** show the percentage reductions in the natural frequencies ϖ_i of the cracked FG shaft, as a function of ΔT and L_{c2}/L for $k = 5.0$, where natural frequency (in rad/s) associated with vertical and horizontal planes are same for an un-cracked FG shaft, and they are 805.36 for $\Delta T = 0$ K, 779.12 for $\Delta T = 300$ K, 740.30 for $\Delta T = 600$ K. **Figures 5.9(a)** and **5.9(b)** show the percentage reduction in natural frequencies ϖ_i decrease with increase ΔT as the material become softer at higher values of ΔT, and the maximum reduction in ϖ_i occurs while two cracks are located close to middle section of the shaft, and the reductions in ϖ_i is much higher in the vertical plane due to crack orientations and self-weight of the shaft.

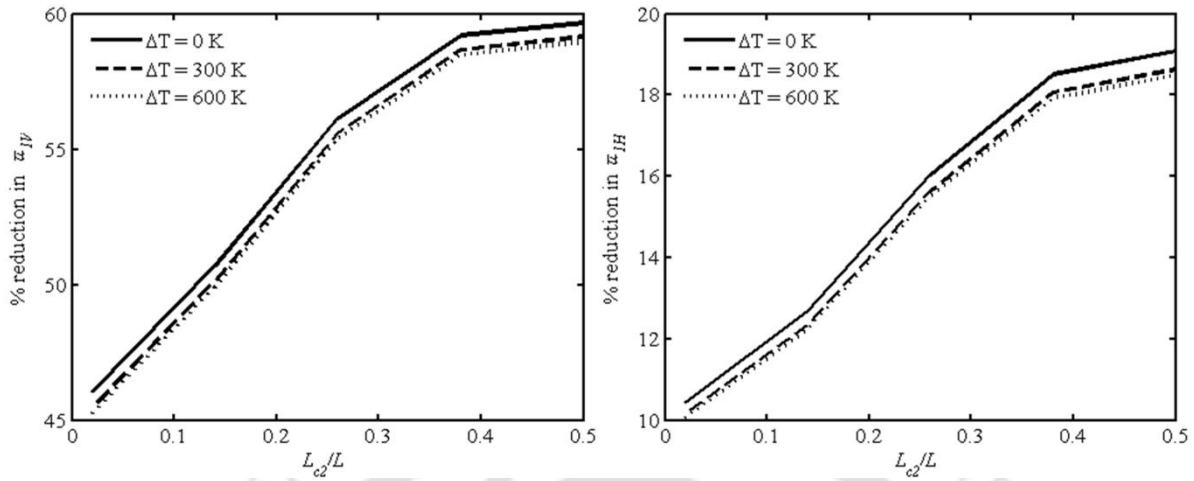

(a) (b)

Fig. 5.9 Percentage reduction of natural frequency for a FG shaft with double cracks with ΔT and L_{c2}/L (a) vertical plane and (b) horizontal plane

5.5.4 Effect of θ_2 on natural frequency for an FG shaft with two transverse cracks

The fundamental frequencies associated with vertical plane ω_{1V} and horizontal plane ω_{1H} are obtained for the FG (SS/ZrO_2) shaft having two transverse cracks with $\alpha_1/R = \alpha_2/R = 0.8,\ L_{c1}/L = 0.34,\ L_{c2}/L = 0.5,$ and the first crack is considered always open ($\theta_1 = 180°$), while the orientation of the second crack (θ_2) is varied and the influences of $L/D,\ k$ and ΔT on the free vibration response has been studied and the results are plotted in **Figs. 5.10(a-b)** to **Figs. 5.12(a-b)**.

Figures 5.10(a) and **5.10(b)** show the percentage reductions in the natural frequencies ϖ_i of the cracked FG shaft, as a function of L/D and θ_2 for $k = 5.0,\ \Delta T = 0$ K, where natural frequency (in rad/s) associated with vertical and horizontal planes for an un-cracked FG shaft, are 805.36 for $L/D = 12.5,$ 1140.45 for $L/D = 10.5,$ and 1737.74 for $L/D = 8.5$. **Figures 5.10(a)** and **5.10(b)** show that the changes in ϖ_i are appreciable in the case of cracked FG shaft having the low L/D, and maximum reduction in ϖ_i occurs while two cracks are fully open, and the highest changes in ϖ_i have occurred in the vertical plane.

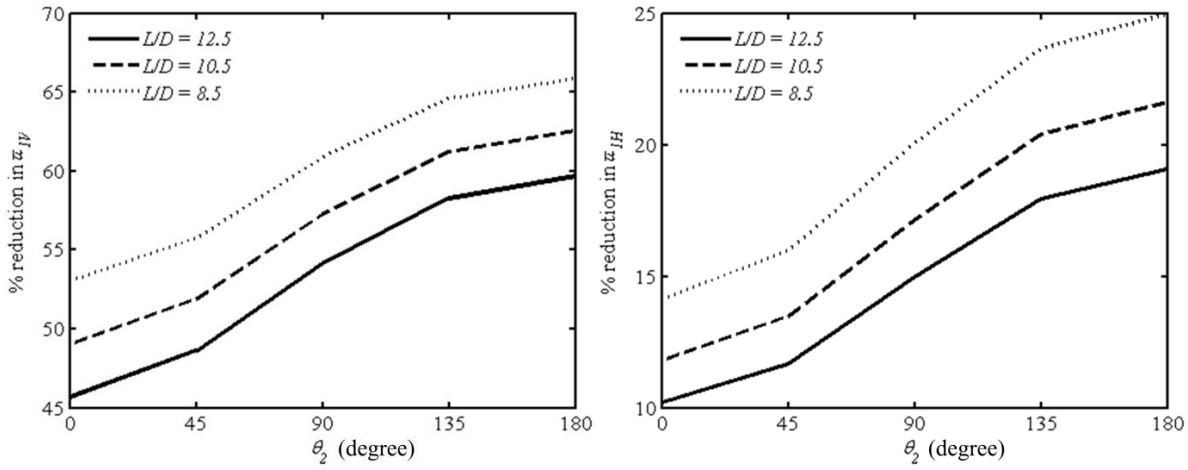

Fig. 5.10 Percentage reduction of natural frequency for a FG shaft with double cracks with L/D and θ_2 for $k = 5.0,\ \Delta T = 0$ K, $\theta_1 = 180°$ (a) vertical plane and (b) horizontal plane

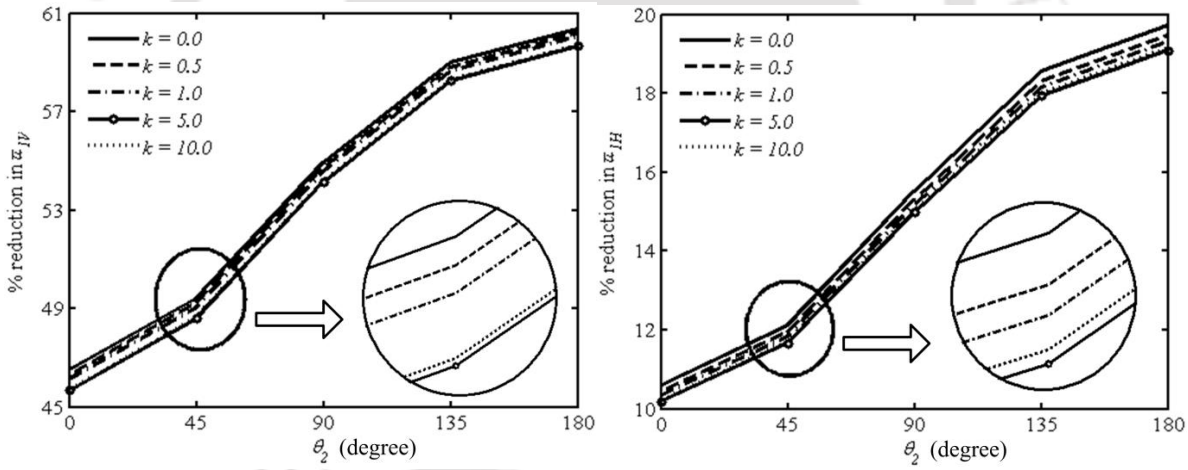

Fig. 5.11 Percentage reduction of natural frequency for a FG shaft with double cracks with k and θ_2 for $L/D = 12.5,\ \Delta T = 0$ K, $\theta_1 = 180°$ (a) vertical plane and (b) horizontal plane

Figures 5.11(a) and **5.11(b)** show the percentage reduction in natural frequencies ϖ_i of the FG cracked shaft with different values of k and θ_2, for $L/D = 12.5$ and $\Delta T = 0$ K. **Figures 5.11(a)** and **5.11(b)** show that the percentage reduction in natural frequencies ϖ_i decreases with the increase in k due to increase in the metal content in the FG shaft and the minimum reduction in ϖ_i in this case is observe for $k = 5.0$. Also the percentage reduction

in natural frequencies ω_i decreases with the increase in crack orientation θ_2 and the maximum reduction occurs while two cracks are fully open, and also the highest reduction in ϖ_i has occurred in the vertical plane due to crack orientations.

Figures 5.12(a) and **5.12(b)** show the percentage reduction in natural frequencies ϖ_i of the FG cracked shaft with different values of ΔT and θ_2, for $L/D = 12.5$ and $k = 5.0$. **Figures 5.12(a)** and **5.12(b)** show that the percentage reduction in natural frequencies ϖ_i decreases with the increase in ΔT in the FG shaft and the maximum reduction occurs while two cracks are fully open. Also the highest reductions in ϖ_i is observed to occur in the vertical plane. It is observed from these figures that the percentage reduction in ϖ_i is higher at lower ΔT even though the difference is not significant. However, the increase in percentage reduction in ϖ_i with increasing relative orientation of the second crack is pronounced and as expected it is highest when the two cracks are in phase.

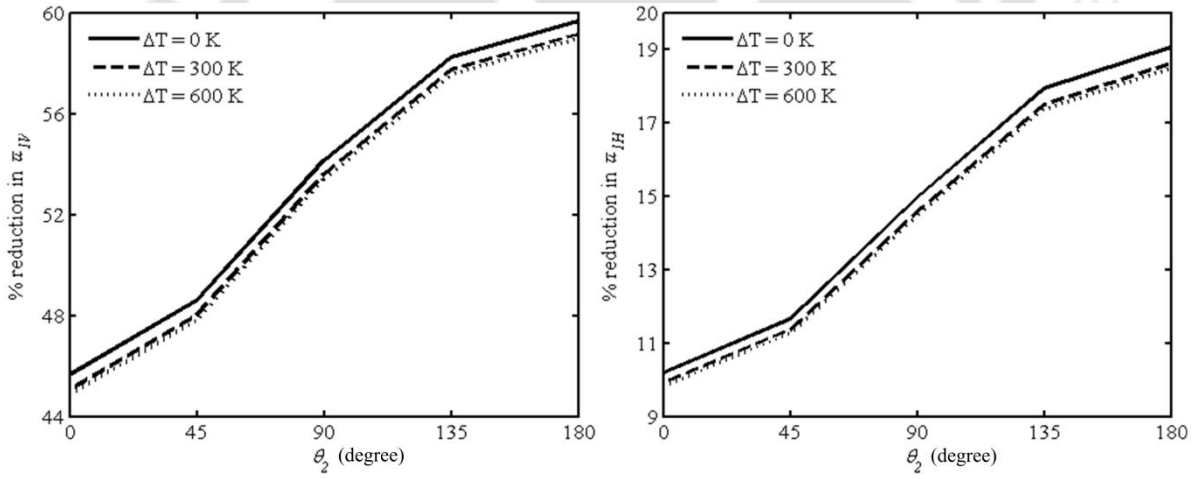

(a) (b)

Fig. 5.12 Percentage reduction of natural frequency for a FG shaft with double cracks with ΔT and θ_2 for $L/D = 12.5,\ k = 5.0,\ \theta_1 = 180°$ (a) vertical plane and (b) horizontal plane

The fundamental frequencies are obtained for the FG (SS/ZrO_2) shaft having two transverse cracks with $L/D = 12.5,\ L_{c1}/L = 0.34,\ L_{c2}/L = 0.5,\ \alpha_1/R = 0.8,\ k = 5.0,$

$\Delta T = 0$ K, and first crack is always open ($\theta_1 = 180°$), while the orientation of the second crack (θ_2) is varied and the influence of depth of second crack α_2/R on the vibration response has been studied and the results are plotted in **Figs. 5.13(a)** and **5.13(b)**. **Figures 5.13(a)** and **5.13(b)** show that the percentage reductions in ϖ_i increases with the increase in α_2/R and θ_2, and highest changes in ϖ_i observed for larger crack size and when both the cracks are in fully open ($\theta_1 = \theta_2 = 180°$) and the reduction is more significant in the vertical plane.

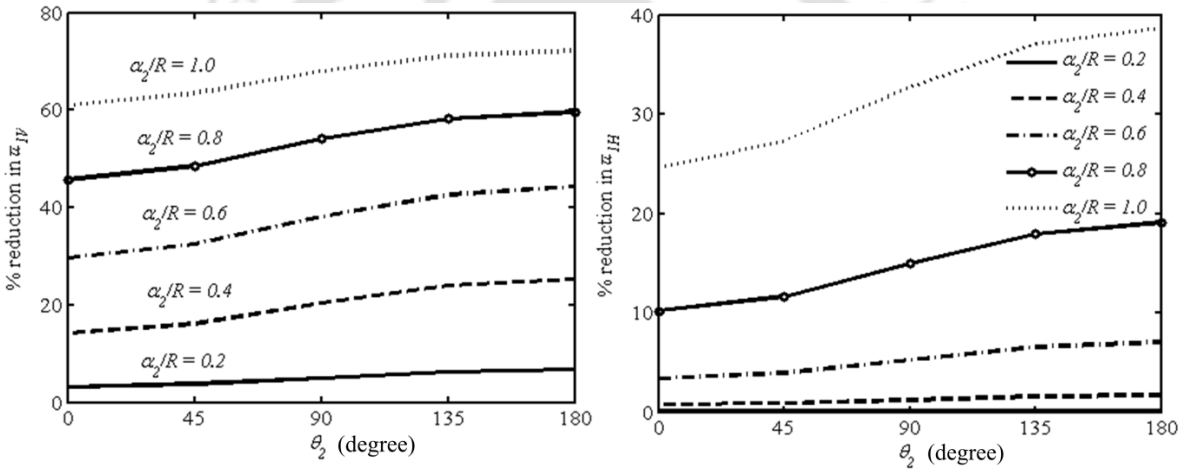

(a) (b)

Fig. 5.13 Percentage reduction of natural frequency for a FG shaft with double cracks with α_2/R and θ_2 for $k = 5.0$, $\Delta T = 0$ K, $\theta_1 = 180°$ (a) vertical plane and (b) horizontal plane

The fundamental frequencies are computed for the FG (SS/ZrO_2) shaft having two transverse cracks with the $L/D = 12.5$, $L_{c1}/L = 0.34$, $\alpha_1/R = \alpha_2/R = 0.8$, $k = 5.0$, $\Delta T = 0$ K, and first crack is always open ($\theta_1 = 180°$), while orientation of the second crack (θ_2) is varied. Also, the influence of second crack location L_{c2}/L has been studied and the results are shown in **Figs. 5.14(a)** and **5.14(b)**. **Figures 5.14(a)** and **5.14(b)** show that the percentage reduction in ϖ_i increases with the increase in L_{c2}/L and θ_2, and the highest changes in ϖ_i is observed when both the cracks are located very close to each other at the

middle of the shaft and are in fully open condition. The reductions in ϖ_i is more significant in the vertical plane.

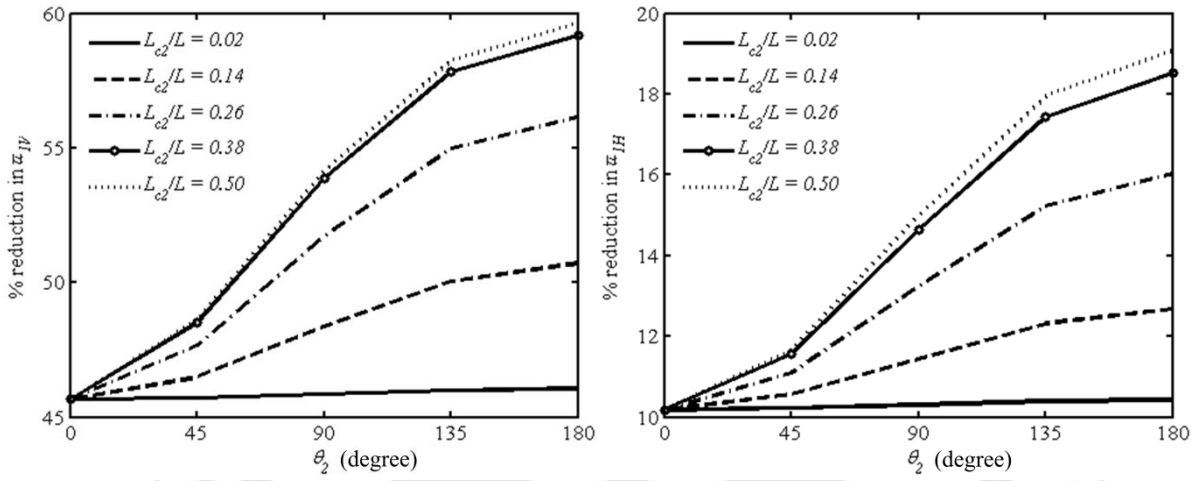

(a) (b)

Fig. 5.14 Percentage reduction of natural frequency for a FG shaft with double cracks with L_{c2}/L and θ_2 for $k = 5.0,\ \Delta T = 0$ K, $\theta_1 = 180°$ (a) vertical plane and (b) horizontal plane

5.6 Analysis of a rotor-bearing system having an FG shaft with two transverse breathing cracks

In the present analysis, transverse vibration characteristics such as whirling frequencies and critical speeds of a rotor-bearing system with a cracked FG (SS/ZrO_2) shaft have been computed by considering the undamped bearing stiffness to understand the influences of important parameters such as relative location of second crack L_{c2}/L, power law gradient index k and temperature gradient ΔT on the dynamic characteristics of such FG system.

5.6.1 Influences of L_{c2}/L, k and ΔT with θ_2 on whirling frequencies

The effects of relative locations and orientations of cracks on the dynamic characteristics such as fundamental frequencies of both forward whirling (FW) and backward whirling (BW) have been examined for the rotor-bearing system with an FG (SS/ZrO_2) shaft having two transverse breathing cracks. The FG (SS/ZrO_2) rotor is supported by identical undamped isotropic bearing with the bearing stiffness coefficients,

$K_{vv}^{b} = K_{ww}^{b} = 1.7513\times10^{7}$ N/m and $K_{vw}^{b} = K_{wv}^{b} = 0$. The FG shaft is considered with $L/D = 12.5$, $\alpha_1/R = \alpha_2/R = 0.8$, $L_{c1}/L = 0.34$, $\theta_1 = 180°$, and results are obtained for different L_{c2}/L, k, ΔT and θ_2 and tabulated in **Tables 5.7** to **5.10** for the spin speeds $\Omega = 418.88$ rad/s (4000 rpm) and $\Omega = 1047.20$ rad/s (10000 rpm).

Table 5.7 Whirling frequency (in rad/s) of an uncracked FG shaft system

ω_i	$\Omega = 418.88$ rad/s, $\Delta T = 0$ K				$\Omega = 1047.20$ rad/s, $\Delta T = 0$ K			
	$k = 0.0$	$k = 0.5$	$k = 1.0$	$k = 10.0$	$k = 0.0$	$k = 0.5$	$k = 1.0$	$k = 10.0$
1BW	241.84	228.47	221.97	207.82	241.57	228.19	221.72	207.56
1FW	242.12	228.79	222.25	207.92	241.84	228.47	221.97	207.92
ω_i	$\Omega = 418.88$ rad/s, $k = 5.0$			$\Omega = 1047.20$ rad/s, $k = 5.0$				
	$\Delta T = 0$ K	$\Delta T = 300$ K	$\Delta T = 600$ K	$\Delta T = 0$ K	$\Delta T = 300$ K	$\Delta T = 600$ K		
1BW	210.06	209.52	207.94	209.91	209.26	207.75		
1FW	210.23	209.78	208.10	210.24	209.52	207.95		

The FW and BW frequencies of the FG uncracked shaft are shown in **Table 5.7** and are used for calculating the percentage reduction in the fundamental FW and BW frequencies. Results in **Table 5.8** shows the percentage reduction in the fundamental FW and BW frequencies with spin speed (Ω) of the FG rotor bearing system with breathing transverse cracks, for $k = 5.0$, $\Delta T = 0$ K with different L_{c2}/L and θ_2. For a given crack configuration, results in **Table 5.8** show that the percentage reduction in the FW and BW frequencies increase with the increase in L_{c2}/L and θ_2, and are more pronounced when the two cracks are located close to the middle section of the shaft and are fully open. Results also show that for higher values of Ω the reductions in whirling frequencies are less.

Table 5.9 shows the percentage reduction in FW and BW frequencies with spin speed Ω of the same rotor-bearing system with breathing transverse cracks, for $L_{c2}/L = 0.5$, $\Delta T = 0$ K with different k and θ_2, where the fundamental FW and BW frequencies of the FG un-cracked shaft are shown in **Table 5.7**. Results in **Table 5.9** shows that reductions in FW and BW frequencies decrease with the increase in k due to transition of the shaft from ZrO_2, which has lower elastic modulus and lower density compared to

those of SS. **Table 5.9** also shows that the reduction in FW and BW frequencies increase with the increase in θ_2. It also shows that for higher values of Ω, the reductions in whirling frequencies are lower. Therefore, while designing such an FG shaft for a specific application, it is possible to choose power law index in such a way that in the event of generation of multiple transverse cracks, the reduction in whirl frequency will be the minimum.

Table 5.8 Percentage reduction in whirling frequency with L_{c2}/L and θ_2 for a FG shaft system

L_{c2}/L	ω_i	$\Omega = 418.88$ rad/s					$\Omega = 1047.20$ rad/s				
		$\theta_2 = 0°$	$\theta_2 = 45°$	$\theta_2 = 90°$	$\theta_2 = 135°$	$\theta_2 = 180°$	$\theta_2 = 0°$	$\theta_2 = 45°$	$\theta_2 = 90°$	$\theta_2 = 135°$	$\theta_2 = 180°$
0.02	1BW	5.90	5.92	5.98	6.03	6.06	5.83	5.85	5.85	5.95	5.99
	1FW	0.65	0.65	0.60	0.69	0.68	0.65	0.63	0.67	0.68	0.68
0.14	1BW	5.90	6.17	6.83	7.47	7.74	5.83	6.10	6.76	7.41	7.67
	1FW	0.65	0.68	0.76	0.84	0.87	0.65	0.66	0.76	0.84	0.87
0.26	1BW	5.90	6.52	7.99	9.42	10.00	5.83	6.46	7.93	9.33	9.93
	1FW	0.65	0.71	0.86	1.06	1.14	0.65	0.72	0.90	1.07	1.14
0.38	1BW	5.90	6.78	8.85	10.82	11.61	5.83	6.72	8.78	10.76	11.55
	1FW	0.65	0.75	0.99	1.24	1.34	0.65	0.75	1.00	1.25	1.35
0.50	1BW	5.90	6.84	9.05	11.14	11.97	5.83	6.78	8.98	11.08	11.92
	1FW	0.65	0.76	1.02	1.29	1.40	0.65	0.76	1.02	1.29	1.40

Table 5.9 Percentage reduction in whirling frequency with k and θ_2 for a FG shaft system

k	ω_i	$\Omega = 418.88$ rad/s					$\Omega = 1047.20$ rad/s				
		$\theta_2 = 0°$	$\theta_2 = 45°$	$\theta_2 = 90°$	$\theta_2 = 135°$	$\theta_2 = 180°$	$\theta_2 = 0°$	$\theta_2 = 45°$	$\theta_2 = 90°$	$\theta_2 = 135°$	$\theta_2 = 180°$
0.0	1BW	7.21	8.37	10.95	13.40	14.35	7.14	8.26	10.85	13.29	14.26
	1FW	0.91	1.05	1.38	1.70	1.83	0.80	0.93	1.26	1.58	1.72
0.5	1BW	6.77	7.82	10.27	12.58	13.49	6.63	7.71	10.16	12.47	13.39
	1FW	0.87	1.00	1.30	1.58	1.72	0.74	0.86	1.16	1.46	1.58
1.0	1BW	6.50	7.52	9.88	12.12	13.01	6.40	7.41	9.78	12.02	12.92
	1FW	0.83	0.95	1.24	1.52	1.64	0.70	0.82	1.11	1.40	1.50
5.0	1BW	5.90	6.84	9.05	11.14	11.97	5.83	6.78	8.98	11.08	11.92
	1FW	0.65	0.76	1.02	1.29	1.40	0.65	0.76	1.02	1.29	1.40
10.0	1BW	5.87	6.81	8.99	11.06	11.89	5.75	6.69	8.87	10.95	11.87
	1FW	0.62	0.75	1.01	1.28	1.39	0.64	0.75	1.01	1.27	1.39

Table 5.10 shows the percentage reduction in fundamental FW and BW frequencies with spin speed Ω of the same rotor bearing system having the FG shaft with transverse breathing cracks, for $L_{c2}/L = 0.5,\ k = 5.0$ and different ΔT and θ_2. The FW and BW frequencies of the FG un-cracked shaft are shown in **Table 5.7**. Results in **Table 5.10** show that the reductions in FW and BW frequencies increase with the increase in ΔT due to decrease in Young's modulus E with temperature rise, and also increase with the increase in θ_2 due to decrease in stiffness. This also shows that for higher values of Ω the reduction in whirling frequencies is less for the same θ_2.

Table 5.10 Percentage reduction in whirling frequency with ΔT and θ_2 for a FG shaft system

ΔT	ω_i	$\Omega = 418.88$ rad/s					$\Omega = 1047.20$ rad/s				
		$\theta_2 = 0°$	$\theta_2 = 45°$	$\theta_2 = 90°$	$\theta_2 = 135°$	$\theta_2 = 180°$	$\theta_2 = 0°$	$\theta_2 = 45°$	$\theta_2 = 90°$	$\theta_2 = 135°$	$\theta_2 = 180°$
0	1BW	5.90	6.84	9.05	11.14	11.97	5.83	6.78	8.98	11.08	11.92
	1FW	0.65	0.76	1.02	1.29	1.40	0.65	0.76	1.02	1.29	1.40
300	1BW	6.44	7.45	9.79	12.02	12.92	6.32	7.33	9.68	11.90	12.79
	1FW	0.82	0.95	1.23	1.52	1.64	0.70	0.82	1.11	1.37	1.51
600	1BW	7.72	8.90	11.63	14.18	15.19	7.63	8.82	11.55	14.11	15.11
	1FW	0.93	1.07	1.42	1.77	1.91	0.86	0.96	1.35	1.72	1.84

5.6.2 Influences of k and θ_2 on critical speeds

In order to understand the influence of power law gradient index k on FG (SS/ZrO_2) rotor, percentage reduction in critical speeds have been computed using the present FE code for the same rotor-bearing system having two transverse breathing cracks for $L/D = 12.5,\ L_{c1}/L = 0.34,\ L_{c2}/L = 0.5,\ \alpha_1/R = \alpha_2/R = 0.8,\ \Delta T = 0$ K, $\theta_1 = 180°$ with different values of k and θ_2, and results are tabulated in **Table 5.11**. Dimensions and material properties for the FG shaft along with the identical undamped isotropic bearing parameters considered are same as stated earlier. It could be seen form **Table 5.11** that the percentage reductions in critical speeds decrease with the increase in k due to transition of the shaft from ZrO_2, which has lower elastic modulus and lower density compared to those of SS. It could be also

seen form **Table 5.11** that the percentage reductions in critical speeds decrease with the increase θ_2 due to decrease in stiffness.

Table 5.11 Percentage reduction in critical speed with k and θ_2 for a FG shaft system

k	ϖ_i	$\theta_2 = 0°$	$\theta_2 = 45°$	$\theta_2 = 90°$	$\theta_2 = 135°$	$\theta_2 = 180°$
0.0	1BW	7.23	8.36	10.95	13.38	14.34
	1FW	0.82	0.96	1.29	1.61	1.74
0.5	1BW	6.77	7.82	10.26	12.58	13.50
	1FW	0.78	0.90	1.20	1.50	1.63
1.0	1BW	6.50	7.51	9.89	12.13	13.01
	1FW	0.73	0.86	1.14	1.43	1.55
5.0	1BW	5.97	6.90	9.08	11.21	12.04
	1FW	0.65	0.76	1.03	1.29	1.40
10.0	1BW	5.87	6.82	9.08	11.07	11.90
	1FW	0.64	0.75	1.02	1.28	1.39

5.7 Summary

A finite element formulation has been developed to study the dynamic behavior of a rotor-bearing system with an FG shaft having multiple transverse breathing cracks. The FG (SS/ZrO_2) rotor is supported by identical undamped isotropic bearing with the bearing stiffness coefficients, $K_{vv}^b = K_{ww}^b = 1.7513 \times 10^7$ N/m and $K_{vw}^b = K_{wv}^b = 0$. LFCs for cracked FG shaft are determined considering temperature dependent material properties. Developed FE model has been validated and used to study the influence of power-law gradient index, temperature gradient, relative locations, depth and orientations of the cracks and the slenderness of the FG shaft on the dynamic behavior of the cracked FG shaft in a rotor bearing system. Some of the important conclusions drawn from the present study are

- For transverse breathing cracks in a spinning FG shaft, the local flexible coefficients and hence the reduction in fundamental frequencies, besides being functions of size, location and orientation of crack, temperature gradient are also influenced by the power law gradient index of the FGM used.

- In an FG shaft, extent of reduction in natural whirling frequencies (FW and BW) and increase in critical speeds due to the presence of multiple transverse cracks besides being affected by relative orientations, locations and size of the cracks are also decided by the power law gradient index of the FGM used. Therefore, the power law gradient index could be suitably chosen in the design of such shafts so that in the event of multiple transverse cracks appearing in the FG shaft, the reduction in stiffness could be minimized.
- In the event of detecting multiple cracks in a spinning FG shaft, it is possible to determine the whirling frequencies and critical speeds of the shaft for deciding the safety of the shaft during operation.
- The present formulation will be useful in arriving at an optimum gradation parameter of FG to be recommended to the manufacturer so to maximize the performance of an FG shaft especially in the event of multiple transverse cracks appearing on the shaft surface during service.

CHAPTER 6

Stability Analysis of a Rotor-Bearing System having an FG Shaft with Transverse Breathing Cracks

6.1 Introduction

This chapter presents stability analysis of a rotor-bearing system having an FG shaft with multiple transverse breathing cracks. The transverse breathing cracks are modeled based on the formulation discussed in **Chapter 3** (Sub-section **3.4.2**). In this study SS/ZrO_2 FGM have been considered for the rotor, where the power law of material gradation is assumed and SS content is assumed to decrease towards the outer diameter. An FE code has been developed using MATLAB, which is capable of performing stability analysis of the rotor-bearing system having an FG shaft with multiple transverse breathing cracks and to study the effect of relative size, location and orientation of cracks, power law gradient index, slenderness ratio, temperature gradient and shaft internal damping (viscous and hysteretic) on the dynamics responses of such system. From practical design point of view, it is important to understand the influence of gradation parameters on dynamic behavior especially the stability threshold speed of an FG shaft in the event of appearance of multiple transverse cracks during the service.

6.2 Rotor-Bearing system details

FG shaft is modeled using two-noded Timoshenko beam element with two translational and two rotational DOFs at each node. Breathing crack is considered during spinning of the FG shaft for accurate prediction of the dynamic responses of the rotor bearing system. The FG shaft is discretized using beam elements supported on simply supported ends as shown in **Fig. 6.1(a)** and flexible end bearings shown in **Fig. 6.1(b)**. In **Fig. 6.1(a)** and **6.1(b)**, L denotes the total length of the shaft and L_e is the length of one element. Depths of the first and second crack are α_1 and α_2 respectively, which are located at a distance L_{c1} and L_{c2}, respectively, from the left end of the shaft. **Fig. 6.1(c)** shows the shaft element, which is subjected to shear forces P_1, P_2, P_5 and P_6, and bending moments P_3, P_4, P_7 and P_8, rotating at a constant speed, Ω. Here, v and w denotes the translation displacements including the

bending and shear deformation along Y and Z direction respectively. β and Γ are the rotational displacements about Y and Z axes, respectively, at a distance s from the left end of a cross-section of the shaft. In the present formulation, axial force and torsional moment are not considered because transverse vibration is considered a primary mode of damage in the studies of cracked FG shaft systems.

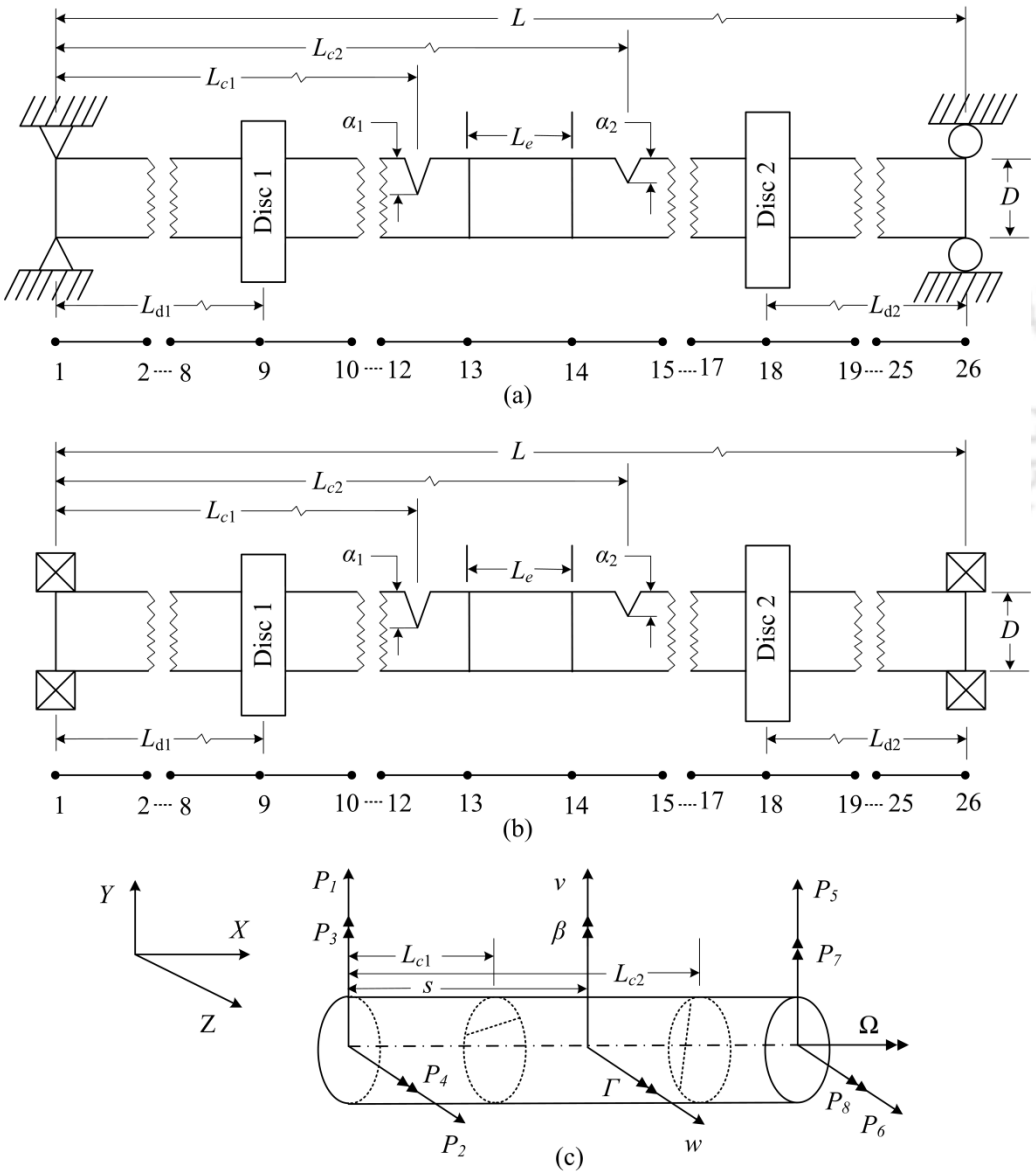

Fig. 6.1 A rotor-disc-bearing system with a cracked FG shaft: **(a)** FE discretization with simply supported ends **(b)** FE discretization with flexible end bearings and **(c)** coordinate system and general loading

In this study, the FG (SS/ZrO_2) shaft is modeled using twenty-five (25) elements as shown in **Fig. 6.1(a)** and **Fig. 6.1(b)**. Diameter of the shaft (D) is considered to be 0.1 m and different lengths of the shaft are considered to obtain different slenderness ratios (SR) of the FG shaft to study the effect of SR. Both simply supported ends and flexible end bearings are considered as supports for the FG shaft to study the effect of such supports. Two discs are mounted on the FG shaft, each having weight of 1.406 kg, polar moment of inertia of 0.002 kg-m^2 and diametral moment of inertia of 0.0135 kg-m^2. The discs are located at 0.4 m and 0.85 m from left end supports as shown in **Fig. 6.1(a)** and **Fig. 6.1(b)**. Density (ρ) considered for SS is 8166 kg/m^3 and that for ZrO_2 is 5700 kg/m^3. **Table 6.1** shows the temperature dependent material properties for the SS/ZrO_2 FGM.

In the present analysis, the values of internal damping coefficients (η_v and η_h) for ZrO_2 is considered in the range between 0.002 to 0.0105 for a corresponding temperature range $0°C$ - $230°C$ as reported in the work by Zhang et al. [165]. For SS, at ambient temperature $(T = 300\ K)$, the value of internal damping coefficients (η_v and η_h) is considered 0.0002 [165]. It is reported that the value of internal damping coefficients (η_v and η_h) increases with the increase in temperature till temperature rise does not lead to substantial softening of the materials [166]. Therefore, in absence of available temperature dependent internal damping coefficients values, linearly increasing trend of the internal damping coefficients (η_v and η_h) with temperature has been considered in the present analysis. The variation of internal damping coefficients (η_v and η_h) with temperature are evaluated using **Eq. (3.2)** for different values of power law gradient indices as tabulated in **Table 6.2** for $\Delta T = 0$ K. The developed FE code is validated before using the same for stability analysis of an FG shaft having two transverse breathing cracks. After validating the FE formulation of the cracked FG shaft considering shaft internal damping, the effects of relative size, location and orientation of cracks, material gradient indices, temperature gradients and shaft internal damping coefficients on the stability threshold speeds of the rotor-bearing system having an FG shaft with two transverse breathing cracks are studied.

Table 6.1 Temperature coefficients value for different mechanical properties of FGM [27]

Properties	Materials	C_0	C_{-1}	C_1	C_2	C_3
E (Pa)	SS	201.04×10^{9}	0	3.079×10^{-4}	-6.534×10^{-7}	0
	ZrO_2	244.27×10^{9}	0	-1.371×10^{-3}	1.214×10^{-6}	-3.681×10^{-10}
ν	SS	0.3262	0	-2.002×10^{-4}	3.797×10^{-7}	0
	ZrO_2	0.2882	0	1.133×10^{-4}	0	0
K (W/m K)	SS	15.379	0	-1.264×10^{-3}	2.092×10^{-6}	-7.223×10^{-10}
	ZrO_2	1.700	0	1.276×10^{-4}	6.648×10^{-8}	0

Table 6.2 Variation of internal damping coefficients (η_v and η_h) with power law gradient index k

Properties	$k=0.0$	$k=0.5$	$k=1.0$	$k=3.0$	$k=5.0$	$k=10.0$	$k=50.0$	SS
η_v(s), η_h	0.002	0.0015	0.0012	0.0007	0.0006	0.00046	0.00038	0.0002

6.3 Validations

The present FE formulation and the developed code are validated in three steps. In the first step, the stiffness, mass, gyroscopic matrices, and bearing conditions are validated through the determination of undamped, damped frequencies and damping ratios of a rotor-disc-bearing system with isotropic damped bearing. In the next step, internal damping formulations and circulatory matrix are validated through the computation of natural frequencies, whirling frequencies and logarithmic decrement of a shaft system with isotropic undamped flexible bearings. In the final step, formulation for determination of stability threshold speeds as a function of crack size, shaft internal viscous and hysteretic damping are compared with the published results for a cracked homogeneous rotor system.

6.3.1 Natural frequencies and damping ratios of a rotor-bearing system with damped bearing

A rotor-bearing system consisting of a rotor, two discs and bearings as shown in **Fig. 6.2** is considered for validating the estimation of whirling frequencies. The rotor and discs are made of steel with $E=211\ \text{GN/m}^2$, $G=81.2\ \text{GN/m}^2$ and $\rho=7810\ \text{kg/m}^3$. Bearings are considered to be isotropic with stiffness of $1\ \text{MN/m}$ and damping $3\ \text{kNs/m}$ in both the

directions. Both the natural frequencies (un-damped ω_n and damped ω_d) and damping ratios ζ have been computed and are compared with the FE solution of Friswell et al. [57]. The computed results and their comparison with the already published results are presented in **Table 6.3** and an excellent agreement has been observed for the stationary and rotating shafts.

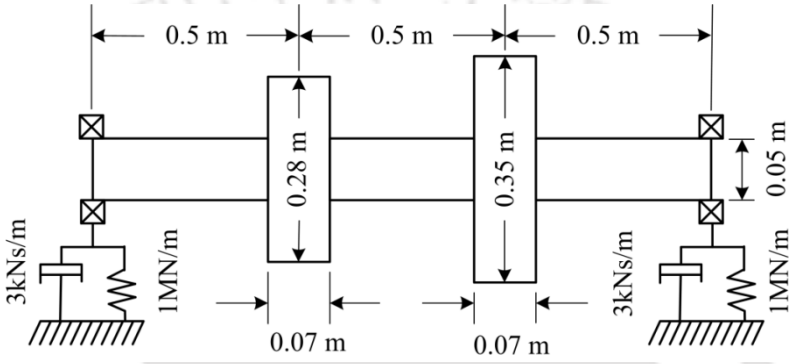

Fig. 6.2 Schematic diagram of a two-disc rotor-bearing system

Table 6.3 Eigen frequencies (Hz) and damping ratios for a rotor-disc system with an isotropic damped bearing

Modes	$\Omega = 0$ rpm								
	Present			Friswell et al. [57]			% Error		
	ω_n	ω_d	ζ	ω_n	ω_d	ζ	ω_n	ω_d	ζ
1st &2nd	13.91	13.89	0.051	13.91	13.89	0.051	0.00	0.00	0.00
3rd & 4th	48.27	46.63	0.258	48.18	46.54	0.258	-0.19	-0.19	0.00
5th & 6th	137.12	102.53	0.664	137.06	103.33	0.658	-0.04	0.77	-0.91
7th & 8th	168.79	132.43	0.620	169.10	132.86	0.619	0.18	0.32	-0.16
Modes	$\Omega = 4000$ rpm								
	Present			Friswell et al. [57]			% Error		
	ω_n	ω_d	ζ	ω_n	ω_d	ζ	ω_n	ω_d	ζ
1st	13.70	13.68	0.048	13.70	13.68	0.048	0.00	0.00	0.00
2nd	14.09	14.07	0.054	14.09	14.07	0.054	0.00	0.00	0.00
3rd	43.72	42.09	0.270	43.61	41.98	0.270	-0.25	-0.26	0.00
4th	52.24	50.71	0.240	52.18	50.65	0.240	-0.11	-0.12	0.00
5th	122.99	103.98	0.534	122.37	104.25	0.524	-0.51	0.26	-1.90
6th	149.54	104.85	0.713	149.81	105.66	0.709	-0.18	0.77	-0.56
7th	168.89	138.05	0.576	168.87	138.23	0.574	-0.01	0.13	-0.35
8th	170.05	129.37	0.649	170.82	130.22	0.647	0.45	0.65	-0.31

6.3.2 Influences of internal damping on whirling frequencies and logarithmic decrement

For validating the present FE model and the developed code, a steel shaft having $L = 1.27$ m and $D = 10.16$ cm is considered. Dimensionless natural frequencies ϖ_n ($\varpi_n^4 = \rho A L^4 \omega^2 / EI$) are computed for a uniform non-rotating simply supported shaft with varying slenderness ratio SR ($= R/2L$). The influence of internal hysteretic damping η_h on the natural frequencies is obtained using the present FE code and is compared with the published works of Özgüven and Özkan [65] and Ku [71]. These results and the comparisons are listed in **Table 6.4**. The results show that the damping causes a negligible change in natural frequencies and the results are in good agreement with the published results.

Table 6.4 Influence of η_h on ϖ_n for a uniform non-rotating simply supported shaft

Modes	SR $R/2L$	$\eta_h = 0.000$			$\eta_h = 0.001$			$\eta_h = 0.002$		
		Present	Ref. [65]	Ku [71]	Present	Ref. [65]	Ku [71]	Present	Ref. [65]	Ku [71]
1st	0.02	3.1300	3.1316	3.1297	3.1308	3.1324	3.1301	3.1316	3.1332	3.1309
	0.04	3.0964	3.1007	3.0942	3.0972	3.1014	3.0946	3.0980	3.1022	3.0954
	0.06	3.0452	3.0476	3.0403	3.0459	3.0484	3.0407	3.0467	3.0491	3.0414
	0.08	2.9815	2.9717	2.9736	2.9823	2.9724	2.9740	2.9830	2.9731	2.9748
	0.10	2.9104	2.8733	2.8995	2.9112	2.8740	2.8999	2.9119	2.8746	2.9006
2nd	0.02	6.2037	6.2146	6.2018	6.2052	6.2161	6.1923	6.2068	6.2177	6.1943
	0.04	5.9873	6.0109	5.9589	5.9888	6.0124	5.9512	5.9903	6.0139	5.9527
	0.06	5.7098	5.7146	5.6540	5.7112	5.7160	5.6476	5.7126	5.7173	5.6490
	0.08	5.4218	5.3556	5.3439	5.4232	5.3567	5.3387	5.4245	5.3579	5.3400
	0.10	5.1478	4.9464	5.0537	5.1491	4.9474	5.0493	5.1504	4.9483	5.0560

Forward whirling (FW) and backward whirling (BW) frequencies, and logarithmic decrement δ of a rotating shaft system supported by two identical isotropic undamped flexible bearings with stiffness coefficients $K_{vv}^b = K_{ww}^b = 1.7513 \times 10^7$ N/m and $K_{vw}^b = K_{wv}^b = 0$ are determined for internal viscous damping $\eta_v = 0.0002$ s and internal hysteretic damping $\eta_h = 0.0002$, for a spin speed $\Omega = 4000$ rpm. The results are presented

in **Tables 6.5** and **6.6** showing the comparisons with the already published results. Results in **Tables 6.5** and **6.6** show an excellent agreement with the published FE solution of Özgüven and Özkan [65] and Ku [71].

Table 6.5 Influence of η_v and η_h on ω_n for a shaft system at a spin speed $\Omega = 4000$ rpm

Modes	$\eta_v = 0.0002$ s			$\eta_h = 0.0002$		
	Present	Ref. [65]	Ku [71]	Present	Ref. [65]	Ku [71]
1 FW	519.79	520.06	519.75	519.83	520.10	519.78
1 BW	521.87	521.79	521.48	519.27	519.54	519.23
2 FW	1095.18	1096.01	1095.13	1094.42	1095.28	1094.40
2 BW	1094.62	1095.34	1094.52	1090.92	1091.77	1090.90
3 FW	2231.49	2222.78	2216.81	2238.08	2244.72	2238.53
3 BW	2230.82	2206.94	2201.25	2223.35	2229.82	2223.80
4 FW	5024.64	4447.40	4413.32	4958.81	5020.12	4968.16
4 BW	4863.98	4411.81	4378.95	4926.63	4986.74	4935.91

Table 6.6 Influence of η_v and η_h on δ for a shaft system at a spin speed $\Omega = 4000$ rpm

Modes	$\eta_v = 0.0002$ s			$\eta_h = 0.0002$		
	Present	Ref. [65]	Ku [71]	Present	Ref. [65]	Ku [71]
1 FW	0.0252	0.0252	0.0252	-2.556×10^{-4}	-2.49×10^{-4}	-2.85×10^{-4}
1 BW	0.2325	0.2321	0.2325	2.576×10^{-4}	2.51×10^{-4}	2.87×10^{-4}
2 FW	0.0347	0.0341	0.0347	-5.780×10^{-5}	-5.11×10^{-5}	-3.66×10^{-4}
2 BW	0.0723	0.0709	0.0723	5.758×10^{-5}	5.09×10^{-5}	3.63×10^{-4}
3 FW	0.7187	0.7830	0.7187	-3.922×10^{-4}	-3.92×10^{-4}	-3.88×10^{-4}
3 BW	1.0529	1.0540	1.0528	3.941×10^{-4}	3.94×10^{-4}	3.90×10^{-4}
4 FW	2.9342	2.9810	2.9409	-5.810×10^{-4}	-5.81×10^{-4}	-6.27×10^{-4}
4 BW	3.5563	3.6070	3.5634	5.848×10^{-4}	5.84×10^{-4}	6.31×10^{-4}

6.3.3 Effect of crack size, η_v and η_h on the stability threshold speed for a cracked rotor system

The ratio of cracked and un-cracked stability threshold speed as a function of crack size α/R with different η_v and η_h, has been obtained for a centrally located cracked steel shaft supported on simply supported ends. Considering identical material properties, disc

specifications and geometrical parameters the obtained results are compared with those of Sekhar and Dey [120] as shown in **Table 6.7**. An excellent agreement of results could be observed in **Table 6.7** thus validating the stability analysis of the cracked rotor system.

Table 6.7 Variation in normalized Ω_{th} with α/R for different η_v and η_h and $L/D = 8.0$

$\frac{\alpha}{R}$	$\eta_v = 1.5\times10^{-4}$ s				$\eta_h = 0.05$			
	$\eta_h = 0.05$		$\eta_h = 0.12$		$\eta_v = 2.5\times10^{-4}$ s		$\eta_v = 3.5\times10^{-4}$ s	
	Present	Sekhar and Dey [120]	Present	Sekhar and Dey [120]	Present	Sekhar and Dey [120]	Present	Sekhar and Dey [120]
no disc								
0.2	0.9619	0.9597	0.9485	0.9405	0.9654	0.9635	0.9671	0.9650
0.4	0.9298	0.9194	0.8918	0.8809	0.9233	0.9197	0.9352	0.9231
0.6	0.8873	0.8944	0.8252	0.8452	0.8545	0.8613	0.8742	0.8672
with disc								
0.2	0.9600	0.9590	0.9399	0.9390	0.9634	0.9629	0.9652	0.9643
0.4	0.9245	0.9180	0.8851	0.8781	0.9228	0.9185	0.9346	0.9285
0.6	0.8857	0.8934	0.8226	0.8538	0.8533	0.8593	0.8730	0.8714

6.4 Influence of L/D, k, ΔT, disc, η_v and η_h on stability threshold speed of a rotating FG shaft in a rotor-bearing system

Considering a two disc rotor-bearing system having an FG shaft supported on isotropic un-damped bearing with $K_{vv}^b = K_{ww}^b = 1.7513\times10^7$ N/m, $K_{vw}^b = K_{wv}^b = 0$, using the present FE code, stability threshold speeds Ω_{th} are computed for different L/D, k, ΔT, η_v and η_h to understand the influences of these parameters. The obtained results are listed in **Tables 6.8** and **6.9** and the corresponding Campbell diagrams are shown in **Figs. 6.3** to **6.5**. In the present analysis, temperature dependent material properties and internal damping coefficients considered are shown in **Tables 6.1** and **6.2**, respectively.

Table 6.8 shows the variation in Ω_{th} with L/D for different k and ΔT for a two-disc rotor-bearing system. Results show that for η_v and η_h corresponding to a given k and ΔT, the Ω_{th} decreases with the increase in L/D. Similarly, for a given L/D and ΔT, Ω_{th}

increases with the decrease in k as the metallic content decrease in the FG shaft and for a given L/D and k, Ω_{th} increases with the decrease in ΔT as the material becomes softer at higher values of ΔT. Therefore, in designing an FG shaft k and ΔT have important roles to decide the operating speeds of such shaft under thermo-mechanical environment.

Table 6.8 Stability threshold speed Ω_{th} (in rpm) of a two-disc rotor system considering an isotropic un-damped bearing with L/D, k and ΔT for η_v and η_h corresponding to k and ΔT

ΔT (K)	L/D	$k=0.0$	$k=0.5$	$k=1.0$	$k=5.0$	$k=10.0$	$k=50.0$	SS
0	12.5	5510	5285	5175	4975	4935	4910	4860
	10.5	6620	6330	6185	5925	5870	5835	5765
	8.5	7925	7550	7370	7030	6965	6920	6830
300	12.5	5175	5050	4985	4855	4830	4810	4775
	10.5	6330	6130	6025	5825	5780	5755	5700
	8.5	7710	7405	7250	6960	6900	6860	6780
600	12.5	5025	4855	4770	4610	4580	4560	4520
	10.5	6195	5955	5835	5610	5570	5540	5480
	8.5	7605	7270	7105	6800	6740	6700	6620

The effect of disc on Ω_{th} for the same rotor-bearing system for different k and ΔT for $L/D=12.5$ are presented in **Table 6.9**. Here, the internal viscous damping η_v and internal hysteretic damping η_h are considered as a function of power law gradient index k and temperature gradient ΔT. The location of single disc is considered 0.6 m from the left end and double discs are considered at 0.4 m and 0.85 m from the left end. The results in **Table 6.9** show that with the increase in number of discs mounting on FG shaft the stability threshold speed Ω_{th} reduced, as expected but the stability threshold speed Ω_{th} decreases with the increase in gradient index k as well as with the increase in temperature gradient ΔT. This is due to the fact that with the decrease in power law gradient index k, the metallic content decrease in the FG shaft and with the increase in temperature gradient ΔT, the material becomes softer.

Table 6.9 Stability threshold speed Ω_{th} (in rpm) of a rotor-bearing system considering an isotropic un-damped bearing with k and ΔT for $L/D = 12.5$ and for η_v and η_h corresponding to k and ΔT

ΔT (K)	No. of disc	$k = 0.0$	$k = 0.5$	$k = 1.0$	$k = 5.0$	$k = 10.0$	$k = 50.0$	SS
0	Nil	5680	5430	5310	5090	5050	5020	4960
	One	5575	5345	5230	5025	4980	4955	4900
	Two	5510	5285	5175	4975	4935	4910	4860
300	Nil	5355	5205	5125	4975	4940	4920	4875
	One	5255	5120	5045	4905	4875	4855	4815
	Two	5175	5050	4985	4855	4830	4810	4775
600	Nil	5220	5020	4915	4730	4695	4670	4620
	One	5120	4930	4825	4665	4630	4605	4560
	Two	5025	4855	4770	4610	4580	4560	4520

Figs. 6.3 to **6.5** show the Campbell diagram for different material gradient index k and corresponding different shaft internal viscous damping η_v and internal hysteretic damping damping η_h (shown in **Table 6.2**) of a two disc rotor-bearing system with an FG shaft supported on isotropic un-damped bearings for slenderness ratio $L/D = 8.5$ and temperature gradient $\Delta T = 0$ K. Values of the logarithmic decrement δ for first forward and backward modes are calculated and shown in the Campbell diagrams. These values of logarithmic decrement δ could be used to decide whether the mode is stable or unstable and are also used to determine the stability threshold speeds Ω_{th}. It is observed from **Figs. 6.3** to **6.5** that for the shafts made of FGM and stainless steel (SS), for the entire range of spin speed considered here, all the backward modes are stable. However, for the forward mode the instability threshold begins at spin speed higher than the critical speeds. It is also observed that with the increase in power law gradient index k, the stability threshold speeds Ω_{th} decreases as metallic composition increases in the FG shaft. Therefore, power law gradient index k could be chosen in designing an FG shaft to operate at a desired range of speed.

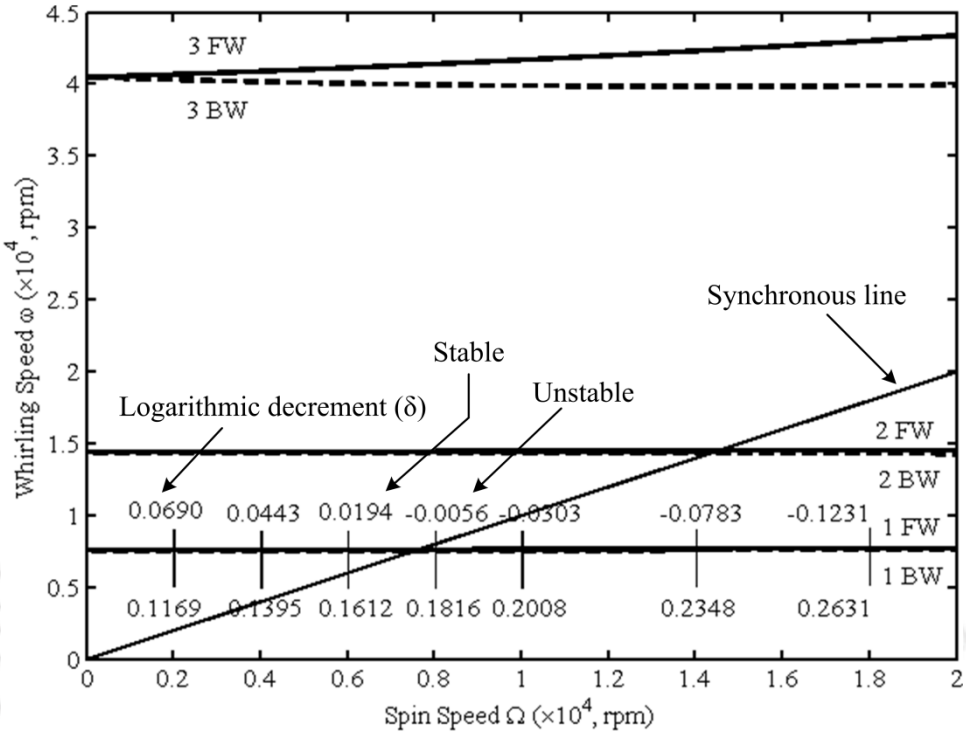

Fig. 6.3 Campbell diagram of a FG shaft system for $k = 0.5$ with $\eta_v = 0.0015$ s and $\eta_h = 0.0015$

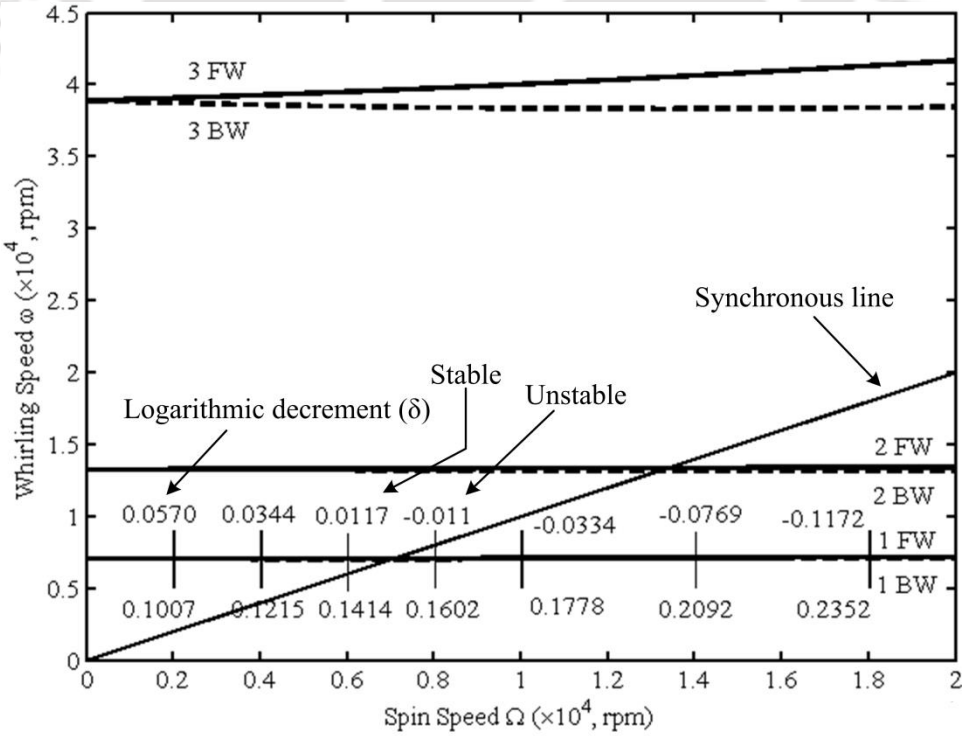

Fig. 6.4 Campbell diagram of a FG shaft system for $k = 5.0$ with $\eta_v = 0.0006$ s and $\eta_h = 0.0006$

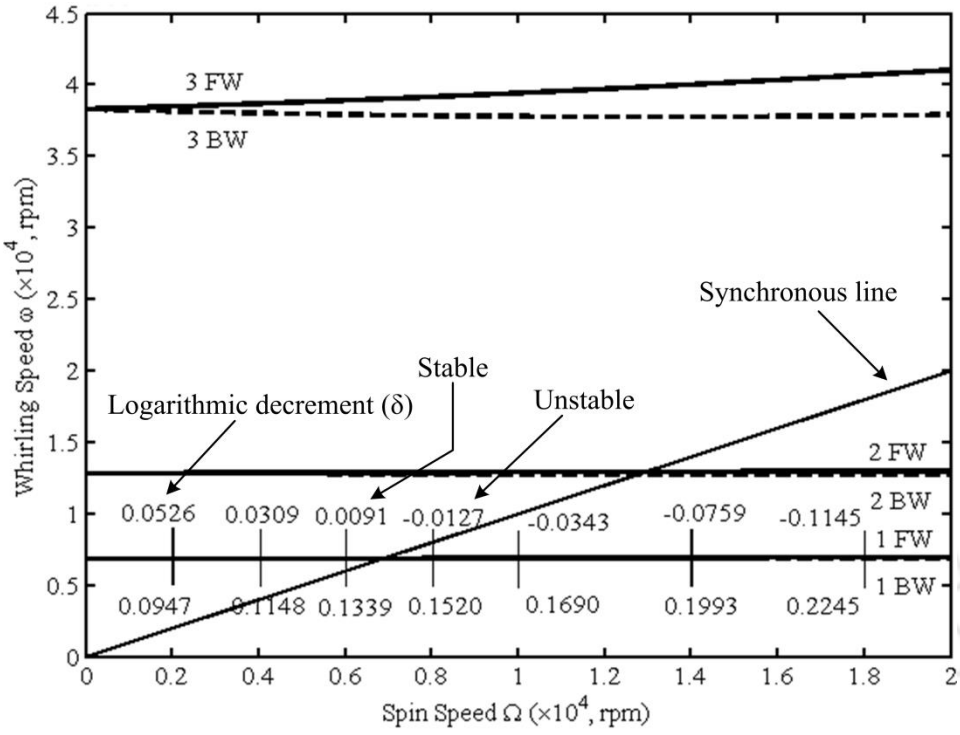

Fig. 6.5 Campbell diagram of a rotor system having a shaft made of SS with $\eta_v = 0.0002$ s and $\eta_h = 0.0002$

6.5 Influence of $\alpha/R, k, \Delta T, \eta_v$ and η_h on stability threshold speed of a rotor-bearing system having an FG shaft with single crack

The influences of α/R, η_v, η_h, k and ΔT on stability threshold speed Ω_{th} have been examined for a two-disc rotor system having an FG shaft with a centrally located fully open transverse crack. Both rigid and flexible end bearings (stiffness coefficients $K_{vv}^b = K_{ww}^b = 1.7513\times10^7$ N/m, $K_{vw}^b = K_{wv}^b = 0$, and damping coefficients $C_{vv}^b = C_{ww}^b = 3\times10^3$ Ns/m, $C_{vw}^b = C_{wv}^b = 0$) supports have been considered for the FG (SS/ZrO_2) shaft. The effects of translational and rotary inertia, bending and shear deformation, gyroscopic, shaft internal viscous and hysteretic damping are considered in the FE formulation of the FG shaft. In the present analysis, temperature dependent material properties and internal damping coefficients considered are shown in **Tables 6.1** and **6.2**, respectively, and the results are shown in **Figs. 6.6** to **6.8(a-b)**, and tabulated in **Tables 6.10** to **6.12**. Stability threshold speed of cracked FG shaft is normalized with respect of an un-cracked shaft.

Considering an FG shaft in a rotor system (ref. **Fig. 6.1(a)**) for $k = 5.0$, $\Delta T = 0$ K, $\eta_v = 0.0006$ s and $\eta_h = 0.0006$, the normalized threshold speeds $\bar{\Omega}_{\text{th}}$ are obtained with different values of α/R and L/D as shown in **Table 6.10** for two values of $L_c/L = 0.14$ and 0.5. It is observed that the changes in $\bar{\Omega}_{\text{th}}$ due to size of crack are appreciable in the case of shaft with low L/D. It is also seen that the effect of reduction is more for crack located at the mid span compared to other location of crack as at the mid span the crack is closer to anti-nodal points.

Table 6.10 Variation in $\bar{\Omega}_{\text{th}}$ of a FG shaft supported on simply supported ends with L/D and α/R for $k = 5.0$, $\Delta T = 0$ K, $\eta_v = 0.0006$ s and $\eta_h = 0.0006$

α/R	$L_c/L = 0.14$			$L_c/L = 0.50$		
	$L/D = 12.5$	$L/D = 10.5$	$L/D = 8.5$	$L/D = 12.5$	$L/D = 10.5$	$L/D = 8.5$
0.0	1.0000	1.0000	1.0000	1.0000	1.0000	1.0000
0.2	0.9987	0.9990	0.9994	0.9933	0.9924	0.9915
0.4	0.9933	0.9924	0.9921	0.9672	0.9615	0.9575
0.6	0.9786	0.9781	0.9830	0.9070	0.8982	0.9108
0.8	0.9498	0.9615	0.9820	0.7885	0.8041	0.9030
1.0	0.9244	0.9605	0.9868	0.5643	0.7551	0.9342

The variations of computed $\bar{\Omega}_{\text{th}}$ with k and α/R, for $L/D = 12.5$, $L_c/L = 0.5$, $k = 5.0$, $\Delta T = 0$ K and $\eta_v = 0.0006$ s and $\eta_h = 0.0006$ are shown in **Fig. 6.6**. It shows that in the presence of crack, with a constant k, $\bar{\Omega}_{\text{th}}$ decreases with the increase in α/R, and for a given α/R, $\bar{\Omega}_{\text{th}}$ decreases as k decreases. Even though the reduction is observed in both the cases, for all values of α/R, the reduction in $\bar{\Omega}_{\text{th}}$ is more pronounced for the values of $k \geq 1$. However, with the increase in α/R the stability threshold speed reduces significantly for all values of η_v and η_h corresponding to k. This is due to the increase in metallic content in the FG shaft with the increase in k, which leads to change in η_v and η_h. Therefore, the change in threshold speed with k is actually due to change in stiffness as well as damping of the shaft.

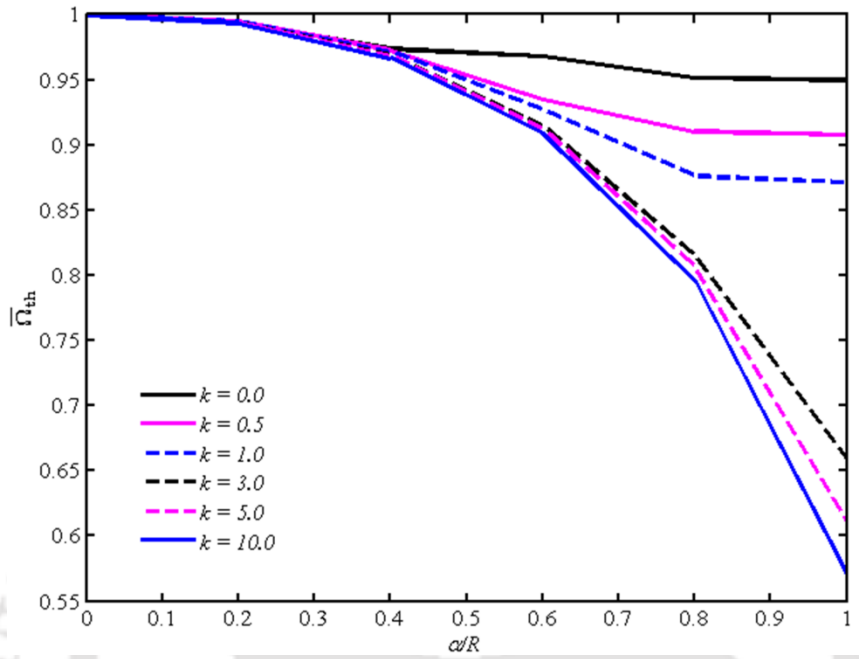

Fig. 6.6 Variation in $\bar{\Omega}_{th}$ with k and α/R for $L/D=12.5$, $\Delta T=0$ K, $L_c/L=0.5$ of a FG shaft system

For simply supported ends, the variation in normalized stability threshold speed $\bar{\Omega}_{th}$ with α/R for different values of η_h corresponding to $\eta_v=0.0006$ s are shown in **Fig. 6.7(a)**, and the variation in $\bar{\Omega}_{th}$ with α/R for different values of η_v corresponding to $\eta_h=0.0006$ are shown in **Fig. 6.7(b)**. Similarly, for flexible end bearing supports, the variation in $\bar{\Omega}_{th}$ with α/R for different values of η_h corresponding to $\eta_v=0.0006$ s are shown in **Fig. 6.8(a)**, and the variation in $\bar{\Omega}_{th}$ with α/R for different values of η_v corresponding to $\eta_h=0.0006$ are shown in **Fig. 6.8(b)**. Here, the parameters for the cracked FG shaft considered are $L/D=12.5$, $L_c/L=0.5$, $k=5.0$ and $\Delta T=0$ K. In the presence of crack, **Figs. 6.7(a)** and **6.8(a)** show that with a constant η_v, $\bar{\Omega}_{th}$ is drastically reduced with the increase in η_h as well as with the increase in α/R. Similarly, **Figs. 6.7(b)** and **6.8(b)** show that for a constant η_h, $\bar{\Omega}_{th}$ is reduced with the increase in η_v and α/R. Even though the reduction is observed for both simply supported ends and flexible end bearings cases, the reduction in $\bar{\Omega}_{th}$ is more when the bearing supports are of flexible, compared to simply supported ends.

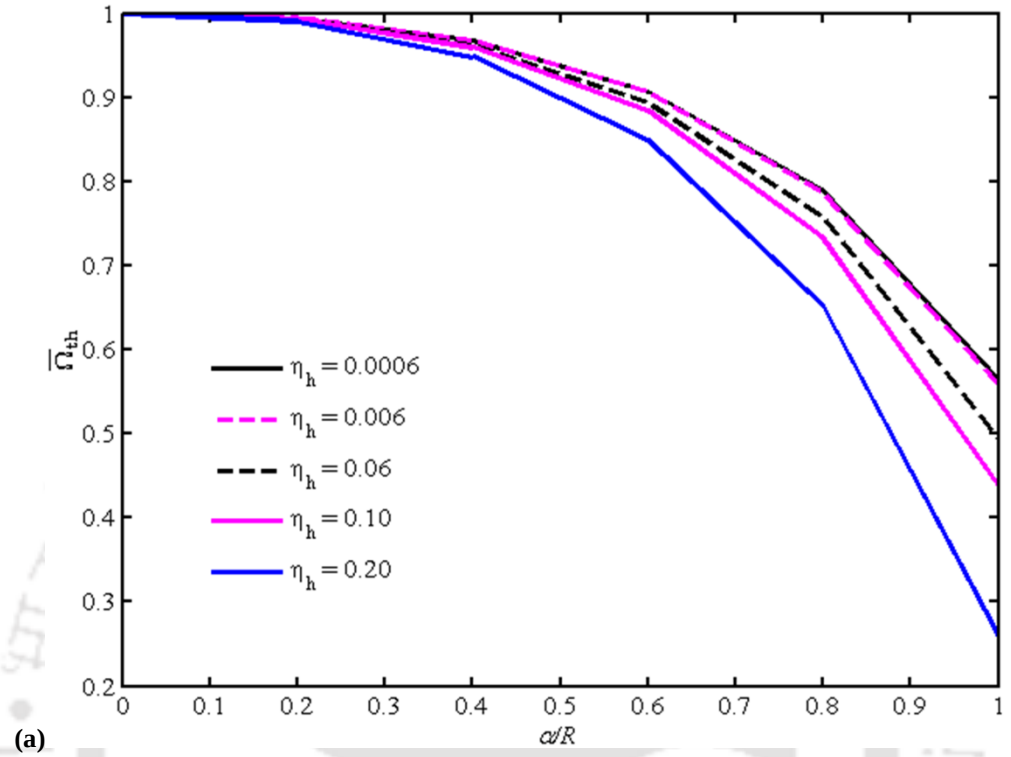

(a)

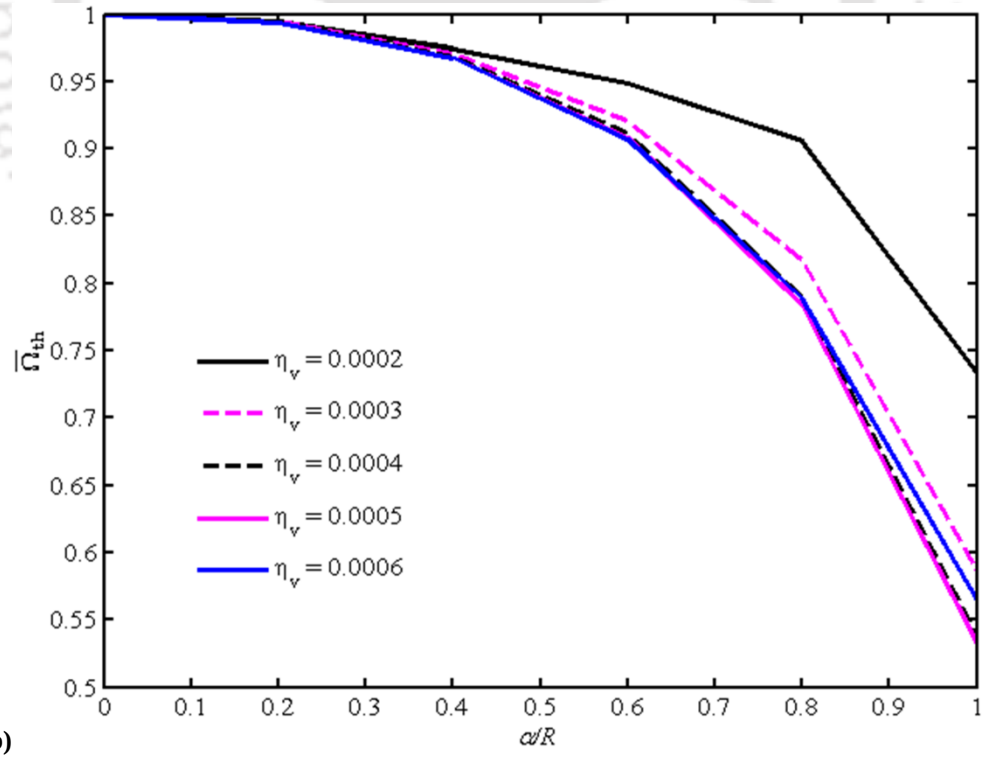

(b)

Fig. 6.7 Variation in $\bar{\Omega}_{th}$ of a FG shaft supported on simply supported ends for $L/D = 12.5$, $L_c/L = 0.5$, $k = 5.0$, $\Delta T = 0$ K with α/R and different (a) η_h for $\eta_v = 0.0006$ s and (b) η_v for $\eta_h = 0.0006$

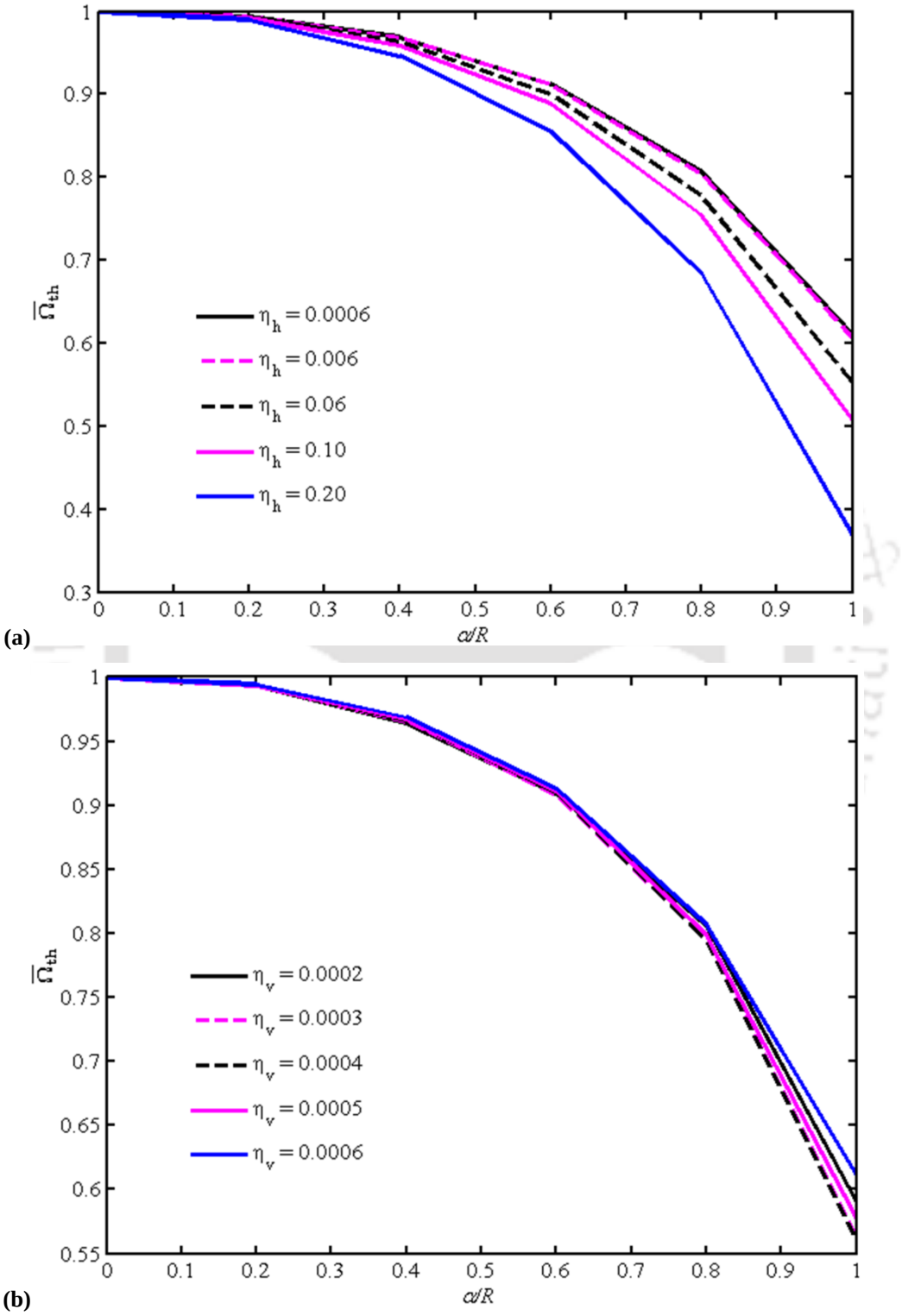

Fig. 6.8 Variation in $\bar{\Omega}_{th}$ of a FG shaft supported on flexible end bearings for $L/D = 12.5$, $L_c/L = 0.5$, $k = 5.0$, $\Delta T = 0$ K with α/R and different (a) η_h for $\eta_v = 0.0006$ s and (b) η_v for $\eta_h = 0.0006$

The variation in normalized stability threshold speed $\overline{\Omega}_{th}$ with power law gradient index k and temperature gradient ΔT are obtained for a centrally located crcak on a FG shaft supported on simply supported ends and flexible end bearings, for slenderness ratio $L/D = 12.5$, crack size $\alpha/R = 0.8$, considering the internal hysteretic and viscous damping corresponding to the values of k and ΔT and are tabulated in **Tables 6.11** and **6.12**. Results in **Tables 6.11** and **6.12** show that for a particular temperature gradient ΔT, normalized stability threshold speed $\overline{\Omega}_{th}$ decreases with the increase in power law gradient index k due to increase in metallic content in the FG shaft. In addition, for a particular value of power law gradient index k, normalized stability threshold speed $\overline{\Omega}_{th}$ also increases with the increase in ΔT as the material becomes softer at higher values of temperature gradient ΔT in the FG shaft. It is also observed that the variation in $\overline{\Omega}_{th}$ are less in the case of flexible bearing supports, compared to that in the case of simply supported ends. Therefore, in the high temperature application the choice of power law gradient index k has a significant importance in designing shaft made of FGMs and also from the design point of view it is much more important to make an FG shaft having an optimal values of power law gradient index k.

Table 6.11 Variation in $\overline{\Omega}_{th}$ of a FG shaft supported on simply supported ends with k and ΔT for $L/D = 12.5$, $\alpha/R = 0.8$ and $L_c/L = 0.5$

ΔT(K)	$k = 0.0$	$k = 0.5$	$k = 1.0$	$k = 3.0$	$k = 5.0$	$k = 10.0$	$k = 50.0$
0	0.9886	0.9455	0.8995	0.8013	0.7885	0.7836	0.7823
300	0.9892	0.9671	0.9401	0.8645	0.8278	0.8011	0.7885
600	0.9984	0.9861	0.9618	0.8930	0.8611	0.8258	0.8057

Table 6.12 Variation in $\overline{\Omega}_{th}$ of a FG shaft supported on flexible end bearings with k and ΔT for $L/D = 12.5$, $\alpha/R = 0.8$ and $L_c/L = 0.5$

ΔT(K)	$k = 0.0$	$k = 0.5$	$k = 1.0$	$k = 3.0$	$k = 5.0$	$k = 10.0$	$k = 50.0$
0	0.9516	0.9104	0.8763	0.8156	0.8068	0.7959	0.7922
300	0.9871	0.9305	0.9053	0.8543	0.8324	0.8161	0.8056
600	0.9942	0.9526	0.9104	0.8706	0.8512	0.8287	0.8161

6.6 Influence of α_2/R, L_{c2}/L, θ_2, k and ΔT on stability threshold speed of a rotor-bearing system having an FG shaft with two transverse breathing cracks

Considering a two disc rotor system having a cracked FG shaft with the shaft internal viscous and hysteretic damping, normalized threshold speeds $\overline{\Omega}_{\text{th}}$ are computed for different crack parameters and material graded parameters. In the present study, two transverse breathing cracks and both simply supported ends and flexible end bearings supports are considered. Temperature dependent material properties and internal damping coefficients are considered, which are shown in **Tables 6.1** and **6.2** and specifications of each disc are as stated earlier. The results are presented in normalized form in the **Figs. 6.9(a-b)** to **6.12(a-b)** and in **Tables 6.13** to **6.18**. Here, also the normalization is done with respect of the un-cracked shaft.

Table 6.13 Variation in $\overline{\Omega}_{\text{th}}$ of a FG shaft supported on simply supported ends with α_1/R, α_2/R and L_{c2}/L for $L/D=12.5$, $L_{c1}/L=0.50$, $k=5.0$, $\Delta T=0$ K, $\theta_1=\theta_2=180°$, $\eta_v=0.0006$ s and $\eta_h=0.0006$

α_1/R	α_2/R	$L_{c2}/L=0.02$	$L_{c2}/L=0.10$	$L_{c2}/L=0.18$	$L_{c2}/L=0.26$	$L_{c2}/L=0.34$	$L_{c2}/L=0.42$
0.2	0.2	0.9946	0.9933	0.9920	0.9906	0.9886	0.9880
	0.4	0.9940	0.9906	0.9833	0.9752	0.9679	0.9632
	0.6	0.9933	0.9819	0.9618	0.9391	0.9183	0.9063
	0.8	0.9913	0.9659	0.9190	0.8648	0.8186	0.7918
	1.0	0.9893	0.9518	0.8762	0.7637	0.6446	0.5770
0.4	0.2	0.9679	0.9672	0.9659	0.9645	0.9632	0.9618
	0.4	0.9672	0.9639	0.9578	0.9505	0.9438	0.9391
	0.6	0.9665	0.9565	0.9378	0.9163	0.8976	0.8869
	0.8	0.9652	0.9404	0.8963	0.8454	0.8025	0.7778
	1.0	0.9632	0.9257	0.8514	0.7436	0.6332	0.5710
0.6	0.2	0.9076	0.9070	0.9063	0.9050	0.9036	0.9029
	0.4	0.9076	0.9050	0.8996	0.8936	0.8882	0.8849
	0.6	0.9070	0.8983	0.8829	0.8648	0.8487	0.8394
	0.8	0.9050	0.8829	0.8440	0.7992	0.7631	0.7423
	1.0	0.9029	0.8661	0.7945	0.6954	0.6031	0.5535

6.6.1 Effect of relative location of second crack (L_{c2}/L)

The normalized stability threshold speeds $\overline{\Omega}_{\text{th}}$ are obtained for a two-disc rotor-bearing system having an FG shaft with two transverse breathing cracks for $L/D=12.5$, $L_{c1}/L=0.50$, $\alpha_1/R=0.8$ (ref. **Figs. 6.1(a)** and **6.1(b)**). Both the cracks are considered always fully open ($\theta_1=\theta_2=180°$) and the influences of k, ΔT, α_2/R and L_{c2}/L on $\overline{\Omega}_{\text{th}}$ are examined. The computed results are shown in **Tables 6.13** to **6.16** and shown in **Figs. 6.9(a)** and **6.9(b)**.

Table 6.14 Variation in $\overline{\Omega}_{\text{th}}$ of a FG shaft supported on flexible end bearings with α_1/R, α_2/R and L_{c2}/L for $L/D=12.5$, $L_{c1}/L=0.50$, $k=5.0$, $\Delta T=0$ K, $\theta_1=\theta_2=180°$, $\eta_v=0.0006$ s and $\eta_h=0.0006$

α_1/R	α_2/R	$L_{c2}/L=0.02$	$L_{c2}/L=0.10$	$L_{c2}/L=0.18$	$L_{c2}/L=0.26$	$L_{c2}/L=0.34$	$L_{c2}/L=0.42$
0.2	0.2	0.9950	0.9936	0.9922	0.9908	0.9893	0.9886
	0.4	0.9943	0.9901	0.9837	0.9751	0.9688	0.9645
	0.6	0.9936	0.9815	0.9616	0.9403	0.9219	0.9112
	0.8	0.9915	0.9645	0.9197	0.8707	0.8310	0.8089
	1.0	0.9886	0.9453	0.8679	0.7685	0.6747	0.6207
0.4	0.2	0.9695	0.9680	0.9666	0.9652	0.9638	0.9631
	0.4	0.9688	0.9652	0.9588	0.9517	0.9453	0.9411
	0.6	0.9680	0.9567	0.9389	0.9190	0.9020	0.8920
	0.8	0.9659	0.9403	0.8977	0.8523	0.8153	0.7947
	1.0	0.9631	0.9205	0.8452	0.7493	0.6619	0.6122
0.6	0.2	0.9134	0.9126	0.9119	0.9105	0.9098	0.9091
	0.4	0.9134	0.9105	0.9048	0.8991	0.8942	0.8906
	0.6	0.9126	0.9034	0.8878	0.8707	0.8572	0.8487
	0.8	0.9105	0.8871	0.8494	0.8097	0.7784	0.7607
	1.0	0.9077	0.8665	0.7947	0.7074	0.6321	0.5902

Influences of size (α_2/R) and location (L_{c2}/L) of second crack on normalized stability threshold speed $\overline{\Omega}_{\text{th}}$ are studied for $k=5.0$, $\Delta T=0$ K, $\eta_v=0.0006$ s and $\eta_h=0.0006$, for different α_1/R and the results are shown in **Tables 6.13** and **6.14** corresponding to simply supported ends and flexible end bearings, respectively. It is

observed that the reduction in $\overline{\Omega}_{th}$ is largest if a crack is at the mid span of the FG shaft. This is because of any reduction in eigenvalue of a mode is largest if the cracks are near to each other and closer to anti-nodal point of that mode. It is also observed that in the case of two cracks with different sizes, the larger size of crack has more influence on the reduction in $\overline{\Omega}_{th}$, even though for smaller size of crack a significant effect on normalized stability threshold speed $\overline{\Omega}_{th}$ is also observed, as expected.

Influences of power law gradient index k and location of second crack L_{c2}/L on normalized stability threshold speed $\overline{\Omega}_{th}$ are studied for $\Delta T = 0$ K, $\alpha_2/R = 0.8$, by taking into account the internal damping coefficients (see in **Table 6.2**) corresponding to the gradient index k and the results are shown in **Figs. 6.9(a)** and **6.9(b)** for both simply supported ends and flexible end bearings, respectively. It is observed that for a given power law gradeient index k, with the increase in location of second crack L_{c2}/L, normalized stability threshold speed $\overline{\Omega}_{th}$ decreases. It is also observed that for $L_{c2}/L < 0.2$, normalized stability threshold speed $\overline{\Omega}_{th}$ decreases with the increase in k due to increase in metallic content in FG shaft but beyond $L_{c2}/L > 0.2$, normalized stability threshold speed $\overline{\Omega}_{th}$ decreases as power law gradient index k increase up to $k = 5.0$ and then again increases as k increase. It could also be observed that for all values of power law gradient index k, maximum reduction in normalized stability threshold speed $\overline{\Omega}_{th}$ occurs while one of the crack is located at middle section of the FG shaft. The value of power law gradient index k at which normalized stability threshold speed $\overline{\Omega}_{th}$ reaches minimum depends on location of second crack L_{c2}/L. **Fig. 6.9** indicates that the reduction in normalized stability threshold speed $\overline{\Omega}_{th}$ is reduced for shaft supported on flexible end bearings compared to simply supported ends. Therefore, in FG shafts, it is important to determine that optimal value of power law gradient index k for a given configuration ensuring a higher safe operating speed and also to design FG shaft operating at higher spin speeds than the metallic shaft.

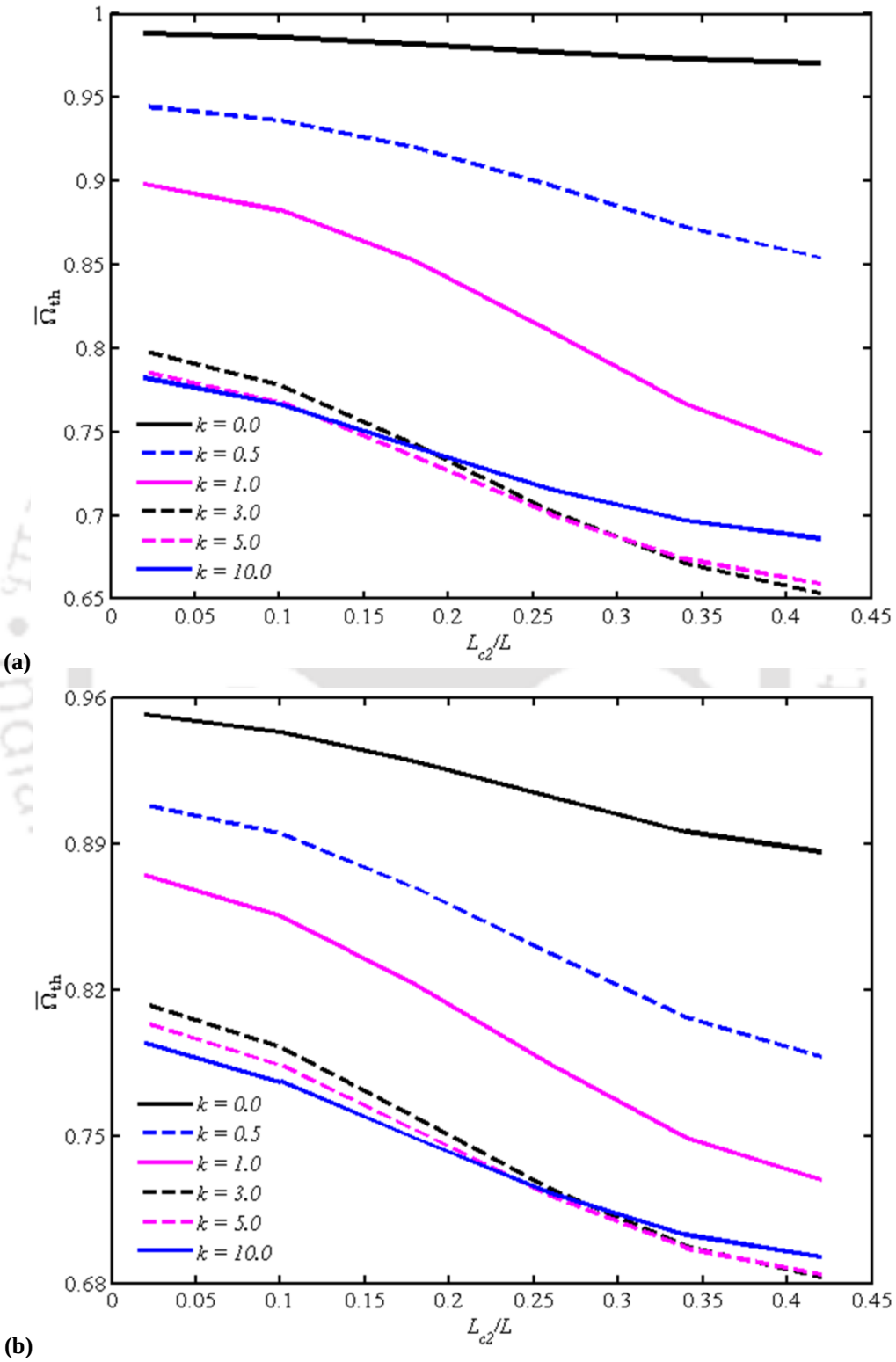

Fig. 6.9 Variation in $\overline{\Omega}_{th}$ with k and L_{c2}/L for $L/D = 12.5$, $L_{c1}/L = 0.50$, $\Delta T = 0$ K, $\alpha_1/R = \alpha_2/R = 0.8$ and $\theta_1 = \theta_2 = 180°$ of a FG shaft supported on (a) simply supported ends and (b) flexible end bearings

Influences of ΔT and L_{c2}/L on $\overline{\Omega}_{\text{th}}$ are examined for $\alpha_2/R=0.8$, $k=5.0$, and for η_v and η_h corresponding to k and ΔT, and the results are shown in **Tables 6.15** and **6.16** for both the simply supported ends and flexible end bearings, respectively. It is observed that with the increase in ΔT, $\overline{\Omega}_{\text{th}}$ increases as the material becomes softer at higher values of ΔT. It is also observed that for all values of ΔT, with the increase in L_{c2}/L, $\overline{\Omega}_{\text{th}}$ decrease and maximum reduction in $\overline{\Omega}_{\text{th}}$ is noticed while second crack is closest to the first crack, which is at the mid span of the FG. It is also observed that the reduction in $\overline{\Omega}_{\text{th}}$ is reduced for shaft supported on simply supported ends compared to flexible end bearings. Therefore, in high temperature application of FG shafts along with k, ΔT is also important parameter to study the stability analysis of an FG shaft in a rotor-bearing system.

Table 6.15 Variation in $\overline{\Omega}_{\text{th}}$ of a FG shaft supported on simply supported ends with ΔT and L_{c2}/L for $L/D=12.5,\ L_{c1}/L=0.50,\ k=5.0,\ \alpha_1/R=\alpha_2/R=0.8,\ \theta_1=\theta_2=180°$

ΔT(K)	$L_{c2}/L=0.02$	$L_{c2}/L=0.10$	$L_{c2}/L=0.18$	$L_{c2}/L=0.26$	$L_{c2}/L=0.34$	$L_{c2}/L=0.42$
0	0.7865	0.7677	0.7349	0.7008	0.6740	0.6593
300	0.8257	0.8051	0.7675	0.7250	0.6889	0.6683
600	0.8595	0.8406	0.8043	0.7593	0.7182	0.6946

Table 6.16 Variation in $\overline{\Omega}_{\text{th}}$ of a FG shaft supported on flexible end bearings with ΔT and L_{c2}/L for $L/D=12.5,\ L_{c1}/L=0.50,\ k=5.0,\ \alpha_1/R=\alpha_2/R=0.8,\ \theta_1=\theta_2=180°$

ΔT(K)	$L_{c2}/L=0.02$	$L_{c2}/L=0.10$	$L_{c2}/L=0.18$	$L_{c2}/L=0.26$	$L_{c2}/L=0.34$	$L_{c2}/L=0.42$
0	0.8047	0.7841	0.7528	0.7216	0.6967	0.6839
300	0.8307	0.8101	0.7762	0.7399	0.7110	0.6953
600	0.8493	0.8284	0.7953	0.7573	0.7251	0.7071

6.6.2 Effect of relative orientation of second crack (θ_2)

The normalized threshold speeds $\overline{\Omega}_{\text{th}}$ are obtained for a two-disc rotor-bearing system having an FG shaft with two transverse breathing cracks for $L/D=12.5,\ L_{c1}/L=0.50,$ $\alpha_1/R=0.8$ and the first crack is considered always fully open ($\theta_1=180°$), while the

orientation of second crack (θ_2) is varied. The influences of k, ΔT, α_2/R and L_{c2}/L on $\overline{\Omega}_{\text{th}}$ are studied and the results are shown in **Figs. 6.10(a-b)** to **6.12(a-b)** and also shown in **Tables 6.17** and **6.18**. In the present analysis, temperature dependent material properties and internal damping coefficients are considered, which are shown in **Tables 6.1** and **6.2** and specifications of each disc are stated earlier.

Influences of k and θ_2 on $\overline{\Omega}_{\text{th}}$ are examined for an FG shaft in a two-disc rotor system for $L_{c2}/L = 0.34$, $\Delta T = 0$ K, $\alpha_2/R = 0.8$ and the values of internal damping coefficients (see in **Table 6.2**) are taken into account corresponding to the gradient index k. The results are shown in **Figs. 6.10(a)** and **6.10(b)** for the simply supported ends and flexible end bearings, respectively. It is observed that with the increase in metallic content (i.e. the value of k) in FG shaft, $\overline{\Omega}_{\text{th}}$ decreases till a particular value of k (depending upon θ_2) after which further increase in k leads to increase in $\overline{\Omega}_{\text{th}}$. For all the values of k, it is observed that with the increase in crack orientation θ_2, $\overline{\Omega}_{\text{th}}$ decreases and the maximum reduction is noticed while both the cracks are fully open leading to maximum degradation of stiffness. Similar trends have also been observed for other combinations of relative locations of the two cracks. **Fig. 6.10** also shows that the reduction in $\overline{\Omega}_{\text{th}}$ is less when the shaft is supported on flexible end bearings compared to that when the shaft is supported on simply supported ends. Therefore, at any arbitrary rotation of FG shaft in the rotor-disc-bearing system, k has an important role in deciding the stability threshold speed.

Influences of ΔT and θ_2 on $\overline{\Omega}_{\text{th}}$ are examined for the FG shaft system with $L_{c2}/L = 0.34$, $\alpha_2/R = 0.8$, $k = 5.0$, for η_v and η_h corresponding to k and ΔT, and the results are shown in **Tables 6.17** and **6.18** for the simply supported ends and flexible end bearings, respectively. It is observed that with the increase in ΔT, $\overline{\Omega}_{\text{th}}$ increases as material becomes softer at higher values of ΔT. In addition, with the gradual increase in θ_2, $\overline{\Omega}_{\text{th}}$ decreases and the maximum reduction is attained while both the cracks are fully open due to maximum degradation of stiffness in the FG shaft. It is also observed that the reduction in

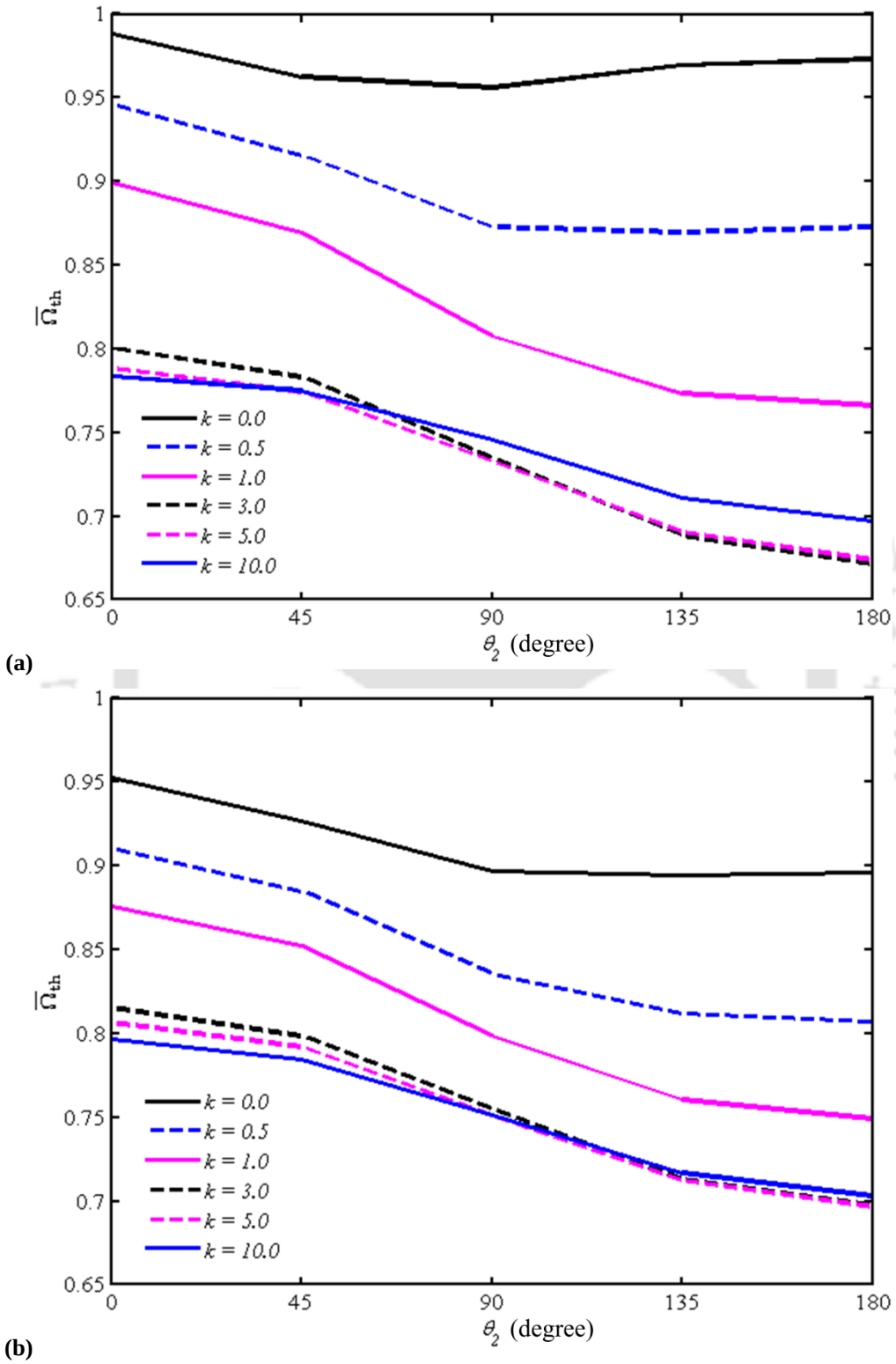

Fig. 6.10 Variation in $\bar{\Omega}_{th}$ with k and θ_2 for $L/D = 12.5$, $L_{c1}/L = 0.50$, $L_{c2}/L = 0.34$, $\alpha_1/R = \alpha_2/R = 0.8$, $\Delta T = 0$ K and $\theta_1 = 180°$ of a FG shaft supported on (a) simply supported ends and (b) flexible end bearings

$\overline{\Omega}_{\text{th}}$ is less for shaft supported on simply supported ends compared to that in the case of flexible end bearings. Therefore, in high temperature application, $\overline{\Omega}_{\text{th}}$ is decided by ΔT and the value of k corresponding to that ΔT needs to be determined ensuring higher operating speed limit.

Table 6.17 Variation in $\overline{\Omega}_{\text{th}}$ of a FG shaft supported on simply supported ends with ΔT and θ_2 for $L/D=12.5,\ L_{c1}/L=0.50,\ L_{c2}/L=0.34,\ k=5.0,\ \alpha_1/R=\alpha_2/R=0.8,\ \theta_1=180°$

ΔT(K)	$\theta_2=0°$	$\theta_2=45°$	$\theta_2=90°$	$\theta_2=135°$	$\theta_2=180°$
0	0.7885	0.7744	0.7329	0.6908	0.6740
300	0.8278	0.8065	0.7527	0.7059	0.6889
600	0.8611	0.8366	0.7774	0.7324	0.7182

Table 6.18 Variation in $\overline{\Omega}_{\text{th}}$ of a FG shaft supported on flexible end bearings with ΔT and θ_2 for $L/D=12.5,\ L_{c1}/L=0.50,\ L_{c2}/L=0.34,\ k=5.0,\ \alpha_1/R=\alpha_2/R=0.8,\ \theta_1=180°$

ΔT(K)	$\theta_2=0°$	$\theta_2=45°$	$\theta_2=90°$	$\theta_2=135°$	$\theta_2=180°$
0	0.8068	0.7919	0.7514	0.7124	0.6967
300	0.8324	0.8142	0.7688	0.7267	0.7110
600	0.8512	0.8313	0.7820	0.7403	0.7251

Influences of α_2/R and θ_2 are examined on $\overline{\Omega}_{\text{th}}$ for an FG shaft in a two-disc rotor-bearing system for $L_{c2}/L=0.34,\ \Delta T=0$ K, $k=5.0$, $\eta_v=0.0006$ s and $\eta_h=0.0006$ and the results are shown in **Figs. 6.11(a)** and **6.11(b)** for the rigid and flexible end bearings respectively. It shows that with the increase in α_2/R, $\overline{\Omega}_{\text{th}}$ decreases as the stiffness are gradually degraded with gradual increase in α_2/R. It is also observed that with the gradual increase in θ_2, $\overline{\Omega}_{\text{th}}$ decreases with the maximum reduction attained while both the cracks are fully open due to maximum degradation of stiffness in the FG shaft. **Fig. 6.11** also show that the reduction in $\overline{\Omega}_{\text{th}}$ is less for shaft supported on simply supported ends compared to that in the case of flexible end bearings. Therefore in FG shafts, size of second crack α_2/R has an important role to study the stability analysis of an FG shaft in the rotor system.

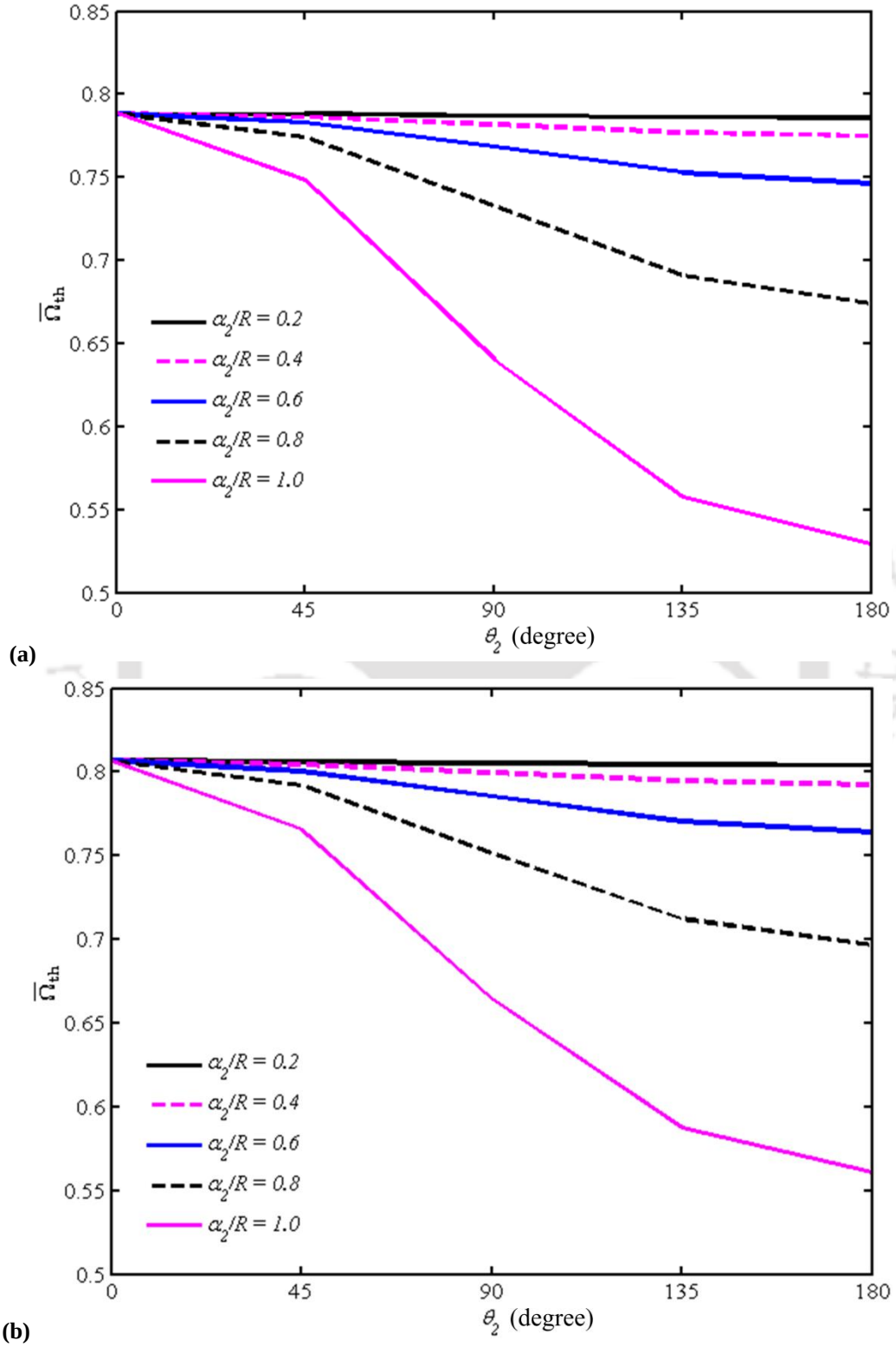

Fig. 6.11 Variation in $\overline{\Omega}_{th}$ with α_2/R and θ_2 for $k = 5.0$, $\Delta T = 0$ K, $\eta_v = 0.0006$ s and $\eta_h = 0.0006$ of a FG shaft supported on (a) simply supported ends and (b) flexible end bearings

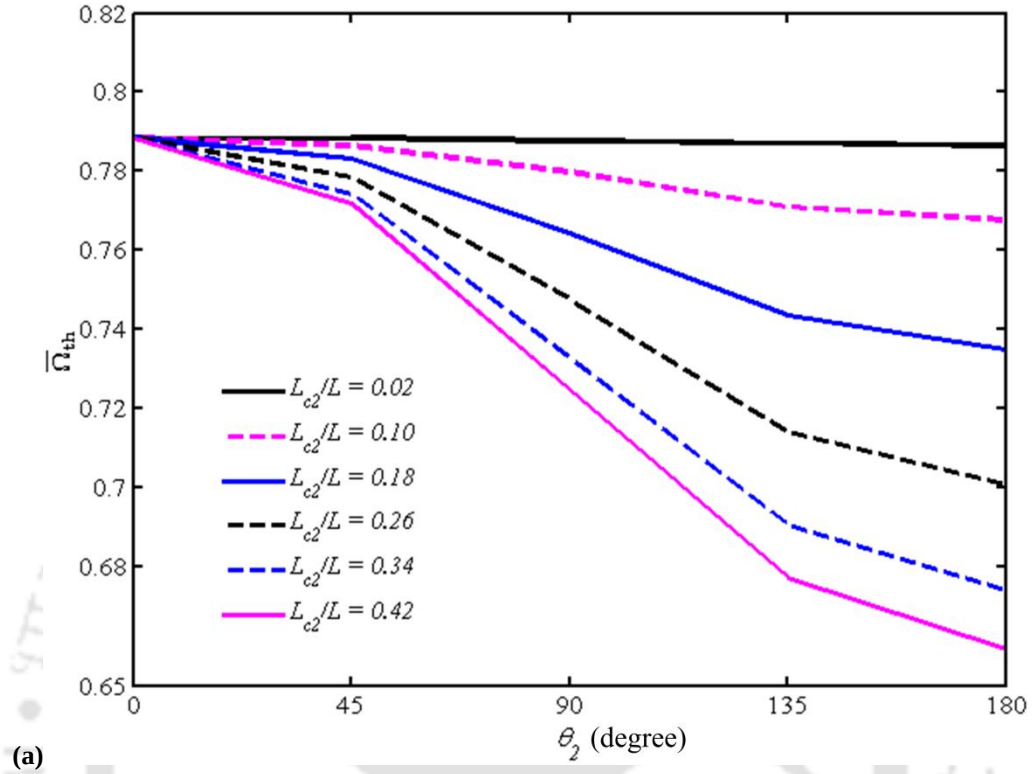

(a)

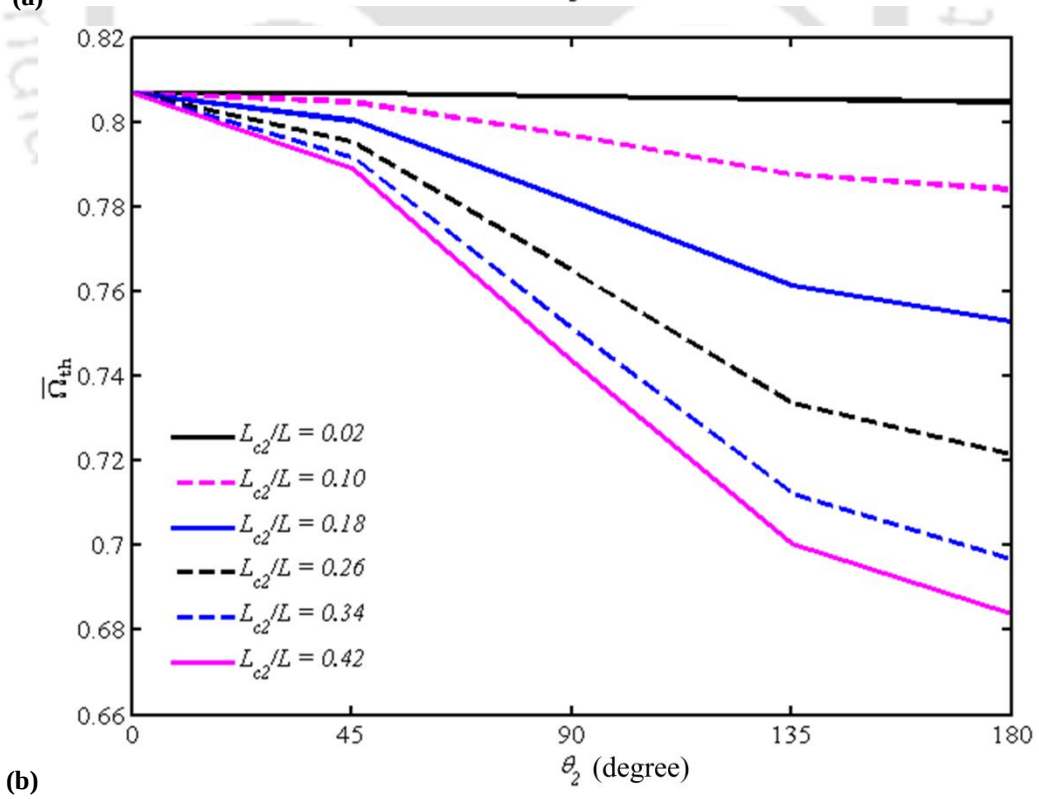

(b)

Fig. 6.12 Variation in $\bar{\Omega}_{\text{th}}$ with L_{c2}/L and θ_2 for $k = 5.0$, $\Delta T = 0$ K, $\eta_v = 0.0006$ s and $\eta_h = 0.0006$ of a FG shaft supported on (a) simply supported ends and (b) flexible end bearings

The normalized threshold speeds $\overline{\Omega}_{\text{th}}$ are obtained for an FG shaft having two transverse breathing cracks in a two-disc rotor system with $\alpha_2/R = 0.8$, $\Delta T = 0$ K, $k = 5.0$, $\eta_v = 0.0006$ s and $\eta_h = 0.0006$, and the influences of L_{c2}/L and θ_2 on are examined. The results are shown in **Figs. 6.12(a)** and **6.12(b)** for the simply supported ends and flexible end bearings, respectively. It is observed that with the increase in L_{c2}/L, $\overline{\Omega}_{\text{th}}$ decreases and the maximum reduction is attained while both the cracks are located near to each other at the mid span of the FG shaft. It is also observed that with the gradual increase in θ_2, $\overline{\Omega}_{\text{th}}$ decrease with the maximum reduction attained while both the cracks are fully open ($\theta_2 = \theta_2 = 180°$) due to maximum degradation of stiffness during rotation of the FG shaft. **Fig. 6.12** also show that the reduction in $\overline{\Omega}_{\text{th}}$ is less for shaft supported on simply supported ends compared to that in the case of flexible end bearings. Therefore, in FG shafts having two cracks, relative lication (L_{c2}/L) of cracks is an important to understand the stability threshold speed in a rotor bearing system having an FG shaft.

6.7 Summary

The stability analysis of an FG shaft with multiple transverse breathing cracks in a two-disc rotor-bearing system is carried out through a FE approach. Temperature dependent material properties are considered and both simply supported ends and flexible end bearings support on the FG shaft are considered. Developed FE model has been validated with the published results and used to study the influences of power law gradient index, temperature gradient, relative depth, location and orientation of cracks and slenderness ratio on the natural whirling frequency and stability threshold speeds of the FG shaft in a two-disc rotor-bearing system. Some of the important observations noticed from the parametric study are

- In the case of cracked FG shaft, internal viscous and hysteretic damping coefficients have significant influence on the stability threshold speed and are functions of power law gradient index. Therefore, proper choice of power law

gradient index will be important in designing such a shaft to ensure safety during operation.

- In the case of cracked FG shaft, temperature dependent material properties have significant impact on the stability threshold speed and also are functions of power law gradient index. Therefore, in high temperature application proper choice of power law gradient index will be important along with temperature gradient in designing such a shaft to ensure higher operating speed limit.
- Increase in power law gradient index, temperature gradient and slenderness ratio leads to reduction in stability threshold speeds. Thus in a high temperature application of FG shafts, power-law gradient index may be chosen in such a way so that the reductions in stability threshold speed with temperature is minimized, while keeping enough material at the outer layer for providing temperature resistance.
- In the case of a cracked FG shaft, with the increase in power law gradient index, temperature gradients, relative distance and angular orientation of second crack, the threshold speeds are reduced. As expected, the highest reduction has been observed while both the cracks are fully open.
- In the presence of crack in an FG shaft, besides crack size and locations, the reduction in stability threshold speed is also significantly affected by power law gradient index and corresponding internal viscous and hysteretic damping coefficients. Therefore, a judicious choice of power law index will ensure stability threshold speed even in the event of transverse surface cracks appearing in the shaft.
- The influence of cracks on the stability threshold speeds is very significant if a crack is at mid span of the FG shaft as any reduction in eigenvalue of a mode is largest if the cracks are near to each other and closer to anti-nodal point of that mode. And also it has been noticed that in the case of two cracks with different size of crack, the larger size of crack has more significant effect on the reduction in

$\overline{\Omega}_{th}$, even though for small size of crack a significant effect on $\overline{\Omega}_{th}$ is also reflected, as expected.

- In the presence of crack, even though the reduction is in both simply supported ends and flexible end bearings cases, the variation in $\overline{\Omega}_{th}$ are more reduced if the bearing supports are made of flexible, compared to simply supported ends.

The present formulation will be useful in arriving at an optimum gradation parameter of an FG shaft to be recommended to the manufacturer so to maximize the performance of the FG shaft especially in the event of multiple breathing cracks appearing on the shaft surface during service.

CHAPTER 7

Conclusions and Scope of Future Work

In this work, finite element (FE) formulations have been developed for analysis of cracked functional graded (FG) shaft considering temperature dependent material properties. Local flexibility coefficients (LFCs) are derived for cracked FG shaft elements using energy method and Paris equation. Formulations for stability analysis of a rotating FG shafts with cracks have been developed. Based on the formulations an FE code has been developed and validated. Numerical simulations have been performed using the developed FE code to understand the dynamic behavior of FG shafts having transverse cracks and the influence of important parameters on such behavior. Based on the results from numerical simulations some of the important conclusions have been drawn. The conclusions drawn from the present work have been presented categorically as general conclusions and specific conclusions. In the specific conclusions, important outcomes are presented, which contributes in depth understanding of dynamic behavior of cracked FG shafts and influence of some of the important design variables in design of such shafts. Finally, possible extension of the present work is stated in the subsection of scope of the future work.

7.1 General conclusions

- It is possible to model FG shafts using two noded Timoshenko beam elements taking into account the different possible material gradations along radial direction.
- Local flexibility coefficients for cracked FG shafts could be derived using Castigliano's theorem and Paris's equations to take into account the presence of cracks in FG shaft.
- The direct and cross couple LFCs are observed to be functions of size of crack, orientation of crack, applied temperature gradient and power law gradient index.
- Temperature dependent material properties have significant impact on LFCs, modified stiffness and hence the dynamic responses of cracked FG shafts.
- Power law gradient index, temperature gradient, size and orientation of crack also affect LFCs and hence the dynamic responses of cracked FG shafts.

- Gradation parameter affects the dynamic performance of the FG rotor system with single/multiple transverse breathing crack/cracks.
- Stability threshold speed is influenced significantly by relative size, location and orientation of cracks, power law gradient index, temperature gradient, internal viscous and internal hysteretic damping for a given crack configuration.
- In the presence of crack, the changes in threshold speeds are appreciable in case of FG shaft with low slenderness ratio and the effect of reduction is more for mid span crack compared to other location of crack, because of crack is closer to antinodal points.

7.2 Specific conclusions

7.2.1 Transverse vibration analysis of a FG shaft system with stationary transverse crack

- Temperature dependence of material properties significantly affects the free vibration characteristics of an FG shaft with fully open transverse crack and hence for accurate results this needs to be considered in FE modeling.
- The direct and cross-couple LFCs of an FG shaft due to the presence of crack are not only a function of crack size but also depend on power law gradient index and applied temperature gradient. Therefore, while designing an FG shaft, a suitable power law index could be chosen to limit the increase in flexibility due to the presence of transverse surface crack.
- Natural frequencies of a cracked FG shaft system decrease with the increase in crack size for a certain crack configuration. However, the amount of reduction is decided by the power law gradient index. Therefore, suitable power law gradient index could be chosen to minimize the extent of reduction in natural frequency.
- It is observed that for a given crack size the reduction in natural frequency is more for higher values of shaft's slenderness. However, this reduction is decided by the values

of power law gradient index. Thus, the power law gradient index could be suitably chosen to limit the reduction thereby allowing more slenderness ratio in design.

- With the increase in power law gradient index, the reduction in fundamental frequency is more pronounced in the case of fixed-fixed boundary condition compared to those in the case of simply supported and cantilever boundary conditions cases, which are related to rigidity of the system.
- Natural whirling frequencies (FW and BW) and critical speeds of cracked FG shaft system decrease with the increase in crack size for a certain slenderness ratio, crack location and power law gradient index. However, the amount of reduction is decided by the value of the power law gradient index chosen in the design of the FG shaft.
- By using an FG shaft with proper material gradient, it is possible to limit the reduction in natural whirling frequencies (FW and BW) due to transverse crack and thus more slenderness ratio could be used in design of such FG rotors.
- By using an FG shaft with suitably chosen material gradient index, it is possible to limit the reduction in natural whirl frequencies and critical speeds due to transverse crack at higher temperature gradient.

7.2.2 Transverse vibration analysis of a FG shaft system with transverse breathing cracks

- For a spinning FG shaft with transverse breathing crack behavior, the direct and cross couple LFCs, and hence the reduction in fundamental frequencies, besides being functions of size, location and orientation of crack, the applied temperature gradient are also influenced by the power law gradient index of the FGM used.
- The variation of LFCs with crack orientation angle θ for different crack size, power law gradient index, applied temperature gradient shows that the magnitude of LFCs increases with increasing crack orientation angle, reaches a maximum at $\theta = 180°$ and decreases as the crack orientation $180° < \theta \leq 360°$.

- In an FG shaft, the percentage reduction in natural frequencies decreases with the increase in power law gradient index due to the increase in metal content in the FG shaft and also with the increase in temperature gradient as the material become softer at higher values of temperature gradient.
- By using an FG shaft with suitably chosen material gradient index, the reduction in natural whirling frequencies (FW and BW) and increase in critical speeds due to the presence of multiple transverse cracks could be minimized, besides being affected by relative orientations, locations and size of the cracks.

7.2.3 Stability analysis of a FG shaft system with transverse breathing cracks

- Internal viscous and hysteretic damping coefficients for an FG cracked shaft material are functions of power law gradient index and have significant influence on the stability threshold speed. Therefore, proper choice of power law gradient index will be important in designing such a shaft to ensure safety during operation.
- Using FG shaft with a suitable material gradient index, it is possible to minimize the reduction in stability threshold speed at high temperature applications and simultaneously providing sufficient material at outer layer for temperature resistance.
- Stability threshold speeds are observed to reduce with the increase in power law gradient index, temperature gradients, relative distance and relative angular orientation of second crack and the reduction is highest for the configuration where both the cracks are fully open.
- In addition to internal viscous and hysteretic damping, power law gradient index also significantly influences the stability threshold speeds. Thus, using an FG shaft with suitable power law gradient index will lead to higher stability threshold speeds even in the event of cracks surfacing on the shafts.
- The influence of cracks on the stability threshold speeds is significant if a crack is at the mid span of the FG shaft and also it is noticed that in the case of two different

size cracks, the effect of larger crack is more pronounced on the reduction in stability threshold speeds.

- The present formulation will be useful in arriving at application specific gradation parameters of an FG shaft to be recommended to the manufacturer so as to maximize the performance of the FG shaft especially in the event of multiple transverse breathing cracks appearing on the shaft surface during service.

7.3 Novelty and major contribution from the thesis

Novelty of the present thesis work is that in the open literature, there is hardly any work reported in the direction of dynamics and stability analysis of FG rotor bearing systems. In this work, a complete FE formulation of cracked FG rotor supported on bearings has been derived. Starting with deriving LFCs for cracked rotors and using those in the FE formulation, stability analysis of FG rotor bearing systems have been formulated. More importantly, the FGE code developed could be used to understand the influences of material gradation on the performance of FG rotor bearing system under thermo-mechanical loading. These issues were not reported till date in open literatures.

7.4 Scope of future work

The present work could be extended to the following directions

- Thermo-elastic material properties can be formed using exponential law of material gradation and sigmoid law of material gradation, which enable to study the dynamic responses of FG shaft system.
- The determination of LFCs for FG shafts could be extended for other types of material gradation law such as exponential and sigmoid law of material gradation.
- The present work can be extended to study the influence of crack parameters on the axial and torsional vibrations of FG shafts.

- The present FE formulation can be extended to perform forced vibration responses of FG shafts with single/multiple transverse crack/cracks.
- Experiments could be performed on FG shafts with single/multiple transverse crack/cracks to further reinforce the developed FE formulation for performing dynamics responses.
- The present FE formulation can be extended to perform crack detection and identification in FG shafts.
- Experiments could also be performed on FG shafts with multiples transverse cracks for detection and identification of cracks.

Appendix A: Elementary matrices

The elementary mass (translational and rotational), gyroscopic, stiffness and circulatory stiffness matrices used are presented here.

A.1 Elementary translational mass matrix for a FG shaft

$$\left[\mathbf{M}_t^e\right]=\frac{m(y)L_e}{420\left\{1+\Phi(y,T)\right\}^2}\left[\mathbf{M}_t\right]_0+\frac{m(y)L_e\Phi(y,T)}{420\left\{1+\Phi(y,T)\right\}^2}\left[\mathbf{M}_t\right]_1+\frac{m(y)L_e\left\{\Phi(y,T)\right\}^2}{420\left\{1+\Phi(y,T)\right\}^2}\left[\mathbf{M}_t\right]_2 \tag{A.1}$$

$$\left[\mathbf{M}_t\right]_0=\begin{bmatrix} 156 & & & & & sym & & \\ 54 & 156 & & & & & & \\ 0 & 0 & 156 & & & & & \\ 0 & 0 & 54 & 156 & & & & \\ 0 & 0 & -22L_e & -13L_e & 4L_e^2 & & & \\ 0 & 0 & 13L_e & 22L_e & -3L_e^2 & 4L_e^2 & & \\ 22L_e & 13L_e & 0 & 0 & 0 & 0 & 4L_e^2 & \\ -13L_e & -22L_e & 0 & 0 & 0 & 0 & -3L_e^2 & 4L_e^2 \end{bmatrix} \tag{A.2}$$

$$\left[\mathbf{M}_t\right]_1=\begin{bmatrix} 294 & & & & & & sym & \\ 126 & 294 & & & & & & \\ 0 & 0 & 294 & & & & & \\ 0 & 0 & 126 & 294 & & & & \\ 0 & 0 & -38.5L_e & -31.5L_e & 7L_e^2 & & & \\ 0 & 0 & 31.5L_e & 38.5L_e & -7L_e^2 & 7L_e^2 & & \\ 38.5L_e & 31.5L_e & 0 & 0 & 0 & 0 & 7L_e^2 & \\ -31.5L_e & -38.5L_e & 0 & 0 & 0 & 0 & -7L_e^2 & 7L_e^2 \end{bmatrix} \tag{A.3}$$

$$\left[\mathbf{M}_t\right]_2=\begin{bmatrix} 140 & & & & & & sym & \\ 70 & 140 & & & & & & \\ 0 & 0 & 140 & & & & & \\ 0 & 0 & 70 & 140 & & & & \\ 0 & 0 & -17.5L_e & -17.5L_e & 3.5L_e^2 & & & \\ 0 & 0 & 17.5L_e & 17.5L_e & -3.5L_e^2 & 3.5L_e^2 & & \\ 17.5L_e & 17.5L_e & 0 & 0 & 0 & 0 & 3.5L_e^2 & \\ -17.5L_e & -17.5L_e & 0 & 0 & 0 & 0 & -3.5L_e^2 & 3.5L_e^2 \end{bmatrix} \tag{A.4}$$

A.2 Elementary rotational mass matrix for a FG shaft

$$\left[\mathbf{M}_r^e\right]=\frac{m(y)R^2}{120L_e\left\{1+\Phi(y,T)\right\}^2}\left[\mathbf{M}_r\right]_0+\frac{m(y)R^2\Phi(y,T)}{120L_e\left\{1+\Phi(y,T)\right\}^2}\left[\mathbf{M}_r\right]_1+\frac{m(y)R^2\left\{\Phi(y,T)\right\}^2}{120L_e\left\{1+\Phi(y,T)\right\}^2}\left[\mathbf{M}_r\right]_2 \quad \text{(A.5)}$$

$$\left[\mathbf{M}_r\right]_0=\begin{bmatrix} 36 & & & & & sym & \\ -36 & 36 & & & & & \\ 0 & 0 & 36 & & & & \\ 0 & 0 & -36 & 36 & & & \\ 0 & 0 & -3L_e & 3L_e & 4L_e^2 & & \\ 0 & 0 & -3L_e & 3L_e & -L_e^2 & 4L_e^2 & \\ 3L_e & -3L_e & 0 & 0 & 0 & 0 & 4L_e^2 \\ 3L_e & -3L_e & 0 & 0 & 0 & 0 & -L_e^2 \quad 4L_e^2 \end{bmatrix} \quad \text{(A.6)}$$

$$\left[\mathbf{M}_r\right]_1=\begin{bmatrix} 0 & & & & & sym & \\ 0 & 0 & & & & & \\ 0 & 0 & 0 & & & & \\ 0 & 0 & 0 & 0 & & & \\ 0 & 0 & 15L_e & -15L_e & 5L_e^2 & & \\ 0 & 0 & 15L_e & -15L_e & -5L_e^2 & 5L_e^2 & \\ -15L_e & 15L_e & 0 & 0 & 0 & 0 & 5L_e^2 \\ -15L_e & 15L_e & 0 & 0 & 0 & -5L_e^2 & 5L_e^2 \end{bmatrix} \quad \text{(A.7)}$$

$$\left[\mathbf{M}_r\right]_2=\begin{bmatrix} 0 & & & & & sym & \\ 0 & 0 & & & & & \\ 0 & 0 & 0 & & & & \\ 0 & 0 & 0 & 0 & & & \\ 0 & 0 & 0 & 0 & 10L_e^2 & & \\ 0 & 0 & 0 & 0 & 5L_e^2 & 10L_e^2 & \\ 0 & 0 & 0 & 0 & 0 & 0 & 10L_e^2 \\ 0 & 0 & 0 & 0 & 0 & 0 & 5L_e^2 \quad 10L_e^2 \end{bmatrix} \quad \text{(A.8)}$$

A.3 Elementary gyroscopic matrix for a FG shaft

$$\left[\mathbf{G}^{e}\right]=\frac{2m(y)R^{2}}{120L_{e}\left\{1+\Phi(y,T)\right\}^{2}}[\mathbf{G}]_{0}+\frac{2m(y)R^{2}\Phi(y,T)}{120L_{e}\left\{1+\Phi(y,T)\right\}^{2}}[\mathbf{G}]_{1}+\frac{2mR^{2}\left\{\Phi(y,T)\right\}^{2}}{120L_{e}\left\{1+\Phi(y,T)\right\}^{2}}[\mathbf{G}]_{2} \tag{A.9}$$

$$[\mathbf{G}]_{0}=\begin{bmatrix}
0 & & & & \textit{skew} & \textit{sym} & & \\
0 & 0 & & & & & & \\
36 & 36 & 0 & & & & & \\
-36 & 36 & 0 & 0 & & & & \\
-3L_e & -3L_e & 0 & 0 & 0 & & & \\
-3L_e & 3L_e & 0 & 0 & 0 & 0 & & \\
0 & 0 & -3L_e & -3L_e & 4L_e^2 & L_e^2 & 0 & \\
0 & 0 & -3L_e & 3L_e & -L_e^2 & 4L_e^2 & 0 & 0
\end{bmatrix} \tag{A.10}$$

$$[\mathbf{G}]_{2}=\begin{bmatrix}
0 & & & & \textit{skew} & \textit{sym} & & \\
0 & 0 & & & & & & \\
0 & 0 & 0 & & & & & \\
0 & 0 & 0 & 0 & & & & \\
0 & 0 & 0 & 0 & 0 & & & \\
0 & 0 & 0 & 0 & 0 & 0 & & \\
0 & 0 & 0 & 0 & 10L_e^2 & 5L_e^2 & 0 & \\
0 & 0 & 0 & 0 & 5L_e^2 & 10L_e^2 & 0 & 0
\end{bmatrix} \tag{A.11}$$

$$[\mathbf{G}]_{1}=\begin{bmatrix}
0 & & & & & \textit{skew} & \textit{sym} & \\
0 & 0 & & & & & & \\
0 & 0 & 0 & & & & & \\
0 & 0 & 0 & 0 & & & & \\
15L_e & -15L_e & 0 & 0 & 0 & & & \\
15L_e & -15L_e & 0 & 0 & 0 & 0 & & \\
0 & 0 & 15L_e & -15L_e & 5L_e^2 & -5L_e^2 & 0 & \\
0 & 0 & 15L_e & -15L_e & -5L_e^2 & 5L_e^2 & 0 & 0
\end{bmatrix} \tag{A.12}$$

A.4 Elementary stiffness matrix for a FG shaft

$$\left[\mathbf{K}^{e}\right]=\frac{E\left(y,T\right)I}{L_e^3\left\{1+\Phi\left(y,T\right)\right\}}\left[\mathbf{K}\right]_0+\frac{E\left(y,T\right)I\Phi\left(y,T\right)}{L_e^3\left\{1+\Phi\left(y,T\right)\right\}}\left[\mathbf{K}\right]_1 \tag{A.13}$$

$$\left[\mathbf{K}\right]_0=\begin{bmatrix} 12 & & & & & & & \\ -12 & 12 & & & & & & \\ 0 & 0 & 12 & & & & & \\ 0 & 0 & -12 & 12 & & & & \\ 0 & 0 & -6L_e & 6L_e & 4L_e^2 & & & \\ 0 & 0 & -6L_e & 6L_e & 2L_e^2 & 4L_e^2 & & \\ 6L_e & -6L_e & 0 & 0 & 0 & 0 & 4L_e^2 & \\ 6L_e & -6L_e & 0 & 0 & 0 & 0 & 2L_e^2 & 4L_e^2 \end{bmatrix} \quad \textit{sym} \tag{A.14}$$

$$\left[\mathbf{K}\right]_1=\begin{bmatrix} 0 & & & & & & & \\ 0 & 0 & & & & & & \\ 0 & 0 & 0 & & & & & \\ 0 & 0 & 0 & 0 & & & & \\ 0 & 0 & 0 & 0 & L_e^2 & & & \\ 0 & 0 & 0 & 0 & -L_e^2 & L_e^2 & & \\ 0 & 0 & 0 & 0 & 0 & 0 & L_e^2 & \\ 0 & 0 & 0 & 0 & 0 & 0 & -L_e^2 & L_e^2 \end{bmatrix} \quad \textit{sym} \tag{A.15}$$

A.5 Elementary matrices for a rigid disc

Elementary translation $\left[\mathbf{M}_t^d\right]$ and rotational mass matrices $\left[\mathbf{M}_r^d\right]$ is given

$$\left[\mathbf{M}_t^d\right]=\begin{bmatrix} m^d & 0 & 0 & 0 \\ 0 & m^d & 0 & 0 \\ 0 & 0 & 0 & 0 \\ 0 & 0 & 0 & 0 \end{bmatrix} \quad \text{and} \quad \left[\mathbf{M}_r^d\right]=\begin{bmatrix} 0 & 0 & 0 & 0 \\ 0 & 0 & 0 & 0 \\ 0 & 0 & I_D^d & 0 \\ 0 & 0 & 0 & I_D^d \end{bmatrix} \tag{A.16}$$

Elementary gyroscopic matrix $\left[\mathbf{G}^d\right]$ and nodal displacement vector $\left\{\mathbf{P}^d\right\}$ is given

$$\left[\mathbf{G}^d\right]=\begin{bmatrix}0&0&0&0\\0&0&0&0\\0&0&0&-I_P^d\\0&0&I_P^d&0\end{bmatrix} \quad \text{and} \quad \left\{\mathbf{P}^d\right\}=\begin{Bmatrix}v\\w\\\beta\\\Gamma\end{Bmatrix} \tag{A.17}$$

A.6 Elementary circulatory stiffness matrix for a FG shaft

$$\left[\mathbf{K}_c^e\right]=\frac{E(y,T)I}{L_e^3\{1+\Phi(y,T)\}}\left[\mathbf{K}_c\right]_0+\frac{E(y,T)I\Phi(y,T)}{L_e^3\{1+\Phi(y,T)\}}\left[\mathbf{K}_c\right]_1 \tag{A.18}$$

$$\left[\mathbf{K}_c\right]_0=\begin{bmatrix}0&&&&&\textit{skew}&\textit{sym}\\0&0&&&&&\\-12&12&0&&&&\\12&-12&0&0&&&\\6L_e&-6L_e&0&0&0&&\\6L_e&-6L_e&0&0&0&0&\\0&0&6L_e&-6L_e&-4L_e^2&-2L_e^2&0\\0&0&6L_e&-6L_e&-2L_e^2&-4L_e^2&0&0\end{bmatrix} \tag{A.19}$$

$$\left[\mathbf{K}_c\right]_1=\begin{bmatrix}0&&&\textit{skew}&\textit{sym}\\0&0&&&\\0&0&0&&\\0&0&0&0&\\0&0&0&0&0&\\0&0&0&0&0&0&\\0&0&0&0&-L_e^2&L_e^2&0\\0&0&0&0&L_e^2&-L_e^2&0&0\end{bmatrix} \tag{A.20}$$

Appendix B: Pseudo-code

MATLAB Pseudo-codes for computational simulations

B.1 Main program

a. ***General inputs***: element number, boundary condition and layer number
b. ***Input for shaft***: length, inner and outer diameter and thickness
c. ***Input for disk***: thickness, inner and outer radisus, density
d. ***Input for bearing***: stiffness and damping coefficients
e. Material property variation function
f. Elementary matrices functions for FG shaft
g. Gyroscopic matrix function for disc
h. General (simply supported, cantilever and fixed) and flexible boundary conditions
i. Solutions for eigenvalue problem and determination of natural frequencies, whirling frequencies, critical speeds and threshold speeds

B.2 Main functions

a. ***Function***: Material property variation

   Input: temperature coefficients value, layer number, inner and outer diameter, temperature variation function, and material gradient index

   Output: material properties at any temperature gradients and radial position

b. ***Function***: Elementary mass, stiffness and circulatory stiffness matrices

   Input: element number, length and material property variation function

   Output: elementary mass, stiffness and circulatory stiffness matrices

c. ***Function***: Elementary gyroscopic matrices

   Input: element number, node position, disc position and disc number

   Output: elementary gyroscopic matrices

d. Function: Elementary cracked stiffness matrix

   Input: element number, length, material property variation function and LFCs function

   Output: elementary cracked stiffness matrix

B.3 Sub functions

a. ***Function***: LFCs

Input: crack depth, layer number, inner and outer diameter, material gradient index, junction temperature, material properties, and crack half width.

Output: magnitude of direct and cross coupled LFCs

b. ***Function***: Temperature variation

Input: layer number, inner and outer diameter, material gradient index, inner and outer surface temperature, and inner and outer surface thermal conductivity.

Output: temperature variation along the radial direction of FG shafts.

References

[1] **M.B. Bever** and **P.E. Duwez**, Invited review gradients in composite materials, Materials Science and Engineering, 10 (1972) 1-8.

[2] **M. Shen** and **M.B. Bever**, Gradients in polymeric materials, Journal of Materials Science 7(7) (1972) 741-746.

[3] **M. Niino**, **T. Hirai** and **R. Watanabe**, The functionally gradient materials, Journal of Japan Society of Composite Materials 13 (1987) 254-264.

[4] **M. Koizumi**, The concept of FGM, Ceramic Transactions 34 (1993) 3-10.

[5] **S. Uemura**, The activities of FGM on new applications, Materials Science Forum 423-425 (2003) 1-10.

[6] **J. Aboudi**, **M.J. Pindera** and **S.M. Arnold**, Higher-order theory for functionally graded material, Composites Part B: Engineering 30(8) (1999) 777-832.

[7] **Y. Miyamoto**, **W.A. Kaysser**, **B.H. Rabin**, **A. Kawasaki** and **R.G. Ford**, (Editors), *Functionally Graded Materials: Design, Processing and Application*, Kluwer Academic Publishers, London, (1999).

[8] **S. Suresh** and **A. Mortensen**, *Fundamentals of Functionally Graded Materials: Processing and Thermomechanical Behavior of Graded Metals and Metal-Ceramic Composites*, IOM Communications Limited, London, (1998).

[9] **V. Birman** and **L.W. Byrd**, Modeling and analysis of functionally graded materials and structures, Applied Mechanics Review 60(5) (2007) 195-216.

[10] **X. Qian** and **D. Dutta**, Design of heterogeneous turbine blade, Computer-Aided Design 35(3) (2003) 319-329.

[11] **A.M. Afsar** and **J. Go**, Finite element analysis of thermoelastic field in a rotating FGM circular disk, Journal of Applied Mathematical Modelling 34(11) (2010) 3309-3320.

[12] **P.M. Przybyowicz**, Stability of activity controlled rotating shaft made of functionally graded materials, Journal of Theoretical and Applied Mechanics 43(3) (2005) 609-630.

[13] **A. Gupta** and **M. Talha**, Recent development in modeling and analysis of functionally graded materials and structures, Progress in Aerospace Sciences 79 (2015) 1-14.

[14] **S. Dunkerley**, On the whirling and vibration of shafts, Philosophical Transactions of the Royal Society of London. A 185 (1883) 279-359.

[15] **H.H. Jeffcott**, The lateral vibration of whirling shafts in the neighborhood of a whirling speed: the effect of want of balance, The London, Edinburgh, and Dublin Philosophical Magazine and Journal of Science Series 6 37(219) (1919) 304-314.

[16] **A. Stodola**, *Dampf- und Gasturbinen*, Verlag von Julius Springer, Berlin, (1924). *English Translation, Steam and Gas Turbines*, Mc Graw-Hill Book Co, New York, (1927).

[17] **A.D. Nashif**, **D.I.G. Jones** and **J.P. Henderson**, *Vibration Damping*, John Wiley & Sons, Inc., New York, (1985).

[18] **C.W. Bert**, Material damping: An introductory review of mathematic measures and experimental technique, Journal of Sound and Vibration 29(2) (1973) 129-153.

[19] **A.L. Kimball**, *Vibration prevention in engineering*, John Wiley & Sons, London (1932).

[20] **E.S. Zorzi** and **H.D. Nelson**, Finite element simulation of rotor-bearing systems with internal damping, ASME Transactions: Journal of Engineering for Power 99(1) (1977) 71-76.

[21] **G. Sabnavis**, **R.G. Kirk**, **M. Kasarda** and **D. Quinn**, Cracked shaft detection and diagnostics: A literature review, The Shock and Vibration Digest 36(4) (2004) 287-296.

[22] **A.D. Dimarogonas**, *Dynamic response of cracked rotors*, General Electric Co., Internal report, Schenectady, New York, USA, (1970).

[23] **N. Bachschmid**, **P. Pennacchi** and **E. Tanzi**, *Cracked Rotors: A Survey on Static and Dynamic Behaviour Including Modelling and Diagnosis*, Springer-Verlag, Berlin Heidelberg, (2010).

[24] **G.R. Irwin**, Fracture dynamics, Fracture of metals, American Society for Metals, Cleveland (1948) 147-166.

[25] **H. Tada**, **P.C. Paris** and **G.R. Irwin**, *The Stress Analysis of Cracks Handbook*, Del Research Corporation, Hellertown, Pennsylvania, USA, (1973).

[26] **J.N. Reddy**, *Thermomechanical behavior of functionally graded materials*, CML Report 98-01, Washington, DC (1998) 1-78.

[27] **J.N. Reddy** and **C.D. Chin**, Thermoelastical analysis of functionally graded cylinders and plates, Journal of Thermal Stresses 21 (1998) 593-626.

[28] **A. Chakraborty**, **S. Gopalakrishnana** and **J.N. Reddy**, A new beam finite element for the analysis of functionally graded materials, International Journal of Mechanical Sciences 45(3) (2003) 519-539.

[29] **G.H. Rahimi** and **A.R. Davoodinik**, Thermal behavior analysis of the functionally graded Timoshenko's beam, IUST International Journal of Engineering Science 19(5-1) (2008) 105-113.

[30] **A. Mahi**, **E.A.A. Bedia**, **A. Tounsi** and **I. Mechab**, An analytical method for temperature-dependent free vibration analysis of functionally graded beams with general boundary conditions, Composite Structures 92(8) (2010) 1877-1887.

[31] **N. Wattanasakulpong**, **B.G. Prusty** and **D.W. Kelly**, Thermal buckling and elastic vibration of third-order shear deformable functionally graded beams, International Journal of Mechanical Sciences 53(9) (2011) 734-743.

[32] **K.S. Na** and **J.H. Kim**, Three-dimensional thermomechanical buckling of functionally graded materials, AIAA Journal 43(7) (2005) 1605-1612.

[33] **S. Li**, **J. Zhang** and **Y. Zhao**, Thermal post-buckling of functionally graded material Timoshenko beams, Applied Mathematics and Mechanics 27(6) (2006) 803-810.

[34] **T. Akis** and **A.N. Eraslan**, Exact solution of rotating FGM shaft problem in the elastoplastic state of stress, Archive of Applied Mechanics 77(10) (2007) 745-765.

[35] **Y. Kiani** and **M.R. Eslami**, Thermal buckling analysis of functionally graded material beams, International Journal of Mechanics and Materials in Design 6(3) (2010) 229-238.

[36] **Y. Kiani** and **M.R. Eslami**, Thermomechanical buckling of temperature-dependent FGM beams, Latin American Journal of Solids and Structures 10 (2013) 223-246.

[37] **H. Argeso** and **A.N. Eraslan**, A computational study on functionally graded rotating solid shafts, International Journal for Computational Methods in Engineering Science and Mechanics 8(6) (2007) 391-399.

[38] **M. Aydogdu** and **V. Taskin**, Free vibration analysis of functionally graded beams with simply supported edges, Materials & Design 28(5) (2007) 1651-1656.

[39] **S. Kapuria**, **M. Bhattacharyya** and **A.N. Kumar**, Bending and free vibration response of layered functionally graded beams: a theoretical model and its experimental validation, Composite Structures 82(3) (2008) 390-402.

[40] **X.F. Li**, A unified approach for analyzing static and dynamic behaviors of functionally graded Timoshenko and Euler-Bernoulli beams, Journal of Sound and Vibration 318(4-5) (2008) 1210-1229.

[41] **M.T. Piovan** and **R. Sampaio**, A study on the dynamics of rotating beams with functionally graded properties, Journal of Sound and Vibration 327(1-2) (2009) 134-143.

[42] **A.E. Alshorbagy**, **M.A. Eltaher** and **F.F. Mahmoud**, Free vibration characteristics of a functionally graded beam by finite element method, Applied Mathematical Modelling 35(1) (2011) 412-425.

[43] **A. Shahba**, **R. Attarnejad**, **M.T. Marvi** and **S. Hajilar**, Free vibration and stability analysis of axially functionally graded tapered Timoshenko beams with classical and non-classical boundary conditions, Composites Part B: Engineering 42(4) (2011) 801-808.

[44] **M. Sheihlou**, **G. Rezazadeh** and **R. Shabani**, Study of torsional vibration of a radially FGM micro-shaft, International Journal of Mechanic Systems Engineering 3(1) (2013) 1-5.

[45] **D. Gayen** and **T. Roy**, Finite element based vibration analysis of functionally graded spinning shaft system, Journal Mechanical Engineering Science Part C 228(18) (2014) 3306-3321.

[46] **A. Boukhalfa**, Dynamic analysis of a spinning functionally graded material shaft by the p-version of the finite element method, Latin American Journal of Solids and Structures 11 (2014) 2018-2038.

[47] **Y. Huang**, **T. Wang**, **Y. Zhao** and **P. Wang**, Effect of axially functionally graded material on whirling frequencies and critical speeds of a spinning Timoshenko beam, Composite Structures 192 (2018) 355-367.

[48] **F.M. Dimentberg**, *Flexural Vibrations of Rotating Shafts*, Butterworths, London (1961).

[49] **J.W. Lund**, The stability of an elastic rotor in journal bearings with flexible, damped supports, ASME Transactions: Journal of Applied Mechanics 32(4) (1965) 911-920.

[50] **E. Gunter**, *Dynamic stability of rotor bearing systems*, NASA Paper No. SP-113 (1966).

[51] **R.L. Ruhl** and **J.F. Booker**, A finite element model for distributed parameter turbogenerator system, ASME Transactions: Journal of Engineering for Industry 94(1) (1972) 126-132

[52] **J.W. Lund**, Stability and damped critical speed of a flexible rotor in fluid-film bearings, ASME Transactions: Journal of Engineering for Industry 96(2) (1974) 509-517.

[53] **J.S. Rao**, *Rotor dynamics*, John Wiley Eastern Ltd., New Delhi, (1983).

[54] **M.J. Goodwin**, *Dynamics of Rotor-Bearing Systems*, Unwin Hyman, London, (1989).

[55] **G. Genta**, *Dynamics of Rotating Systems*, Springer Science, New York, (2005).

[56] **C. Sujatha**, *Vibration and Acoustics: Measurement and Signal Analysis*, Tata McGraw-Hill Education Private Limited, New Delhi, (2009).

[57] **M.I. Friswell**, **J.E.T. Penny**, **S.D. Garvey** and **A.W. Lees**, *Dynamics of Rotating Machines*, Cambridge University Press, New York, (2010).

[58] **R. Tiwari**, *Rotor Systems: Analysis and Identification*, CRC Press, Boca Raton, Florida, (2017).

[59] **R.L. Ruhl**, *Dynamics of Distributed Parameter Rotor Systems: Transfer Matrix and Finite Element Techniques*, Doctoral dissertation, Cornell University, Ithaca, New York, (1970).

[60] **A.D. Dimarogonas**, A general method for stability analysis of rotating shafts, Ingenieur-Archiv 44(1) (1975) 9-20.

[61] **P.N. Bansal** and **R. G. Kirk**, Stability and damped critical speeds of rotor-bearing systems, ASME Transactions: Journal of Engineering for Industry 97(4) (1975) 1325-1332.

[62] **H.D. Nelson** and **J.M. McVaugh**, The dynamics of rotor-bearing systems using finite elements, ASME Transactions: Journal of Engineering for Industry 98(2) (1976) 593-600.

[63] **H.D. Nelson**, A finite rotating shaft element using Timoshenko beam theory, ASME Transactions: Journal of Mechanical Design 102(4) (1980) 793-803.

[64] **D.A. Glasgow** and **H.D. Nelson**, Stability analysis of rotor-bearing systems using component mode synthesis, ASME Transactions: Journal of Mechanical Design 102(2) (1980) 352-359.

[65] **H.N. Özgüven** and **Z.L. Özkan**, Whirl speeds and unbalance response of multibearing rotors using finite elements, ASME Transactions: Journal of Vibration, Acoustics, Stress, and Reliability in Design 106(1) (1984) 72-79.

[66] **L.W. Chen** and **D.M. Ku**, Dynamic stability analysis of a rotating shaft by the finite element method, Journal of Sound and Vibration 143(1) (1990) 143-151.

[67] **L.W. Chen** and **D.M. Ku**, Finite element analysis of natural whirl speeds of rotating shafts, Computers & Structures 40(3) (1991) 741-747.

[68] **H.L. Wettergren** and **K.O. Olsson**, Dynamic instability of a rotating asymmetric shaft with internal viscous damping supported on anisotropic bearings, Journal of Sound and Vibration 195(1) (1996) 75-84.

[69] **D.S. Kumar**, **C. Sujatha** and **N. Ganesan**, A Modified semi-analytical approach towards the modelling of shaft-disc system, Computers and Structures 61(1) (1996) 189-191.

[70] **D.S. Kumar**, **C. Sujatha** and **N. Ganesan**, Disc flexibility effects in rotor bearing systems, Computers and Structures 62(4) (1997) 715-719.

[71] **D.M. Ku**, Finite element analysis of whirl speeds for rotor-bearing systems with internal damping, Mechanical Systems and Signal Processing 12(5) (1998) 599-610.

[72] **A.S. Das**, **M.C. Nighil**, **J.K. Dutt** and **H. Irretier**, Vibration control and stability analysis of rotor-shaft system with electromagnetic exciters, Mechanism and Machine Theory 43(10) (2008) 1295-131.

[73] **R. Srinath**, **A. Sarkar** and **A.S. Sekhar**, Instability of asymmetric continuous shaft system, Journal of Sound and Vibration 383 (2016) 397-413.

[74] **A.K. Jain**, **V. Rastogi** and **A.K. Agrawal**, A novel approach to study effects of asymmetric stiffness on parametric instabilities of multi-rotor-system, Journal of Sound and Vibration 413 (2018) 159-172.

[75] **A.D. Dimarogonas**, **S.A. Paipetis** and **T.G. Chondros**, *Analytical Methods in Rotor Dynamics*, Springer Science, New York, (2013).

[76] **J. Wauer**, On the dynamics of cracked rotors: literature survey, Applied Mechanics Reviews 43(1) (1990) 13-17.

[77] **R. Gasch**, A survey of the dynamic behaviour of a simple rotating shaft with a transverse crack, Journal of Sound and Vibration 160(2) (1993) 313-332.

[78] **A.D. Dimarogonas**, Vibration of cracked structures: a state of the art review, Engineering Fracture Mechanics 55(5) (1996) 831-857.

[79] **C.A. Papadopoulos**, The strain energy release approach for modeling cracks in rotors: A state of the art review, Mechanical Systems and Signal Processing 22(4) (2008) 763-789.

[80] **V.H. Cortínez** and **F.E. Dotti**, Mode I stress intensity factor for cracked thin-walled open beams, Engineering Fracture Mechanics 110 (2013) 249-257.

[81] **H. Yuan**, **W.J. Liu** and **Y.J. Xie**, Mode-I stress intensity factors for cracked special-shaped shells under bending, Engineering Fracture Mechanics 207 (2019) 131-148.

[82] **S.D. Akbas**, Large deflection analysis of edge cracked simple supported beams, Structural Engineering and Mechanics 54(3) (2015) 433-451.

[83] **S.D. Akbas**, Analytical solutions for static bending of edge cracked micro beams, Structural Engineering and Mechanics 59(3) (2016) 579-599.

[84] **M.A. Khorshidi**, **M. Shaat**, **A. Abdelkefi** and **M. Shariati**, Nonlocal modeling and buckling features of cracked nanobeams with von Karman nonlinearity, Applied Physics A 123(2) (2017), Article No. 62. DOI: doi.org/10.1007/s00339-016-0658-7.

[85] **A. Alijani**, **M.M. Abadi**, **A. Darvizeh** and **M.Kh. Abadi**, Theoretical approaches for bending analysis of founded Euler–Bernoulli cracked beams, Archive of Applied Mechanics 88(6) (2018) 875-895.

[86] **I.W. Mayes** and **W.G.R. Davies**, Analysis of the response of a multi-rotor-bearing system containing a transverse crack in a rotor, ASME Transactions: Journal of Vibration, Acoustics, Stress, and Reliability in Design 106(1) (1984) 139-145.

[87] **C.A. Papadopoulos** and **A.D. Dimarogonas**, Coupled longitudinal and bending vibrations of a rotating shaft with an open crack, Journal of Sound and Vibration 117(1) (1987) 81-93.

[88] **N. Papaeconomou** and **A. Dimarogonas**, Vibration of cracked beams, Computational Mechanics 5(2-3) (1989) 88-94.

[89] **O.S. Jun**, **H.J. Eun**, **Y.Y. Earmme** and **C.W. Lee**, Modelling and vibration analysis of a simple rotor with a breathing crack, Journal of Sound and Vibration 155(2) (1992) 273-290.

[90] **W.M. Ostachowicz** and **M. Krawwczuk**, Coupled torsional and bending vibrations of a rotor with an open crack, Archives of Applied Mechanics 62(3) (1992) 191-201.

[91] **S.M. Cheng**, **X.J. Wu**, **W. Wallace** and **A.S.J. Swamidas**, Vibrational response of a beam with a breathing crack, Journal of Sound and Vibration 225(1) (1999) 201-208.

[92] **T.G. Chondros**, **A.D. Dimarogonas** and **J. Yao**, Vibration of a beam with a breathing crack, Journal of Sound and Vibration 239(1) (2001) 57-67.

[93] **J.K. Sinha** and **M.I. Friswell,** Simulation of the dynamic response of a cracked beam. Computers and Structures 80(18-19) (2002) 1473-1476.

[94] **A.K. Darpe**, **A. Chawla** and **K. Gupta**, Analysis of the response of a cracked Jeffcott rotor to axial excitation, Journal of Sound and vibration 249(3) (2002) 429-445.

[95] **A.K. Darpe**, **K. Gupta** and **A. Chawla**, Coupled bending, longitudinal and torsional vibrations of a cracked rotor, Journal of Sound and Vibration 269(1-2) (2004) 33-60.

[96] **C.A. Papadopoulos**, Some comments on the calculations of the local flexibility of cracked shafts, Journal of Sound and Vibration 278 (2004) 1205-1211.

[97] **J. Sinou** and **A.W. Lees**, The influence of cracks in rotating shafts, Journal of Sound and Vibration 285(4-5) (2005) 1015-1037.

[98] **A.C. Chasalevris** and **C.A. Papadopoulos**, Cross coupled bending vibrations of rotating shaft due to a transverse breathing crack, IFToMM 7th International Conference on Rotor Dynamics (2006) 25-28.

[99] **J. Sinou** and **A.W. Lees**, A non-linear study of a cracked rotor, European Journal of Mechanics-A: Solids 26(1) (2007) 152-170.

[100] **M. Kisa** and **M.A. Gurel**, Free vibration analysis of uniform and stepped cracked beams with circular cross sections, International Journal of Engineering Science 45(2-8) (2007) 364-380.

[101] **S. El Arem** and **H. Maitournama**, Cracked beam finite element for rotating shaft dynamics and stability analysis, Journal of Mechanics of Materials and Structures 3(5) (2008) 893-910.

[102] **G.I. Giannopoulos**, **S.K. Georgantzinos** and **N.K. Anifantis**, Coupled vibration response of a shaft with a breathing crack, Journal of Sound and Vibration 336 (2015) 191-206.

[103] **W.M. Ostachowicz** and **M. Krawczuk**, Analysis of the effect of cracks on the natural frequencies of a cantilever beam, Journal of sound and vibration 150(2) (1991) 191-201.

[104] **T.C. Tsai** and **Y.Z. Wang**, The vibration of a multi-crack rotor, International Journal of Mechanical Sciences 39(9) (1997) 1037-1053.

[105] **A.S. Sekhar**, Vibration characteristics of a cracked rotor with two open cracks, Journal of Sound and Vibration 223(4) (1999) 497-512.

[106] **A. K. Darpe**, **K.Gupta** and **A. Chawla**, Dynamics of a two-crack rotor, Journal of Sound and Vibration 259(3) (2003) 649-675.

[107] **A.C. Chasalevris** and **C.A. Papadopoulos**, Identification of multiple cracks in beams under bending, Mechanical Systems and Signal Processing 20(7) (2006) 1631-1673.

[108] **M. Kisa** and **M.A. Gurel**, Modal analysis of multi cracked beams with circular cross section, Engineering Fracture Mechanics 73(8) (2006) 963-977.

[109] **K. Aydin**, Vibratory characteristics of axially-loaded Timoshenko beams with arbitrary number of cracks, Journal of Vibration and Acoustics 129(3) (2007) 341-354.

[110] **H. Khorrami**, **S. Rakheja** and **R. Sedaghati**, Vibration behavior of a two-crack shaft in a rotor disc-bearing system, Mechanism and Machine Theory 113 (2017) 67-84.

[111] **J.P. Spagnol**, **H. Wu** and **K. Xiao**, Dynamic response of a cracked rotor with an unbalance influenced breathing mechanism, Journal of Mechanical Science and Technology 32(1) (2018) 57-68.

[112] **Y. Yang**, **Q. Wu**, **Y. Wang**, **W. Qin** and **K. Lu**, Dynamic characteristics of cracked uncertain hollow-shaft, Mechanical Systems and Signal Processing 124 (2019) 36-48.

[113] **J.K. Sinha**, **M.I. Friswell** and **S. Edwards**, Simplified models for the location of cracks in beam structures using measured vibration data. Journal of Sound and Vibration 251(1) (2002) 13-38.

[114] **S.K. Singh** and **R. Tiwari**, Identification of a multi-crack in a shaft system using transverse frequency response functions, Mechanism and Machine Theory 45 (2010) 1813-1827.

[115] **J.K. Sinha** and **K. Elbhbah**, A future possibility of vibration based condition monitoring of rotating machines, Mechanical Systems and Signal Processing 34 (2013) 231-240.

[116] **C.A. Papadopoulos** and **A.D. Dimarogonas**, Stability of cracked rotors in the coupled vibration mode, ASME Transactions: Journal of Vibration, Acoustics, Stress, and Reliability in Design 110 (1988) 356-359.

[117] **S.C. Huang**, **Y.M. Huang** and **S.M. Shieh**, Vibration and stability of a rotating shaft containing a transverse crack, Journal of Sound and Vibration 162(3) (1993) 387-401.

[118] **L. Chen** and **H. Chen**, Stability analyses of a cracked shaft subjected to the end load, Journal of Sound and Vibration 188(4) (1995) 497-513.

[119] **C. Guo**, **M.A. AL-Shudeifat**, **J. Yan**, **L.A. Bergman**, **D.M. McFarland** and **E.A. Butcher**, Stability analysis for transverse breathing cracks in rotor systems, European Journal of Mechanics - A/Solids 42 (2013) 27-34.

[120] **A.S Sekhar** and **J.K Dey**, Effects of cracks on rotor system instability, Mechanism and Machine Theory 35(12) (2000) 1657-1674.

[121] **Q. Han** and **F. Chu**, Parametric instability of a rotor-bearing system with two breathing transverse cracks, European Journal of Mechanics - A/Solids 36 (2012) 180-190.

[122] **H. Peng**, **Q. He**, **P. Zhai** and **Y. Zhen**, Stability analysis of an open cracked rotor with the anisotropic rotational damping in rotating operation, Applied Mathematical Modelling 45 (2017) 405-421.

[123] **F. Erdogan**, Fracture mechanics of functionally graded materials, Composite Engineering 5(7) (1995) 753-770.

[124] **Z.H. Jin** and **R.C. Batra**, Some basic fracture mechanics concepts in functionally graded materials, Journal of the Mechanics and Physics of Solids 44(8) (1996) 1221-1235.

[125] **P. Gu** and **R.J. Asaro**, Cracks in functionally graded materials, International Journal of Solids and Structures 34(1) (1997) 1-17.

[126] **N. Noda** and **Z.H. Jin**, Thermal stress intensity factors for a crack in a strip of a functionally gradient material, International Journal of Solids and Structures 30(8) (1993) 1039-1056.

[127] **F. Erdogan** and **B.H. Wu**, The surface crack problem for a plate with functionally graded properties, ASME Transactions: Journal of Applied Mechanics 64(3) (1997) 449-456.

[128] **B.L. Wang**, **J.C. Han** and **S.Y. Du**, Functionally graded penny-shaped cracks under dynamic loading, Theoretical and Applied Fracture Mechanics 32(3) (1999) 165-175.

[129] **B.L. Wang**, **J.C. Han** and **S.Y. Du**, Crack problems for functionally graded materials under transient thermal loading, Journal of Thermal Stresses 23(2) (2000) 143-168.

[130] **B.L. Wang**, **Y.W. Mai** and **N. Noda**, Fracture mechanics analysis model for functionally graded materials with arbitrarily distributed properties, International Journal of Fracture 116(2) (2002) 161-177.

[131] **Z.H. Jin**, Fracture mechanics of functionally graded materials, Advances in Mechanics and Mathematics 4 (2003) 1-108.

[132] **J. Yang** and **Y. Chen**, Free vibration and buckling analyses of functionally graded beams with edge cracks, Composite Structures 83(1) (2008) 48-60.

[133] **D. Broek**, *Elementary Engineering Fracture Mechanics*, Martinus Nijhoff Publishers, Dordrecht, (1986).

[134] **L.L. Ke**, **J. Yang**, **S. Kitipornchai** and **Y. Xiang**, Flexural vibration and elastic buckling of a cracked Timoshenko beam made of functionally graded materials, Mechanics of Advanced Materials and Structures 16(6) (2009) 488-502.

[135] **L.L. Ke**, **J. Yang** and **S. Kitipornchai**, Postbuckling analysis of edge cracked functionally graded Timoshenko beams under end shortening, Composite Structures 90(2) (2009) 152-160.

[136] **K. Sherafatnia**, **G.H. Farrahi** and **S.A. Faghidian**, Analytic approach to free vibration and buckling analysis of functionally graded beams with edge cracks using four engineering beam theories, International Journal of Engineering 27(6) (2014) 979-990.

[137] **J. Yang**, **Y. Chen**, **Y. Xiang** and **X.L. Jia**, Free and forced vibration of cracked inhomogeneous beams under an axial force and a moving load, Journal of Sound and Vibration 312(1-2) (2008) 166-181.

[138] **M.S. Matbuly**, **O. Ragb** and **M. Nassar**, Natural frequencies of a functionally graded cracked beam using the differential quadrature method, Applied Mathematics and Computation 215(6) (2009) 2307-2316.

[139] **H.Z. Ferezqi**, **M. Tahani** and **H.E. Toussi**, Analytical approach to free vibrations of cracked Timoshenko beams made of functionally graded materials, Mechanics of Advanced Materials and Structures 17(5) (2010) 353-365.

[140] **R. Zhang**, Free vibration of cracked functionally graded beams with piezoelectric patches, Journal of Theoretical and Applied Mechanics 41(3) (2011) 3-18.

[141] **T. Yan** and **J. Yang**, Forced vibration of edge-cracked functionally graded beams due to a transverse moving load, Procedia Engineering 14 (2011) 3293-3300.

[142] **D. Wei**, **Y. Liu** and **Z. Xiang**, An analytical method for free vibration analysis of functionally graded beams with edge cracks, Journal of Sound and Vibration 331(7) (2012) 1686-1700.

[143] **K. Aydin**, Free vibration of functionally graded beams with arbitrary number of surface cracks, European Journal of Mechanics A/Solids 42 (2013) 112-124.

[144] **S. Kitipornchai**, **L. Ke**, **J. Yang** and **Y. Xiang**, Nonlinear vibration of edge cracked functionally graded Timoshenko beams, Journal of Sound and Vibration 324(3-5) (2009) 962-982.

[145] **J. Yang** and **T. Yan**, Nonlinear frequency response of parametrically excited functionally graded Timoshenko beams with a crack, Materials Science and Engineering 10(1) (2010) 1-10.

[146] **L.L. Ke**, **Y.S. Wang**, **J. Yang**, **S. Kitipornchai** and **F. Alam**, Nonlinear vibration of edged cracked FGM beams using differential quadrature method, Science China Physics, Mechanics and Astronomy 55(11) (2012) 2114-2121.

[147] **S.D. Akbas**, Geometrically nonlinear static analysis of edge cracked Timoshenko beams composed of functionally graded material, Mathematical Problems in Engineering 2013 (2013) 1-14.

[148] **D. Chakraborty**, **M. Ranjan** and **A. Kumar**, Dynamic analysis of functionally graded shell structure using finite element method, 9th International Conference on Mechanical Engineering (ICME-2011), December 18-20, 2011, Dhaka, Bangladesh.

[149] **M. Ranjan** and **D. Chakraborty**, Finite element analysis of functionally graded shell structures, Proceedings of 3rd Asian Conference on Mechanics of Functional Materials and Strcutures (ACMFMS 2012), December 5-8, 2012, IIT Delhi, India.

[150] **M. Amirpour**, **R. Das** and **E.I.S. Flores**, Analytical solutions for elastic deformation of functionally graded thick plates with in-plane stiffness variation

using higher order shear deformation theory, Composites Part B: Engineering 94 (2016) 109-121.

[151] **M. Amirpour**, **R. Das** and **E.I.S. Flores**, Bending analysis of thin functionally graded plate under in-plane stiffness variations, Applied Mathematical Modelling 44 (2017) 481-496.

[152] **T.V. Do**, **D.K. Nguyen**, **N.D. Duc**, **D.H. Doan** and **T.B. Quoc**, Analysis of bi-directional functionally graded plates by FEM and a new third-order shear deformation plate theory, Thin-Walled Structures 119 (2017) 687-699.

[153] **Z. Yu** and **F. Chu**, Identification of crack in functionally graded material beams using the p-version of finite element method, Journal of Sound and Vibration 325(1-2) (2009) 69-84.

[154] **M. Eftekhari**, **M. Eftekhari** and **M. Hosseini**, Crack detection in functionally graded beam using conjugate gradient method, International Journal of Engineering Transactions C 27(3) (2014) 367-374.

[155] **M.H. Abolbashari**, **F. Nazari** and **J.S. Rad**, A multi-crack effects analysis and crack identification in functionally graded beams using particle swarm optimization algorithm and artificial neural network, Structural Engineering and Mechanics 51(2) (2014) 299-313.

[156] **T. Yan**, **S. Kitipornchai**, **J. Yang** and **X.Q. He**, Dynamic behaviour of edge-cracked shear deformable functionally graded beams on an elastic foundation under a moving load, Composite Structures 93(11) (2011) 2992-3001.

[157] **T. Yan**, **S. Kitipornchai** and **J. Yang**, Parametric instability of functionally graded beams with an open edge crack under axial pulsating excitation, Composite Structures 93(7) (2011) 1801-1808.

[158] **T. Yan**, **J. Yang** and **S. Kitipornchai**, Nonlinear dynamic response of an edge-cracked functionally graded Timoshenko beam under parametric excitation, Nonlinear Dynamics 67(1) (2012) 527-540.

[159] **H.V. Tung** and **N.D. Duc**. Nonlinear analysis of stability for functionally graded plates under mechanical and thermal loads, Composite Structures 92(5) (2010) 1184-1191.

[160] **Y.S. Touloukian**, *Thermophysical Properties of High Temperature Solid Materials*, McMillan, New York, (1967).

[161] **R. Karwa**, *Heat and Mass Transfer*, Springer, Singapore, (2017).

[162] **M. Bayat**, **B.B. Sahari**, **M. Saleem**, **A. Ali** and **S.V. Wong**, Thermoelastic solution of a functionally graded variable thickness rotating disk with bending based on the first-order shear deformation theory, Thin-Walled Structures 47 (2009) 568-582.

[163] **C.L. Dym** and **I.H. Shames**, *Solid Mechanics – A Variational Approach*, McGraw-Hill Book Company Inc., New York, (1973).

[164] **A.S. Sekhar** and **B.S. Prabhu**, Crack detection and vibration characteristics of cracked shafts, Journal of Sound and Vibration 157(2) (1992) 375-381.

[165] **J. Zhang**, **R.J. Perez** and **E.J. Lavernia**, Documentation of damping capacity of metallic, ceramic and metal-matrix composite materials. Journal of Materials Science 28(9) (1993) 2395-2404.

[166] **M. Oravcová**, **P. Palček**, **M. Chalupová** and **M. Uhríčik**, Temperature dependent measurement of internal damping of austenitic stainless steels, in: MATEC Web of Conference 157 (2018) 07008. DOI: doi.org/10.1051/matecconf/201815707008.

List of Publications

Publications from the Present Thesis Work

Journals Publications (International)

1. **Debabrata Gayen**, Rajiv Tiwari and Debabrata Chakraborty, "Static and dynamic analyses of cracked functionally graded structural components: A review", ***Composites Part B: Engineering*** 173 **(2019)** 106982. **(Elsevier)**. DOI: doi.org/10.1016/j.compositesb.2019.106982

2. **Debabrata Gayen**, Rajiv Tiwari and Debabrata Chakraborty, "Finite element based stability analysis of a rotor–bearing system having a functionally graded shaft with transverse breathing cracks", ***International Journal of Mechanical Sciences*** 157-158 **(2019)** 403-414. **(Elsevier)**. DOI: doi.org/10.1016/j.ijmecsci.2019.04.056

3. **Debabrata Gayen**, Debabrata Chakraborty and Rajiv Tiwari, "Free vibration analysis of functionally graded shaft system with a surface crack", ***Journal of Vibration Engineering & Technologies*** 6(6) **(2018)** 483-494. **(Springer)**. DOI: doi.org/10.1007/s42417-018-0065-9

4. **Debabrata Gayen**, Debabrata Chakraborty and Rajiv Tiwari, "Finite element analysis for a functionally graded rotating shaft with multiple breathing cracks", ***International Journal of Mechanical Sciences*** 134 **(2017)** 411-423. **(Elsevier)**. DOI: doi.org/10.1016/j.ijmecsci.2017.10.027

5. **Debabrata Gayen**, Debabrata Chakraborty and Rajiv Tiwari, "Whirl frequencies and critical speeds of a rotor-bearing system with a cracked functionally graded shaft - Finite element analysis", ***European Journal of Mechanics – A/Solids*** 61 **(2017)** 47-58. **(Elsevier)**. DOI: doi.org/10.1016/j.euromechsol.2016.09.003

6. **Debabrata Gayen** and Debabrata Chakraborty, "Variation of local flexibility coefficients of functionally graded cracked shaft", ***Procedia Engineering*** 144 **(2016)** 1443-1450, (ICOVP 2015). **(Elsevier)**. DOI: doi.org/10.1016/j.proeng.2016.05.176

Conference Publications (International)

1. **Debabrata Gayen**, Debabrata Chakraborty and Rajiv Tiwari, "Transverse vibration and stability of a cracked functionally graded rotating shaft system", ***International Conference on Advances in Materials and Manufacturing Engineering*** **(ICAMME)**, March 15-17, **2019**, School of Mechanical Engineering, KIIT, Bhubaneswar, India. **(Paper No. 226)**

2. **Debabrata Gayen**, Debabrata Chakraborty and Rajiv Tiwari, "Stability behavior of two-crack functionally graded shaft in a rotor-disc system: finite element approach", ***3rd International Conference on Advances in Materials and Manufacturing Applications*** **(IConAMMA),** August 16-18, **2018**, Amrita School of Engineering, Bengaluru, India. **(Paper No. 92)**

3. **Debabrata Gayen**, Debabrata Chakraborty and Rajiv Tiwari, "FE approach for dynamic response of a functionally graded spinning shaft system containing a transverse fully open crack", ***3rd International Conference on Advances in Materials and Manufacturing Applications*** **(IConAMMA)**, August 16-18, **2018**, Amrita School of Engineering, Bengaluru, India. **(Paper No. 72)**

4. **Debabrata Gayen**, Debabrata Chakraborty and Rajiv Tiwari, "FE based free vibration and stability analysis of a rotor-disk-bearing system having a functionally graded shaft: A thermo-mechanical analysis", ***2nd International Conference on Advances in Dynamics, Vibration and Control*** **(ICADVC)**, June 6-8, **2018**, NIT Durgapur, Durgapur, India. **(Paper No. 7)**. Published in Int. Journal of Mechanical and Production Engineering Research and Development (IJMPERD), 9-16 (**2018**).

5. **Debabrata Gayen**, Debabrata Chakraborty and Rajiv Tiwari, "Free vibration and stability analysis of a functionally graded spinning shaft in rotor-disk-bearing system: Finite element approach", ***2nd International Conference on Advances in Dynamics, Vibration and Control*** **(ICADVC)**, June 6-8, **2018**, NIT Durgapur, Durgapur, India. **(Paper No. 6)**. Published in Int. Journal of Mechanical and Production Engineering Research and Development (IJMPERD), 478-485 (**2018**).

6. **Debabrata Gayen**, Debabrata Chakraborty and Rajiv Tiwari, "Parametric study on free vibration and instability of a functionally graded cracked shaft in a rotor-disc-bearing system: finite element approach", ***3rd International Conference on Design, Analysis, Manufacturing & Simulation*** **(ICDAMS)**, April 6-7, **2018**, Saveetha University, Chennai, India. **(Paper No. 161 & Best paper award)**. Published in **MATEC Web of Conferences** 170, 03009-16 (**2018**). DOI: doi.org/10.1051/matecconf/201817203009

7. **Debabrata Gayen**, Debabrata Chakraborty and Rajiv Tiwari, "Finite element approach for a parametric study on vibration response of a functionally graded shaft using temperature dependent material properties", ***7th International Conference on Theoretical, Applied, Computational and Experimental Mechanics*** **(ICTACEM)**, December 28-30, **2017**, IIT Kharagpur, Kharagpur, India. **(Paper No. 642)**

8. **Debabrata Gayen**, Debabrata Chakraborty and Rajiv Tiwari, "Finite element analysis for dynamic response of rotor-bearing system with cracked functionally graded turbine shaft", ***Proceedings of the ASME Gas Turbine India Conference*** **(GTINDIA)**, December 7-8, **2017**, Bangalore, India. **(Paper No. GTINDIA 2017-4534)**. DOI: doi:10.1115/GTINDIA2017-4534

9. **Debabrata Gayen**, Debabrata Chakraborty and Rajiv Tiwari, "Determination of local flexibility coefficients of a functionally graded shaft with breathing crack", ***13th International Conference on Vibration Problems*** **(ICOVP)**, November 29 – December 2, **2017**, IIT Guwahati (India) and IŞIK University (Turkey), IIT Guwahati, Guwahati, India. **(Paper No. 18)**

10. **Debabrata Gayen**, Debabrata Chakraborty and Rajiv Tiwari, "Finite element analysis for free vibration analysis of functionally graded shaft", ***Proceedings of 61st Congress of The Indian Society of Theoretical and Applied Mechanics*** **(ISTAM)**, December 11-14, **2016**, VITU, Vellore, India. **(Paper No. 404)**

11. **Debabrata Gayen**, Debabrata Chakraborty and Rajiv Tiwari, "A FE model for dynamic behavior of a functionally graded rotor-bearing system", ***6th International***

Congress on Computational Mechanics and Simulation **(ICCMS)**, June 27 – July 1, **2016**, IIT Bombay, Mumbai, India. **(Paper No. 169)**

Conference / Symposium Publications (National)

1. **Debabrata Gayen**, Rajiv Tiwari and Debabrata Chakraborty, Thermo-mechanical analysis of a rotor-bearing system having a functionally graded shaft with transverse breathing cracks", ***6th National Symposium on Rotor Dynamics*** **(NSRD)**, July 2-3, **2019**, CSIR-National Aerospace Laboratories, Bangalore, India. **(Paper No. 33)**

About the Author

Mr. Debabrata Gayen is youngest son of Mr. Nirmal Gayen and Ms. Rani Bala Gayen and he born in the year of 1990. He completed his Class – X and Class – XII from West Bengal Board in the year 2005 and 2007 respectively secureing first division in both the examinations. He completed his Bachelor of Technology (BTech) in Mechanical Engineering from Jalpaiguri Government Engineering College, West Bengal in the year of 2011 securing first division. He completed his Master of Technology (MTech) in Machine Design and Analysis from Mechanical Engineering Department of National Institute of Technology Rourkela (NIT Rourkela) in 2013 and secured first division. He joined Mechanical Engineering Department, Indian Institute of Technology Guwahati (IIT Guwahati) as a regular research scholar in the year 2013. His areas of research are finite element based linear vibration of Rotor dynamical systems, structures made of functionally graded materials (FGMs) and composites materials, and fracture mechanics.